Dissimilar titanium and titanium aluminide joints manufactured by laser beam welding and laser additive manufacturing

Vom Promotionsausschuss der

Technischen Universität Hamburg

zur Erlangung des akademischen Grades

Doktor-Ingenieurin (Dr.-Ing.)

genehmigte Dissertation

von

Irmela Irene Solveig Burkhardt

aus

Moers

2021

1. Gutachter: Herr Prof. Dr.-Ing. habil. Norbert Huber
2. Gutachter: Herr Prof. Dr.-Ing. habil. Florian Pyczak

Vorsitzender des Prüfungsausschusses: Herr Prof. Dr.-Ing. habil. Bodo Fiedler

Tag der mündlichen Prüfung: 12.10.2020

DOI: https://doi.org/10.15480/882.3228

Abstract

The growing awareness concerning the effects of climate change increases the demand for lightweight constructions in aviation and space industry. Consequently, the call for new material combinations, design and manufacturing concepts raises significantly. To obtain constructions with less weight, lighter or stronger materials must substitute prevalent ones. Furthermore, the utilization of different materials in the structure enables the tailoring of structural properties. For this purpose, suitable manufacturing processes for joining and generating are required.

Titanium aluminides, and in particular γ-TiAl such as TNM, are promising candidates for lightweight constructions, which are already applied in aircraft engines. Nevertheless, due to their crack-sensitivity resulting from evolving brittle phases and thermally induced stresses, fusion welding of γ-TiAl is still very challenging. Moreover, to generate dissimilar joints, the differing thermophysical properties and chemical compositions have to be considered. Laser beam welding is an efficient and established joining method, whereas laser additive manufacturing processes such as laser metal deposition gain increasing importance in production of metallic structures. Both laser processes utilize a localized laser beam as a moving heat source implying certain process similarities. Currently, there is a lack of knowledge and approaches for obtaining dissimilar Ti-alloy joints and especially γ-TiAl-Ti-alloy joints. Furthermore, knowledge about the influence of microstructure and phases at the interfaces on the resulting mechanical properties is missing.

The present thesis aims to obtain crack-free dissimilar Ti- and γ-TiAl-Ti-alloy joints, despite the crack-sensitivity of γ-TiAl and the different thermophysical properties as well as chemical compositions, by focusing on laser beam welding as the joining method. For this purpose, theoretical considerations, process parameter studies and various characterization techniques were used in order to gain a deeper understanding of the crack formation, microstructure and phase evolution of dissimilar joints. Moreover, the influence of the microstructure-phase combination at the interface on the mechanical properties was investigated. Based on the obtained knowledge from laser beam welding and extending the thesis, the transferability to laser metal deposition, with focus on the interface evolution and crack formation, was studied.

In the course of a comprehensive experimental study, crack-free joints of γ-TiAl-Ti-alloy sheet material were obtained by preheating. Due to the overlapping process windows for the similar Ti-alloys and γ-TiAl joints, no additional measures were necessary. Furthermore, the crack formation could be correlated to the microstructure-phase evolution for laser beam welded similar γ-TiAl and γ-TiAl-Ti-alloy joints. The assessment of the dissimilar γ-TiAl-Ti-alloy joints by tensile tests revealed the influence of the dissimilar interface on the fracture position and tensile properties. The gained knowledge from laser beam welding regarding the microstructure and phase evolution at the interface could be successfully transferred to the laser metal deposited dissimilar Ti-Ti-alloy and γ-TiAl-Ti-alloy depositions. Besides, the limited transferability concerning the crack formation was demonstrated. Hence, the fundamentals for crack-free γ-TiAl-Ti-alloy joints by laser beam welding and laser metal depositions were established.

Zusammenfassung

Durch das steigende Bewusstsein über die Auswirkungen des Klimawandels, nehmen die Anforderungen für Leichtbaukonstruktionen in der Luft- und Raumfahrt zu. Daher werden Leichtbaukonstruktionen mit unterschiedlichen Materialien, neuen Design- und Herstellungskonzepten erforderlich. Um Konstruktionen mit geringerem Gewicht zu erhalten, können eingesetzte Materialien durch leichtere oder höherfestere Materialien substituiert werden. Die Notwendigkeit maßgeschneiderter Struktureigenschaften ruft den Einsatz von unterschiedlichen Materialien in einem Bauteil hervor, weshalb geeignete Herstellungsprozesse für das Fügen und Generieren benötigt werden.

Titanaluminide und insbesondere γ-TiAl-Legierungen, wie TNM, werden bereits in Flugzeugtriebwerken eingesetzt und sind vielversprechende Kandidaten für Leichtbaukonstruktionen. Aufgrund ihrer Rissempfindlichkeit, welche aus spröden Phasen und thermisch induzierten Spannungen resultiert, ist das Schmelzschweißen von γ-TiAl weiterhin herausfordernd. Zudem müssen bei der Herstellung von ungleichartigen Verbindungen die unterschiedlichen thermophysikalischen Eigenschaften und chemischen Zusammensetzungen berücksichtigt werden. Das Laserstrahlschweißen ist ein effizientes und etabliertes Fügeverfahren, während die Bedeutung der laserbasierten additiven Fertigung, wie das Laserauftragschweißen, für metallische Strukturen steigt. Derzeit existiert eine Wissenslücke und ein Mangel an Konzepten, um ungleichartige Ti- und im speziellen γ-TiAl-Ti-Legierungs-Verbindungen herzustellen. Zudem liegen keine Erkenntnisse bezüglich des Einflusses der Mikrostruktur und Phasen an der Grenzfläche auf die mechanischen Eigenschaften vor.

Mit dem Fokus auf dem Laserstrahlschweißen ist das Ziel der vorliegenden Arbeit rissfreie ungleichartige Ti- und γ-TiAl-Ti-Legierungs-Verbindungen, trotz der Rissempfindlichkeit von γ-TiAl und der unterschiedlichen thermophysikalischen Eigenschaften sowie chemischen Zusammensetzungen, herzustellen. Um ein tiefergehendes Wissen über die Rissbildung, Mikrostruktur- und Phasenentwicklung bei ungleichartigen Verbindungen zu gewinnen, wurden theoretische Abschätzungen, Parameterstudien sowie verschiedene Charakterisierungsmethoden eingesetzt. Ferner wurde der Einfluss der vorliegenden Mikrostruktur und Phasen an der Grenzfläche auf die mechanischen Eigenschaften untersucht. Als Erweiterung der Arbeit wurde die Übertragbarkeit des mittels Laserstahlschweißen gewonnen Wissens auf das Laserauftragschweißen, mit dem Fokus auf die Entwicklung der Grenzfläche und der Rissentstehung, geprüft.

Im Zuge einer umfassenden experimentellen Studie konnten rissfreie γ-TiAl-Ti-Legierungs-Verbindungen aus Blechen mittels vorgeheiztem Laserstahlschweißen hergestellt werden. Aufgrund der überlappenden Prozessfenster der gleichartigen Ti- und γ-TiAl-Legierungs-Verbindungen waren hierfür keine weiteren prozesstechnischen Maßnahmen notwendig. Darüber hinaus konnte die Rissbildung bei laserstahlgeschweißten gleichartigen γ-TiAl- und ungleichartigen γ-TiAl-Ti-Legierungs-Verbindungen der Mikrostruktur- und Phasenentwicklung zugeordnet werden. Die mechanische Prüfung der γ-TiAl-Ti-Legierungs-Verbindungen zeigte den Einfluss der Grenzfläche auf den Versagensort und die Zugeigenschaften auf. Als Erweiterung der Arbeit konnte das mittels Laserstrahlschweißen gewonnene Wissen bezüglich der Mikrostruktur- und Phasenentwicklung an der Grenzfläche erfolgreich auf laserauftragsgeschweißte ungleichartige Ti-Ti- und γ-TiAl-Ti-Legierungs-Strukturen übertragen werden. Außerdem wurden die Grenzen der Übertragbarkeit hinsichtlich der Rissbildung aufgezeigt. Folglich wurden die Grundlagen für die Herstellung rissfreier γ-TiAl-Ti-Legierungs-Verbindungen mittels Laserstrahlschweißen und Laserauftragsschweißen erarbeitet.

Content

Nomenclature

Variables and material parameters

A	(mm^2)	Laser spot size
A/V	(m^{-1})	Surface-to-volume ratio
BTDT	(°C)	Brittle-to-ductile temperature
C_{gas}	(l/min)	Carrier gas flow rate
CTE	($°C^{-1}$)	Thermal coefficient of linear expansion
d	(mm)	Laser spot diameter
d_{max}	(µm)	Grain diameter major axis
d_{min}	(µm)	Grain diameter minor axis
E	(W)	Energy
f	(mm)	Focal position laser beam
K-factor	(-)	Ratio of filler wire speed and process velocity
LE	(J/m)	Line energy
N_{gas}	(l/min)	Nozzle gas flow rate
Ø	(mm)	Filler wire diameter
P	(kW)	Laser power
Q	(W)	Welding power
R	(rmp)	Powder plate rotational speed
R_m	(MPa)	Tensile strength
$R_{p0.2}$	(MPa)	Yield strength
t	(s)	Time
T_0	(K)	Initial workpiece temperature
T_{eu}	(°C)	Eutectic temperature
T_{ph}	(°C)	Preheating temperature
t_s	(m)	Sheet thickness
T_β	(°C)	β-transus temperature
$T_{\gamma, solv}$	(°C)	γ-solvus temperature
UTS	(MPa)	Ultimate tensile strength
v	(m/min)	Process velocity
YS	(MPa)	Yield strength
v_w	(m/min)	Filler wire speed
η	(m·Pa·s)	Viscosity
λ	($W\ m^{-1}\cdot K^{-1}$)	Thermal conductivity
ρ	(kg/m^3)	Density
ρ_P	(W/m^3)	Power density
σ	($N\cdot m^{-1}$)	Surface tension
τ	(-)	Differentiation parameter for Rosenthal equations

Abbreviations

AM	Additive Manufacturing
Bcc	Body center cubic
BM	Base material
DED	Direct energy deposition
EBSD	Electron backscatter diffractometry
EDX	Energy dispersive X-ray analysis
FC	Furnace cooled
FL	Fusion line
FZ	Fusion zone
g	Heat source
HAZ	Heat-affected zone
Hcp	Hexagonal closely packed
HIP	Hot isostatic pressed
LBW	Laser beam welding
LMD	Laser metal deposition
LMpD	Laser metal powder deposition
LMwD	Laser metal wire deposition
OM	Optical microscopy
p	Powder
PBF	Powder bed fusion
PWHT	Post weld heat treatment
RD	Rolling direction
RT	Room temperature
s	Substrate
SEM	Scanning electron microscope
SLM	Selective laser melting
TD	Transversal direction
TTT	Time-temperature-transformation diagram
w	Filler wire
WAAM	Wire and arc manufacturing
X=(ξ,η,ς)	Room directions
X_e	Variable paramteres
XRD	X-ray diffraction

1. Introduction

1.1. Motivation

The political and social pressure to decrease the CO_2 emission is consistently growing. In 2014, the share of aviation to climate change was about 2.5 % [1]. To decrease the CO_2 emission three different approaches are intended: generating a higher aerodynamic efficiency, increasing the efficiency of engines and substituting prevalent materials by stronger or lighter new ones.

Titanium (Ti) alloys possess a high strength-to-weight ratio, good oxidation and creep properties [2]. Hence, they are used in a wide range of applications, in which the aerospace industry is the largest user [2]. The most widely used Ti-alloy is Ti-6Al-4V (Ti64) because of its balanced properties [2]. In contrast, Ti-6Al-2Mo-4Zr-2Sn (Ti6242) is a classical high temperature alloy with the advantages of a higher creep resistance [2,3] and lower oxidation kinetics [4] compared to Ti64. Furthermore, a higher service temperature can be utilized as the long-term service temperature of Ti64 is in the range of 300 °C to 400 °C and for Ti6242 between 425 °C and 450 °C [2,3]. For titanium aluminides (TiAl), large research activities started in the 1980s [5], which extent the service temperature for Ti-based alloys up to 800 °C [6] (Figure 1 (a)). In spite of having half the density of nickel superalloys, the elastic modulus of TiAl at its operating temperature reaches the value of nickel superalloys [6,7]. Furthermore, their specific strength at the operating temperatures 600 °C to 800 °C is at least similar to nickel superalloys [8] (Figure 1 (b)). Therefore, TiAl has the potential to partly replace nickel superalloys. However, the main challenge of TiAl is their low room temperature (RT) ductility and crack sensitivity. To improve the ductility of the brittle material, so called β-solidifying γ-TiAl like TNM (Ti-43.5Al-4Nb-1Mo-0.1B) was developed [6]. γ-TiAl is already applied in turbochargers [9] and since 2011 most successfully in the GEnX jet engine of General Electric [5]. Moreover, TNM blades equip the new geared turbofan (GTF™) by Pratt and Whitney, which is employed in the Airbus A320neo [10].

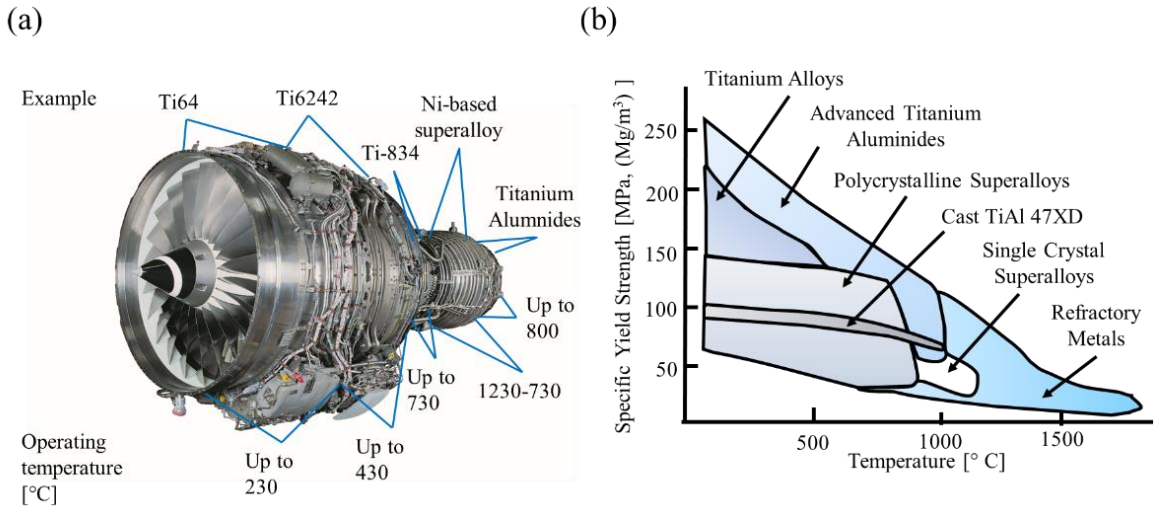

Figure 1: (a) Setup of an aircraft engine utilizing different Ti-alloys for different operating temperatures with kind authorization of MTU Aero Engines AG. (b) Specific yield strength dependent on temperature according to [8].

1. Introduction

The requirement of sheet materials possessing a high temperature stability, a low weight and a high strength for aircraft engine exhaust linings was the motivation for γ-TiAl sheets, which led to the development of TNM sheets [11]. For TNM sheets, the production by conventional rolling was possible [6] and the resulting mechanical properties are influenced by the evolving microstructure and phases [12,13]. Besides, the sheet properties fulfilled the requirements of flat hot gas structures in aircraft engines [11]. Further applications for TNM sheets in air- and spacecrafts are the skin material, thermal and acoustic protection systems, gas leading parts [14,15] and exhaust nozzles [16].

To produce the aforementioned applications of TNM sheets, the manufacturing of complex parts must be enabled. Therefore, the joining to the same and other materials, hence manufacturing of similar and dissimilar joints, is the crucial key for the industrial utilization. Dissimilar joints can be necessary depending on the operating conditions accounting for different mechanical properties required in different part regions, materials and expense saving as well as design complexity [17–19] (Figure 1 (a)). Nevertheless, in the past the complex issue of dissimilar joints has attracted less attention [18]. The complexity can be divided in the process- and the material-based challenges. From the material point of view, joining of dissimilar alloys is challenging due to different thermomechanical properties and chemical compositions influencing the microstructure and phase evolution [20]. Consequences can be the generation of brittle phases [21], asymmetric joints [22], caused by different melting points and thermal conductivities, the formation of porosity and cracks, especially for the crack sensitive γ-TiAl. Furthermore, the different thermophysical properties can lead to different mixing behaviors and hence to inhomogeneous chemical compositions. The mixing behavior is also influenced by the utilized joining process, which determines the degree of melting of the joining partners to a certain extent. All these factors have an effect on the processability and the resulting mechanical properties. Moreover, for dissimilar joints, special attention has to be paid to the interface evolution, especially concerning their influence on the mechanical properties. As the service temperature increases from Ti64 via Ti6242 to TNM, joining of the three aerospace authorized alloys to each other would enable new design possibilities and enlarge the use of γ-TiAl alloys. This is the key motivation of the present thesis. Fusion welding has shown its suitability for welding of Ti-alloys by arc, laser and electron beam welding [3,23,24]. Additionally, fusion welding is beneficial, because it is suitable for various joint types and the resulting joints have a high strength compared to most conventional welding methods [25]. Compared to the other fusion welding processes, laser beam welding (LBW) is advantageous due to the low process time, high flexibility of the weld geometry as well as the small heat-affected zone (HAZ) [26,27] and therefore suitable for joining sheets.

Ti64 and Ti6242 are weldable and hence LBW of similar Ti64 and Ti6242 joints is established, even so the research results on Ti6242 are limited [3,28–32]. In contrast, the joining of γ-TiAl is still challenging due to its tendency to form brittle phases [33–35], their high reactivity [2] and crack susceptibility [35–38]. Cold cracking is the result of thermally induced stresses and the formation of brittle phases [37,39,40]. Investigated joining methods are brazing [41–43], diffusion bonding [20,44–46], friction welding [47], reactive joining [33,48] and fusion welding [34,35,37,49,50]. Nevertheless, the general knowledge about similar TNM joints is very limited. Few LBW studies dealing with TNM, one using bead-on-plate specimens [51] and another utilizing a defocused CO_2 laser beam to preheat the TNM sheets prior to LBW [52], exist. Moreover, for similar LBW TNM joints the correlation

between the microstructure-phase evolution and the crack formation is unknown. This motivates the investigation of similar TNM joints. For LBW some dissimilar Ti-Ti- and Ti-Al-alloy joints have been investigated [17,18,53,54], but no data for Ti64-Ti6242 joints is available. Dissimilar γ-TiAl joints with nickel superalloys [43,55], steel [56] and Ti-alloys [20,22] as a joining partner were investigated by LBW. Dissimilar TNM-steel and TNM-nickel superalloy joints by friction welding and fusion welding with a CO_2 laser showed insufficient reproducibility [52]. Consequently, data for dissimilar TNM joints obtained by LBW is missing.

Enabling new design possibilities, material saving and the generation of complex parts, additive manufacturing (AM) gains increasing importance [57]. Furthermore, by its layer-by-layer process principle, AM could be another manufacturing route for the generation of dissimilar joints. Focusing on the direct energy deposition (DED) processes with a laser beam as a heat source, known as laser metal deposition (LMD), two feedstock materials, wire and powder, are available for the deposition on a substrate. Laser metal wire deposition (LMwD) is typically utilized for the fabrication of large parts. Compared to LMwD, laser metal powder deposition (LMpD) is predominantly used for the fabrication of small parts with higher surface quality [58–60]. LBW and LMD utilize a laser beam as a heat source, which melts the material. Thereby, comparable to LBW, the solidification and hence the microstructure as well as phase evolution are influenced [58]. Hence, the mature knowledge of LBW and metallurgy can provide powerful synergistic benefits for the deeper understanding of AM.

Similar LMwD and LMpD research focuses on Ti64 feedstock material and only a few studies on Ti6242 powder are available [61–64]. γ-TiAl tested powders by LMpD included TNM [65,66]. For LMwD and LMpD most research focuses on similar Ti64 depositions [62–64], whereas research on dissimilar Ti-Ti-alloy depositions is lacking. For dissimilar γ-TiAl depositions, the available data is even more restricted. Due to the unavailability of γ-TiAl wire, no dissimilar depositions by LMwD are conducted. LMpD dissimilar deposition with two different γ-TiAl powders, utilizing mostly Ti64 as a substrate were performed [67–69].

Moreover, utilizing the Mo-equivalent [2] for the β-stabilizing element and assuming a homogeneous mixing, in the Calphad database no information for lower aluminum (Al) contents (< 32.5 mol.%) regarding the evolving phases in dissimilar TNM-Ti6242 and TNM-Ti64 joints is available (Figure 2).

Consequently, for the three authorized aerospace alloys Ti64, Ti6242 and TNM a knowledge gap for dissimilar Ti64-Ti6242 as well as dissimilar TNM joints and depositions by laser-based processes arises, which further motivates the thesis.

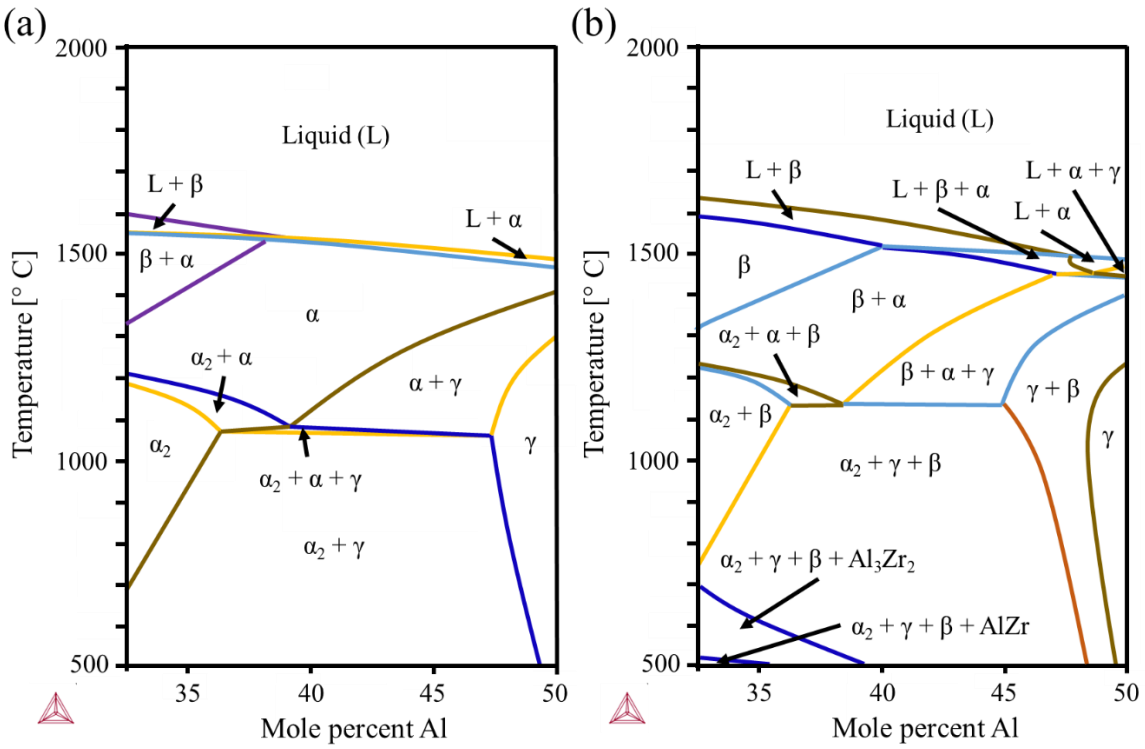

Figure 2: Generated phase diagram with Calphad database for (a) dissimilar TNM-Ti64 and (b) TNM-Ti6242 joints depending on the Al content. For the calculation, the Mo-equivalent of the *β*-stabilizing elements is applied. In the calculation of the phase diagram, a homogeneous mixing of the respective alloys is assumed.

1.2. Objectives

The demand for multi-material structures, and the lacking process as well as material science knowledge concerning dissimilar Ti-Ti- and *γ*-TiAl-Ti-alloy joints motivate the objectives of this thesis. Due the mature knowledge on LBW similar joints, the major focus is on LBW of thin sheets for dissimilar Ti64-Ti6242 and dissimilar TNM-Ti-alloy joints. Taking the increasing importance of LMD and its close relationship to LBW into account, a minor part of the thesis also deals with dissimilar Ti64-Ti6242 and dissimilar TNM-Ti-alloy depositions. The objectives are as follows:

1. The first objective is to establish overlapping LBW process windows of the similar joints, despite the different thermophysical properties and chemical compositions, to establish the fundamental requirement of dissimilar joints without further measures.
2. The second objective is the development of crack-free dissimilar LBW joints with TNM sheets to identify the technological requirements for these. This is challenging due to the crack sensitivity of *γ*-TiAl alloys, the different thermophysical properties and chemical compositions of the utilized alloys.
3. The third objective is the characterization of the evolving microstructures, phases, chemical compositions, mechanical properties of dissimilar LBW TNM joints and the subsequent interlinking to the LBW process parameters. Considering the dissimilarity of the joints, a special focus is on the evolving interface region. To investigate the mechanical properties, a suitable manufacturing process for tensile samples and a new testing set-up for similar and dissimilar sheet

joints for high temperature tests must be developed. Thereby, the material science based fundamentals for dissimilar LBW TNM joints are determined.

4. Extending the present thesis and emphasizing the relevance of the gained knowledge, the fourth objective is the investigation of the transferability of findings from LBW to LMD in terms of microstructure, phases and crack formation. The focus is on thin sheet substrates as an extension of the LBW dissimilar thin sheet joints and the evolving dissimilar interface region.

1.3. Structure of thesis

To obtain the mentioned objectives, the structure in Figure 3 is utilized. For reasons of transferability and comparison between the processes the laser type, optic and fiber are kept as far as possible the same. Only for LMpD a different laser type, optic and fiber has to be utilized. As the first deposited layer is the most fundamental region for the bonding of dissimilar depositions [70], a special focus has to be given to the evolving interface region in dissimilar joints. For this reason, only single-layer LMD depositions are investigated in this thesis.

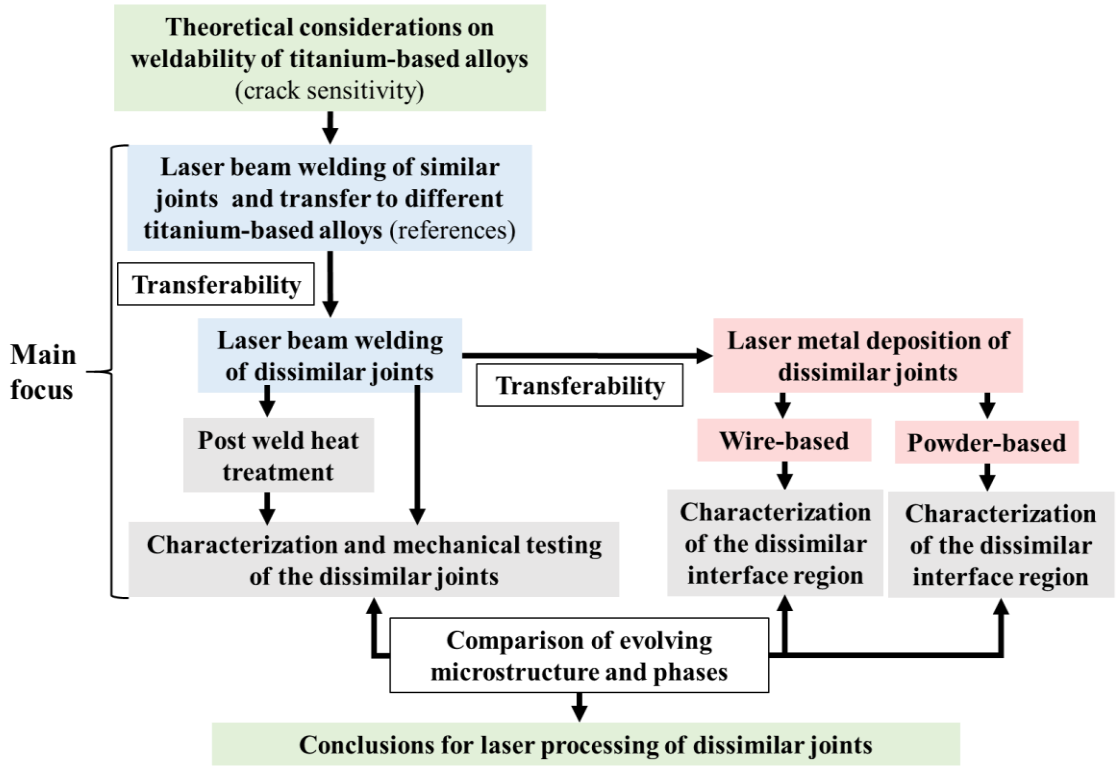

Figure 3: Structure of the thesis decipting the scientific approach.

The main focus is on LBW, the most mature joining process in this thesis (Chapter 5.1). Due to the crack sensitivity of TNM, theoretical considerations regarding the cooling rate and temperature distribution are utilized to maintain a further comprehension concerning the crack formation in similar and dissimilar TNM joints manufactured by LBW (Chapter 5.1., 5.2.). Starting with similar Ti64, then similar Ti6242 and finally similar TNM joints, the cost of the material increases and furthermore the amount of knowledge as well as degree of weldability decreases. Each alloy has its own process window for similar joints and through the investigation of the process windows, it is determined, whether the process windows overlap. Consequently, if the fundamental requirement for dissimilar LBW joints

without further measures, overlapping process windows of similar joints, is achieved (Chapter 5.1.). Besides, effects of the laser beam-material interactions are studied. For crack-free similar TNM joints, the influence of different preheating temperatures, laser powers and process velocities are examined. The joints are characterized with regard to their microstructure, phases, chemical composition and mechanical properties with a particular focus on the interface regions. Thereby, the process, microstructure, phase and mechanical properties are correlated to each other.

Chapter 5.2. deals with the generation of dissimilar Ti64-Ti6242, TNM-Ti64 and TNM-Ti6242 joints by LBW. For dissimilar TNM-Ti-alloy joints the focus is on dissimilar TNM-Ti6242 joints as the service temperatures of these alloys are closest. To achieve crack-free dissimilar TNM-Ti-alloy joints, different preheating temperatures are tested. The subsequent characterization in terms of microstructure, evolving phases, chemical composition and local mechanical properties, enable the identification of the relationship between them and the process. The dissimilar interface regions are analyzed in particular.

With regard to potential applications at elevated service temperature, tensile tests at different temperatures for similar Ti6242, TNM and dissimilar TNM-Ti6242 joints are performed to determine the mechanical properties and the fracture behavior (Chapter 5.3.). Thus, the correlation between process, evolving microstructure and phases as well as mechanical properties for the aforementioned joints are identified.

In means of transferability of the knowledge gained by LBW and as an extension of the thesis, two LMD processes for dissimilar Ti-Ti alloy (Chapter 6.1.) and dissimilar TNM-Ti-alloy (Chapter 6.2.) depositions are investigated. The theoretical cooling rates of LBW and both LMD processes are utilized to analyze similarities and differences of the processes. In the subsequent characterization, results of the microstructure, phase evolution, chemical composition and local mechanical properties of dissimilar deposition are compared to dissimilar LBW joint results. Due to the dissimilar nature of the depositions, special attention is given to the interface region and the transferability is examined regarding the microstructure and phase evolution at this position. Furthermore, for dissimilar TNM-Ti-alloy depositions the transferability from LBW to LMD concerning the crack formation is studied. Thereby, the transferability of gained knowledge by LBW to LMD and its limits are revealed.

As no γ-TiAl wire is available for LMwD, the dissimilar LMwD and LMpD depositions in Table 1 are tested.

Table 1: Investigated dissimilar depositions by LMwD and LMpD.

LMD process	**Filler material (filler wire (w)/powder (p))**	**Substrate (s)**
LMwD	Ti6242	Ti64
	Ti6242	TNM
	Ti64	TNM
LMpD	Ti6242	Ti64
	TNM	Ti64

2. Titanium-based materials

Ti has a density of 4.5 g/cm³ and therefore belongs to the light metals. The allotrope element with the body center cubic (bcc) high-temperature phase β and the hexagonal closely packed (hcp) low-temperature phase α is displayed in Figure 4 [2].

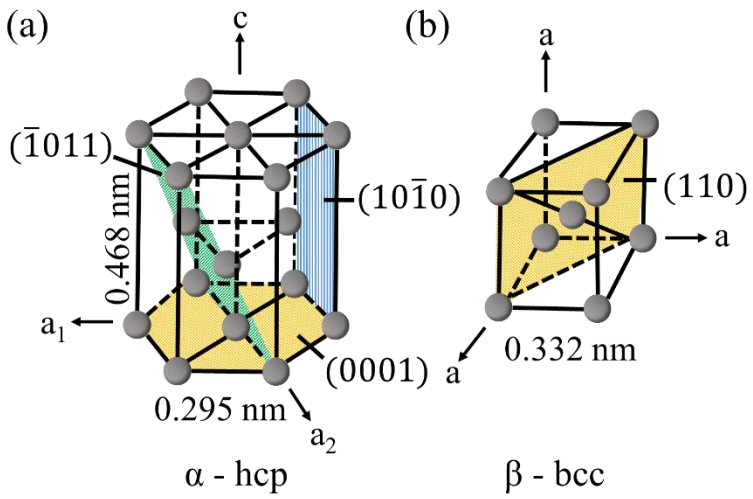

Figure 4: Crystal structure of the (a) hcp low-temperature phase α and (b) the bcc high-temperature phase β according to [2].

The temperature at which the phase change occurs is called β-tranus temperature and is influenced by the alloying elements as for example molybdenum (Mo), niob (Nb), vanadium (V) [2]. The solid-state transformation from $\beta \rightarrow \alpha$ follows the Burgers orientation relationship: $\{110\}_\beta \parallel (0001)_\alpha$ and $<111>_\beta \parallel <11\bar{2}0>_\alpha$ [2]. The microstructure and phase composition is influenced by the cooling rate and heat treatments. Ti is notch sensitive and has anisotropic mechanical properties [3]. Furthermore, its high affinity to air constituents results in a high reactivity of the melt. For this reason, the melt pool needs protection against oxidation for example through shielding gas [2].

2.1. Titanium alloys

Ti-alloys have a high strength-to-weight ratio, good oxidation and creep properties, are biocompatible and corrosion resistant against many medias [2,71]. The service temperature of special Ti-alloys is up to 600 °C. Hence, they are used for a wide range of applications in lightweight constructions, chemical industry, medical applications, aircraft and space industry. In general, the diffusionless transition from bcc β-phase to martensite occurs in all Ti-alloys for sufficiently high cooling rates above the martensite start temperature. Depending on the start temperatures hexagonal α`martensite or for lower temperatures ~900 °C orthorhombic α``martensite is formed [2].

Ti-6Al-4V (Ti64) is an α+β alloy and the most commonly used Ti-alloy [2]. Due to its balanced properties, it is applied in aircrafts, the chemical industry and medical devices [72]. The β-transus temperature is 995 °C and the long-term service temperature in the range between 300 °C to 400 °C [2,3]. When α+β alloys are cooled form the β-phase field at high cooling rates, a high dislocation density is created [72]. Fully martensitic microstructures are achieved with cooling rates above 410 °C/s [73].

Ti-6Al-2Sn-4Zr-2Mo (Ti6242) is a classical high temperature near-α alloy, which is primarily utilized for gas turbine components like compressor blades, sheets for engines after the burner structure and hot air skin applications. Ti6242 sheets consist of 80-90 % of primary α-phase [3]. The β-transus temperature is 995 $\pm$ 15 °C and the long-term service temperature between 425 °C and 450 °C [2,3]. Advantages compared to Ti64 are the higher creep resistance [2,3], lower oxidation kinetics [4] and the higher long-term service temperature [2,3].

2.2. Titanium aluminide alloys

Intermetallic γ-TiAl-alloys were introduced to extend the utilization of Ti-alloys especially in aerospace applications [5]. These are characterized by a low density (3.9-4.2 g/cm³), high specific strength, particular between 600-800 °C, resistance against "titanium fire", good oxidation and creep resistance [5,6,8]. Having a similar or inferior specific strength (Figure 1 (b)), the aim is to replace or partially substitute the heavier nickel superalloys, having a density of ~ 8 g/cm³, [5,8,10,74].

The major challenge for γ-TiAl is the low RT ductility of approximately 1-2 % [8]. In literature even RT ductilities as low as 0.2 % are reported [75,76]. Depending on the alloy and the process route the RT yield strength of γ-TiAl is between ~400–950 MPa [77,78]. The temperature, where the fracture mode changes from brittle to ductile, is called brittle-to-ductile temperature (BTDT), which is influenced by the chemistry, microstructure and the testing conditions [6].

The main phases in γ-TiAl during solidification are the bcc β- and ordered cubic β_O-, hexagonal α- and ordered hexagonal α_2-, and ordered tetragonal γ-phase (Figure 4, Figure 5). Below 950 °C further stable and unstable phases, which are related to α_2- and β_O-phase, can evolve.

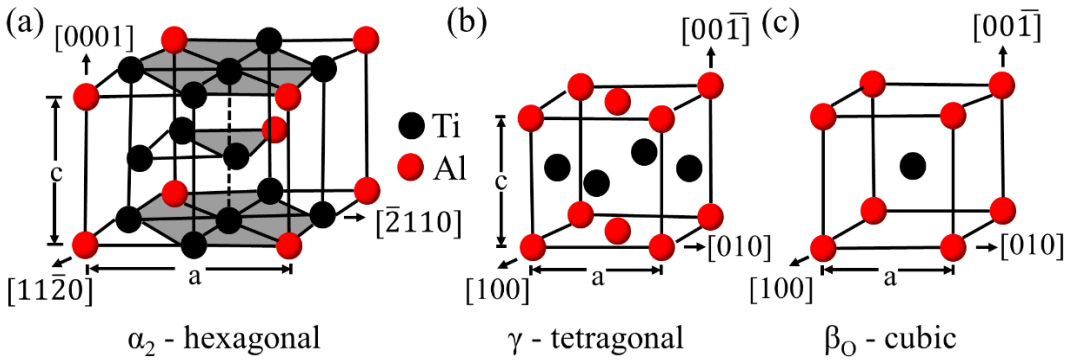

Figure 5: Crystallographic structure of the ordered (a) hexagonal α_2-, (b) tetragonal γ- and (c) cubic β_O-phase according to [7].

The high temperature bcc β-phase (crystal structure A2) has a fast transformation kinetic to α [13]. The retained β-phase can undergo the fast phase ordering process to the β_O-phase (crystal structure B2). Regarding the hardness, the value is higher for the β_O-phase than for the α_2-phase [79]. Moreover, the β_O-phase tends to embrittle the material [6]. Concerning the deformation of β- and β_O-phase, the slip systems of β- and β_O-phase depend on the alloy composition, the degree of order, the point defect situation and deformation condition. In the β-phase, sufficient independent slip systems are available. For the β_O-phase the slip system choice depends on the degree of order. Alloys with a high ordering

energy have the tendency for only three independent slip systems, while for weakly ordered β_O-phase the von Mises criteria is satisfied [7].

For the hexagonal phase, a high temperature unordered α-phase (crystal structure A3) and low temperature ordered α_2-phase (Ti_3Al; crystal structure $D0_{19}$) configuration exists [7]. The ordering reaction occurs at the eutectic temperature T_{eu} [6]. The ordering process is very fast, hence it is practical impossible to obtain unordered α-phase at RT [80]. The α_2-phase is more brittle than the γ-phase [81]. Besides, the α_2-phase shows a plastic anisotropic and inhomogeneous deformation behavior [82]. For extremely fast to high cooling rates the martensitic α_2'-phase is generated [2,83,84].

The ordered face-centered tetragonal γ-phase (crystal structure $L1_0$) deforms plastically [85], and the presence of γ-grain boundaries seems to be essential for RT ductility [75]. The orientation relationship between α_2- and γ-phase according to Blackburn is as follows: $\{111\}_\gamma \parallel (0001)_{\alpha 2}$ and $<1\bar{1}0>_\beta \parallel <11\bar{2}0>_{\alpha 2}$.

Below 950 °C the orthorhombic *O*-phase (crystal structure A2BC), B19 and the hexagonal ω_O-phase (crystal structure $B8_2$) can evolve. Dependent on the Nb content the *O*-phase is transferred from the α_2-phase [86] or β_O-phase (Nb 20-25 at%) [87]. The β_O-phase can decompose to the hexagonal ω_O-phase by a layer collapse and diffusion mechanisms (Figure 6) [88,89]. The layer collapse is characterized by the peak splitting of the β_O-phase {110} peak in X-ray diffractometer (XRD) measurements [89,90]. For high cooling rates metastable trigonal ω-type phases can form (Figure 6 (b), (c)) [88,91–94]. The ω'-phase is an idealized state with a diffusionless ω-collapse and thus inherits the chemical composition of the β_O-phase [88]. The ω''-phase is seen as a precursor of the ω_O-phase and the formation involves additional chemical ordering processes [88,95]. For long annealing times the ω_O-phase can form from the α_2-phase [96].

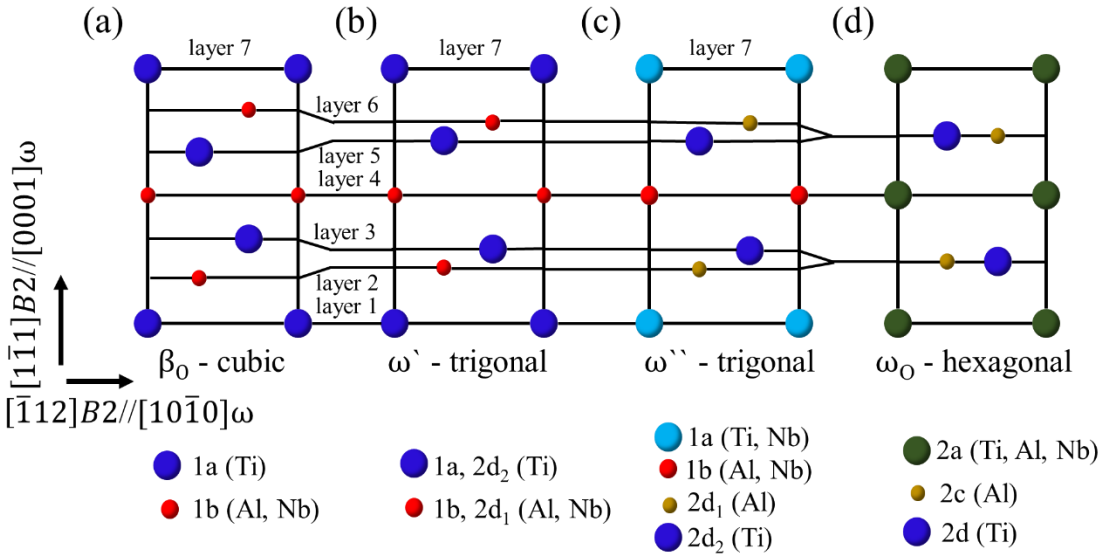

Figure 6: Schematic illustrations of crystal structures and Wyckoff positions of (a) cubic β_O-, (b) trigonal ω'-, (c) trigonal ω''- and (d) hexagonal ω_o-phase according to [92].

Until a grain size of ~50 nm, the small ω_O-phase particles exhibit a coherent interface with the β_O-phase [91]. With increasing amount of ω_O-phase in the β_O-phase the hardness increases [91]. Moreover, a high

defect density can provide the nucleation energy for the ω_O-phase formation as the ω_O-phase has been reported to nucleate at point defects [97]. Nb segregations and the Nb alloy amount increase the growth rate and the amount of ω_O-phase [89,92]. The ω_O-phase has the highest estimated hardness with 11.2 GPa in comparison to α_2-, β_O- and γ-phase with 8.3 GPa, 8.0 GPa and 6.9 GPa, respectively [91]. Furthermore, the hardness value of the β_O-phase with small ω_O-phase particles with 11.2 GPa is even higher than for the α_2-phase with a lamellar size between 1 µm and 2 µm with 9.3 GPa [91,98]. As the solidification of ω_O-phase via β_O-phase is diffusion controlled, the phase transformation $\beta_O \rightarrow \omega''$ is faster than the transformation $\beta_O \rightarrow \omega_O$. The ω''-phase evolves at cooling rates $\geq$ 100K/min [93] and for water-quenching [88,94]. For cooling rates of at least 900 K/min the formation of ω_O- and ω''-phase can be suppressed [91]. Elongation failure for tensile tests of <0.5 % at RT is reported and associated to the detrimental ω_O-phase presence [99].

For technical TiAl alloys two solidification paths are relevant. Dependent on the chemical composition and the process, the solidification path of γ-TiAl-alloys with an aluminum content (Al) >45 at% follows up to two peritectic transformations: $L \rightarrow L+\beta \rightarrow \alpha+\beta \rightarrow \alpha \rightarrow \alpha+\gamma \rightarrow \alpha_2+\gamma$ [100]. These alloys are characterized by a strong texture and segregations [2,7]. A typical representative is Ti-48Al-2Cr-2Nb (Ti-48-2-2). For Al contents <45 at% γ-TiAl is β-solidifying via the path: $L \rightarrow L+\beta \rightarrow \beta \rightarrow \alpha+\beta \rightarrow \alpha \rightarrow \alpha+\gamma \rightarrow \alpha_2+\gamma$. The phase transformation occurs in the solid state. Hence, different α-grain orientations in one β-grain are possible. Furthermore, β-solidifying γ-TiAl alloys have a smaller amount of segregations [101]. Typical β-solidifying γ-TiAl alloys are TNM and TNB-V5.

TNM (Ti-43.5Al-4Nb-1Mo-0.1B) was developed to improve the ductility of the brittle γ-TiAl and even TNM sheets by conventional rolling are producible [6]. The equilibrium solidification path for TNM is: $L \rightarrow L+\beta \rightarrow \beta \rightarrow \beta+\alpha \rightarrow \alpha+\alpha_2+\gamma+\beta_O \rightarrow \alpha_2+\gamma+\beta_O$ [102,103]. The microstructure can be adjusted by heat treatments [12,13]. The β_O-phase forms a semi-coherent interface with α_2 and γ [104]. The interface of nanometer size ω_O particles with the β_O-phase is coherent. If the ω_O particles grow, a misfit dislocation is installed and the interface becomes semi-coherent [105]. The hardness of $\beta_O+\omega_O$-phase is higher than for α_2-phase with a lamellar size between 1-2 µm [91,98]. The colony size and the γ-grain volume fraction are responsible for the ductility below the brittle-to-ductile temperature [105]. Tensile tests on TNM revealed, that initial elastic deformation occurs in all intermetallic phases, even so the α_2- and β_O-phase undergo inhomogeneous elastic straining. The γ-phase starts to deform plastically. Furthermore, load partioning between different oriented γ-grains and the load transfer from the plastic γ-phase onto elastic deformed α_2- and β_O-phase occurs. Favorable oriented α_2-grains deform plastically. The β_O-phase accommodates the deformation of neighboring grains only elastically and deforms elastically until failure. Of central importance is the elastic anisotropic development of stress concentrations of phases in the elastic regime. Even in a single phase significant differences in stress and strain levels emerge, when different sets and grain orientations are compared [85]. The β_O-phase at colony boundaries has a strengthening effect at RT, suppresses grain growth [13], but a continuous β_O-phase is detrimental on the RT ductility, the fracture toughness and creep properties [105–107]. Once a microcrack is initiated in β_O-phase, the crack propagates fast in the brittle phase [106]. In as-cast as well as as-cast and subsequently hot isostatic pressed (HIP) specimens, the crack path is along the β_O-phase at colony boundaries and interlamellar fracture appeared in regions with a discontinuous β_O-phase

seam. For forged specimens there was no preferred crack path, since no continuous β_O-phase is present [77]. The yield strength of TNM depends on the microstructure, hence on the heat treatment and ranges at RT between 680-950 MPa and at 800 °C between 450-680 MPa [13]. For as-cast and as-cast + HIP specimens, the elongation was <0.5 % and for forged specimens 1.5 % [77]. In heat treatments, the first step is to obtain supersaturated the α_2-phase and reduce the β/β_O-phase, to achieve a fine lamellar spacing in a second stabilizing treatment with an annealing temperature close to the service temperature [13,103]. With increasing cooling rates the amount of retained α_2-phase increases and the amount of γ-phase decreases [108]. The γ-phase precipitates from α-phase for medium and high cooling rates, while at low cooling rates, furnace cooling, γ-phase grows from α-grain boundaries [109].

2.3. Chemical compositions and physical properties

The chemical composition and the most relevant thermophysical properties of Ti64, Ti6242, γ-TiAl and TNM are summarized in Table 2 and Table 3. It has to be mentioned that the data availability in particular in case of TNM is low.

Table 2: Main alloying elements and chemical compositions of Ti64, Ti6242, TNM as well as acceptable deviations (Δ) [110–112].

Alloy	Al [wt%]	ΔAl [wt%]	V [wt%]	ΔV [wt%]	Sn [wt%]	ΔSn [wt%]	Mo [wt%]	ΔMo [wt%]	Zr [wt%]	ΔZr [wt%]	Nb [wt%]	ΔNb [wt%]
Ti64	6	+0.75/ -0.5	4	+/-0.5	-	-	-	-	-	-	-	-
Ti6242	6	+/-0.5	-	-	2	+/-0.25	2	+/-0.25	3	+/-0.5	-	-
TNM	28.6	+/-0.7	-	-	-	-	2.3	+/-0.5	-	-	9.2	+/-0.5

Table 3: Thermophysical properties of Ti64, Ti6242, γ-TiAl and TNM.

Property	Ti64	Ti6242	TNM (γ-TiAl)
Service temperature T_{Serv} [C°]	≤400 [3]	425 [3]	600-800 [6]
Liquidus temperature T_{Liq} [°C]	1655 [113]	1705 [113]	(γ-TiAl: 1540 [114])
Density ρ [kg/m³]	4430 [3]	4540 [111]	4160 [112]
Eutectic temperature T_{eu} [°C]	N/A	N/A	Different compositions: 1160 [13]; 1175 [108]
Tγ,solv [°C]	N/A	N/A	Different compositions: 1255 [13], 1265 [108]
Tβ_O→Tβ [°C]	N/A	N/A	Different compositions: 1175-1205 [13]; 1195-1215 [108]
Tβ [°C]	995 [3]	995 [3]	1405 [13]
Surface tension at T_{Liq} σ [N·m^{-1}]	1.52 [114]	1.52 [114]	(γ-TiAl: 1.24 [114])
dσ/dT [N·(m·°C)$^{-1}$]	-5.52·10^{-4} [114]	-8.73·10^{-4} [114]	(γ-TiAl: -5.03 · 10^{-4} [114])
Viscosity η (temperature range [°C]) [m·Pa·s]	3.70 (1740 ± 50) [114] 4.76 (1626 ± 40) [114]	3.92 (1824 ± 50) [114] 4.82 (1670 ± 40) [114]	(γ-TiAl: 9.2 [114])
Thermal conductivity λ (temperature range [°C]) [W m^{-1}·k^{-1}]	6.6 (RT) [3] 7.3 (93) [3]	7 (RT) [3] 7.1 (100) [3]	~10 at RT [115,116] (γ-TiAl: 20 at RT [37]) 11.4 (100) [116] 15.7 (400) [116] 18.0 (600) [116] 21.9 (800) [116]
Specific heat capacity c (temperature range [°C]) [J·kg^{-1}·K^{-1})]	565 (93) [3]	460 (100) [3]	600 [116]
Thermal coefficient of linear expansion CTE (temperature range [°C]) [°C^{-1}]	9.0 · 10^{-6} (0 - 100) [3] 9.5 · 10^{-6} (0 - 315) [3] 10.1 · 10^{-6} (0 - 540) [3]	7.7 · 10^{-6} (0 - 100) [3] 8.1 · 10^{-6} (315 -540) [3]	0.99 · 10^{-5} (100) [116] 1.11 · 10^{-5} (500) [116] 1.18 · 10^{-5} (800) [116]

3. Laser joining processes

3.1. Laser beam welding of titanium-based alloys

According to DIN 8593 joining methods can be divided in different groups for example in joining through welding and joining through brazing. Regarding the physical process DIN 1910 divides the welding processes in pressure welding and fusion welding. Pressure welding utilizes a force, which locally heats up the joining partners, even up to melting. Thereby, cohesive bonding is achieved through plasticization and local deformation. Pressure welding processes are for example diffusion bonding and friction welding. Local melting without a force is associated with fusion welding. In this case, cohesive bonding is attained by melting and subsequent solidification of the joining partners and a possible filler material. Arc welding, electron beam and LBW are fusion welding methods. LBW is beneficial because it is suitable for various joint types and relatively high strength compared to conventional welding processes is obtained [25]. Three distinct regions in the weld seam can be differentiated (Figure 7 (a)). The fusion zone (FZ), which undergoes melting and solidification. The thermally exposed and maybe solid-state transformation undergoing heat-affected zone (HAZ) and the unaffected base material (BM). The heat transfer and fluid flow affect the size and shape of the weld pool, and hence the cooling rate, as well as the kinetics and extent of solid-state transformation [117]. Characteristic weld seam imperfections are porosity, spatter, underfill, reinforcement and cracks (Figure 7 (b)).

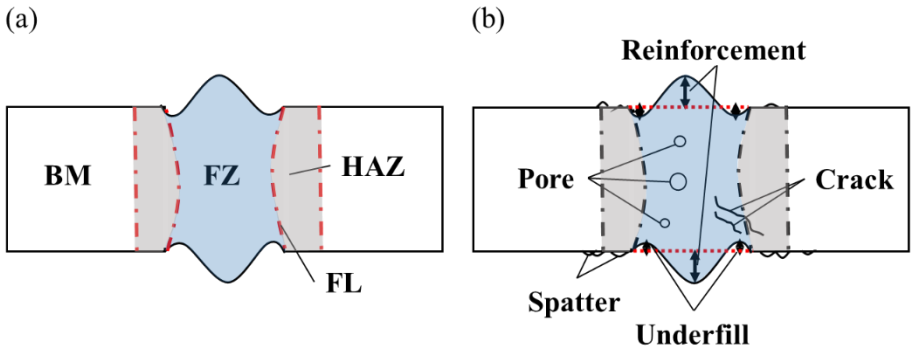

Figure 7: (a) Distinct weld regions: FZ, fusion line (FL), HAZ, BM. (b) Weld seam imperfections.

Different lasers, as for example CO_2, Nd:YAG and fiber lasers are available for welding, differing in wavelength, energy efficiency and laser beam-material interaction. Plasma shielding occurs for CO_2 lasers, especially for deep penetration welding, and diminishes the heat input into the weld material [25]. Consequently, to avoid plasma shielding fiber lasers with a 100 times lower absorption of free electrons are utilized [118]. Moreover, fiber lasers have a high beam quality and relatively high output efficiency compared to CO_2 and Nd:YAG lasers [25]. Nevertheless, another shielding effect, a so-called metal-vapor cloud is reported for fiber lasers. The metal-vapor cloud consists of small particles that absorb and scatter the laser radiation. Hence, the propagation of the laser radiation is attenuated above the keyhole, a vapor capillary formed during deep penetration welding. Thus, only a part of the laser energy is coupled in the material. A cross-jet in welding direction showed insufficient behavior on the negative impact of the metal-vapor cloud [119].

The heat input, can be estimated by the line energy (LE) and has an influence on the weld seam geometry [28].

$$LE = \frac{P}{v} \tag{1}$$

P – laser power, v – process velocity

A V-shaped weld seam is the result of a low line energy [28,120] and associated with a closed keyhole mode [121] and a higher welding efficiency [28,121]. For high line energies a X-shaped weld seams and therefore an open keyhole mode develops [28,120]. Entrapped gases can escape through the top and bottom of the weld seam [121] and this results in a lower welding process efficiency [28]. A further weld seam shape is the I-shape, which is beneficial, since the weld pool is smaller than for the other two shapes and a finer microstructure is achieved. Finer microstructures have a higher crack initiation resistance than coarse microstructures [122] and the stress distribution along the fusion line (FL) is advantageous.

In the FZ two typical grain structures are reported (Figure 8). The first grain structure are straight axial columnar grains in the middle of the weld seam with growth direction in welding direction. The grain size can be reduced by increasing the process velocity [123]. Transverse tensile tests of aluminum joints failed in the region with axial columnar grains [124]. Axial grains are furthermore susceptible to centerline solidification cracks [125]. Curved columnar grains growing from the FZ boundary in opposite direction of the maximum temperature gradient are the second grain structure type [123]. The maximum solidification rate emerges at the centerline, while the maximum temperature gradient is at the FL.

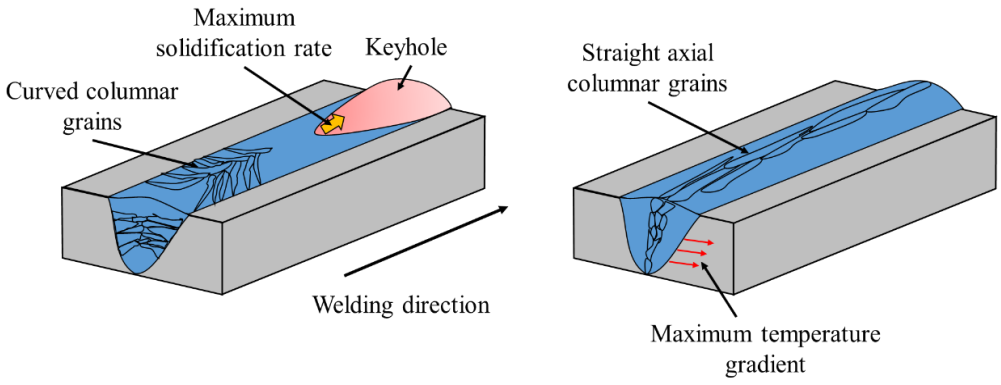

Figure 8: LBW and grain growth characteristics.

The plume dynamic is connected to the keyhole oscillation, thus to the process stability. Gas is entrapped, if violent evaporation on the keyhole wall occurs, which leads to a swinging plume [126]. Consequently, porosity is generated. Large weld pools have a high possibility for process-induced porosity because of the more complex fluid system with recirculation at the bottom of the weld seam. Smaller weld pools are created through e.g. higher process velocities [127]. The decrease in energy density is favorable, since the probability for process-induced porosity is reduced [127]. Porosity is a fracture starting point [128].

The different parameters, as laser power P, process velocity v, laser focus position f and preheating temperature T_{ph}, influence the weld seam geometry, weld seam imperfections and microstructure of the resulting joint. Typical weld seam imperfections are the underfill, reinforcement, spatter, porosity and cracks (Figure 7 (b)). Except for cracks, weld seam imperfections are permitted until certain limits according to DIN EN ISO 13919-1:1996 and 5817:2014.

3.2. Laser additive manufacturing of titanium-based alloys

Enabling integrated parts, reduction in part count, production on demand, the generation of multi-material structures, complex and/or customized parts and repair of parts can be achieved by AM [58,67,129]. High performance components for aerospace, medical, energy and automotive applications produced by AM exist. The process distinction of AM according to ASTM Standard F2792 differentiates for directly produced net shape parts between two DED categories, also known as LMD, and powder bed fusion (PBF). Furthermore, the primary heat sources can be divided in laser beam, electron beam, plasma arc and gas tungsten arc [130]. Different feedstock materials as filler wire and powder are available. Filler wires are generally used for larger parts, and powders are chosen for smaller parts [58].

Focusing here on the LMD processes with a laser beam as a primary heat source, filler wire and powder as feedstock material can be utilized (Figure 9). The general principle of LMD can be described as follows. The laser beam generates a melt pool on the substrate or the underlying layer. The feedstock is fed in the melt pool, where it is molten and afterwards solidifies [58]. For LMwD, filler wire produced for welding industry and retro-fitted welding stations can be utilized. Furthermore, the filler wire can be fed lateral and coaxial. An important parameter in LMwD is the so-called K-factor:

$$K = \frac{v_w}{v} \tag{2}$$

v_w – filler wire velocity, v – process velocity

LMpD is utilized for structural build-up and repair processes [61,131,132]. A high powder quality is critical, due to the high surface-to-volume (A/V) ratio [58], and since the powder characteristics, powder shape, size distribution and surface morphology, influence the net shape part properties [133,134].

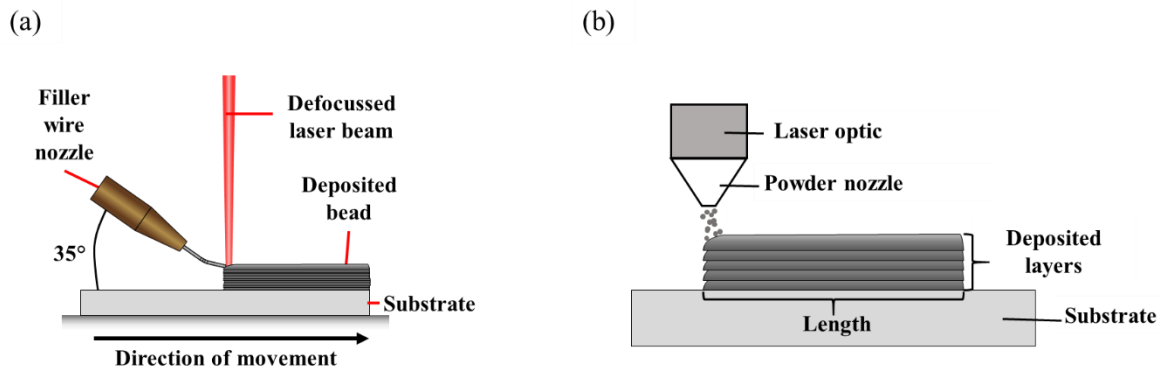

Figure 9: (a) Schematic process of lateral LMwD. (b) Schematic process of coaxial LMpD.

The surface-to-volume (A/V) ratio influences the vaporization and therefore the loss of element. Filler wire has a smaller A/V than powder, hence oxidation, absorption of moisture and contaminations are less likely. Therefore, the A/V ratio is a controlling factor for the magnitude of possible composition changes [117]. Besides, filler wire is easier to store and handle, less hazardous than powder and higher deposition rates can be maintained [135]. Filler wire diameters smaller than 0.8 mm are scare, consequently the melt pool needed is larger compared to LMpD [58]. Contrary to powder, filler wire cannot be reused, the melting efficiency is lower and the final surface is relatively rough [59,60].

Nucleation for epitaxial growth from the substrate or underlying layer is not required for AM structures with the same chemical composition, since these have the same crystal structure [136]. For dissimilar metals nucleation may be required [58]. The solidification structure close to the substrate is dominated by the BM [125], further away competitive growth is dominant [137]. In competitive growth, the easy growth direction is aligned close to the maximum heat flow direction. Through heterogeneous nucleation, rare equiaxed grains can form [138].

There are three main types of cracks in AM [139]. Similar to welding solidification cracks can occur along grain boundaries [125,140]. Columnar grains near the track centerline orientated nearly parallel to the deposition direction are susceptible to solidification cracks [58]. Liquidation cracking is observed in partially solidified or molten zones [58,125]. The separation of two consecutive layers, delamination, is caused by residual stresses [141]. Other common defects are pores and lack of fusion [62,142–144], which have an adverse effect on mechanical properties [145,146]. Porosity formation can emerge in both processes at high power intensities through entrapped gases. Pore formation can also be due to the formation of a keyhole, and the subsequent collapse of the keyhole caused by instabilities [147]. The formed porosity is almost spherical [148]. Gas entrapped in powder, lack of fusion, insufficient penetration of the substrate or underlying layer, can also cause pores [134,149]. Elongated pores are caused by inadequate penetration [62,150].

For the power or energy density two expressions are found in literature [68,151,152]:

$$\rho_P = \frac{P}{v * d} \tag{3}$$

$$\frac{E}{A} = \frac{P * t}{\frac{\pi}{4} * d^2} = \frac{4 * P}{\pi * v * d} \tag{4}$$

$$t = \frac{d}{v} \tag{5}$$

ρ_P – power density, P – laser power, v – process velocity, d – laser spot diameter, E – energy
A – laser spot surface, t – time

Moreover, post-machining in welding is possible, while for LMD structures the surface finish is important if used in as-fabricated state. The mature knowledge about LBW and metallurgy can provide a powerful synergistic effect for the deeper understanding of LMD [58].

Focusing on laser-based processes, the main differences between LBW and LMD are their placement in the field of application and welding mode. Welding is utilized for the joining of semi-finished parts to more complex components [58]. LMD fabricates single components layer by layer [130] and can be utilized for the repair of parts [129,153]. Similar to welding, the LMD process utilizes kilowatt lasers with a spot size of several millimeters [154]. In both processes, the laser creates a localized melt pool. For LBW the keyhole mode is preferred, while in LMD the formation of a keyhole, thus deep penetration welding, is avoided and the conduction mode is favored [58]. Furthermore, all thermophysical properties and process parameters affect the development of the FZ [58]. Differences occur in the interaction with the laser beam and the feeding material. The LBW FZ is surrounded by two solid sides and the LMD FZ only by one solid side (Figure 10). In general, the melt pool size in LBW is larger than in LMD [58]. The grain growth orientation in LBW and LMD is affected by the shape and size of the melt pool [155]. Growth direction and velocity are dependent on the crystallographic orientation and local heat flow [58]. For LBW and LMD, the preferred crystallographic growth direction tends to align grains in the FZ parallel to the maximum temperature gradient [58] (Figure 10). Hence, normal to the solidifying surface of the melt pool [156]. Thus, grains grow continually by shifting direction to align to the maximum temperature gradient [155] and columnar grains are perpendicular to the local curvature of the melt pool. Therefore, curved grains develop [156]. In principle, the solidification microstructure is governed by planar, cellular, columnar dendritic or equiaxed grain growth [155]. LMD structures often resemble multi-pass welds [58] and hence the LMD grain structure as well as evolving phase transformations are often similar to fusion welding [58,156]. The time-temperature-transformation (TTT) diagram can also be used for LMD, since the cooling rates are comparable to welding [58]. There are two cooling ranges, where cooling rates are most important. First, from solidus to liquidus temperature, when features of the solidification microstructure like cells and dendrites are generated [157]. Second, the thermal history that determines the extent of solid state transformation. Caused by the high cooling rates in LMD, phase transformations are similar to LBW [58].

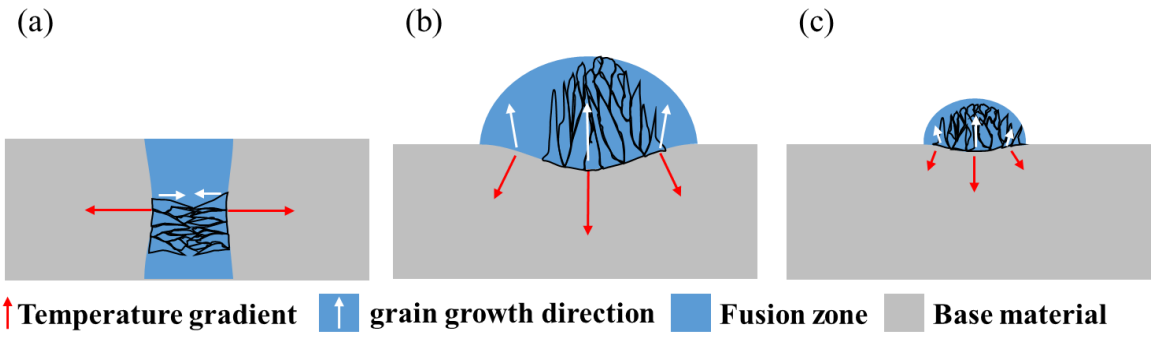

Figure 10: Schematic temperature gradient and grain growth direction in (a) LBW, (b) LMwD and (c) LMpD.

3.3. Theoretical cooling rates according to Rosenthal

To calculate the theoretical cooling rates in welding by analytically deriving the heat flow equation, Rosenthal assumed a steady-state heat flow, a point source, constant thermal properties, no heat losses from the workpiece surface, negligible heat of fusion and no convection in the weld pool [158]. Moreover, it has to be differentiated between the two-dimensional (2D) heat flow for thin plates, where

the temperature variations in the thickness direction are assumed negligible, and the three-dimensional (3D) heat flow for thick plates [158].

Thereby, the following two equations for theoretical cooling rates along the weld centerline can be distinguished.

For thin plates the theoretical cooling rate is calculated according to:

$$\frac{dT}{dt} = 2\pi\lambda\rho c(T - T_0)^3 \frac{v^2 {t_s}^2}{P^2} \tag{6}$$

The equation for thick plates is:

$$\frac{dT}{dt} = 2\pi\lambda(T - T_0)^2 \frac{v^2}{P^2} \tag{7}$$

T – temperature, t – time, λ – thermal conductivity, ρ – density, c – specific heat capacity, T_0 – preheating temperature, v – process velocity, t_s – sheet thickness, P – laser power

For determining whether the 2D or 3D Rosenthal equation should be applied, which is influenced by material and process parameters, the following equation can be used:

$$\tau = t_s \sqrt{\frac{\rho c(T - T_0)v}{P}} \tag{8}$$

For $\tau<0.6$ the 2D and for $\tau>0.9$ 3D Rosenthal equation is considered. In the case of $0.6<\tau<0.9$, the lower cooling rate of the both is the more accurate one [25]. The different heat flow states for the three cases are schematically illustrated in Figure 11.

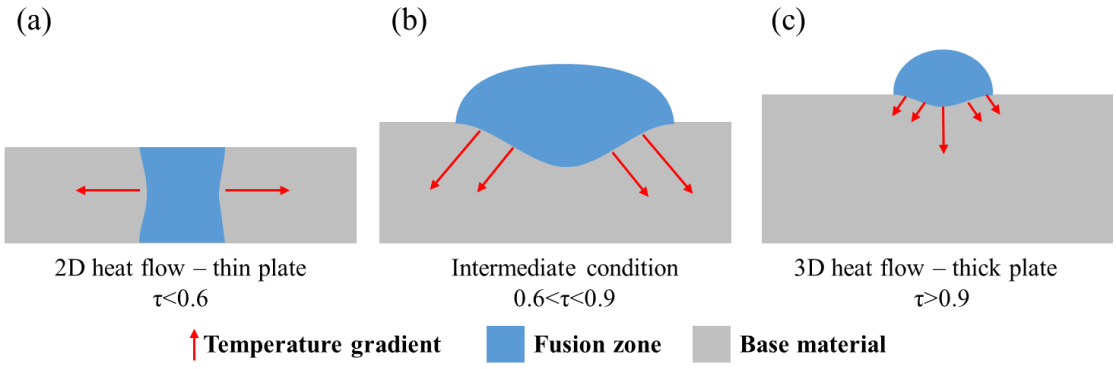

Figure 11: Schematic illustration of differing heat flow states for the Rosenthal equation: (a) 2D heat flow for thin plates, (b) Intermediate condition, (c) 3D heat flow for thick plates.

3.4. Crack sensitivity of titanium-based alloys

The principal factor for the crack formation are residual stresses that develop during cooling as the FZ contracts. Besides, the materials' susceptibility to cracking is determined by its ductility in the zone with residual stresses, which is influenced by intergranular liquid films, material phase changes and the introduction of certain gases. Essential for the crack formation is that stresses extend the fracture

strength. Common crack types in LBW are hot, liquidation, and cold cracks [25]. Hot and liquidation cracks are due to liquid films, while cold cracks are formed as the result of brittleness, due to high cooling rates, and occur as the material has cooled down [25]. Different crack positions are displayed in Figure 12.

Ti-alloys itself have a low estimated crack susceptibility during fusion welding. Nevertheless, for high stress conditions hot cracks in the weld center and along grain boundaries of columnar β- and prior β-crystals in the HAZ of $\alpha+\beta$ alloys are possible [71]. Solid-state cracking of Ti64 is rather originated from deficiencies in preweld-cleaning and shielding of the melt pool [3]. The interstitial inclusion of oxygen, nitrogen and hydrogen leads to an embrittlement of Ti-alloys [71].

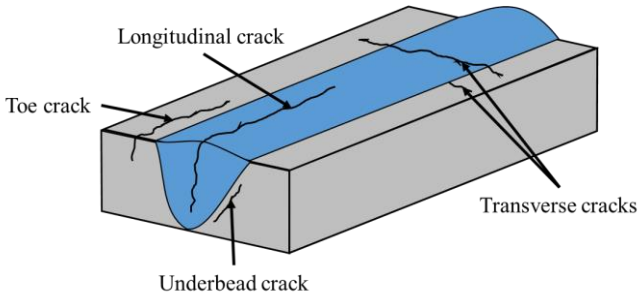

Figure 12: Different crack positions in a weld seam.

In comparison, the fusion welding of γ-TiAl is more challenging due to its tendency to form brittle phases [33–35], its high reactivity with air [2] and crack-susceptibility [34,36–38]. Therefore, over almost three decades, only a few studies on fusion welding of γ-TiAl are available [159]. Based on internal brittleness [34,38] and resulting from thermally induced stresses [35,37], cracks can develop (Figure 12). Mainly, the development of transversal cracks was reported [35–37,39,160]. No evidence of grain-boundary liquidation and therefore susceptibility to hot or liquidation cracking was observed [36,47,160]. However, susceptibility to cold cracking due to high cooling rates was encountered [160]. For crack-free weld seams, reducing thermally induced stresses and enabling the decomposition of the α_2-phase through preheating and obtaining low cooling rate, was shown to be beneficial [37,39,40]. Depending on the investigated γ-TiAl alloy tested preheating temperatures were between 230 °C and 900 °C [34,37,39]. The crack frequency was reduced with increasing preheating temperature [37,39] as thermal gradients and thereby thermally induced stresses are diminished. Moreover, the crack frequency, which was attributed to high thermally induced stresses and microstructural changes promoting a limitation in strain accommodation [160], decreases with decreasing cooling rates [34].

Due to the similarities of LBW and LMD processes (Chapter 3.2.), comparable challenges as the high crack sensitivity by brittle phases and thermally induced stresses arise for the generation of γ-TiAl LMD depositions. Crack-free structures could be obtained by preheating above the brittle-to-ductile

temperature [65,67], and adjusting the laser focus position by moving the highly focused laser position into the powder cloud. Thereby, the powder particles are in-situ preheated and the cooling rate was reduced [152]. Furthermore, for TNM powder utilized in the selective laser melting (SLM) process, crack-free structures were even obtained with α_2-phase as the main phase and the β-phase being bone-like present [161].

3.5. Similar titanium-based joints and depositions

3.5.1. Laser beam welding

Titanium alloys

The advantages of LBW of Ti-alloys compared to other fusion joining processes are the low process time, high flexibility of the weld geometry, a small HAZ [26,27] and that LBW does not require vacuum as electron beam welding [25]. Therefore, LBW is a suitable process for welding of Ti-alloy thin sheets. During LBW of Ti-alloys, melt pool protection against oxidation by a shielding gas is mandatory [3]. For Ti-alloys, the cooling rate below the β-transus temperature leads to the evolving α/β microstructure [145]. The LBW process for the most commonly utilized Ti-alloy, **Ti64**, [3,28–30,162] and welding with filler wire [27,30,163] is established. By LBW with filler wire, the underfill that can act as a notch in the notch sensitive Ti-alloy, can be reduced or eliminated. Hence, the fatigue strength is improved [164].

The different process parameters, as the laser power, process velocity and laser focal position, influence the weld seam geometry, shape and imperfections of Ti64 similar joints in the following ways. Low cooling rates by increasing the laser power or decreasing the process velocity result in an increasing of the weld seam top and bottom width [165,166], an acicular martensitic structure and larger prior β-grains [165,167]. Danger of incomplete penetration due to narrow root widths [165,167], a finer martensitic structure and smaller prior β-grains in the FZ [165], are obtained by higher cooling rates through decreasing laser power or increasing process velocity. Increasing the laser power or process velocity results in a rising reinforcement [164,165] and a more parallel weld seam shape [166]. For a rising process velocity also an increasing amount of spatter occurs [165]. With an increasing laser focal position, the weld seam top and bottom width increases [165,166]. Furthermore, a smaller sheet thickness leads to a lower level of imperfections [168]. Often a finer martensitic structure is reported in the FZ [165,169]. A complete martensitic structure in the FZ is achieved for cooling rates higher than 410 °C/s. Massive transformation is observed for cooling rates between 410 °C/s and 20 °C/s. During massive transformation, colonies of lamellae start to grow at prior β grain boundaries, leading to decorated prior β-grain boundaries with α-phase colonies. No significant difference in chemical composition between massive α-phase and martensite occurs [73]. The HAZ mostly consists of martensite and the acicular α-phase [165]. For low cooling rates, the formation of colonies and for intermediate cooling rates, the formation of a basket-weaver structure is reported. A characteristic hardness increase from the BM via the HAZ to the FZ emerges, which is caused by the microstructure [167].

In spite of the reduced elongation caused by the rigid FZ, ultimate tensile strength (UTS) and yield strength (YS) values around the BM values can be achieved for similar Ti64 joints [164]. Decrease in UTS can be attributed to an excessive increase in microhardness [170], significant growth in grain size and porosity [28]. Another possibility is that a non-perfect alignment of the weld coupons occurred, resulting in a mismatch of the joint, which then could lead to a decrease in UTS [170]. Failure has been reported for the BM [164,171] and the FZ [28]. For the BM, damage nucleation in the vicinity of the β-phase and α-grain boundaries occurs. Furthermore, a heterogeneous plastic flow in neighboring α-grains is obtained. In the FZ, the martensite $\alpha`$ lath tend to crystallographically rotate and align to $<10\bar{1}0>$

direction with the tensile axis. Crack initiation along specific laths interface, 45 ° to tensile axis, former β-grain boundaries and twinned martensitic needles emerge [172].

Research results for laser beam welded **Ti6242** are limited [30–32]. For high laser powers and high process velocities, increased underfill develops. The line energy influences the FZ and HAZ width. The porosity level in Ti6242 butt joints is low. Microstructural features and the microtexture are insignificantly affected by the process parameters [31]. Based on the TTT diagram [173], the critical cooling rate for attaining a fully $\alpha`$ martensitic microstructure in Ti6242 can be established as 1303 °C/s. The starting temperature for $\alpha`$ martensite formation is 800 °C [32]. The FZ consisted of $\alpha`$ martensite and the HAZ of $\alpha`$ martensite and acicular α-phase. A hardness increase from BM to FZ with a symmetric profile emerges [31,32]. The major alloying elements are uniformly distributed in the BM, HAZ and FZ [32]. Tensile properties of the BM can be achieved at RT [31]. Lower UTS and YS than the BM are related to porosity [32] and underfill [31,32]. On the one hand, the increased hardness in the FZ and HAZ can provide a shielding effect against mechanical damage in tensile tests [31]. However, the increased hardness also lowers the elongation [32]. Fracture in the FZ is related to pores and was ductile [32]. Tensile tests of similar Ti6242 joints at elevated temperature are not reported.

Titanium aluminide alloys

LBW of different similar TiAl alloys has been successfully performed [35,37,51,174–176]. For TNM the number of studies is restricted to two. One study utilized bead-on-plate welding with a very low laser power, process velocity and one preheating temperature [51]. The other study focuses on the LBW of casted or extruded TNM with a CO_2 laser. Preheating to 650 °C is performed by an oven or a priori defocused laser beam. The obtained crack-free TNM joints had a toe underfill of 0.2 mm to 0.4 mm [52].

For high heating rates the solid-solid phase transformation is suppressed, while for low heating rates diffusion based transformation is observed and coarse lamellae are formed after welding [174]. With increasing cooling rate the solid-solid phase transformation changes from massive α_2+massive γ+lamellar (α_2+ γ) → massive α_2+massive γ → α_2. The single α_2-phase is observed for cooling rates above 4000 K/s [37]. For defect-free similar Ti-22Al-25Nb joints a cooling rate of 960 K/s was calculated [175] and for similar Ti-46Al-2Mo joints a cooling rate below 30 K/s was necessary. Fine grains and lamellas decrease the local stress concentration [38]. Crack-free joints for different TiAl alloys are reported for preheating temperatures between 300 °C-900 °C [35,37,51] and decreasing welding speeds (0.3-5 m/min) [37,51]. Besides, cracking decreased when the hardness was below 400 HV [37]. For electron beam welding it is assumed that crack nucleation is caused by dislocation stack according to the anisotropic deformation of the lath structure [177]

A large amount of α_2-phase is reported in the weld [35,176]. The grain size is refined when the laser power is increased from 300 W to 600 W [174]. For welding of Ti-48Al-2Nb-2Cr with pure titanium filler wire utilizing a pulsed laser, the alloying element distribution was non-uniform. This was accounted to the periodical change of heat input [176]. Grain growth occurred from the FL and along the center line [178].

Tensile properties similar to BM [37,175] and inferior to BM [51,174–176] are reported. Furthermore, fracture emerged in the BM [37,175], FZ [51,175] or initiated in the weld toe [176]. The weld toe is often the weak link, since usually a higher stress concentration develops and therefore cracks easily can be produced [176]. Elongation is decreased compared to BM [51,175]. Reported UTS for the similar TNM joints welded with a CO_2 laser were in the range 231 MPa to 708 MPa and 296 MPa to 740 MPa at RT and 700 °C, respectively [52]. At RT no fracture elongation of 1 % or above was obtained [52].

Through conventional and in-situ laser heat treatments the decomposition of the α_2-phase is achieved [35,179]. Massive γ-phase is formed after in-situ laser heat treatment and a convoluted microstructure after conventional heat treatment at 1260 °C [179]. Furthermore, residual stresses are released, coarsening of acicular colonies and the reduction of β_O-phase can be realized [51]. For conventional heat-treated micro-tensile specimens at 750 °C, the tensile properties improved and fracture occurred in the BM [179].

3.5.2. Laser metal deposition

Titanium alloys

Most LMwD research of Ti-alloys focuses on Ti64. Therefore, if not mentioned differently, the following section deals with LMwD results with Ti64 filler wire for similar material structures. Moreover, no crack sensitivity for Ti-alloys in LMwD is reported.

The wire position relative to the substrate affects the molten material transfer. A continuous molten pool with a smooth height and surface is generated, if the droplet touches the substrate before detaching. For a wider beam, higher feed rates can be achieved, more power is absorbed by the substrate and the danger of process halt is decreased. Consequently, for a narrower beam the risk of a process collapse is increased, but the process is more efficient [60]. Layer bulging, hence convexity, parallel to the deposition plane is formed [63]. The laser power influences the width and seems to leave the height unaffected for small changes. A low laser power may prevent the homogenous deposition [142]. With decreasing cooling rate by increasing laser power, the width of the prior β-grains in the FZ and the size of the prior β-grains in the HAZ increase [70]. In contrast, with higher cooling rates through increasing the process velocity, smaller prior β-grain widths in the FZ, smaller prior β-grains in the HAZ and a slight increase in hardness are obtained [70,180]. A wider and higher layer, larger angles between layer and substrate, a higher prior β-grain width in the FZ and size in the HAZ are achieved with increasing K-factors [70,142].

Except in the top region, for multi-layer depositions parallel bands occurred [63,64,180,181]. These are related to the β-transus temperature [137,182] and the cooling rate by increasing the laser power or decreasing process velocity [64]. Columnar elongated prior β-grains grow epitaxially from the bottom to the top across layers following the largest temperature gradient [60,63,135,180]. Most β-phase is

transformed to martensite or α-phase [63,182,183]. Distinct microstructure regions can be differentiated. The main microstructure at the bottom is a basket-weaver structure. Globular prior β-grains can result from the globular microstructure of the BM, since the heat input leads to the growth of the grains in the first millimeters [137]. Columnar prior β-grains are the result of solidification. Grain size and width decreases near the substrate [60,63]. An increased occurrence of the β-phase is the result

of the fast cooling rates [63]. Grid structures are attributed to martensite [63,137]. Due to competitive growth, the number of prior β-grains decreases with building height [137]. Directional heating and cooling during deposition, especially in the top region, leads to an angled growth of these grains [180]. The upper region is characterized by a smaller grain size due to rapid cooling [60] and lamellar colonies starting at grain boundaries [63].

Concerning porosity, some micropores due to internal oxidation [60] with random distribution, pores sizes between 110-520 µm and a percentage in the standard as for laser beam welding are obtained [142]. Macroscopic pores are the result of high powers above a given threshold [142]. For the TC17-alloy, the laser power determines the width and height, while the process velocity influences the width and depth of the remolten zone. Furthermore, the surface quality is not influenced by the change of parameters and the main defect pores, 50-500 µm, can be reduced by optimized parameters [143].

In single depositions, the hardness increases from the substrate to the deposited layer. This is attributed to the martensitic transformation and fine microstructure [142]. For multi-layer deposition higher hardness values in the top region are reported [63]. Anisotropy of tensile properties depending on the sample orientation emerges [63,135,180,183,184]. The UTS is between 800-1000 MPa [135,180,185]. Variation in one orientation is related to the α colonies and their crystal orientation [63,184]. More critically affected by the LMwD process are the elongation values [63], which often are decreased.

Similar to LMwD, most LMpD studies focus on Ti64 [62,64,186]. Few studies on Ti-6Al-2Sn-4Zr-6Mo and Ti6242 are available [61,187]. No severe crack sensitivity for Ti-alloys with LMpD was reported. Moreover, powder with a wider particle size distribution have a higher density and flowability, but lower powder mass flow compared to powders with a narrower particle size distribution [188].

Higher laser power results in wider layers [189] and increasing α+β lath size [62,190]. Furthermore, columnar prior β-grains can be gradually replaced by large equiaxed grains, since the cooling rate increases and additional nuclei can form. But normally planar growth is dominant [191] and colony structures evolve [62]. For lower process velocities the layers are wide [189] and for higher process velocities the layer height is reduced [144]. The grain size decreases with increasing process velocity [62].

Layer bands that do not develop in the top region and are attributed to the β-transus temperature, are visible [62,182,192]. Their thickness can be reduced by a very high laser power or process velocity [62]. Epitaxial growth of the prior β-grains from the substrate and growth across layers is obtained [62,190]. These are nearly perpendicular to the substrate and slightly tilted in the direction of laser motion [64]. The size varies from the edge to the center and bottom to top. In multi-layer deposition, top grains re-melt and serve as nuclei [62]. Due to the increasing difficulty of heat conduction with build height in multi-layers, the temperature of the buildup increases, the microstructure changes and three distinct regions can be differentiated [62,192]. At the bottom the cooling rate is high, martensite

α` [188,190,192] and the highest β-phase content are found [192]. In the center region, the microstructure coarsens through annealing along the building height, thus coarser colony α+β lamellae are generated [188,190,192]. Influenced by the cooling rate, the top region has a finer microstructure than the center region and prior β-grain boundaries can be decorated with the α-phase [64,192]. For

very fast cooling rates no α-phase exists in the β-grains [181]. For optimal parameter sets no severe alloying element loss occurs [192]. Moreover, a heterogeneous microtexture is reported [192]. Layer bands are also observed for Ti-6Al-2Sn-4Zr-6Mo and Ti6242. Epitaxial growth for Ti6242 is reported [61]. A sharp transition between substrate and the deposited layer emerge for Ti-6Al-2Sn-4Zr-6Mo and Ti6242 [61,187].

Gas porosity and lack of fusion decreases with increasing laser power, until a threshold is reached [144]. Similar for higher process velocities, gas porosity decreases until for very high process velocities porosity occurs again [62,144]. For low laser powers and increasing feeding rates porosity due to incomplete melting, called lack of fusion, can develop [62]. Afterwards higher porosity emerges, especially in the FZ [189].

No significant hardness difference between the layer bands and the surrounding microstructure is measured [64]. The characteristic hardness increase from the substrate to the deposited layers is attributed to the microstructural change [146]. Furthermore, LMpD displayed higher hardness values than LMwD [181]. Anisotropic mechanical behavior is the result of the anisotropic microstructure [145,193,194]. Higher strength in the samples from the bottom than the top region are the result of the finer bottom region microstructure [145]. UTS typically lies between 900 and 1150 MPa [145,193,194].

Titanium aluminide alloys

Due to its brittleness no γ-TiAl wire can be drawn and moreover no data on LMwD depositions on γ-TiAl substrates have been found. Functionally graded TiAl structures by double wire and arc additive manufacturing (WAAM) using a gas tungsten arc were achieved with a Ti and a Al filler wire [195–197]. A heating blanket and interpasses are utilized to generate crack-free structures [196]. To obtain TiAl structures with Ti and Al filler wire by LMwD, a large spot size would be necessary, which appears to be inconvenient.

The generation of similar TNM, Ti-48Al-2Cr-2Nb, Ti-47Al-2.5V-1Cr, and Ti-40Al-2Cr structures is already established [66,132,198].

Fine grained prior β-grain regions at the bottom and in other regions coarser microstructures evolve [65,198]. Besides, at the bottom equiaxed and columnar prior β-grains can be found [198], while in the other regions columnar grains occur [66,198]. A chemical and microstructural inhomogeneous structure is obtained along the building height [65,66,198,199]. The overall microstructure consists of α_2/γ lamellae and for TNM also a low β_O-phase content is maintained [66,199]. Moreover, for the SLM process, crack-free structures with α_2 as the main phase and bone-like β as the minor phase were obtained in [161].

The hardness values are higher than for as-cast γ-TiAl-alloys [65,198]. UTS of as-deposited specimens is lower than for heat-treated specimens. Reported UTS for Ti-47Al-2.5V and Ti-40Al-2Cr at RT is 650 MPa and 600 MPa, respectively. Elongation is in the range of 0.6 % [66].

3.6. Dissimilar titanium-based joints and depositions

3.6.1. Challenges for laser processing

Various dissimilar configurations for joints and depositions by laser processing are possible (Figure 13). Dissimilar joints by LBW can be achieved by utilizing a different filler wire material for welding two weld coupons of the same material (Figure 13 (a)) or by welding two weld coupons with differing chemical compositions (Figure 13 (b)). Dissimilar LMD depositions can be obtained by applying a different filler material compared to the substrate, for LMwD a filler wire (Figure 13 (c)) and LMpD powder (Figure 13 (d)).

Nevertheless, due to different chemical compositions (Table 2) and differing thermophysical properties (Table 3), intermetallic phases, cracks, distortion and asymmetric dissimilar joint geometries can evolve, causing the challenges to manufacture dissimilar joints and depositions. Consequently, the number of studies on dissimilar joints and depositions by laser processing is limited. Hence, in the following also solid-state joining processes and other fusion welding processes are consulted for further knowledge. Solid-state joining processes are friction welding [200,201], diffusion bonding [20,56,202] and brazing [43,203,204]. Besides, dissimilar joints of TNM with steel and Inconel by friction welding were not reproducible [52].

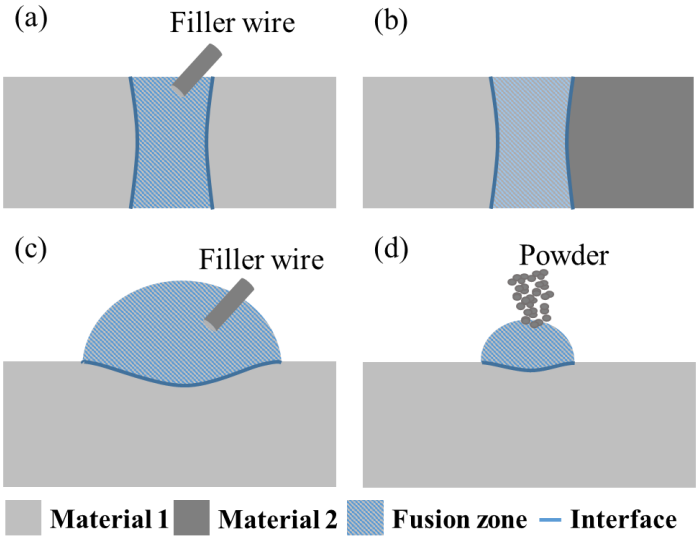

Figure 13: Different possible configurations of dissimilar joints with possible positions of interlayers. (a) LBW similar joint with dissimilar filler wire. (b) LBW dissimilar joint. (c) LMwD substrate material and dissimilar filler wire. (d) LMpD substrate material and dissimilar powder.

Regarding the differing thermophysical properties, the thermal conductivity, thermal expansion and the bonding environment influence the bonding in diffusion processes [20]. In electron beam welding, asymmetric joints of dissimilar structural materials can be the result of different thermal conductivities [22]. Moreover, different thermal expansion coefficients are the main reason for cracks in multi-material structures and deteriorate the thermal cycle stability in different fusion joining methods [43,205].

Only a few studies on fusion welding methods for dissimilar γ-TiAl-Ti-alloy joints like electron beam welding [22], LBW [21,178,206] and LMD [67–69] were conducted. For electron beam welding crack-free joints could be attained by pre- and post-heating. The cracks are attributed to the fine acicular microstructure, which leads to high hardness values and residual stresses in the FZ. The cracks occur in the FZ and can stop at the FL on the Ti-alloy side [22]. In the following, the present knowledge regarding dissimilar Ti-Ti- and TiAl-Ti-alloy joints and depositions by LBW and LMD is introduced in detail.

3.6.2 Laser beam welding

Tested **dissimilar Ti-alloy** joints for material combinations are Ti17 (β-rich α+β alloy)-Ti6242 [17] and Ti64-Ti6Al6V2Sn [18]. In the FZ for dissimilar Ti-alloy joints a chemical composition between the two alloys, small α needles and a non-uniform distribution of alloying elements occurred. The chemical composition in the HAZ was close to the BM composition [17]. For dissimilar Ti-alloy joint tensile tests, the crack started in the FZ [17] and notch tensile values in the range of 90-100 % of the BM could be obtained [18]. Ti64-AlMgSi [53] and AA5754-T40 [54] are investigated material combinations for dissimilar Ti-Al-alloy joints. Crack formation due to the formation of TiAl and Ti_3Al could be avoid by the use of niobium foil in Ti-Al-alloy joints [53]. An intermetallic layer < 1 µm at the FL is achieved by focusing the laser spot on the Ti-alloy side in Ti-Al-alloy joints [54]. Furthermore, in Ti-Al-alloy joints, the fracture during tensile testing occurred in the intermetallic layer [54].

Dissimilar γ-TiAl-alloy joints have been tested with the following different material combinations and processes different to LBW: nickel superalloys [43,55], steel [56], Ti64, Ti6242 and Ti600 [20,22,205,207].

Crack-free LBW joints of Ti-48Al-2Nb-2Cr with a nickel superalloy are achieved by a vanadium-copper interlayer, which reduced the formation of brittle phases, and a reduction in process velocity [21]. The α'-, β_O-phase, and a martensitic microstructure are reported to evolve in the FZ of dissimilar Ti-22Al-25Nb-Ti-alloy joints [178,208]. For LBW Ti-48Al-2Nb-2Cr joints with pure titanium filler wire, the FZ consists mainly of α_2-phase [176]. Growth of the prior β-grains started from the FL [178]. Homogenous [178] and inhomogeneous [208] mixture in the FZ is obtained for different alloy combinations. For dissimilar Ti-22Al-25Nb-Ti-alloy joints, the lowest average hardness is measured in the FZ [178,208], while for Ti-48Al-2Nb-2Cr joints with pure titanium filler wire and the γ-TiAl-Ni-alloy joint the FZ exhibits the highest average hardness [21,176]. The fracture crack in the electron beam welded dissimilar γ-TiAl-Ti600 joint progresses across the FL and in the HAZ on the γ-TiAl alloy side [22]. Similar results are found for the LBW γ-TiAl-Ni-alloy joint, where the brittle fracture occurred at the FL. UTS of RT tensile tests was 60 % of the γ-TiAl BM and 25 % of the nickel BM. Tensile tests at 600 °C revealed at UTS of 46 % of the γ-TiAl BM and 41 °% of the nickel BM [21]. For dissimilar LBW Ti-22Al-25Nb joints the fracture mode changes from RT to 650 °C from brittle to ductile. The fracture position was in the FZ and BM. The UTS was in the range of the BM at RT and below the BM values at higher temperatures [178,208].

3.6.3. Laser metal deposition

Some dissimilar **Ti-TiAl-alloy** LMpD structures for selected γ-TiAl alloys have been investigated [67–69]. Data for dissimilar Ti-Ti- and Ti-TNM-alloy depositions by LMwD as well as LMpD is lacking. Available Ti-TiAl-alloy combinations are using Ti-47Al-2Cr-2Nb and Ti-48Al-2Cr-2Nb powders [67,129,209]. Mostly Ti64 is utilized as a substrate [129,209]. For one investigation Ti6242 is employed [67]. Functionally graded structures are also investigated [19,210].

Crack-free structures are achieved through a second heat source positioned at the back of the nozzle, hence preheating, and optimized parameters [68,129,209,211]. With decreasing process velocity or powder feed rate the cooling rate decreases and cracks are less likely to occur [129,211]. For excessive laser power greater melting of the substrate and deeper penetration of the powder is achieved [67]. Some dilution, melting of the substrate, is required to attain a sufficient bonding. However, a major change of the chemical composition of the deposited layer or structure should be minimized [129]. Moreover, a defocused laser beam leads to a reduced temperature gradient and a moderate heat distribution in a larger area [209]. For slow process velocities, hence lower cooling rates, dendritic structures are developed. Dendrites are almost not visible and grains with distinct grain boundaries emerge for medium process velocities. With increasing process velocity, thus higher cooling rate, the hardness increases [68,209]. Only small isolated porosity between layers is detected [129]. Besides, the interlayer thickness between substrate and the first deposited layer decreases with higher laser power and lower process velocity [212].

Interface thicknesses between 20-280 µm are reported [19,67,212]. In the interface the γ+α_2- [210] and the α+β_O-phase [19] are detected. In the later case, the missing of the γ-phase is attributed to the β-phase stabilizing elements Mo and Nb. The β_O-phase is preferentially located at the colony boundaries [19]. Further data on the interface is missing. At the bottom a finer microstructure and in the upper regions columnar dendrites perpendicular to the growth front emerged [210]. Hence the microstructure is non-uniform [129]. Results for diffusion processes are contradictory. In functionally graded layers diffusion processes took place, proven by energy dispersive X-ray analysis (EDX) [210], while in coating substrate elements are not detected [67]. The overall microstructure consists of γ lamellas with some α_2-phase [19,67].

The high hardness values are attribute to the fine microstructure and α_2-phase [68,209,213]. Mechanical properties are anisotropic due to the microstructure. UTS for different material combinations is between 519-1200 MPa [19,68,210]. Fracture is brittle and elongations were between 0.2-1.7 % [68,210].

4. Experimental procedure

4.1. Criteria for parameter selection

For all laser processes, parameter studies were conducted to determine the parameter windows. Since for LBW and LMD of Ti- and γ-TiAl alloys no international standard exists, the selection was performed according to DIN EN ISO 13919-1:1996 and 5817:2014. To identify the boundaries of the process window the following criteria were applied:

1. Homogenous outer appearance
2. No or low amount of spatter
3. No material accumulation
4. No wire breakage
5. No weld ripples
6. No outer or inner cracks
7. No line porosity
8. No macropores
9. No or low amount of micropores
10. For laser beam welded joints: full penetration

4.2. Laser beam welding

4.2.1. Titanium joints

LBW of similar Ti64-Ti64, Ti6242-Ti6242 and dissimilar Ti64-Ti6242 butt joints was conducted with a laser equipped CNC machine center (IXION ULM) (Figure 14). Throughout the experiments, an 8 kW fiber laser (IPG YLS-8000-S2-Y12), a 300 mm laser optic, a 300 µm fiber laser, a focus diameter of 746 µm with a wavelength of 1070 nm was utilized. For weld pool protection, the weld coupons (50 mm × 25 mm), cut with the short side in rolling direction (RD), were clamped in a gas shielding box, which is mounted on a x-y-table and lamellar flooded from below with argon (Ar) 15 l/min. The laser focus was set on the weld coupon surface and the welding edge. Furthermore, for some experiments a filler wire was utilized and the filler wire nozzle had a tilt angle of 35 ° with the weld coupon. For feeding the 0.8 mm Ti6242 filler wire from E.Wagner Sondermetalle GmbH, an industrial wire feeding system (Dinse DIX WD 300) was utilized. Process monitoring of the welding process itself and the effect of the cross-jet on the welding plume could be conducted with a high-speed camera (Optronics Cam Record 600).

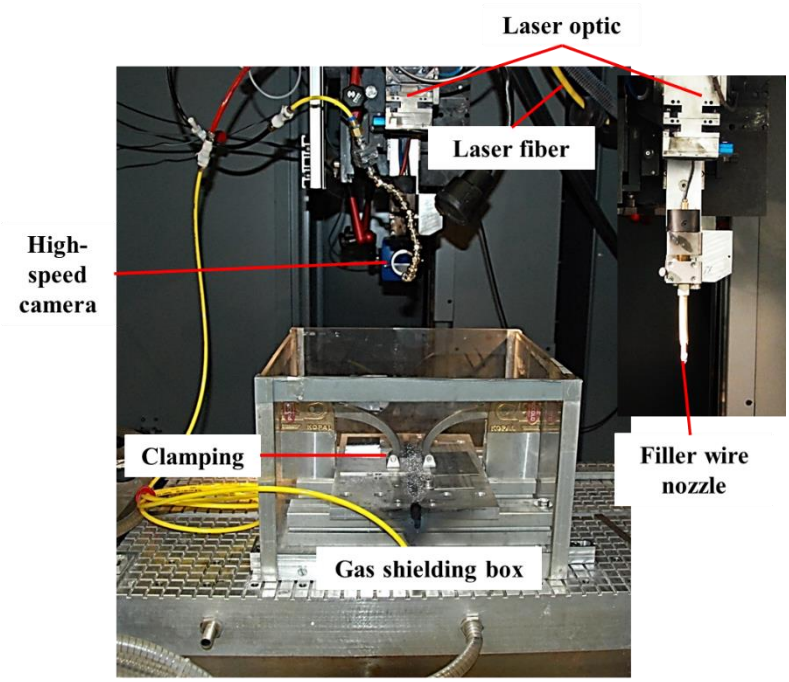

Figure 14: Experimental setup for similar and dissimilar Ti-alloy joints welded in flat position.

Rolled Ti64 (t_s = 2.54 mm) and Ti6242 (t_s = 2.00 mm) sheets from VSMPO-Avisma were used for the LBW experiments. The parameter development was performed with Ti64. To investigate the parameter transferability from Ti64 to Ti6242 and for LBW of dissimilar Ti64-Ti6242 joints, Ti64 was uniformly milled from two sides to a thickness of 2 mm. The investigated parameter windows for similar Ti64-Ti64 and Ti6242-Ti6242 joints are displayed in Table 4. For dissimilar Ti64-Ti6242 joints the parameter sets P = 1.75 kW + v=0.7 m/min, P = 3.5 kW + v = 4 m/min and P = 4.5 kW + v = 3 m/min were utilized.

Table 4: Investigated parameter sets for similar Ti64-Ti64 and Ti6242-Ti6242 joints. Weld coupon size 50 mm × 25mm. Ar gas shielding box flow rate: 15 l/min.

Joint	**Sheet thickness t_s [mm]**	**Laser power P [kW]**	**Process velocity v [m/min]**	**Cross-jet Ar gas flow rate [l/min]**	**Ti6242 filler wire speed v_w [m/min]**
Ti64-Ti64	2.54	1.25-6.00	0.5-6.0	-	-
Ti64-Ti64	2.00	1.75-8.00	0.7-5.0	-	-
Ti6242-Ti6242	2.00	1.75-8.00	0.7-5.0	-	-
Ti6242-Ti6242	2.00	1.75-5.00	0.7-4.0	-	2.0-5.0

4.2.2. Titanium and titanium aluminide joints

For similar and dissimilar TNM joints 1.5 mm and 2 mm thick rolled TNM sheets from GfE Metalle und Materialien GmbH were preheated in an in-house constructed system (Figure 15). In case of dissimilar TNM joints Ti64 (t_s = 2 mm), milled from both sides, and Ti6242 (t_s = 2 mm) were utilized.

Both rolled Ti-alloy sheets were from VSMPO-Avisma. The system consists of an oven mounted on a linear motion unit, which is itself fixed in a closable chamber. As for Ti-alloy joints a shielding gas, Ar, was lamellar fed from below in the box. Welding was performed with the same laser equipment as for Ti-alloy joints, an 8 kW fiber laser (IPG YLS-8000-S2-Y12), a 300 mm laser optic, 300 µm fiber laser, a focus diameter of 746 µm and a wavelength of 1070 nm. The laser beam was focused on the weld coupon surface and adjusted on the welding edge. Joints were welded in horizontal position according to DIN EN ISO 6947 (Figure 15 (b)). For reasons of simplicity, the horizontal position is in the following referred to as out-of-position. The Ti-alloy weld coupon was positioned at the bottom and the TNM coupon at the top. Furthermore, the system can be equipped with a filler wire nozzle. Therefore, a motion unit with the filler wire nozzle was fixed on the laser optic (Figure 15 (a)). To avoid softening and melting of the filler wire setup during preheating, the filler nozzle was moved towards the weld coupons only directly before welding and the filler wire was adjusted on the welding edge. Wire feeding was conducted with an industrial wire feeder (Dinse DIX DVP 4332 KDP). As for Ti-alloy joints Ti6242 filler wire with a diameter of 0.8 mm from E.Wagner Sondermetalle GmbH was used. For dissimilar TNM-Ti6242 and similar Ti6242 joints the tested filler wire speed was ~3.6 m/min. Process monitoring could be conducted with two high speed cameras, positioned at the front side (Optronics CR-S3500) and back side (Optronics Cam Record 600) of the LBW system (Figure 15 (a)). Temperature monitoring for selected joints was executed by a thermocouple (Type N, TC Direct). The thermocouple was positioned in the middle of the TNM weld coupon 5 mm away from the welding edge and was 0.5 mm deep.

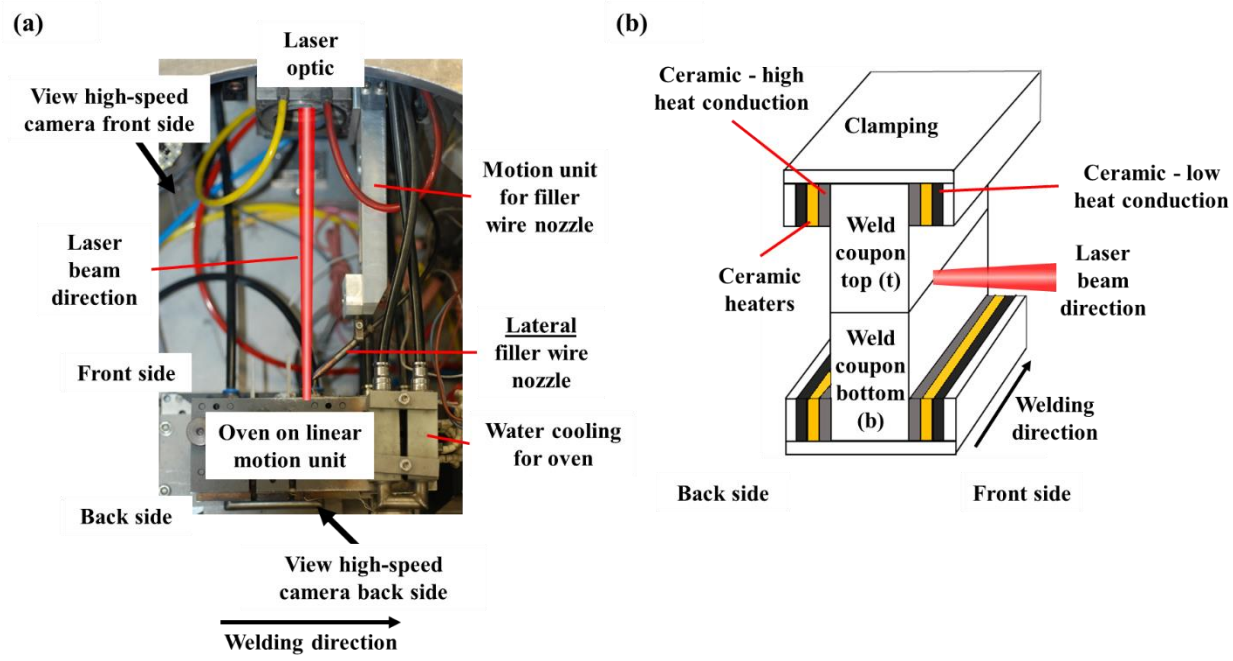

Figure 15: Experimental setup for similar and dissimilar TNM joints welded in out-of-position. (a) Top view. (b) Schematic setup of oven.

Preheating of the weld coupons was realized by ceramic heaters (Figure 15 (b)). To ensure proper heat transfer to the weld coupons, ceramics with a high heat conduction were placed between the ceramic heaters and the weld coupons. Ceramics with a low heat conduction at the outer part were utilized for

insulation. Besides, the preheating setup was clamped. The in-house-constructed oven itself was cooled with a water cooling system (Figure 15 (a)). To verify the heat transfer between the set point temperatures of the ceramic heaters, the actual temperature of the ceramic heaters and the weld coupon temperature, preliminary preheating tests were conducted for the set point temperatures 400 °C, 600 °C and 800 °C (Table 5).

Table 5: Preliminary preheating tests of the heat conduction between set point and actual temperature of the ceramic heaters, as well as the actual temperature at the weld coupon using type N thermocouple. Weld coupon size: TNM (25 mm × 15 mm × 1.5 mm), Ti6242 (25 mm × 25 mm × 2.0 mm). Heating rate 100 °K/min.

Material	**Set point temperature ceramic heaters [°C]**	**Actual temperature ceramic heaters [°C]**	**Actual temperature weld coupon [°C]**
TNM	400	404	405
TNM	600	604	613
TNM	800	804	814
Ti6242	400	404	376
Ti6242	600	604	596
Ti6242	800	804	798

Through applying different preheating temperatures, the crack susceptibility of similar and dissimilar TNM joints was investigated (Table 6). Enabling the comparison of weld seam characteristics of similar Ti6242 with dissimilar TNM-Ti6242 joints, preheating of similar Ti6242 joints for selected welding parameter sets was carried out. To distinguish between the differing TNM sheet thicknesses of the weld coupons, for 1.5 mm thick TNM sheets TNM(1.5) is written and for 2 mm thick TNM sheets just TNM.

Table 6: Investigated preheating temperatures for similar TNM, dissimilar TNM-Ti6242 and dissimilar TNM-Ti64 joints.

Joint	**Sheet thickness t_s [mm**	**Preheating temperature T_{ph} [°C]**	**Heating rate [K/min]**	**Cooling rate [K/min]**
TNM-TNM	2.0	400-800	100	100
TNM-TNM	1.5	300-800	100	100
TNM-Ti6242	2.0-2.0	400-800	100	100
TNM-Ti64	2.0-2.0	400-800	100	100
TNM-Ti6242	1.5-2.0	300-800	100	100

In accordance to the parameter development for similar Ti-alloy joints and in spite of the different physical properties [3] , the transferability of parameter sets to first similar TNM and then dissimilar TNM joints was examined (Table 7).

Table 7: Tested parameter sets for similar TNM-TNM, dissimilar TNM-Ti64 and TNM-Ti6242 joints.

Joint	**Sheet thickness t_s [mm]**	**Weld coupon size [mm × mm]**	**Laser power P [kW]**	**Process velocity v [m/min]**	**Ti6242 filler wire speed v_w [m/min]**
TNM-TNM	2.0	50 mm × 25 mm	2.5-4.5	2.0-4.0	-
TNM-TNM	1.5	25 mm × 15 mm	2.5-5.0	2.0-5.0	-
TNM-TNM	1.5	25 mm × 25 mm	2.0-7.5	1.6-5.0	-
TNM-TNM	1.5	50 mm × 25 mm	4.5	3.0	-
TNM-Ti6242	2.0	50 mm × 25 mm	2.5-4.5	2.0-4.0	-
TNM-Ti64	2.0	50 mm × 25 mm	4.5	3.0	-
TNM-Ti6242	1.5-2.0	25 mm × 15 mm - 25 mm × 25 mm	4.5	3.0	
TNM-Ti6242	1.5-2.0	50 mm × 25 mm	4.5	3.0	
TNM-Ti6242	2.0	50 mm × 25 mm	4.5	3.0	~3.6 m/min

4.2.3. Post weld heat treatment of similar and dissimilar TNM joints

Post weld heat treatment (PWHT) of dissimilar TNM-Ti6242 joints with Ti6242 filler wire and a similar TNM joint preheated to 800 °C were performed to investigate the influence on the FZ microstructure. Dissimilar TNM-Ti6242 joints with Ti6242 filler wire were chosen since Ti- and γ-TiAl-alloys are notch sensitive [3]. By the use of filler wire, the underfill can be reduced and thus this joint configurations can be more interesting for industrial applications. To avoid a microstructural change in the sheets, especially a coarsening of the microstructure on the Ti6242 side, a heat treatment temperature below the β-transus temperature of Ti6242, 995 ± 15 °C [3] was chosen . Moreover, one typical heat treatment temperature of TNM 1290 °C, which was above the β-transus temperature of Ti6242, was tested for a similar TNM and a dissimilar TNM-Ti6242 joint with filler wire preheated to 800 °C. One heat treatment temperature for the dissimilar TNM joints was 950 °C for 2 h and the sample was furnace cooled (FC). To keep coarsening, especially of the Ti6242 side small, for 1290 °C the heat treatment time was reduced to 1 h. Moreover, FC was conducted. Heat treatments were executed with a Xerion Advanced Heating. The oven was flooded with Ar 150 l/h to avoid oxidation and oven pressure was 110 mbar.

4.3. Laser metal deposition

4.3.1 Wire-based laser metal deposition

For LMwD, the CNC machine center (IXION ULM) for LBW was retrofitted with a filler wire nozzle and a wire feeding system (DINSE DIX WD 300) (Figure 16). Similar to the LBW process, the substrate was clamped in a gas shielding box. For the protection of the deposited layer against oxidation, the gas shielding box was lamellar flooded with Ar from below. The CNC machine center was equipped with an 8 kW fiber laser (IPG YLS-8000-S2-Y12), a 300 mm laser optic, 300 µm fiber laser, a focus diameter of 746 µm and a wavelength of 1070 nm. The dragging filler wire deposition was conducted

with a defocused position of +26 mm and a tilt angle of 35 ° between the filler wire nozzle and the substrate.

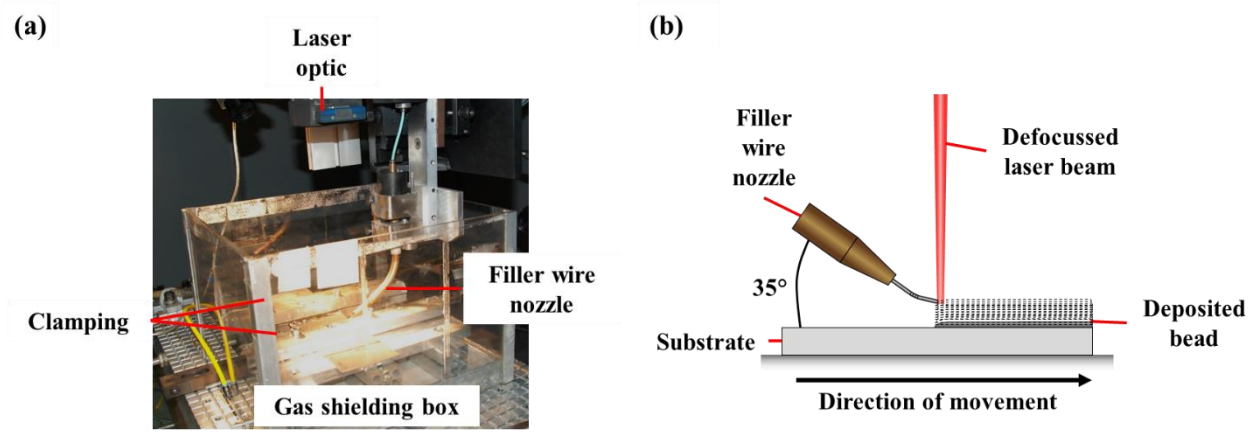

Figure 16: Experimental setup for LMwD depositions. (a) Side view. (b) Schematic filler wire nozzle positioning.

As substrates Ti64 (t_s = 2.54 mm) from VSMPO-Avisma and TNM (t_s = 2.00 mm), GfE Metalle und Materialien GmbH, were available. Ti6242 filler wire (Ø = 0.80 mm), E. Wagner Sondermetalle GmbH, or Ti64 filler wire (Ø = 1.00 mm) was deposited. Parameter development was conducted with the same Ti6242 filler wire as for LBW on Ti64 substrate (Table 8). Subsequent, parameter transferability to different substrate materials and Ti64 filler wire were investigated. The deposition length was 60 mm.

Table 8: Investigated parameter sets for LMwD depositions. Laser focus position f = +26 mm. Single layer length: 60 mm. Ti64 substrate (t_s = 2.54 mm). Ti6242 substrate (t_s = 3.00 mm). TNM substrate (t_s = 2.00 mm).

Wire	**Substrate**	**Laser power P [kW]**	**Process velocity v [m/min]**	**K-factor v_w/v**	**Filler wire speed v_w [m/min]**	**Number of layers**	**Gas flow rate [l/min]**
Ti6242	Ti64	1.75-4.50	0.4-1.0	4.00-20.00	2.5-12.0	1	15
Ti6242	TNM	2.00	0.4	6.25	2.5	1	15
Ti64	TNM	2.00	0.4	6.25	2.5	1	15

4.3.2. Powder-based laser metal deposition

LMpD was performed with a 2.2 kW Rofin-Sinar Nd:YAG laser with a laser spot size (A) of 300 µm, 300 µm laser fiber, 200 µm laser optic and a wavelength of 1064 nm. Ar was utilized as a shielding and powder nozzle carrier gas as for LBW and LMwD. The substrate, Ti64 (t_s = 2.54 mm) from VSMPO-Avisma, was hydraulically clamped with a system mounted on an industry robot (KUKA Agilus) (Figure 17 (b)). The industrial robot, coaxial powder nozzle, laser optic and two powder feeders were positioned in a glovebox (GS Glovebox Systemtechnik) (Figure 17 (a)). Spherical Ti6242 powder from AP&C with a powder range of 15-45 µm or in-house EIGA gas-atomized spherical TNM powder with a powder range of 25-90 µm were available. Powder transport was conducted by the powder suppling system (GTV PF2-2). To achieve a homogenous TNM powder flow in spite of the larger particle size

range, stirring of the powder feeder was set to 50 %. The coaxial powder nozzle COAX8 (Fraunhofer Institut für Werkstoff- und Strahltechnik) enables the powder supply through four powder connectors.

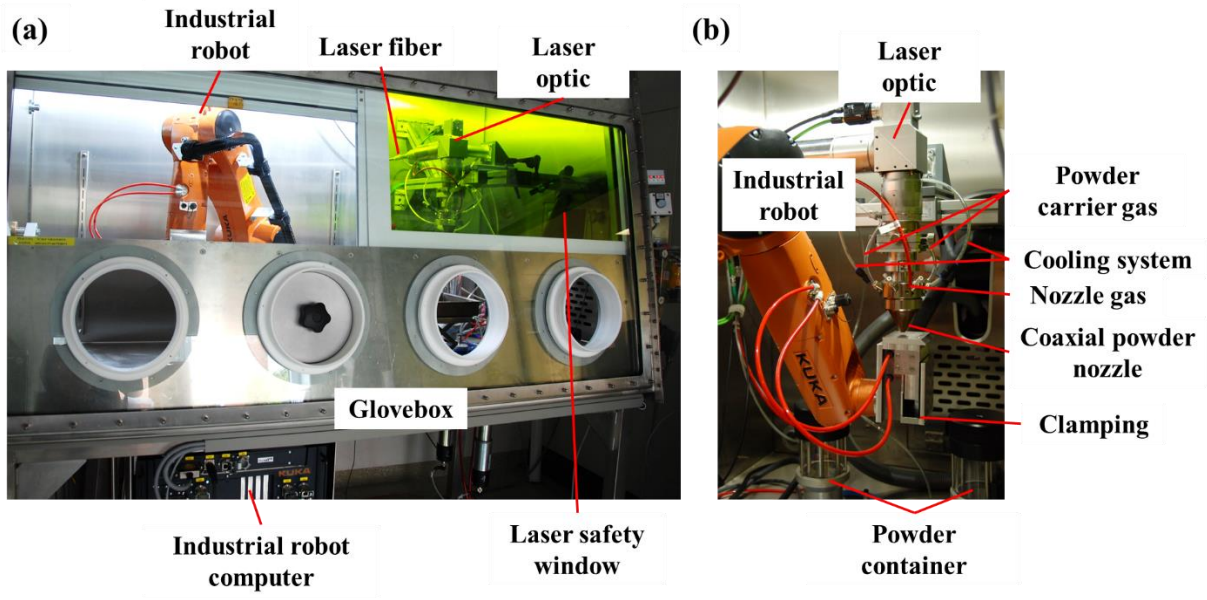

Figure 17: Experimental setup for LMpD depositions. (a) Outside view of glovebox. (b) Inside view of glovebox.

According to the manufacturer a high powder efficiency and quality is achieved when the deposition is conducted in the powder focus. The convention for determination of the laser focus and the schematic powder deposition process are displayed in Figure 18 (a) and (b).

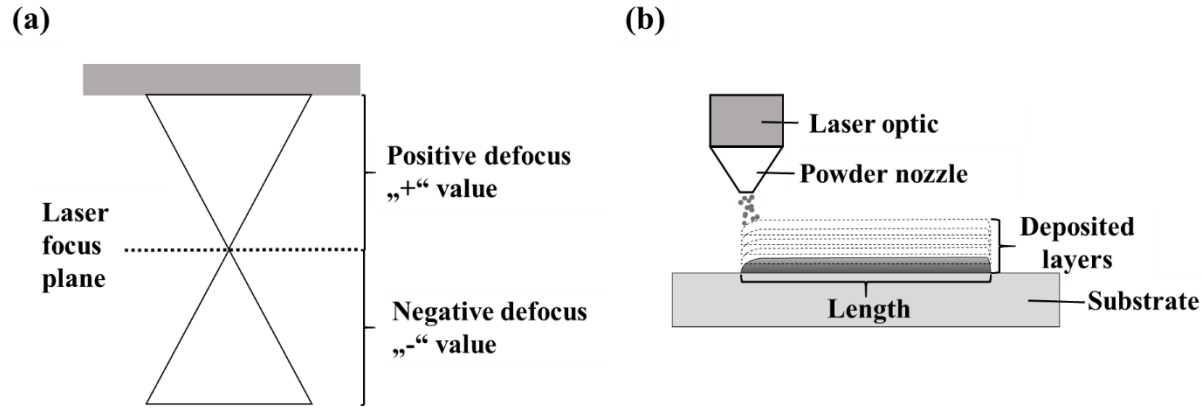

Figure 18: (a) Utilized laser focus convention. (b) Schematic LMpD process.

LMpD parameter development was executed with Ti6242 powder single layers and the successive parameter transfer to TNM powder, with different physical properties and a larger particle size range, was studied (Table 9). Deposited layers were 40 mm long.

Table 9: Tested parameter sets for LMpD single layers on Ti64 substrate (t_s = 2.54 mm). Powder nozzle gas flow rate N_{gas} = 4 l/min. Focal position powder nozzle F_{powder} =0 mm. Deposition length: 40 mm. TNM powder feeder stirring 50 %.

Powder material	**Substrate**	**Laser power P [kW]**	**Process velocity v [m/min]**	**Powder plate rotational speed R [rpm]**	**Carrier gas flow rate C_{gas} [l/min]**	**Laser focus position f [mm]**
Ti6242	Ti64	0.2-1.1	0.48-2.7	2 - 8	2 - 6	+4 - +11
TNM	Ti64	0.7-1.1	0.18-1.2	1 - 6	2 - 4	+4 - +10

4.4. Characterization methods

4.4.1. Visual inspection

Through visual inspection the outer appearance of the welds and LMD structures were analyzed with normal eyesight or aid of an optical instrument. Macro photographs were taken with a Nikon D80 equipped with an appropriate objective. For LBW and LMD pictures were taken with top and bottom view. The focus of the inspection was on insufficient or excess penetration for LBW, annealing colors, spatters, surface defects and cracks of large dimensions for LBW and LMD. Since for LBW and LMD of Ti- and γ-TiAl alloys no international standard exists, the visual inspection was performed according to DIN EN ISO 13919-1:1996 and 5817:2014.

4.4.2. Radiography

Investigating inner defects such as cracks and pores, radiography was performed with a Seifert Isovolt 320/13 with a resolution limit of 50 µm and a focal spot of 1.5 mm × 1.5 mm according to EN ISO 17636-1 test category B. A radiation sensitive film (Agfa Structrix D4 DW ETE) was positioned opposite of the specimen. The test arrangement was adapted for LBW joints and LMD depositions. Butt joints and LMD depositions were X-rayed from above. Radiographic films were processed by an automatic processing unit (GE NDT S eco 5320/300) and scanned with a high resolution film digitizer (GE FS50B). Due to undifferentiated contrast on the film, in-plane cracks with a small crack opening in thickness direction cannot be detected. Utilizing the software Rhythm a scale bar was calibrated, enabling the measurement of pore and crack characteristics. Through the application of a shadowing filter the detection of defects such as pores and cracks was facilitated.

4.4.3. Microstructural and phase analysis

Cross-sections were taken from the middle of the weld seam or the deposited layer (Figure 19 (a), (b)), embedded with a view in welding or deposition direction, grinded, polished and etched with Kroll's solution. Optical microscopy (OM) was conducted with the Leica DMI 5000M. Measurements of weld seam or LMD deposition characteristics such as weld seam width, which corresponds to the FZ width, HAZ width, reinforcement, underfill and deposited width and height of LMD deposition, corresponding to the FZ, were conducted with Adode Photoshop CS6 (Figure 19 (c), (d)). Therefore, the OM images were loaded into Adode Photoshop CS6, and using the scale bar in the OM images, a ruler was calibrated. For a more detailed investigation polished samples were mounted in a scanning electron microscope (SEM; Jeol JSM-6490LV). Analyzation of the chemical composition, phase mixing and

segregations was performed by energy dispersive X-ray analysis (EDX; EDAX genesis). EDX analysis were conducted with 15 kV at a working distance of 10 mm and a predetermined measurement time of 15 s. The measurement accuracy of the EDX analysis against standards is about 1 % and the detection sensitivity is 0.1 % for elements with a atomic number greater than 10 [214]. Depending on the shell of the ejected electron and the shell from which the electron comes to refill the electron hole, characteristic X-rays K_α, K_β, L_α etc. are emitted. Through executing electron backscatter diffraction measurements (EBSD; EDAX TSL OIM), the phase composition, grain size and further details of the microstructure were studied. For EBSD, the voltage was 30 kV, the working distance 13 mm and the tilt angle 70 °. The scanning step size depended on the magnification and was 1.3 µm for 150 ×, 0.6 µm for 350 × and 0.3 µm for 700 ×. For the differentiation of ordered and unordered as well as closely related crystallographic phases, quantitative XRD measurements of selected cross-sections were conducted. Therefore, a Bruker D8 Advance X-ray diffractometer using Cu-K_α radiation was applied. A scanning step size of 0.02 ° in a range of 2θ=20° - 90° was used. The software PANalytical X'Pert HighScore together with the JCPDS database and generated peaks by the program PowderCell2.4 with the lattice parameters in Table 10 were utilized for the phase identification.

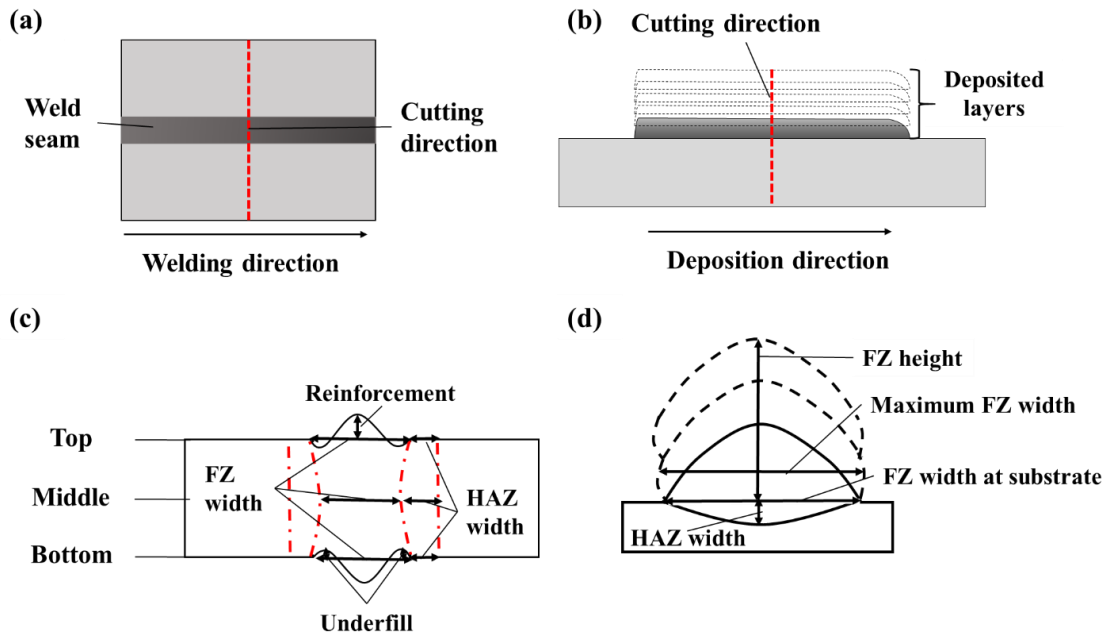

Figure 19: (a) Schematic cutting direction for cross-sections of LBW joints. (b) Schematic cutting direction for cross-sections of LMD deposition. (c) Weld seam characteristics. (d) LMD layers characteristics.

Table 10: Lattice parameters of γ-TiAl phases for XRD identification [89].

Phase	**a [Å]**	**b [Å]**	**c [Å]**
α_2	5.7750	5.7750	4.6380
β_O	3.2160	3.2160	3.2160
ω_O	4.5800	4.5800	5.5200
γ	3.9760	3.9760	4.0490

4.4.3. Microhardness measurements

A Shimadzu HMV-2000 was utilized for the Vickers microhardness measurements (HV 0.3). The indentation time was 15 s and the indentation velocity 0.1 mm/min. The butt joints microhardness measurements were performed in the middle of the weld seam (Figure 20 (a)) and for LMD depositions in the middle from the substrate to the top of the deposited layer (Figure 20 (b)). The measurement distance for butt joints was 0.16 mm and for LMD structures 0.2 mm in the BM and 0.16 mm in the HAZ and FZ in accordance with DIN EN ISO 6507:2006-03.

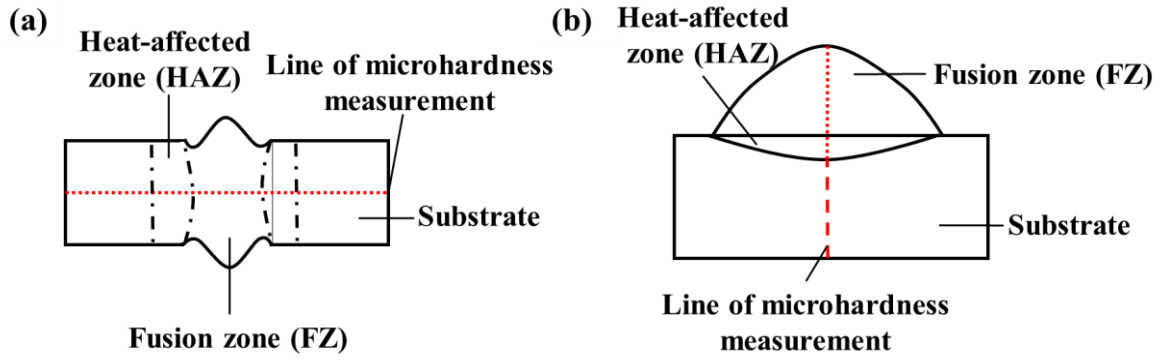

Figure 20: Schematic position of microhardness measurement for (a) LBW joints, (b) LMwD and LMpD layers.

4.4.5. Tensile test

Ti6242 tensile samples were extracted from the BM and the welded joints by electrical discharge machining. TNM tensile samples were also extracted from the BM and the welded joints by electrical discharge machining. Moreover, the edges were milled to the final sample geometry to obtain a surface roughness $R_z < 4$ in a reasonable time (Figure 21). As machining is time consuming and expensive first as-welded tensile samples were tested. In the case of unfavorable fracture positions or mechanical properties, the surface of selected tensile samples were grinded. The weld seam was in the middle of the tensile sample. TNM BM tensile samples were tested to determine the direction of the rolled sheet with the high tensile strength. According to the result, TNM weld coupons were cut to produce tensile specimens.

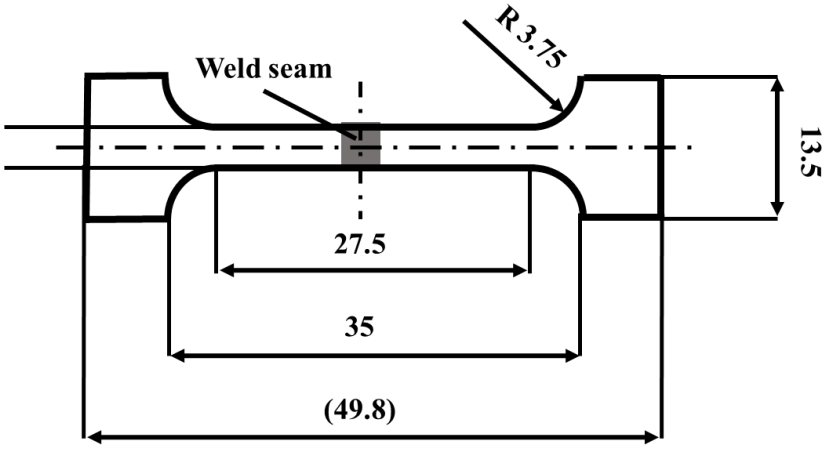

Figure 21: Technical drawing of utilized tensile sample. Specimen dimensions are in (mm).

Tensile tests were performed with a MTS 810 equipped with an oven in air atmosphere (Figure 22) according to DIN EN 2002-001 and DIN EN 2002-002. The oven temperature was controlled through two thermocouples positioned at the lower and upper part of the tensile sample. The strain rate was 2.38 x 10^{-5} s^{-1} and the elongation was measured with an air cooled extensometer (MTS 632.41F-10). Prior to the tests, the width and thickness at two positions were measured. The average width and thickness were utilize for calculating the area.

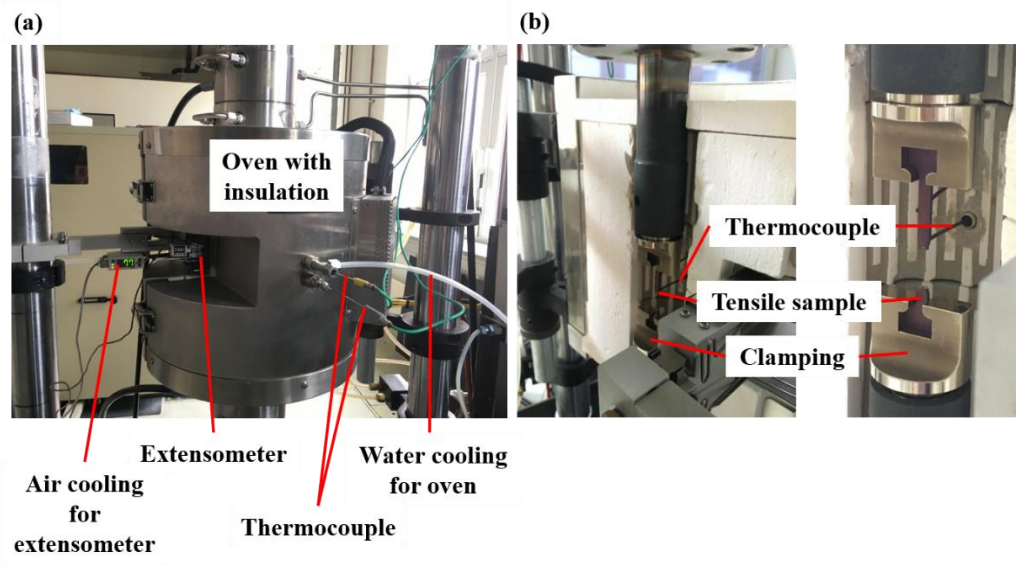

Figure 22: Experimental setup for tensile measurements. (a) Outside view with closed oven. (b) Inside view with open oven.

Tensile tests for Ti6242 and TNM were conducted at different temperatures (Table 11). Temperatures above RT were chosen with respect to the maximum long-term temperatures, 425 °C for Ti6242 and 800 °C for the TiAl alloy TNM [3]. The performance of BM tensile samples, similar Ti6242, similar TNM and dissimilar TNM-Ti6242 joint tensile samples were examined. The LBW parameter sets of welded tensile samples are shown in Table 12. As-welded and grinded similar TNM as well as dissimilar TNM-Ti6242 tensile samples were tested. Macro photographs were taken from the examined tensile samples with a Nikon D80 equipped with an appropriate objective.

Table 11: Testing temperatures of tensile samples. ✓ :performed. X: not performed.

Material	**RT**	**425 °C**	**800°C**
BM			
Ti6242	✓	✓	✓
TNM TD	✓	X	✓
TNM RD	✓	✓	✓
Joint			
Ti6242-Ti6242	✓	✓	X
TNM-TNM	✓	X	✓
TNM-Ti6242	✓	✓	✓

Table 12: LBW parameter sets utilized for tensile samples. Ar shielding gas flow rate: Similar Ti6242 joints 15 l/min, similar and dissimilar TNM joints 50 l/min.

Material	**Laser power [kW]**	**Welding speed [m/min]**	**Preheating temperature T_{ph} [°C]**	**Heating rate [K/min]**	**Cooling [K/min]**	**Filler wire**
Ti6242-Ti6242	1.75	0.7	-	-	-	-
Ti6242-Ti6242	3.50	4.0	-	-	-	-
TNM-TNM	4.50	3.0	800	100	100	-
TNM-Ti6242	4.50	3.0	800	100	100	-
TNM-Ti6242	4.50	3.0	800	100	100	Ti6242 Ø=0.8 mm, v_w=~3.6 m/min

5. Development of an approach for dissimilar joints by laser beam welding

In this chapter, an approach for dissimilar Ti-Ti-alloy and TiAl-Ti-alloys joints is developed. Therefore, similar joints were utilized as references. Due to the differing welding positions for similar Ti-alloy and TiAl-alloy joints process characteristics were examined. Furthermore, it is verified if an overlap between the parameter windows of the similar joints occurs. This is the fundamental requirement to obtain dissimilar joints without further measures. Based on the attained process windows of similar joints, dissimilar joints were welded. The evolving inner defects, weld seam characteristics, microstructure, chemical composition and phases of similar as well as dissimilar joints were investigated by the methods presented in Chapter 4.4. A special focus is on the influence of the evolving microstructure and phase on the crack development of similar and dissimilar TNM joints. Moreover, local mechanical properties were studied by microhardness measurements. In the last subsection, tensile experiments of selected similar and dissimilar joints are presented to evaluate the influence of the evolved microstructure and phases on the tensile properties.

5.1. Fundamentals for dissimilar joints by similar Ti-Ti- and TiAl-TiAl-alloy joints

To establish the fundamentals for dissimilar joints, similar Ti-alloy and TNM joints are studied. As a lack of knowledge regarding the crack development in similar TNM joints was presented in Chapter 1 and 3, theoretical considerations are used to assess the influence of the theoretical cooling rate and the preheating temperature on the crack formation. Similar Ti-alloy joints were welded in the flat position (Figure 14), while similar TNM joints were welded out-of-position (Figure 15). To monitor the influence of the welding position on the process characteristics, high speed camera images were utilized. Inner defects, especially the crack formation and the correlation to the preheating temperature, were assessed by radiography images. As the minimal preheating temperature for similar TNM joints is unknown (Chapter 3), the minimal preheating temperature was determined by variation. Evolving weld seam characteristics and microstructures were examined by cross-sections. Moreover, the influence of process parameters and the transferability in terms of overlapping process windows was studied. Thereby, it is verified, if the fundamental requirement of overlapping similar joint process windows for dissimilar joints without further measures exists. Chemical and phase analysis were utilized to investigate the influence of the LBW process on the chemical composition concerning segregations in the FZ and the evolving phases. Furthermore, the crack development of similar TNM joints is correlated to the microstructure and phase evolution. Microhardness measurements were utilized to assess the local mechanical properties.

5.1.1. Theoretical considerations

To assess the crack development of TNM, theoretical cooling rates according to the 2D Rosenthal equation for thin sheets are calculated (Equation 6) and correlated to the occurrence of cracks (Figure 23 (a), (b)). The thermophysical properties are taken from Table 3. As the starting temperature T 1500 °C is chosen, which is below the liquidus temperature of TNM and above the first phase transformation (Table 3). For the laser power, the process velocity and preheating temperature, investigated LBW parameter sets are utilized. The term “crack-free” is here referring to no transversal

cracks in the radiography image and no cracks in the cross-section. Moreover, the theoretical temperature distribution in the cross-section according to the heat conduction equation with finite extent assuming a moving point source is determined according to the program of Herrnring et al. [215]. The program solves the linear heat conduction equation with the Green's function equation (9) (Figure 23 (c)). The Green's function is solved for a plate with the length of 50 mm, width of 50 mm and thickness of 2 mm. The heat source g has a Gaussian distribution.

$$\nabla^2 T + \frac{1}{\lambda} g = \frac{1}{\alpha} \frac{\partial T}{\partial t} \tag{9}$$

$$g = (\xi, \eta, \varsigma) = Q f_\xi(\xi) f_\eta(\eta) f_\varsigma(\varsigma) \tag{10}$$

$$f_X(X) = \frac{2}{\sqrt{\pi} X_e [\mathrm{erf}\left(\frac{X''}{X_e}\right) - \mathrm{erf}\left(\frac{X'}{X_e}\right)]} e^{-(\frac{X}{X_e})^2} \tag{11}$$

T – temperature, t – time, λ – thermal conductivity, g – heat source, α – thermal diffusivity, $X = (\xi, \eta, \varsigma)$ – room directions, Q – welding power, X_e – variable parameter

The following parameter sets are utilized in the theoretical considerations (Table 13):

Table 13: Parameter sets for theoretical considerations of similar TNM joints.

Parameter set	Sheet thickness t_s (mm)	Laser power P (kW)	Process velocity v (m/min)
1, 2	1.5	3.5	2.00
1a, 1b	2	4.5	3.00
2a, 2b	2	3.5	2.00
3	2	2.5	3.00
4	2	4.0	4.00

For similar TNM joints using a 1.5 mm thick sheet, the theoretical cooling rate decreases exponentially with increasing preheating temperature (Figure 23 (a)). Parameter set 1 and 2 in Figure 23 (a) represent the same LBW parameter sets with differing preheating temperatures. As known from Equation 6, the black dot-dash lines illustrate the influence of the utilized LBW parameter sets on the theoretical cooling rate (Figure 23 (a)). Hence, by adjusting the preheating temperature or the LBW parameter sets, comparable theoretical cooling rates can be achieved. Due to the thinner sheet thickness and the resulting lower cooling temperature, different threshold preheating temperatures for 1.5 mm and 2.0 mm thick crack-free similar TNM joints are obtained (Figure 23 (a), (b)). Crack-free similar TNM joints with a sheet thickness of 1.5 mm were obtained with a preheating temperature of 400 °C, while 600 °C was necessary to achieve crack-free 2 mm similar TNM joints.

For similar TNM 2.0 mm joints, the resulting crack formation is further correlated to the LBW parameter sets, the preheating temperature and the obtained theoretical cooling rates (Figure 23 (b)). In general, the theoretical cooling rates increase with decreasing line energy for the same preheating temperature (Figure 23 (b) arrow). The black dot-dash lines represent the theoretical cooling rates for

constant parameter sets. As indicated by these, comparable theoretical cooling rates can be achieved by varying parameter sets at different preheating temperatures. The parameter set 1a and 1b as well as 2a and 2b have the same LBW parameter set with differing preheating temperatures. The preheating temperature for parameter set 1a and 2a is 400 °C and for parameter set 1b and 2b 600 °C. Nevertheless, parameter sets 2a and 1b have a comparable theoretical cooling rate (Figure 23 (b)). Consequently, no general theoretical threshold cooling rate for crack-free similar TNM joints exist. To obtain crack-free joints the cooling rate has to be controlled (Chapter 3.4.). In spite of the highest cooling rate for parameter set 3, this joint is crack-free. Differently, parameter sets 1a, 2a with lower theoretical cooling rates and a lower preheating temperature than parameter set 3 exhibit transversal cracks. In contrast to the local influence of the cooling rate, the preheating temperature is globally effecting the welding process and the resulting thermally induced stresses, microstructures and phases. Therefore, the preheating temperature and not the local theoretical cooling rate seems to dominantly influence the crack formation. Concluding from the theoretical cooling rates of Figure 23 (a) and (b), no general theoretical threshold cooling rate exists, but the theoretical cooling rate for crack-free similar TNM joints depends on the sheet thickness and the LBW parameter sets. Moreover, due to the global effect of the preheating temperature compared to the local influence of the parameter sets, the preheating temperature seems to be the dominant factor on the crack development.

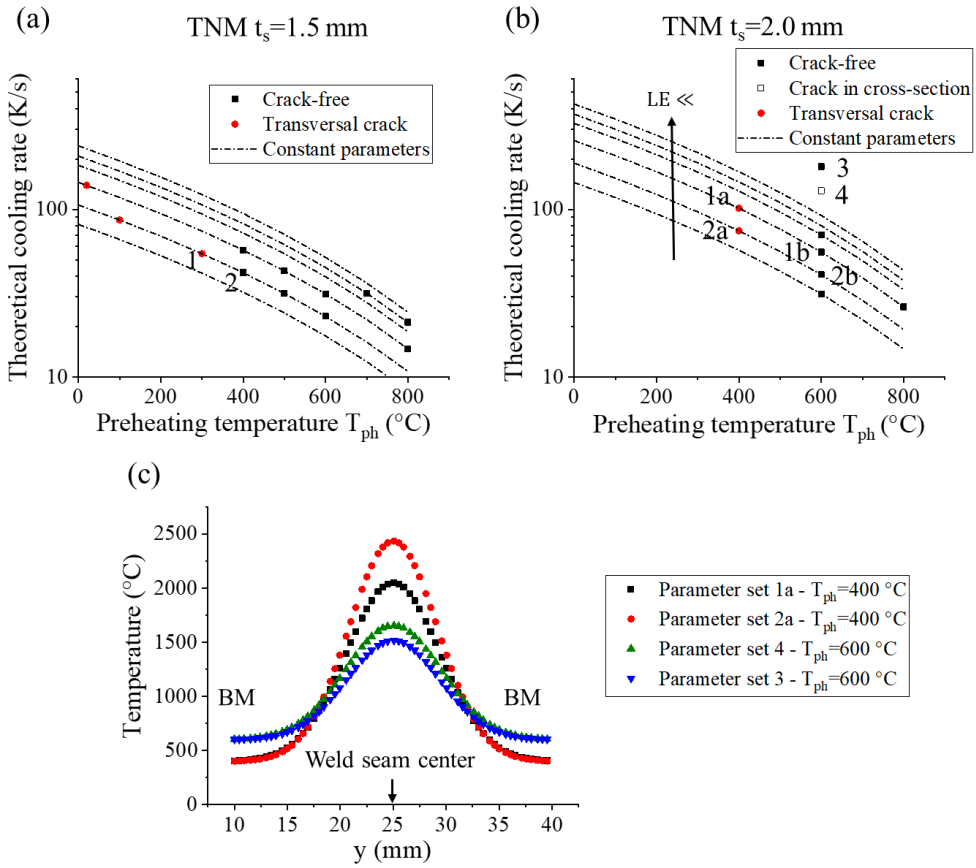

Figure 23: (a)-(b) Effect of theoretical 2D Rosenthal cooling rate (Equation (6)) and preheating temperature on crack formation of similar TNM joints. (a) t_s=1.5 mm. Crack-free (black square). Transversal crack (red circle). (b) t_s=2.0 mm. Crack-free (black solid square). Crack in cross-section (black open square). Transversal crack (red circle). (c) Theoretical temperature distribution in similar TNM 2.0 mm joint cross-sections calculated with the program of Herrnring et al. [215].

Parameter set 1a and 2a with cracks have the highest temperature in the weld seam center and the lowest preheating temperatures (Figure 23 (c), black square, red circle). In contrast, the crack-free parameter set 3 corresponding to the highest theoretical cooling rate in Figure 23 (b) reveals a lower weld seam temperature and higher preheating temperature (Figure 23 (c), blue bottom triangle). Hence, the large temperature gradient from the weld seam center in y-direction for parameter set 1a and 2a should lead to the transversal crack formation (Figure 23 (c), black square, red circle). For parameter set 4 (Figure 23 (c), green top triangle), an almost similar temperature distribution as for parameter set 3 is calculated (Figure 23 (c), blue bottom triangle). Hence, from the theoretical considerations (Figure 23 (b), (c)) a crack-free joint is expected. Therefore, in contrast to the transversal cracks, the crack in the cross-section seems not to be related to the theoretical cooling rate and temperature distribution

To evaluate the crack formation in the cross section welded with parameter set 4, which could not be explained by the theoretical considerations (Figure 23 (b), (c)), a cross-section of the same parameter set at differeing welding position is displayed in Figure 24. In spite of the unmolded weld coupon edge, no crack in the cross-section occurs in Figure 24 (b). The unmolten edge resulted in an area that is not joined, which was caused from a laser beam positioning too far away from the weld coupon edge. Therefore, the unmolten edge acts as a starting crack in the joint and in combination with the sheet-offset is the main reasons for the crack in the cross-section (Figure 24 (a)). Hence, besides the influence of the preheating temperature on the crack formation (Figure 23), the laser beam positioning and the weld coupon alignment are crucial to attain crack-free similar TNM joints.

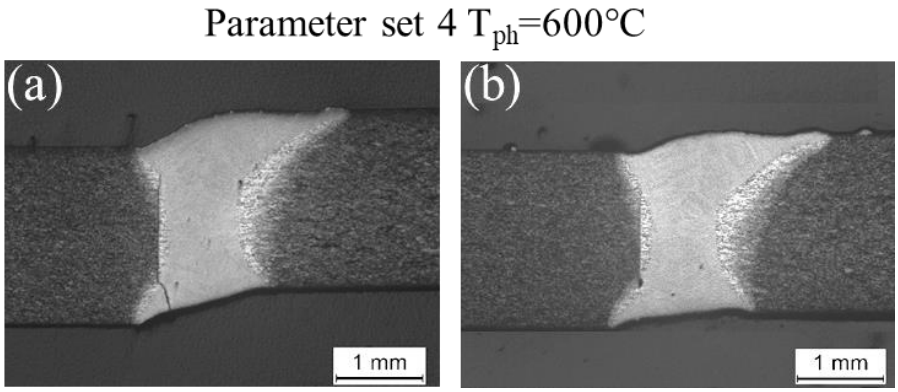

Figure 24: Cross-section of parameter set 4 T_{ph}=600 °C at differing weld seam positions. (a) Crack in cross-section. (b) No crack in cross-section.

The theoretical considerations can be summed up as follows: No general theoretical threshold cooling rate for crack-free similar TNM joints exists and the preheating temperature influences globally the temperature gradient and distribution. Consequently, the preheating temperature appears to be the more dominant factor for the crack development compared to the theoretical cooling rate. Hence, the experimental approach to obtain crack-free similar and dissimilar joints by variation of the preheating temperature is justified.

5.1.2. Process characteristics and inner defect development

The influence of the differing welding positions was investigated by high-speed camera and radiography images, since similar Ti-alloy joints were welded in flat position and similar as well as dissimilar TNM joints are welded out-of-position. Moreover, the use of filler wire on the inner defect development of similar Ti6242 joints was examined. To obtain crack-free similar TNM joints, the preheating temperature was varied.

The process monitoring with the high-speed camera revealed differences between the metal-vapor clouds for the differing welding positions (Figure 25), which are the flat position and out-of-position (Figure 14, Figure 15). The formation of a distinct metal-vapor cloud only occurs for LBW in the flat position (Figure 25 (a)) as reported for welding with fiber lasers [119]. The metal-vapor cloud attenuates the laser radiation above the keyhole [119]. In contrast, the metal-vapor cloud for out-of-position LBW is considerable smaller (Figure 25 (b)). This is advantageous as less laser radiation should be attenuated.

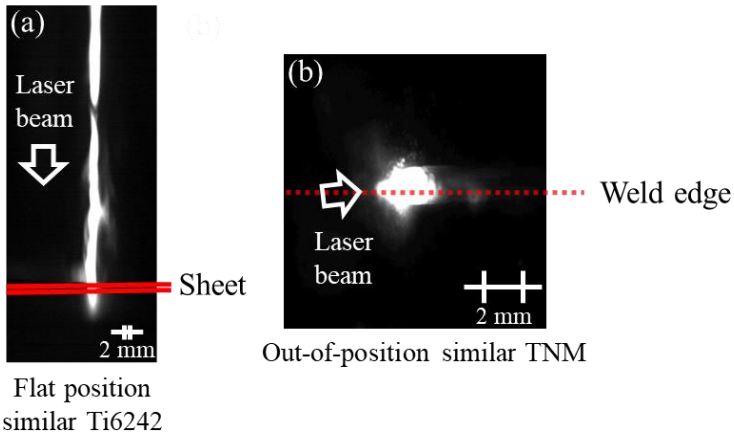

Figure 25: High-speed camera images during LBW of similar Ti6242 and TNM joints. (a) Flat position LBW similar Ti6242 joints P=2.5 kW, v=3 m/min RT. (b) Out-of-position LBW similar TNM joints P=4.5 kW, v=3 m/min, T_{ph}=600 °C.

Radiography images are utilized to examine the influence of the welding position, the use of filler wire and the preheating of weld coupons on inner defects (Figure 26). As Ti-alloys are notch sensitive [164] and no studies on the use of Ti6242 filler wire are available (Chapter 3.5.1.), the influence of Ti6242 filler wire on flat position and out-of-position LBW is investigated in a pre-study. Furthermore, as the use of Ti6242 filler wire was investigated for preheated dissimilar TNM-Ti6242 joints (Chapter 4.2.2.), the influence of preheating together with the use of Ti6242 filler wire on similar Ti6242 joints was examined.

No cracks emerge in all similar Ti6242 joints for the investigated parameter sets, which is in accordance to the low estimated crack sensitivity of Ti-alloys [71] (Figure 26). By the choice of parameter sets sound similar Ti6242 joints can be obtained. For some similar Ti6242 joints spatter is obtained (Figure 26), which can result in the formation of porosity [216]. Nevertheless, according to international standards some spatter is acceptable [217,218]. The influence of the welding position on the spatter formation is minor (Figure 26 (a), (b)). Comparing the radiography results of flat position and out-of-position LBW for the same parameter set, the influence of the welding position on the porosity formation is insignificant (Figure 26 (a), (b)). Hence, the role of degassing. In contrast, utilizing Ti6242

filler wire for a comparable filler wire velocity as in the flat position (Figure 26 (c)), results in line porosity with a pore size between 0.17 - 0.60 mm for the out-of-position LBW with Ti6242 filler wire (Figure 26 (d)). The pores are larger than for the joint welded autogenously in out-of-position LBW (Figure 26 (b)), which can be associated with differing degassing behaviors, as melting the filler wire could reduce the melt pool temperature, and induce process instabilities. Thus, the welding position can hinder degassing in the case of out-of-position LBW with filler wire. By applying a typical TiAl preheating temperature of about 800 °C to the out-of-position LBW process with the same filler wire parameter set, the line porosity is removed (Figure 26 (e)). Therefore, using a preheating temperature and thereby decreasing the cooling rate, enables degassing during out-of-positon LBW of similar Ti6242 joints with Ti6242 filler wire. Summarizing, suitable parameter sets for flat position and out-of-position LBW are developed and in both welding positions degassing is crucial for obtaining a low porosity.

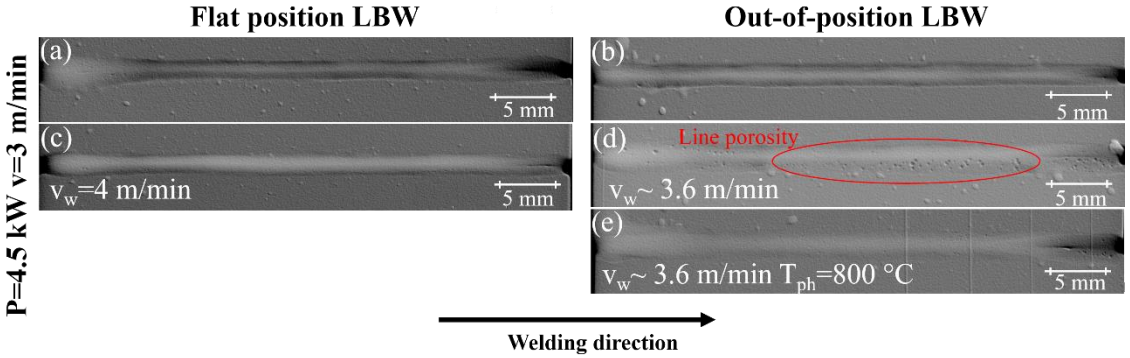

Figure 26: Radiography images of similar Ti6242 joints welded in different welding positions, with or without filler wire and preheated.

As TiAl is crack sensitive [34,36–38] and the required minimal preheating temperature for similar TNM joints is unknown [51,52], the influence of the preheating temperature and the sheet thickness on the

crack development for similar TNM joints was examined. At first visual inspection was utilized (Figure 27). All similar TNM joints display full penetration. For the 1.5 mm thick TNM sheet, a transversal crack occurs at 300 °C (Figure 27 (a)) and for the same parameter set with a preheating temperature of 400 °C the similar joint is crack-free (Figure 27 (b)). 400 °C is much below the brittle-to-ductile temperature described in literature, which depends on the chemical composition, microstructure and is approximately 700 °C [8]. In Figure 27 (c) with a 1.5 mm thick TNM sheet, the resulting joint is crack-free. Utilizing the same parameter set for a 2.0 mm thick TNM sheet, transversal cracks emerge (Figure 27 (d)). The different sheet thicknesses affect the theoretical cooling rate and temperature distribution, which influence the phase transformation and the thermally induced stresses and could lead to the differing crack formations. Nevertheless, statistically effects cannot be neglected.

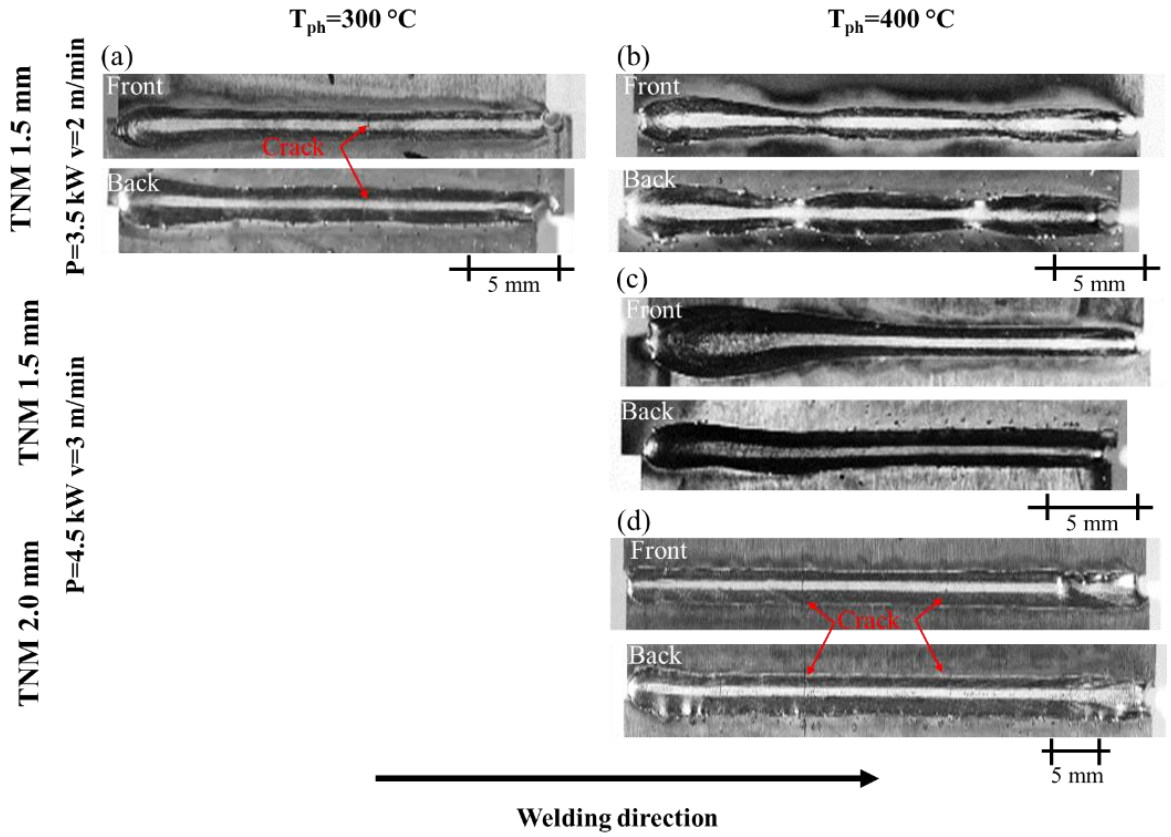

Figure 27: Photographs of similar TNM joints welded with different sheet thicknesses, welding parameters and preheating temperatures.

To further assess the crack development and verify crack-free similar TNM joints, radiography was utilized (Figure 28). The radiographs confirm crack-free similar TNM joints of 1.5 mm thick sheets with a preheating temperature of 400 °C (Figure 28 (b), (c)). At 300 °C, a transversal crack is present (Figure 28 (a)). As the minimal preheating temperature for crack-free similar TNM joints with a sheet thickness of 2.0 mm is higher than 400 °C, at 400 °C five transversal cracks are displayed (Figure 28 (d)). Furthermore, despite full penetration (Figure 27 (d)) an unmelted weld edge is visible. This edge could be due to the used welding position, since the liquid melt can flow in direction of gravity (Figure 15), the sheet-offset or the laser beam alignment. Crack-free similar TNM joints for 2.0 mm sheet thickness are obtained with a preheating temperature of 600 °C (Figure 28 (e)). Moreover, in all similar

TNM joints no macroporosity, but a low level of microporosity is found. Thus, the amount of spatter is acceptable [217,218] and no process instabilities developed, which otherwise could have led to porosity formation. Concluding, the occurrence of transversal cracks (Figure 28 (a), (d)) seems to be linked to the preheating temperature. Due to different theoretical cooling rates for differing sheet thicknesses (Figure 23 (a), (b)) and thus different evolving thermally induced stresses, the number of transversal cracks could be also influenced by the sheet thickness (Figure 28 (a), (d)).

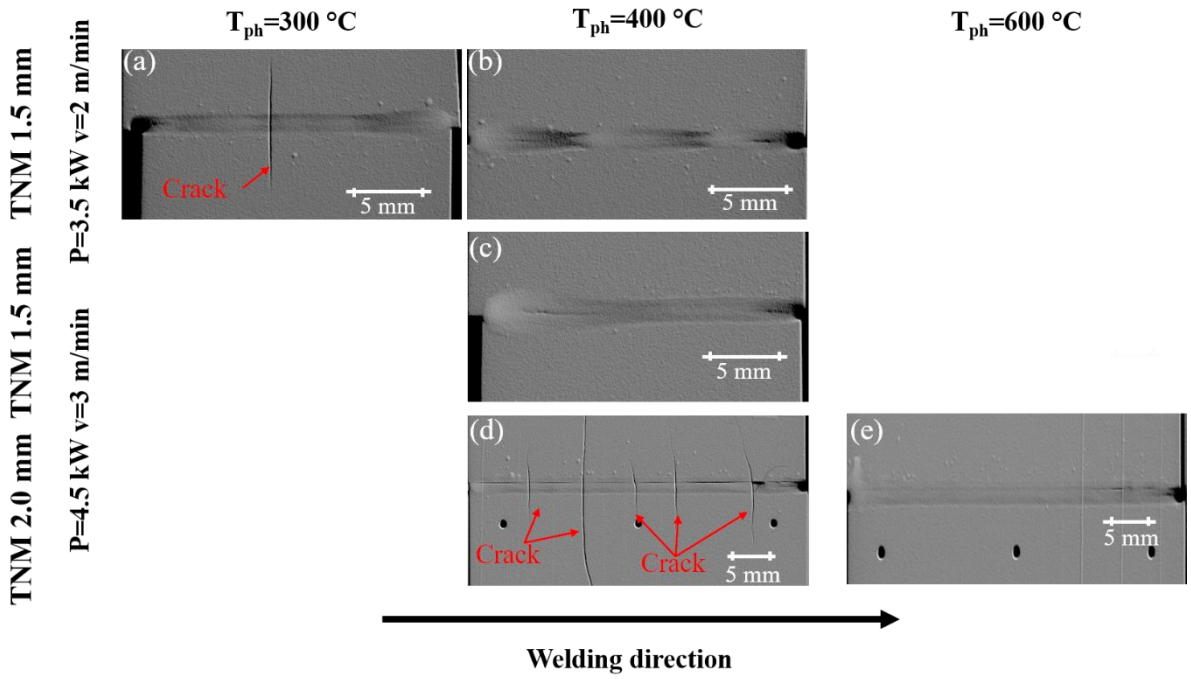

Figure 28: Radiography images of similar TNM joints welded with different sheet thicknesses, welding parameters and preheating temperatures.

5.1.3. Weld seam characteristics and microstructure analysis

Weld seam characteristics as the weld seam shape, reinforcement and underfill were examined by cross-sections. Besides, the influence of the welding position on the weld seam shape is assessed. The evolving microstructure was specified in OM and SEM images. Furthermore, the overlapping of the process windows for similar joints was examined.

The parameter set transfer from similar Ti64 joints to similar Ti6242 joints is investigated by cross-sections in Figure 29. For both similar joints welded with the same parameter sets, the weld seam shape, the underfill and reinforcement are alike. This could be related to the comparable thermophysical properties (Table 3). Due to the slightly different alloying elements (Table 2), a differing etching behavior arises. Two different characteristic weld seam shapes, an X-shape (Figure 29 (a), (b), (d)-(f), (h)) and an Y-shape (Figure 29 (c), (g)) occur. For similar Ti64 joints, for low line energies an V-shape with a closed keyhole-mode and for high line energies an X-shape with an open keyhole-mode is formed [28,120,121]. Comparable to literature, here for a low line energy (60 MJ/m) with a low laser power and process velocity an Y-shape, which is close to the V-shape, is developed (Figure 29 (c), (g)). An X-shape is achieved by high line energies (150 MJ/m) with a low process velocity and laser power (Figure 29 (a), (e)) or with higher process velocities and laser powers for medium (90 MJ/m) and low line energies (52.5 MJ/m) (Figure 29 (b), (d), (f), (h)). By the highest line energy (150 MJ/m), lowest laser power and process velocity, a very large FZ with large prior β-grains, nearly no reinforcement and no underfill is achieved (Figure 29 (a), (e)). Due to the largest underfill in Figure 29 (b), (f) and the

notch sensitivity of Ti-alloys [164], this parameter set is not further considered in the characterization. The prior β-grain size seems to increase with increasing line energy (Figure 29). The length of the prior β-grains rises with the line energy 52.5 MJ/m to 150 MJ/m, from 0.18 mm to 0.61 mm for Ti64 and

0.19 mm to 0.6 mm for Ti6242 (Figure 29 (a), (d), (e), (h)). Comparably, the prior *β*-grain width increases with the line energy 52.5 MJ/m to 150 MJ/m, from 0.07 mm to 0.23 mm for Ti64 and 0.07 mm to 0.18 mm for Ti6242 (Figure 29 (a), (d), (e), (h)). Furthermore, the characteristic grain growth opposite to the maximal temperature gradient can be seen (Figure 10, Figure 29). As references for the dissimilar joints, two parameter sets of sound welds with the same weld seam shape and an acceptable underfill had to be chosen for further examination of the microstructure and local mechanical properties. Due to the absent underfill of the parameter set P=1.75 kW, v=0.7 m/min, LE=150.0 MJ/m, the minor underfill and comparable weld shape of the parameter set P=3.5 kW, v=4.0 m/min, LE=52.5 MJ/m, these two are investigated further. Summing up the results, the parameter sets could be successfully transferred for similar Ti-alloy joints.

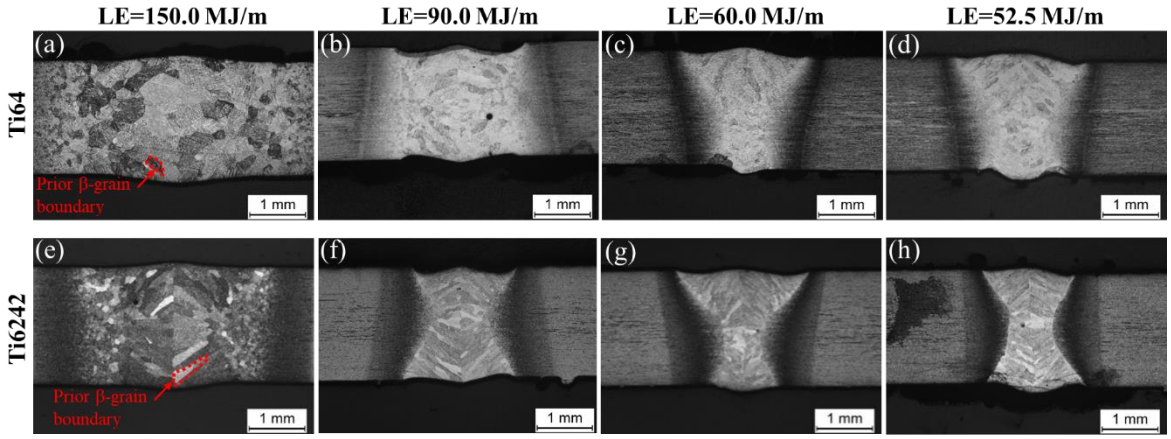

Figure 29: Cross-section of similar Ti64 joints (t_s=2.0 mm) and similar Ti6242 joints. (a)-(d) Ti64. (e)-(h) Ti6242. (a), (e) P=1.75 kW, v=0.7 m/min, LE=150 MJ/m. Red dotted lines: Exemplarily prior *β*-grain boundary. (b), (f) P=4.5 kW, v=3 m/min, LE=90 MJ/m. (c), (g) P=2.0 kW, v=2 m/min, LE=60 MJ/m. (d), (h) P=3.5 kW, v=4 m/min, LE=52.5 MJ/m.

For similar Ti6242 joints the parameter set could be successfully transferred from the flat position LBW to the out-of-position LBW (Figure 30 (a), (d)). Moreover, through the use of filler wire, the underfill could be decreased (Figure 30 (b), (c), (e), (f)). In both welding positions, the amount of reinforcement is increased by the utilization of filler wire. Caused by the out-of-position LBW, pore formation due to overheating and the hindering of degassing, is the main reason for the large pores in Figure 30 (e). Overheating induces local vaporization and if gases cannot escape, pores are obtained. Consistently, the flat LBW parameter set of Figure 30 (c) reveals no macroporosity (Figure 26 (c)), even so a higher filler wire speed was applied. Working towards dissimilar TNM joints, a preheating temperature of 800 °C was tested to enable the degassing process (Figure 30 (f)). Through preheating the line porosity is removed as degassing is enabled (Figure 26 (e)). Additionally, the HAZ grows and the FL is blurring its contours, which could be due to activated diffusion controlled atom migrations by preheating. In contrast, the prior *β*-grains in the FZ do not seem to grow further compared to RT similar Ti6242 joints with filler wire. This could be attributable to the filler wire acting as a nucleus and hindering further growth of the prior *β*-grains in the FZ.

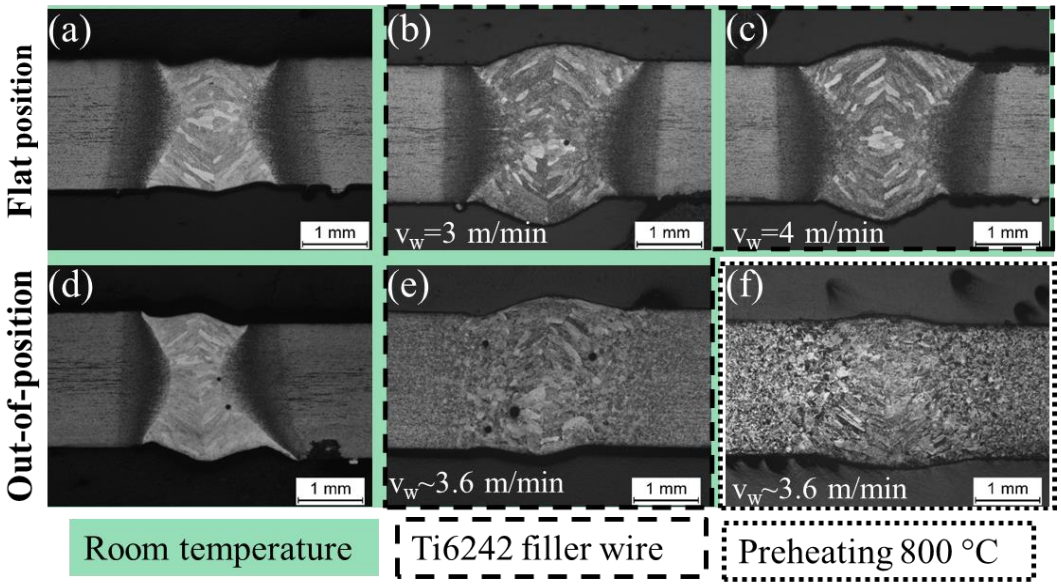

Figure 30: Influence of welding position and Ti6242 filler wire on cross-sections of similar Ti6242 joints welded with P=4.5 kW, v=3 m/min.

Figure 31 (a) shows the investigated parameter windows of similar Ti64, Ti6242 and TNM joints in this study. The investigated parameter windows are overlapping. Thus, in this term and despite their different thermophysical properties (Table 3), parameter sets could be successfully transferred from similar Ti64 to similar Ti6242 and to similar TNM joints. In detail, for similar Ti64 and Ti6242 joints welded in the flat position two characteristic comparable weld seam shapes develop (Figure 31 (b)-(g)). Hence, for similar Ti64 and Ti6242 joints also the weld seam shape is transferable. The metal-vapor cloud could be reduced for similar TNM joints in out-of-position LBW (Figure 25 (b)) and more energy could couple in the material. Consequently, only the X-shape is achieved for similar TNM joints welded in out-of-position LBW (Figure 31 (h)-(j)). Even for the parameter set P=2.5 kW and v=3 m/s, where a Y-shape is obtained for similar Ti64 and Ti6242 joints welded in flat position (Figure 31 (b), (e)). Therefore, due to the differing welding positions and even so the investigated parameter windows of similar Ti-alloy and TNM joints overlap, the weld seam shape cannot be transferred. For similar TNM joints the underfill-reinforcement contour is less distinct compared to similar Ti6242 joints (Figure 31 (e)-(j)). Despite the out-of-position LBW for similar TNM joints, a symmetric weld seam shape is achieved. Therefore, the difference in the underfill-reinforcement contour could be attributed to the lower surface tension of TiAl compared to Ti64 and Ti6242 (Table 3). Moreover, as the investigated process windows of similar joints overlap, the fundamental requirement to achieve dissimilar sound welds with the same parameter sets and no further measures preexist.

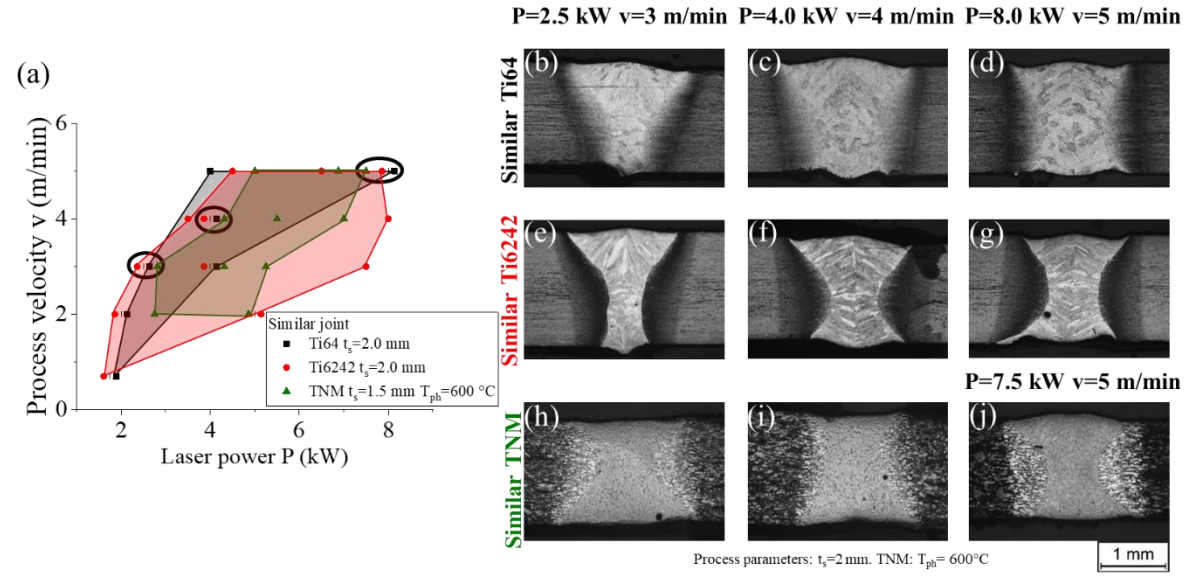

Figure 31: (a) Overlap of investigated parameter windows of similar Ti64, Ti6242, TNM (1.5) joints. The black ellipse indicates the positions of the cross-sections in (b)-(j). (b)-(j) Comparison of similar Ti64, Ti6242 and TNM joints welded with different parameter sets.

In the next step, the influence of the preheating temperature and the sheet thickness on the weld seam shape and microstructure of similar TNM joints is examined (Figure 32). For all parameter sets independent of the preheating temperature and sheet thickness through etching no prior β-grains in the cross-section are visible. Only X-shaped weld seams are obtained. The underfill is more pronounced than the reinforcement, which could be the result of the surface tension and viscosity in combination with the welding position [25]. For similar TNM joints with a sheet thickness of 2.0 mm and 4.0 mm welded by a CO_2 laser in the flat position, underfills at the weld seam top of 0.2 mm to 0.4 mm were reported [52]. In contrast, by welding the similar TNM joints in out-of-position LBW, the underfill of the weld seam top could be successfully reduced to values between 0 mm and 0.13 mm for 2.0 mm thick TNM sheets.

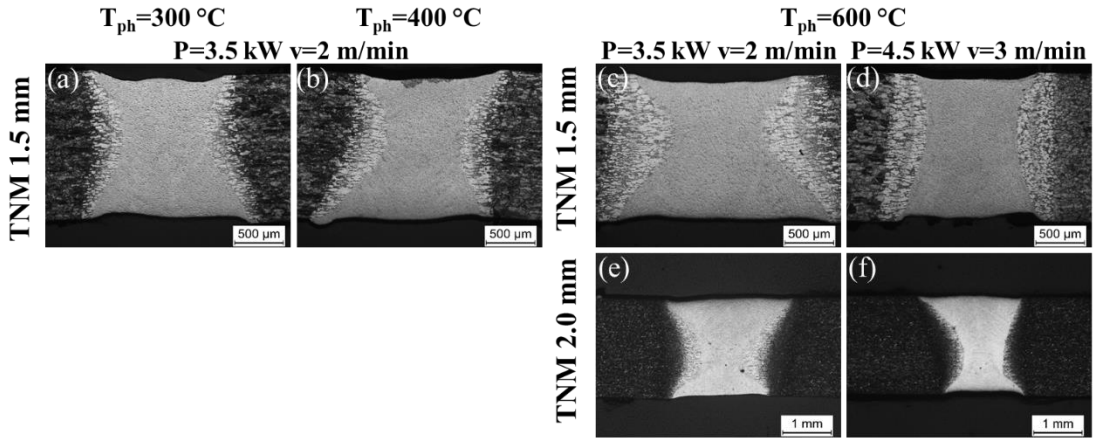

Figure 32: Cross-sections of similar TNM joints with different sheet thicknesses, parameter sets and preheating temperatures.

In order to release welding stresses and to homogenize the microstructure, a similar TNM joint was heat-treated exemplarily for 1 h at 1290 °C and then cooled down by furnace cooling (FC). The

temperature of 1290 °C is in the range of typical TNM post heat treatment temperatures for forged structures, laser beam welded joints and laser additive manufacturing structures [13,52,65].

In the present case the microstructure of the sheet and the FZ coarsened through the heat treatment compared to the as-welded joint (Figure 33 (a)-(d)). The BM and FZ microstructures assimilate and a clear distinction between both becomes difficult (Figure 33 (a), (b)). Moreover, the microstructural gradient between the HAZ and the FZ significantly decreased (Figure 33 (c), (d)). In comparison to that, the BM microstructure of the heat-treated joint is slightly coarser than the BM microstructure (Figure 33 (d), (e)). By the heat treatment, the α_2 martensitic microstructure in the FZ is converted to a typical TNM microstructure with α_2-γ domains, β/β_0 and γ grains (Figure 33 (c), (d), (e)). In this regard, a further adjustment of grain size could be obtained by the modification of the duration of the heat treatment.

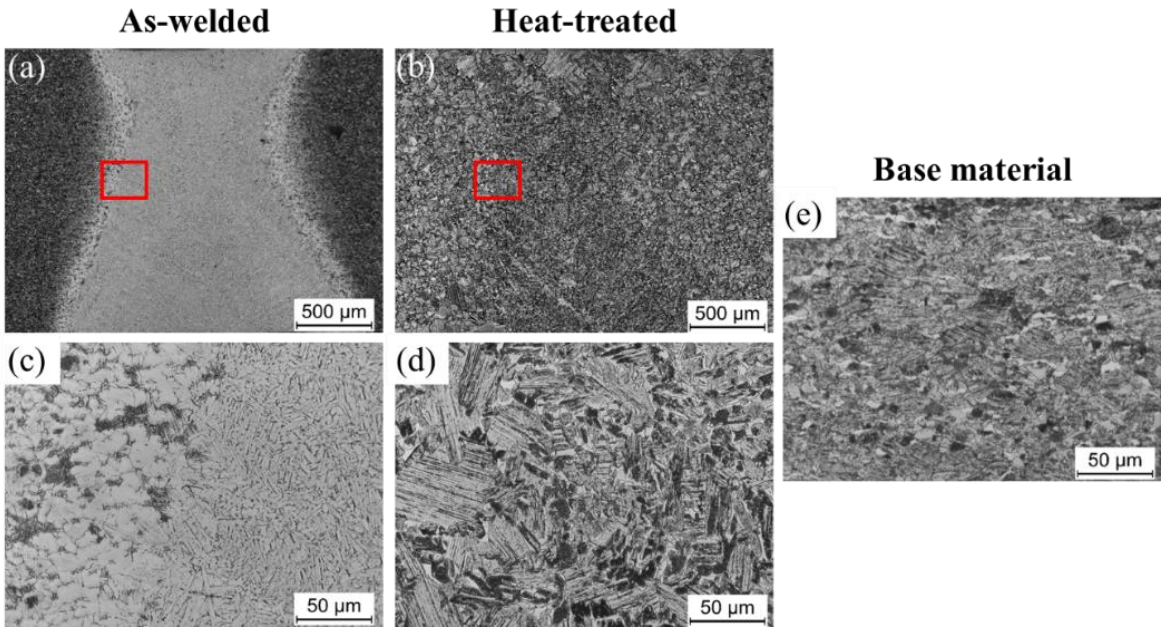

Figure 33: Comparison of as-welded and heat-treated similar TNM joint cross-sections by OM. P=4.5 kW, v=3 m/min T_{ph}=800 °C. (a), (c) As-welded joint. Red square in (a) indicates position of (c). (b), (d) Heat-treated joint. Heat treatment: 1290 °C, 1h FC. Red square in (b) indicates position of (d). (e) TNM BM cross-section by OM.

To analyze the evolving microstructure, SEM images of the FZ and FL are utilized (Figure 34, Figure 35). For both similar Ti6242 joints prior β-grains are visible in the FZ (Figure 34 (a), (d)). Due to the high cooling rates by LBW, the microstructure in both joints is martensitic. As the line energy of 150 MJ/m is higher in Figure 34 (b) and thus a lower cooling rate should emerge, the needles formed in the FZ are longer than for the similar Ti6242 joint with the lower line energy of 52.5 MJ/m (Figure 34 (e)). Needles that grew from the prior β-grain boundary in the FZ, can be seen in Figure 34 (b). Moreover, as already observed in OM images (Figure 29 (a), (e)), prior β-grains belonging to the FZ and HAZ emerge, which indicates epitaxial growth of the prior β-grains at the FL for both similar Ti6242 joints (Figure 34 (c), (f), (g)).

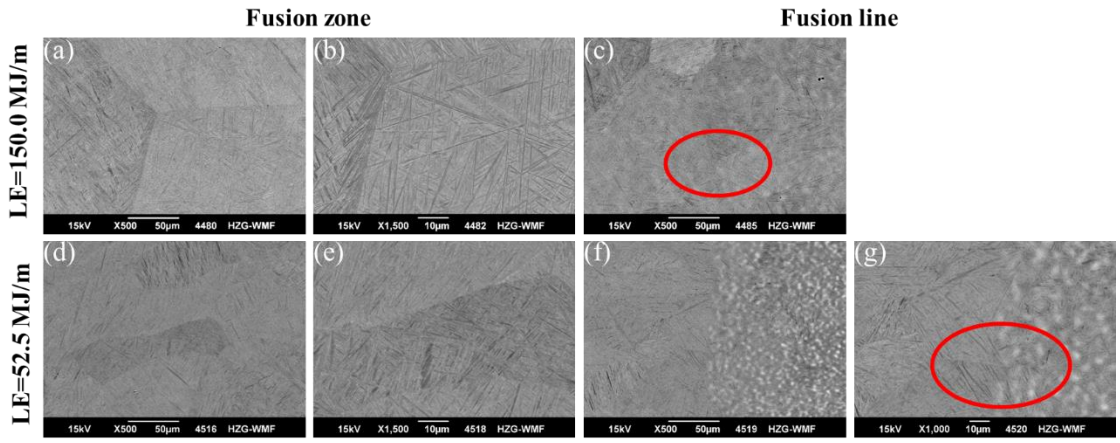

Figure 34: SEM images of (a)-(g) similar Ti6242 joints. (a)-(b), (d)-(e) FZ. (c), (f)-(g) FL. (a)-(c) P=1.75 kW, v=0.7 mm, LE=150 MJ/m. (d)-(g) P=3.5 kW, v=4 m/min, LE=52.5 MJ/m. Red ellipse marks exemplarily positions of heteroepitaxial growth.

In contrast, the prior *β*-grains are hardly visible in the FZ of the similar TNM joint (Figure 35 (a)). Besides, the microstructure in the FZ shows distinct differences compared to that of the similar Ti-alloy joints (Figure 34 (a), (d), Figure 35 (a)). A coarser, more lamellar-like microstructure evolves for the similar TNM joint (Figure 35 (a)). A continuous transition from the HAZ to the FZ is present for the similar TNM joint (Figure 35 (b)). Thus, indicating epitaxial growth at the FL as for similar Ti-alloy joints. The BM microstructure transforms in the HAZ ((Figure 35 (b), (c)). The differing backscattered electron contrasts in the FZ of similar Ti6242 and TNM joints could be explained by altering orientations or segregations (Figure 34, Figure 35).

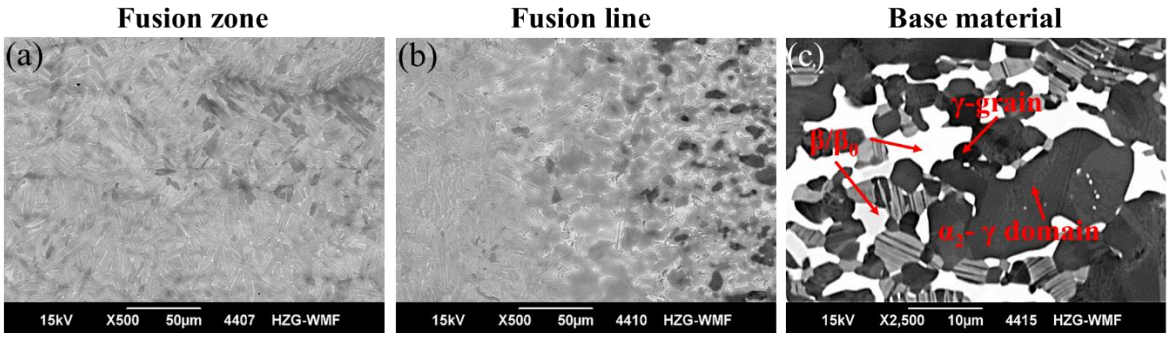

Figure 35: SEM images of similar TNM joints welded with P=4.5 kW, v=3 m/min, T_{ph}=800 °C.

5.1.4. Chemical and phase analysis

To assess the influence of the LBW process on segregations, chemical analysis by EDX analysis was utilized. Phase analysis by EBSD revealed the evolving phases. Besides, thereby the correlation of the crack development to the evolving microstructure and phases is facilitated.

For that reason, exemplarily a SEM image with an EDX line analysis for the similar Ti6242 joint parameter set with a line energy of 52.5 MJ/m is shown (Figure 36). Despite the fast cooling rate, the overall chemical mixture is homogeneous. The composition in the FZ is 84.76 wt.-% Ti, 6.46 wt.-% Al, 4.28 wt.-% Zr, 2.48 wt.-% Mo, 2.02 wt. % Sn and taking measurement inaccuracies into account within permitted deviation limits of Ti6242 (Table 2). Furthermore, as expected no distinct segregations of the

major alloying elements (Figure 36 (c)) and minor alloying elements (Figure 36 (d)) occur. Thus, the LBW process has an insignificant effect on the chemical composition. The different backscattered electron contrasts should be due to different grain orientations (Figure 36 (a), (b)).

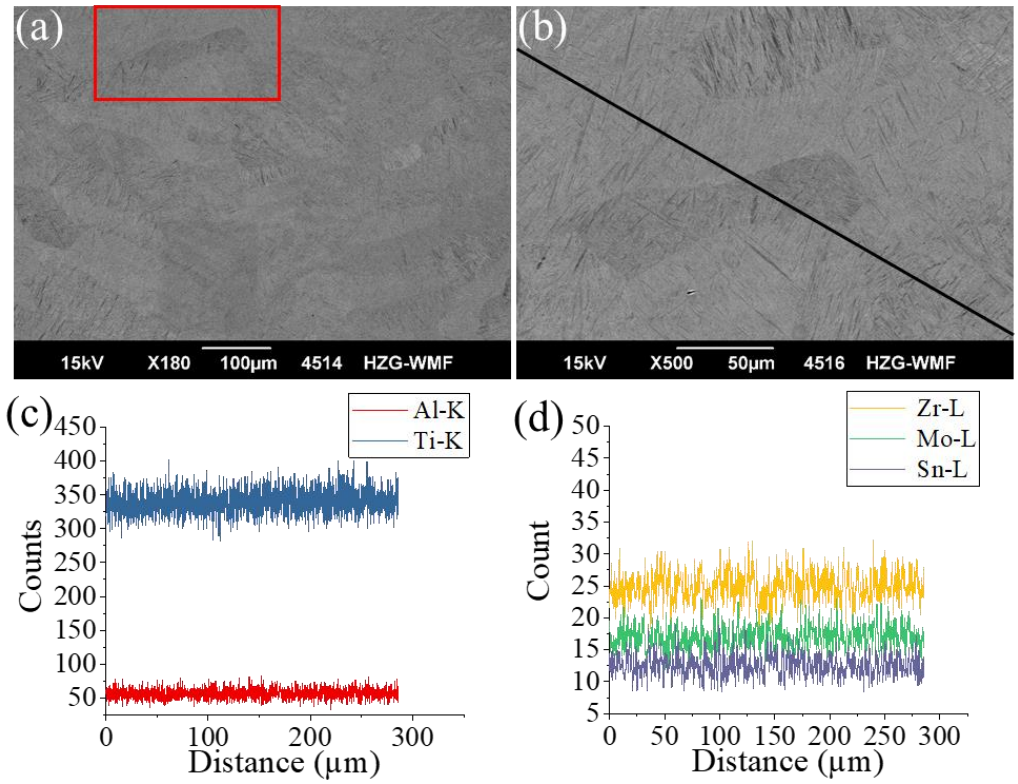

Figure 36: (a), (b) SEM images of the similar Ti6242 joint FZ welded with P=3.5 kW, v=4 m/min, RT. (a) Red square position of (b). (b) Line scan position (black line). (c) EDX line analysis of Ti (blue) and Al (red). (d) EDX line analysis of Zr (yellow), Mo (green) and Sn (purple) smoothened with 5 points averaged adjacent function.

As β-solidifying γ-TiAl alloys like TNM exhibit modest micro-segregations [74,103,219], the chemical composition of similar TNM joints is examined. Comparable to the results of the similar Ti6242 joints, the overall chemical mixture for similar TNM joints is homogeneous (Figure 37). The chemical composition in the FZ is 59.45 wt.-% Ti, 28.07 wt.-% Al, 9.18 wt.-% Nb and 3.31 wt.-% Mo, which is very close to the nominal TNM composition (Table 2). Besides, no segregations of the major or minor alloying elements are detected (Figure 37 (c), (d)). The chemical composition in the HAZ is 59.46 wt.-% Ti, 27.74 wt.-% Al, 9.46 wt.-% Nb and 3.34 wt.-% Mo.

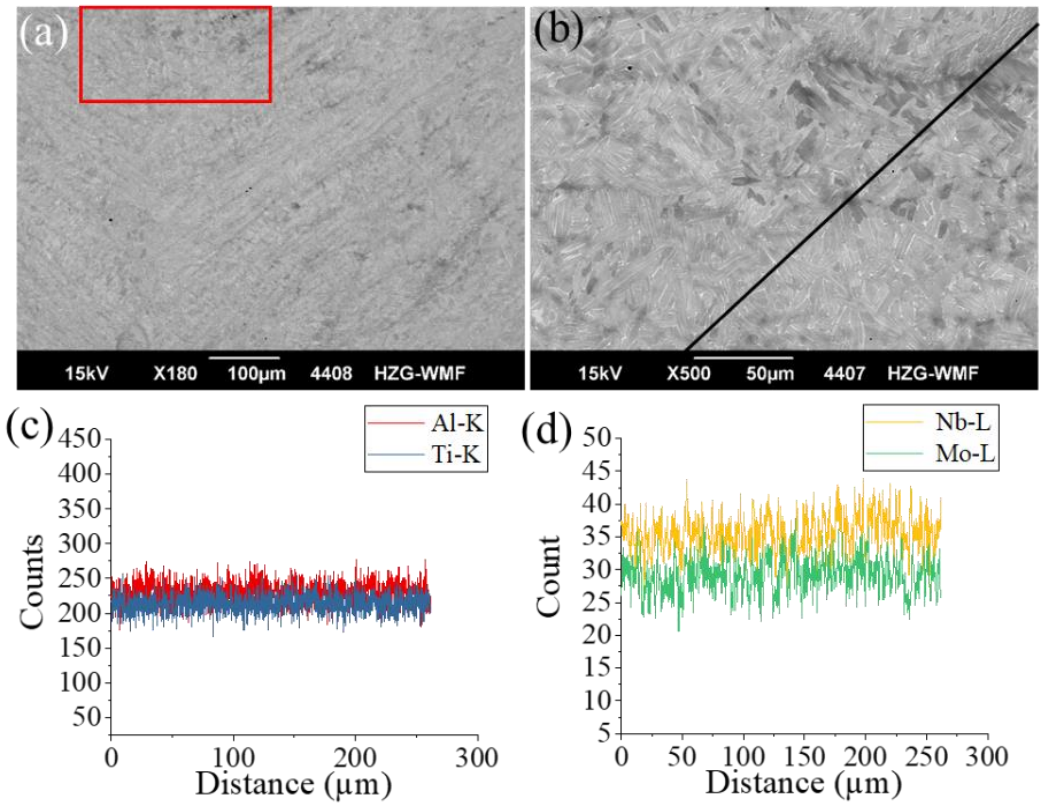

Figure 37: (a), (b) SEM images of the similar TNM joint FZ welded with P=4.5 kW, v=3 m/min, T_{ph}=800 °C. (a) Red square position of (b). (b) Line scan position (black line). (c) Line scan of Ti (blue) and Al (red). (d) Line scan of Nb (yellow) and Mo (green) smoothened with a 5 points averaged adjacent function (AAv).

The FZ of both similar Ti6242 joints consists of the α-phase (Figure 38 (a), (b)). In similar TNM joint, the α_2-phase (Ti_3Al) can be presumed due to the fast phase ordering process from the α-phase [80]. For the similar TNM joint, the preheating temperature is high enough that the phase transformation from α_2 to γ occurs in the FZ (Figure 38 (c)). However, the FZ main phase is α_2, whereas the γ-phase is only a minor component. Owing to the chemical composition in the FZ and the high cooling rates for LBW, it can be assumed that the α_2-phase could be supersaturated. As the cooling process for LBW is fast, even a massive α_2-phase formation could be supposed [101,220]. As a crack-free similar TNM joint with a minor γ-phase amount is obtained (Figure 38 (c)), in contrast to the reports for fusion welding in literature [37,39,40], the phase transformation from α_2 to γ might not be obligatory for crack-free similar TNM joints. The continuous microstructure transition of the HAZ to the FZ revealed by the SEM image of the similar TNM joint (Figure 35 (b)) is sustained by the continuous phase change (Figure 38 (d)). The amount of β/β_O-phase and γ-phase decreases from the HAZ to the FZ, while the amount of α_2-phase increases. According to the fast phase ordering process $\beta \rightarrow \beta_O$ and the solidification path of TNM (Chapter 2.2), where β_O-phase is present at RT [102,103], the related β-phase present at the FL should be the β_O-phase. Nevertheless, due to the theoretical cooling rates (Figure 23) and the reported results in literature for the phase transformation $\beta_O \rightarrow \omega$-phase type (Chapter 2.2.), the formation of the β_O-phase related ω_O- and ω''-phase cannot be excluded. Moreover, the continuous phase change at the FL further indicates epitaxial growth.

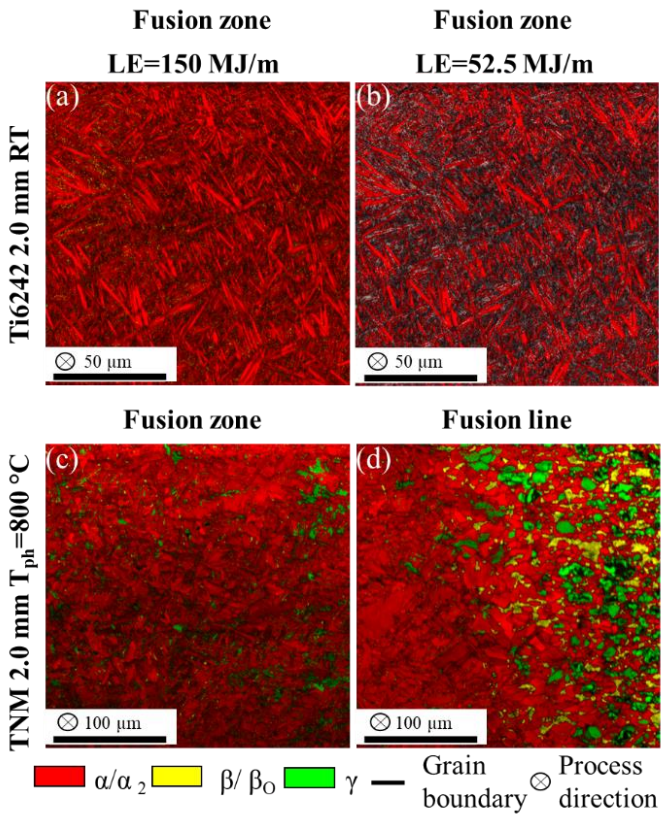

Figure 38: Phase maps of similar Ti6242 joints and similar TNM joint. α/α_2-red. β/β_O-yellow. γ-green. Grain boundary-black. (a)-(b) FZ similar Ti6242 joint welded with (a) P=1.75 kW, v=0.7 m/min, LE=150.0 MJ/m, RT and (b) P=3.5 kW, v=4 m/min, LE=52.5 MJ/m, RT. (c)-(d) Similar TNM joint welded with P=4.5 kW, v=3 m/min, T_{ph}=800 °C. (c) FZ. (d) FL.

Focusing on the influence of the evolving phase on the crack formation, phase analysis of similar TNM joints with different preheating temperatures for 1.5 mm thick TNM sheets using the EBSD method were conducted (Figure 39). Literature states that for crack-free fusion welded joints, the phase transformation from α_2 to γ is necessary [37,39,40]. For preheating to 300 °C a transversal crack is detected in the radiography image (Figure 28 (a)). The retained large β/β_O-phase block surrounded by α_2-phase can form at this condition (Figure 39 (a)). The β_O-phase deforms elastically until fracture [85] and forms a semi-coherent interface with α_2-phase [104]. Thereby, the evolving stresses at the semi-coherent interface could exceed the elastic deformation of the β/β_O-phase block, leading to the formation of a transversal crack. Increasing the preheating temperature from 300 °C to 400 °C, the β/β_O-phase amount in the FZ decreases (Figure 39 (a), (b)). As a result for preheating temperatures of 400 °C and higher, in the FZ no β/β_O-phase block is present and the small β/β_O grains are dispersed in the α_2-phase matrix (Figure 39 (b)-(d)). The surrounding α_2-phase matrix can deform plastically [85], which could result in a stress reduction in the remaining β/β_O grains. Consistently to findings for TNM structures manufactured by SLM, the crack-free similar TNM joints with an α_2-phase matrix and dispersed β/β_O grains supports the hypotheses that the phase transformation from α_2 to γ might not be mandatory. Similar to the FZ, the amount of β/β_O-phase decreases at the FL (Figure 39 (e)-(h)). The large black areas at the FL with a preheating temperature of 300 °C, could be an indicator for a high defect density (Figure 39 (e)). Summing up, for crack-free similar TNM joints the phase transformation from β to α_2

and a dispersed presence of β/β_O-phase seems to be crucial. Consequently, the crack formation in similar TNM joints could be correlated to the microstructure and phase evolution.

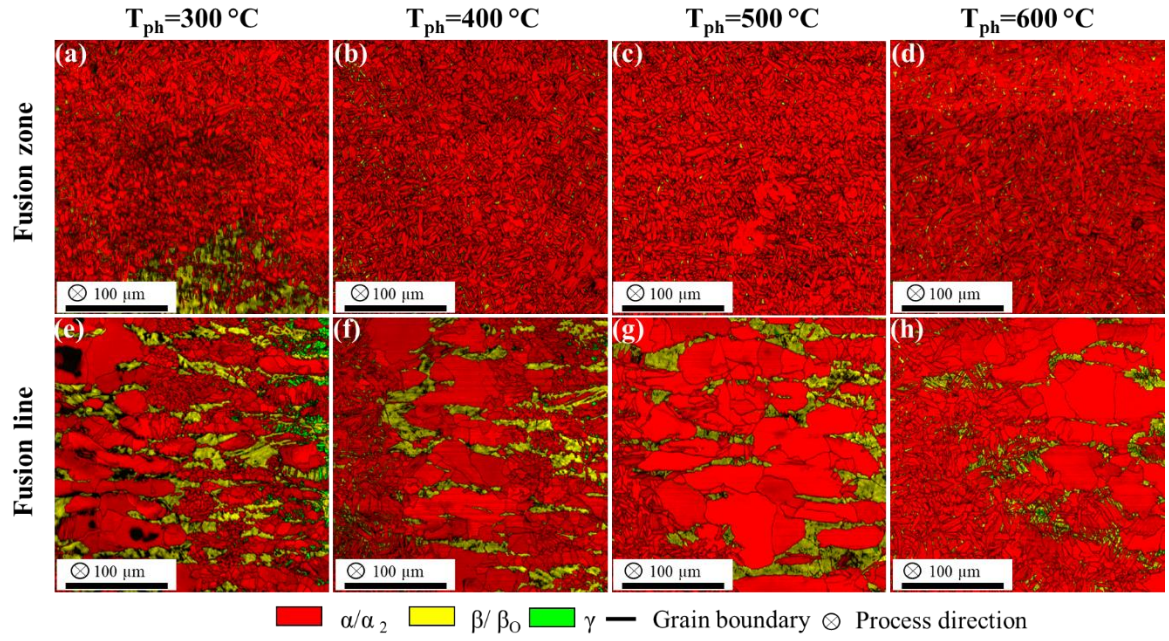

Figure 39: Phase maps of similar TNM joints with different preheating temperatures welded with P=3.5 kW, v=2 m/min, t_s=1.5 mm. α_2-red. β/β_O-yellow. γ-green. Grain boundary-black.

5.1.5. Microhardness measurements

The influence of the evolving microstructure and phases on the local mechanical properties was examined by microhardness measurements (Figure 40, Figure 41). Furthermore, the parameter influence on the microhardness is assessed.

The different LBW parameter sets for sound weld seams have only a minor influence on the microhardness profiles for similar Ti6242 joints (Figure 40 (a)). The characteristic microhardness increase from the BM to the FZ is about 80 HV0.3. The slightly smaller average microhardness in the FZ of 409 $\pm$ 15 HV0.3 (black square) can be attributed to the coarser microstructure (Figure 34 (a)), due to a high line energy of 150 MJ/m. For the lowest line energy of 52.5 MJ/m (Figure 40 (a), red circle), the average microhardness in the FZ is 439 $\pm$ 7 HV0.3, whereas for medium line energy 90 MJ/m (Figure 40 (a), green triangle) the microhardness is 416 $\pm$ 4 HV0.3. In accordance to previous findings, the change of the welding position has an insignificant influence on the microhardness (Figure 40 (b), black square, red circle). By preheating to 800°C the abrupt hardness increase in the FZ can be diminished for autogenous and filler wire LBW (Figure 40 (b), green top triangle, blue bottom triangle). The preheating procedure can be considered as a short term heat treatment of the similar Ti6242 joint, which influences the microstructure. Microhardness variations in the FZ are in the range of the BM scatter (Figure 40 (b), green top triangle, blue bottom triangle). Consequently, a homogenization of the microstructure in the BM and FZ was achieved by preheating.

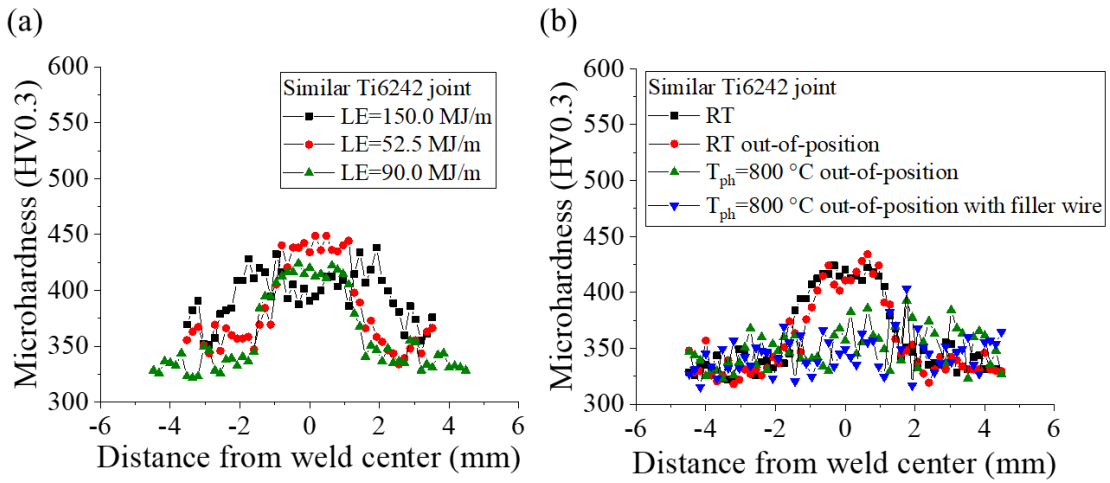

Figure 40: Microhardness measurements of similar Ti6242 joints. (a) Influence of different parameter sets. P=1.75 kW, v=0.7 m/min, LE=150.0 MJ/m (black square). P=3.50 kW, v=4.0 m/min, LE=52.5 MJ/m (red circle). P=4.50 kW, v=3.0 m/min, LE=90.0 MJ/m (green triangle). (b) Influence of welding positions, filler wire and preheating temperature welded with P=4.5 kW, v=3.0 m/min. RT (black square). RT out-of-position LBW (red circle). T_{ph} = 800 °C out-of-position LBW (green top triangle). T_{ph} = 800 °C out-of-position LBW and Ti6242 filler wire with v_w~3.6 m/min (blue bottom triangle).

Assessing the microhardness measurements of the similar TNM joints, the difference in average microhardness values of the base material TNM sheet dependent on the differing degrees of deformation and microstructures have to be taken into account (Figure 41 (a)-(c)). For as-welded similar TNM joints, a characteristic microhardness increase from the BM to the FZ of about 70 HV0.3 and 120 HV0.3 occurs for the TNM sheet thickness of 1.5 mm and 2.0 mm, respectively (Figure 41 (e), (f)). The variation of the preheating temperature has an insignificant influence on the microhardness in the FZ of similar TNM joints (Figure 41 (e), (f)). The average microhardness values in the FZ of 1.5 mm thick as-welded similar TNM joints are 519 $\pm$14 HV0.3 (black square), 515 $\pm$21 HV0.3 (red circle) and 503 $\pm$17 HV0.3 (green triangle), for preheating temperatures of 400 °C, 500 °C and 600 °C, respectively (Figure 41 (e)). For the 2.00 mm thick similar TNM joints, the average microhardness values in the FZ are lower with 491 $\pm$17 HV0.3 and 473 $\pm$14 HV0.3 for a preheating temperature of 600 °C (black square) and 800 °C (red circle), respectively (Figure 41 (f)). Differences in the average microhardness in the FZ of the different sheet thicknesses could be the result of the different theoretical considerations (Figure 23) or different chemical compositions of the BMs.

For similar TNM joints preheated to 600 °C with differing parameter sets, the average microhardness values in the FZ are 523 $\pm$25 HV0.3 (black square), 468 $\pm$17 HV0.3 (red circle) and 470 $\pm$27 HV0.3 (green triangle) (Figure 41 (g)). As the average microhardness values are within eachs deviation, for sound welds the combination of laser power and process velocity, thus the line energy has a minor influence on the microhardness. The OM of the at 1290 °C heat-treated similar TNM joint cross-section revealed a homogeneous microstructure (Figure 33 (b)). Moreover, the characteristic microhardness increase is absented and values are within the deviation range of the BM (Figure 41 (f), green triangle). Hence, in contrast to earlier reports of heat-treated similar TNM joints [52], the microstructure of the similar TNM joint preheated to 800 °C is homogenized by the applied heat treatment.

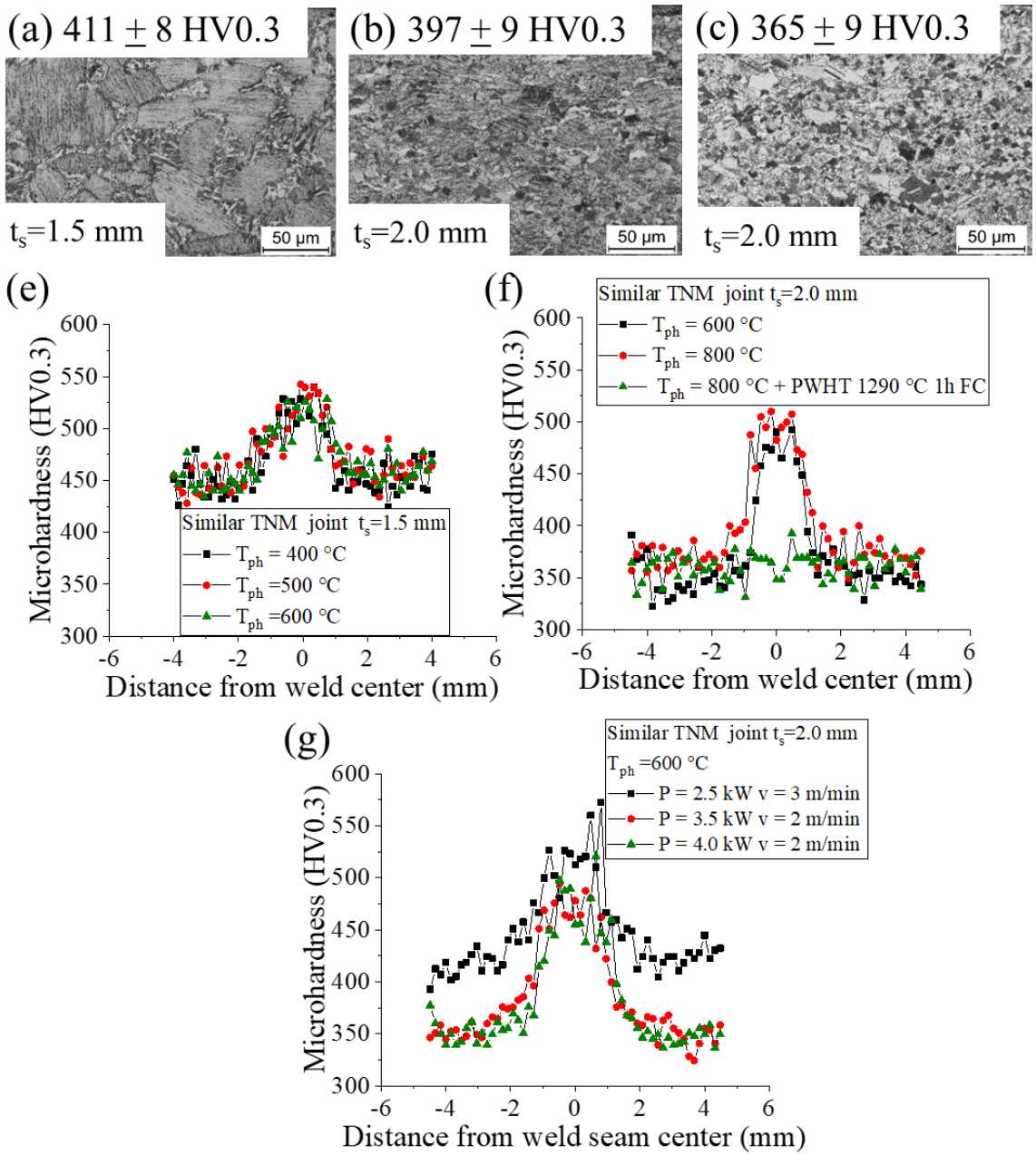

Figure 41: (a)-(c) OM images of BM of different TNM sheets with measured average microhardness. (e)-(g) Microhardness measurements of similar TNM joints. (e) Influence of preheating temperature on microhardness of similar TNM(1.5) joints welded with P=4.5 kW, v= 3 m/min. (f) Influence of preheating temperature and PWHT on microhardness of similar TNM joints welded with P=4.5 kW, v=3 m/min. (g) Influence of different parameter sets on microhardness of similar TNM.

5.2. Development and characterization of dissimilar Ti-Ti- and TiAl-Ti-alloy joints

After establishing overlapping process windows for similar joints in the previous chapter, the aim is to obtain crack-free dissimilar joints with parameter sets in the overlapping section. To clarify the crack formation in dissimilar TNM joints theoretical considerations, radiography images, microstructure and phase analysis were utilized. Besides, weld seam characteristics of dissimilar joints were studied by cross-sections and compared to the results of similar joints. The microstructure, chemical composition and evolving phases were investigated and interlinked to the LBW process parameters. Through the

chemical analysis furthermore the mixing behavior of the alloys was examined. Microhardness measurements were utilized to study the local mechanical properties and the influence of the microstructure and phase evolution as well as possible segregations. Due to the dissimilarity of the joints, a special focus was on the evolving interfaces.

5.2.1. Theoretical considerations

The crack formation in dissimilar TNM joints is examined by the theoretical cooling rate for similar Ti64, Ti6242 and TNM joints according to the 2D Rosenthal equation (6), and by the time-temperature development of these by similar joints according to the program of Herrnring et al. [215] (Figure 42).

The theoretical cooling rate decreases with the preheating temperature for Ti64, Ti6242 and TNM (Figure 42 (a)). Due to the higher thermal conductivity (Table 3), TNM possess the highest theoretical cooling rate for preheating temperatures from 400 °C to 800 °C (Figure 42 (a), green triangle). As Ti6242 has the lowest specific heat capacity and in spite of Ti6242 having the higher thermal conductivity compared to Ti64 (Table 3), the theoretical cooling rate at 400 °C of Ti64 (Figure 42 (a), black square) is lower than for Ti6242 (red circle). This difference could influence the microstructure-phase evolution and thus the crack formation. Resulting from the Ti6242 lowest specific heat capacity of 460 J/(kg·K) compared to 565 J/(kg·K) and 600 J/(kg·K) for Ti64 and TNM, respectively [3,116], the theoretical time-temperature curves at a preheating temperature of 400 °C show the highest peak temperature for Ti6242 (Figure 42 (b)). Besides, for Ti6242 the cooling rate after the peak temperature (red curve) is higher than for Ti64 (black curve) and similar to the TNM slope (green curve). TNM and Ti64 display a comparable peak temperature, due to the similar specific heat capacities (Table 3). Comparing the cooling rates of Ti64 and Ti6242 by the theoretical cooling rate and the temperature-time development, which can be seen as the temperature evolution, differing cooling rates can be deduced. Therefore, the question arises, if differences in the crack formation and microstructure-phase evolution of dissimilar TNM-Ti64 and TNM-Ti6242 joints emerge.

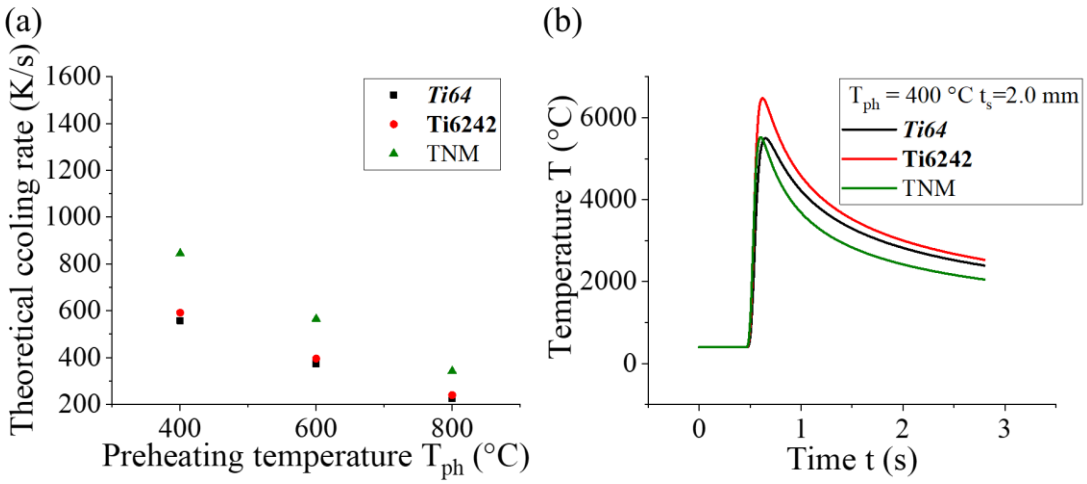

Figure 42: (a) Theoretical cooling rate according to 2D Rosenthal equation (6). (b) Time-temperature development for P=4.5 kW, v=3 m/min, T_{ph}=400 °C and t_s=2 mm Ti64, Ti6242 and TNM calculated with the program by Herrnring et al. [215].

5.2.2. Inner defect development

The inner defect development was studied by radiography images and correlated to the theoretical considerations. As the minimal preheating temperature for crack-free similar TNM joints was determined in Chapter 5.1.2., crack-free dissimilar TNM joints were at least expected for the same preheating temperatures. Moreover, the question arises, if by the Ti-alloy joining partner, the crack formation can be influenced and lower minimal preheating temperatures for dissimilar TNM joints can be achieved.

The radiography images of dissimilar Ti64-Ti6242 joints disclose crack-free joints (Figure 43), which is linked to the low crack susceptibility of Ti-alloys [71]. Due to the different chemical compositions and densities, different grey scales for Ti64 and Ti6242 are visible. In contrast to the line porosity free similar Ti64 and Ti6242 joints with the same parameter set, for a line energy of 150 MJ/m, line porosity is detected on the Ti6242 side of the dissimilar Ti64-Ti6242 joint (Figure 43 (a)). Overheating could cause the pore formation, as the line energy is with 150 MJ/m high and in particular as Ti6242 exhibits a high theoretical peak temperature (Figure 42 (b)). Moreover, differing cooling behaviors on the FLs should occur. The theoretical cooling rate of Ti6242 is higher than for Ti64 (Figure 42 (a)), and the temperature evolution after the peak temperature, represented by the slope, is faster (Figure 42 (b)). This could lead to a faster solidification on the Ti6242 side compared to the Ti64 side of the weld seam. Hence, degassing could be unfeasible on the Ti6242 side, while still possible on the Ti64 side. The pore size is between 0.16 µm and 0.40 µm (Figure 43 (a)). For higher laser powers and process velocities, thus the line energies of 90 MJ/m and 52.5 MJ/m, the joints are free of line porosity and macroporosity (Figure 43 (b), (c)). Even for an increased amount of spatter, which are an indicator for process instabilities, for the dissimilar Ti64-Ti6242 joint with a line energy of 90 MJ/m, the weld seam porosity is very low and the maximum pore size is 0.28 µm (Figure 43 (b)).

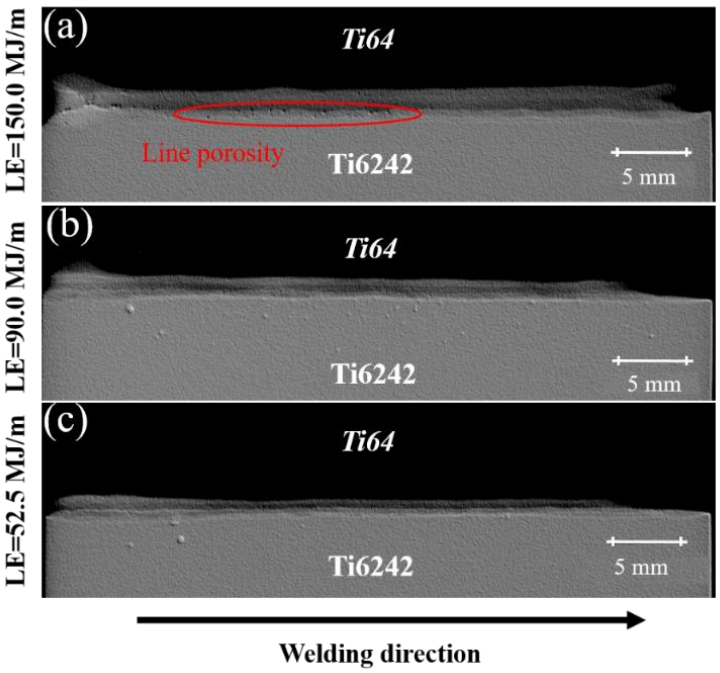

Figure 43: Radiography images of dissimilar Ti64-Ti6242 joints welded with (a) P=1.75 kW, v=0.7 m/min, LE=150.0 MJ/m, (b) P=4.50 kW, v=3.0 m/min, LE=90.0 MJ/m and (c) P=3.50 kW, v=4.0 m/min, LE=52.5 MJ/m.

The theoretical considerations of similar TNM joints have revealed, that the global influence of the preheating temperature seems to be more important than the local influence of the parameter sets (Figure 23). Therefore, the crack development of dissimilar TNM joints depending on the preheating temperature, the joining partner and the TNM sheet thickness was studied by radiography images (Figure 44).). As defined in the experimental producure to distinguish between the differing TNM sheet thicknesses of the dissimilar TNM joints, for 1.5 mm thick TNM sheets TNM(1.5) is written and for 2 mm thick TNM sheets just TNM.

Fewer and shorter cracks are detected in dissimilar TNM joints compared to similar TNM joints (Figure 28, Figure 44). In contrast, to the similar TNM 2.0 mm joint (Figure 28 (d)) and dissimilar TNM-Ti6242 joint (Figure 44 (d)), the dissimilar TNM-Ti64 joint preheated to 400 °C is crack-free (Figure 44 (a)). As the TNM sheet thickness and the parameter sets are the same, it can be concluded that the chemical composition of the joining partner and thus the alloying elements could influence the crack formation. Ti6242 exhibits a higher ductility than TNM and the occurrence of brittle phases is improbable [13,32], consequently thermally induced stresses can be compensated by the deformation of Ti6242. Thereby, the end of the crack in the FZ or FL at the Ti6242 side of dissimilar TNM-Ti6242 joints with and without filler wire preheated to 400 °C could be explained (Figure 44 (d), (g)). Hence, due to the lower crack sensitivity and higher ductility of Ti6242, Ti6242 seems to stop the crack propagation in the BM. As the crack occurs in both cases at a similar weld seam length, the same fundamental reason, emerging thermally induced stresses, caused the crack formation. Comparable to dissimilar TNM-Ti6242 joints preheated to 400 °C (Figure 44 (d), (g)), for the dissimilar TNM(1.5)-Ti6242 joint with a preheating temperature of 300 °C also a crack develops as the evolving thermally induced stresses should exceed the fracture strength and the crack does not propagate in the Ti6242 BM (Figure 44 (j)). Due to the different TNM sheet thicknesses and in contrast to dissimilar TNM-Ti6242 joints preheated to 400 °C with otherwise constant parameters (Figure 44 (d), (g)), preheating dissimilar TNM(1.5)-Ti6242 to 400 °C leads to crack-free joints (Figure 44 (k)). This results from differing cooling rates, thermally induced stresses and temperature evolutions. Thus, different microstructures or phases could evolve, which would influence the crack formation. Utilizing a preheating temperature of 600 °C, all dissimilar TNM joints are crack-free (Figure 44 (b), (e), (h)).

In spite of the higher spatter amount by the use of Ti6242 filler wire, no significant increase of porosity or the formation of macroporosity for preheating temperatures of 600 °C and 800 °C is detected (Figure 44 (h), (i)) compared to autogenously welded dissimilar TNM-Ti6242 joints (Figure 44 (e), (f)). In contrast and emphasizing the influence of the TNM sheet thickness on the pore formation, for dissimilar TNM(1.5)-Ti6242 joints preheated to 800 °C an increased number of pores with a maximum pore size of 0.53 µm evolves (Figure 44 (l)). Through the thinner sheet thickness and the preheating temperature of 800 °C, the threshold temperature for pore formation due to overheating seems to be exceeded.

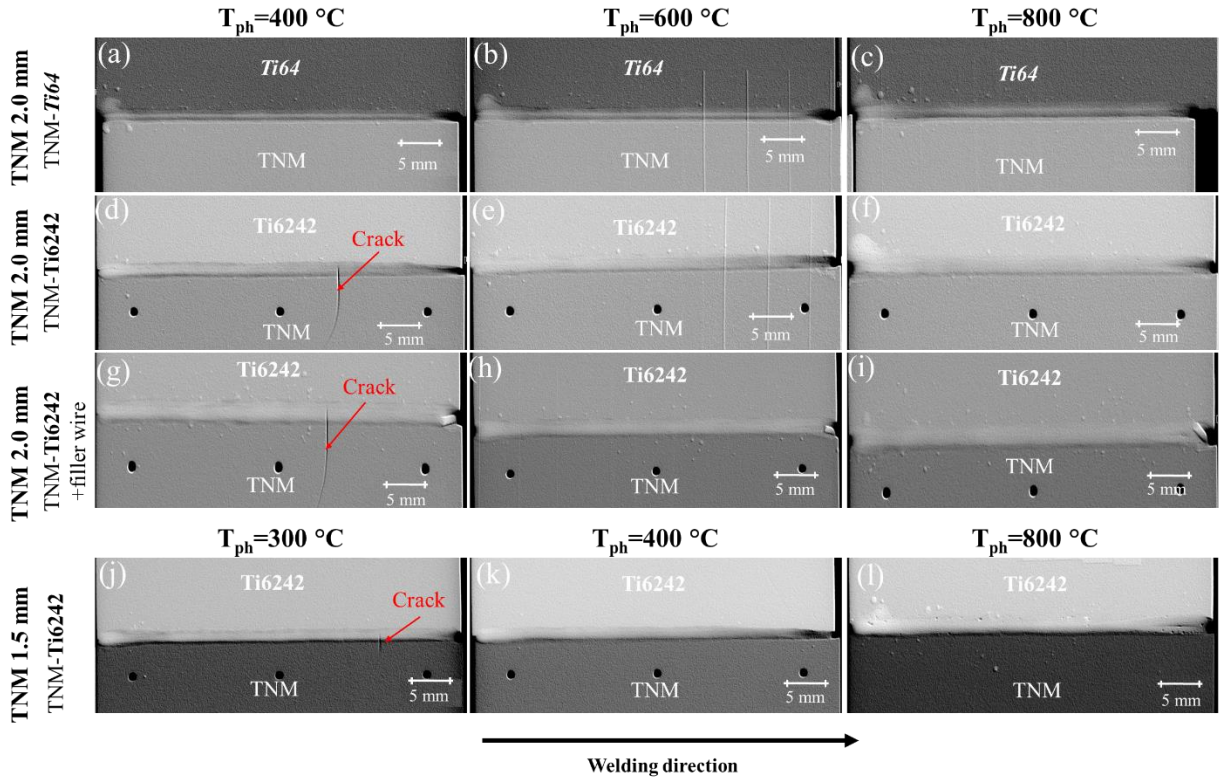

Figure 44: Radiography images of dissimilar TNM joints with different preheating temperatures, Ti-alloy joining partners and sheet thicknesses welded with P=4.5 kW, v=3 m/min.

5.2.3. Weld seam characteristics and microstructure analysis

To investigate the parameter set transferability, different parameter sets suitable for similar joints were tested for LBW of dissimilar joints. Furthermore, first the effect on the microstructure evolution of dissimilar Ti64-Ti6242 joints and then on dissimilar TNM joints was studied. Moreover, different PWHT temperatures and times were investigated for dissimilar TNM-Ti6242 joints to study if the microstructure can be homogenized as for the similar TNM joints (Chapter 5.1.).

The weld seam shape, geometry, the prior *β*-grain size and interfaces of dissimilar Ti64-Ti6242 joints are first investigated by cross-sections (Figure 45). As for similar Ti-alloy joints (Figure 29), an X-shape emerges for dissimilar Ti64-Ti6242 joints (Figure 45). Furthermore, resulting from the comparable liquidus temperaturs and thermal conductivities (Table 3), all joints are almost symmetric (Figure 45). Moreover, as for the similar Ti-alloy joint (Figure 29 (a), (e)), for the dissimilar Ti64-Ti6242 joint with the highest line energy (LE=150 MJ/m), the largest prior *β*-grains emerge and nearly no underfill or reinforcement is formed (Figure 45 (a)). Due to the different chemical composition and long-term service temperatures (Table 2, Table 3), the prior *β*-grains in the Ti6242 HAZ are smaller than in the Ti64 HAZ. This can be best seen in Figure 45 (a) with an average length of 0.23 mm and 0.16 mm and width of 0.17 mm and 0.11 mm for the prior *β*-grains in the Ti64 and Ti6242 HAZ, respectively. The width of the HAZ decreases with decreasing line energy (Figure 45). As the thermal conductivities are alike (Table 3), no significant difference between the HAZ width of Ti64 and Ti6242 emerges. In general, comparable to the HAZ, the average prior *β*-grain length and width decreases in the FZ with decreasing line energy from 0.55 mm to 0.23 mm and from 0.16 mm to 0.06 mm for a line energy of 150 MJ/m and 52.5 MJ/m, respectively (Figure 45 (a), (c)). Due to the different etching

behavior, no distinct FL on Ti64 side is visible. Nevertheless, as a continuous transition between HAZ to FZ on both sides occurs, prior β-grains belonging to the FZ and HAZ are present (Figure 45, red squares). Therefore, heteroepitaxial growth is indicated as the grain growth mechanisim at the FL. Heteroepitaxial growth is the epitaxial growth on a differing material. As the growth mechanism should be the same on the Ti6242 side of Figure 45 (c), heteroepitaxial growth is also assumed here.

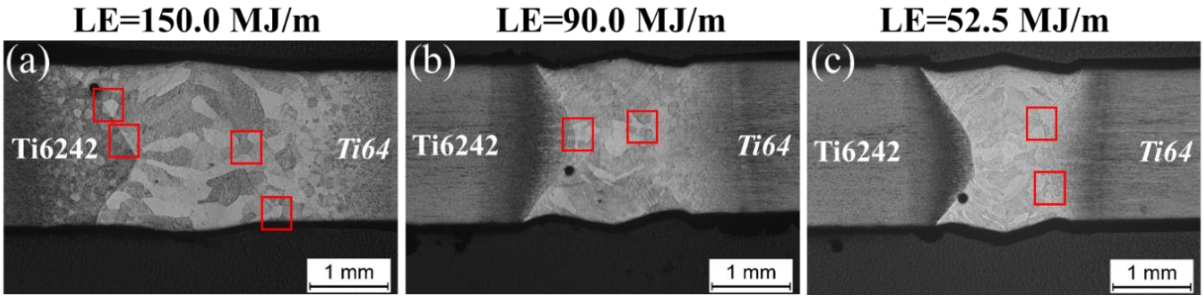

Figure 45: Cross-sections of dissimilar Ti64-Ti6242 joints welded with (a) P=1.75 kW, v=0.7 m/min, LE=150 MJ/m, (b) P=4.5 kW, v=3 m/min, LE=90 MJ/m and (c) P=3.5 kW, v=4 m/min, LE=52.5 MJ/m. Red squares mark exemplarily positions of heteroepitaxial growth.

Independent of the preheating temperature, the joining partner or the sheet thickness all dissimilar TNM joints exhibit an X-shaped weld seam (Figure 46). The etching behaviors differ and therefore a more distinct FL on the TNM side is present. Caused by the higher thermal conductivity of TNM (Table 3), the HAZ width on the Ti-alloy side is always larger than for the TNM side (Figure 46). Due to the lower long-term service temperature of Ti64 compared to Ti6242 (Table 3), the prior β-grains in the HAZ on Ti64 side for dissimilar TNM-Ti64 are larger than on the Ti6242 side for dissimilar TNM-Ti6242 joints (Figure 46 (a)-(f)). With increasing preheating temperature, the size of the FZ increases for all joint configuration (Figure 46). Vortexes in the FZ of the dissimilar TNM joints emerge (Figure 46). These could result from the fluid flow, due to the mixing process of the two different alloys and could indicate segregations. Moreover, for the same sheet thicknesses and autogenous LBW, the symmetry of the weld seam shape increases with increasing preheating temperature (Figure 46 (a)-(f)). In contrast, for dissimilar sheet thicknesses the opposite is true (Figure 46 (i)-(k)). Besides, comparable to the similar TNM joints (Figure 32), small to no underfill and reinforcement occurs for the dissimilar TNM joints (Figure 46). Thus, the different surface tensions do not seem to influence the formation of the underfill and reinforcement (Figure 46 (a)-(f)). As for the similar TNM joint (Figure 24 (a)), the misalignment in Figure 46 (d) could influence the obtained cooling rate and thermally induced stresses. Consequently, these could be the reason for the visible crack in the cross-section (Figure 46 (d), red square). The position of this cross-section crack close to the weld seam root supports this hypothesis. The FZs welded with filler wire are larger than the FZs welded autogenously (Figure 46 (a)-(h)). Moreover, the weld seam shape of the dissimilar TNM-Ti6242 joints with filler wire is more symmetric (Figure 46 (g), (h)) compared to the autogenously welded dissimilar TNM-Ti6242 joints (Figure 46 (d)-(f)). By the use of Ti6242 filler wire, joints with nearly no underfill and a low reinforcement are achieved (Figure 46 (g), (h)). Despite the sheet thickness difference leading to a sheet misalignment, no cross-section cracks are visible for dissimilar TNM(1.5)-Ti6242 joints (Figure 46 (i)-(k)). The difference in TNM sheet thickness results in an altered cooling rate, which could lead to a different microstructure and phase

evolution. Moreover, due to the differing sheet thicknesses, the stress distribution could be impacted,as the cross-section geometry of the dissimilar TNM(1.5)-Ti6242 joint is different (Figure 46 (i)-(k)) compared to the dissimilar TNM-Ti6242 joints (Figure 46 (d)-(f))

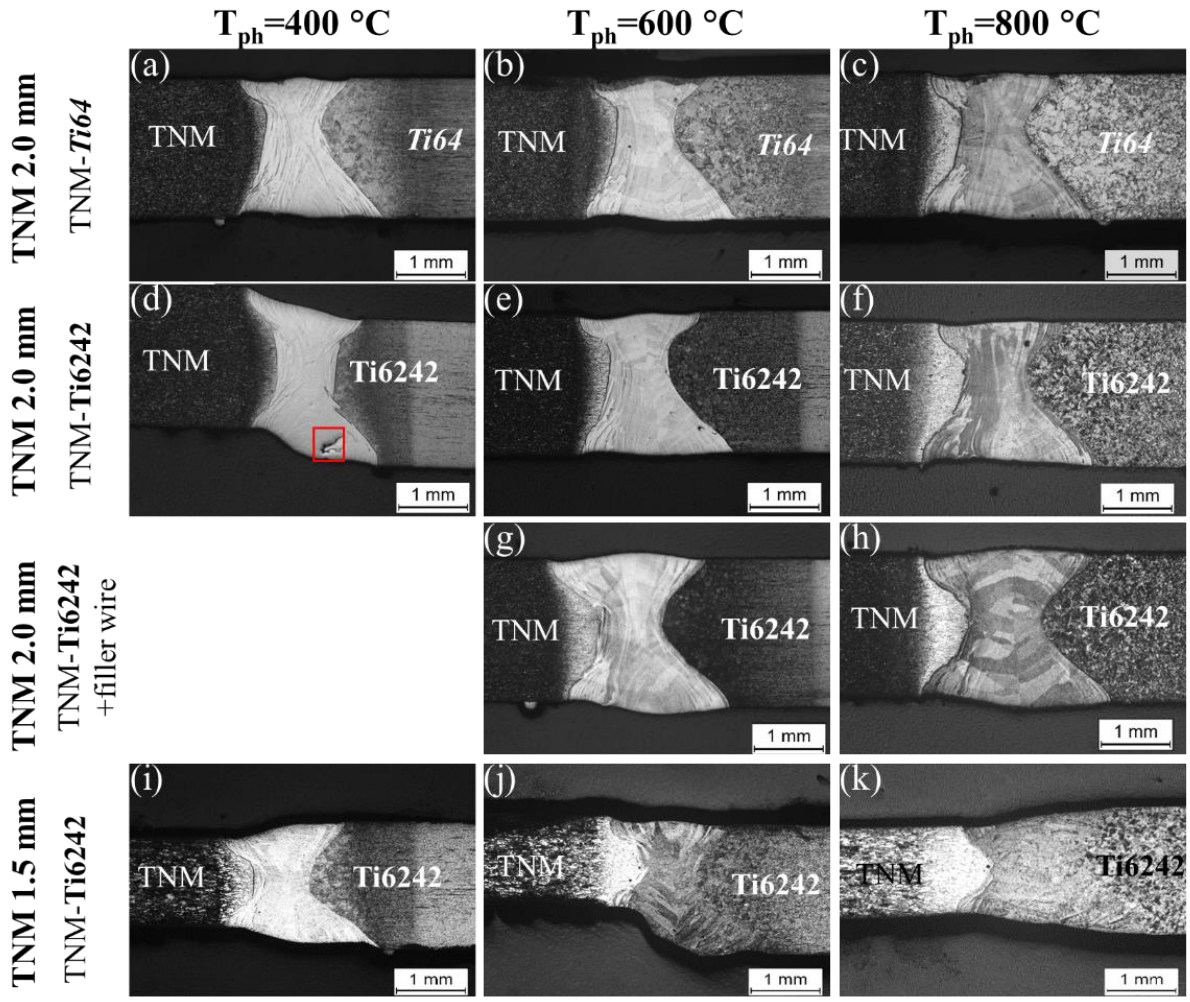

Figure 46: Cross-sections of dissimilar TNM joints with different preheating temperatures, Ti-alloy joining partners and sheet thicknesses welded with P=4.5 kW, v=3 m/min. Red square indicats position of crack in cross-section.

With the constraint that the dissimilar TNM joints have to be preheated to 600 °C in order to achieve crack-free joints, the parameter transfer from similar joints to dissimilar Ti64-Ti6242 and TNM-Ti6242 joints, as shown by the overlapping of the investigated parameter windows, is successfully achieved (Figure 47 (a)). As low process velocities and low laser powers have shown to be unsuitable for 1.5 mm thick similar TNM joints (Figure 31 (a)), these parameters were not investigated. Furthermore, in contrast to similar Ti-alloy joints and comparable to similar TNM joints, only dissimilar TNM-Ti6242 joints with X-shaped FZs are obtained (Figure 47 (b)-(d)).

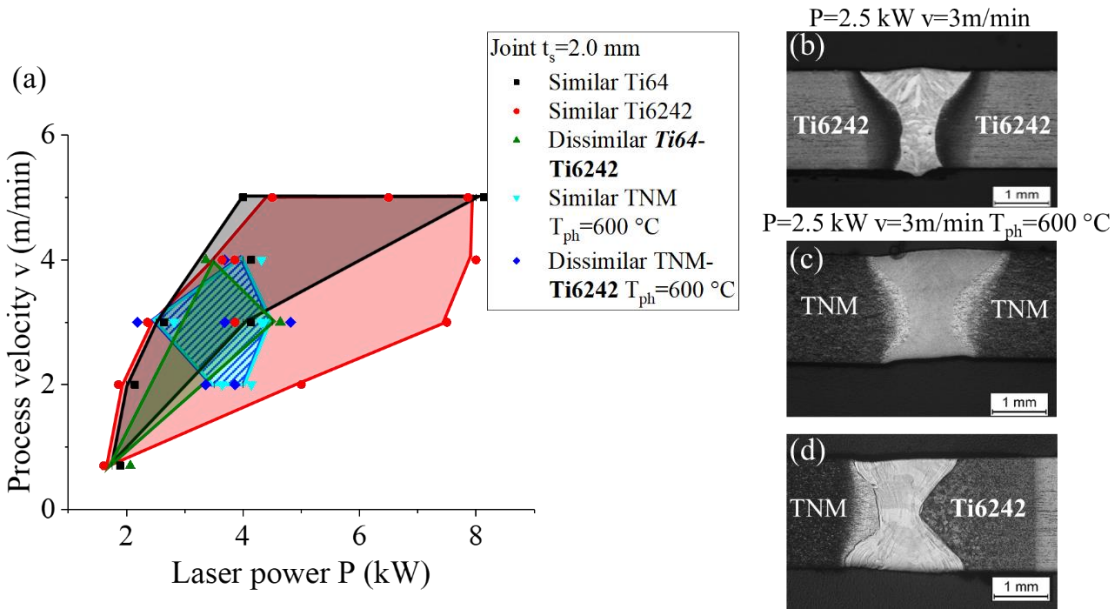

Figure 47: (a) Overlap of investigated parameter windows of LBW similar Ti64 (black square), Ti6242 (red circle), TNM (green triangle top), dissimilar Ti64-Ti6242 (light blue triangle bottom) and dissimilar TNM-Ti6242 (blue diamond) joints. (b)-(d) Comparison of a similar Ti6242, TNM and dissimilar TNM-Ti6242 joint with t_s=2.0 mm.

PWHTs of dissimilar TNM-Ti6242 joints were conducted to reduce thermally induced stresses in the joints and to study the microstructural convertibility of the joints with special regard to the seam on TNM side (Figure 48). Moreover, a parameter set using Ti6242 filler wire is chosen, since Ti-alloys are notch sensitive and it is reported that the use of filler wire is beneficial [164]. Two temperatures 950 °C, which is close to the β-transus temperature of Ti6242 [3], and 1290 °C, a typical TNM heat treatment temperature [13,65], consequently much above the β-transus temperature of Ti6242 (Table 3), were selected. Considering the PWHT temperature differences and as 1290 °C exceeds the long-term service temperature of Ti6242 (Table 3), the PWHT time is reduced from 2 h for 950 °C to 1 h for 1290 °C. A seam on the FL on the TNM side is present in Figure 48. No continuous transition at the TNM FL occurs in the as-welded state (Figure 48 (a), (d)) and after PWHT with 950 °C (Figure 48 (b), (e)) The amount of vortexes increased after the PWHT at 950 °C, indicating increased diffusion controlled atom migrations [221]. After the PWHT at 1290 °C a bright line at the TNM FL is visible (Figure 48 (c), (f)). The transition between TNM BM and the FZ is continuous. The bright line could be the former seam. As the PWHT temperature of 1290 °C is much higher than the Ti6242 β-transus temperature of 995 °C [3], an extreme grain growth on the Ti6242 side and the Ti6242 closer FZ emerges. This is caused by the α/α_2-phase no longer operating as a pinning phase in the single β-phase region. The term pinning means inhibiting grain growth in the presence of small particles by preventing the motion of grain boundaries. Diffusion controlled atom migrations have to take place, as two zones in the FZ, close to TNM smaller lamellas and close to Ti6242 larger lamellas and grains, are visible (Figure 48 (c)). Due to the initial chemical composition of TNM and Ti6242, the zones in the FZ are influenced differently.

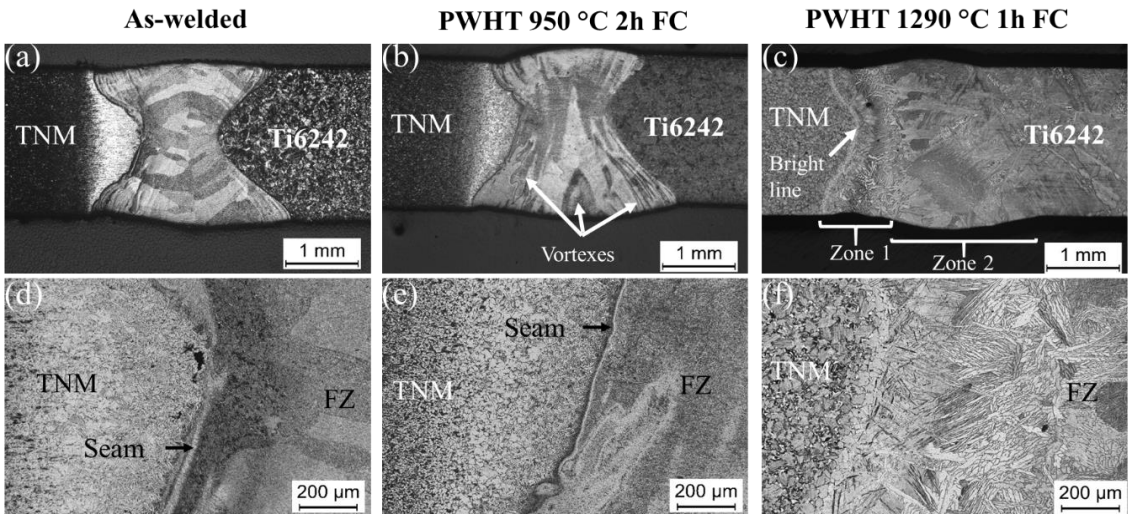

Figure 48: Influence of PWHT on cross-sections of dissimilar TNM-Ti6242 joints welded with P=4.5kW, v=3.0 m/min, T_{ph}=800 °C, t_s=2.0 mm v_w~3.6 m/min. (a)-(c) Overview. (d)-(f) FL on TNM side. (c) Zone 1: FZ close to TNM with small lamellas. Zone 2: FZ close to Ti6242 with large lamellas and grains.

For a more detailed analysis of the dissimilar Ti64-Ti6242 and dissimilar TNM joint microstructures, SEM analysis was utilized. SEM images confirm a continuous transition from the HAZ to the FZ on both sides of the dissimilar Ti-alloy joint, where needles grow across the FL (Figure 49 (a), (c), red ellipse). Both HAZ microstructures are martensitic. As for similar Ti6242 joints (Figure 34 (a), (d)), prior β-grains and a martensitic microstructure are observed in the FZ of dissimilar Ti64-Ti6242 joints (Figure 49 (b)). Due to the martensitic microstructure and based on the Ti64 cooling rate for a martensitic microstructure, the cooling rate should be 410 °C/s or higher [73]. As SEM images are taken in the electron backscatter mode, different grey scales are associated with the chemical composition and the grain orientation. Hence, the dark area in the FZ center could indicate microsegregations (Figure 49 (b)).

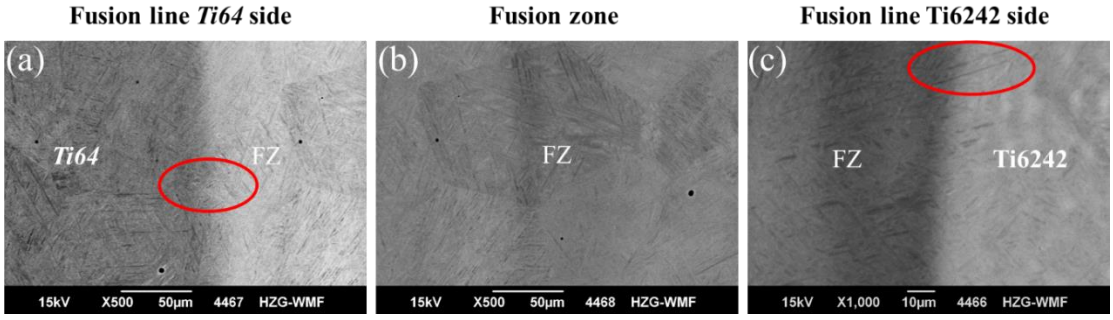

Figure 49: SEM image of dissimilar Ti64-Ti6242 joints. P=4.5kW, v=3.0 m/min, LE=90 MJ/m. (a) FL on Ti64 side. (b) FZ. (c) FL on Ti6242 side. Red ellipse marks exemplarily position of needle growth across FL.

Depending on the preheating temperature, the joining partner and the sheet thickness, the different evolving microstructures in the FZ of dissimilar TNM joints were examined (Figure 50). Preheating dissimilar TNM joints to 400 °C, prior β-grain boundaries are visible (Figure 50 (a), (d), (g)). Nevertheless, differing microstructures for dissimilar TNM-Ti64 and TNM-Ti6242 joints develop with a preheating temperature of 400 °C. For dissimilar TNM-Ti64 joints small fine needles are confirmed in Figure 50 (c). The needles in the dissimilar TNM-Ti64 FZ could be assumed as α/α_2 needles. To

differentiate between α/α_2, further investigations are necessary. In contrast, for dissimilar TNM-Ti6242 joints no needles are detected and a grain-like microstructure occurs (Figure 50 (g)). This leads to the assumption that the phase transformation from $\beta \rightarrow \alpha/\alpha_2$ has not or only partly taken place. Moreover, the theoretical cooling rate after the peak temperature of Ti64 is lower than for Ti6242 (Figure 42 (b)), supporting the hypothesis of different phase evolutions in the joints. The grain-like microstructure and assumed β/β_O-phase in the FZ of the dissimilar TNM-Ti6242 preheated to 400 °C could be the reason for the crack formation (Figure 44 (d)). Using the same parameter set and a thinner TNM sheet in dissimilar TNM(1.5)-Ti6242 joints compared to the dissimilar TNM-Ti6242 joint, a lower cooling rate for the dissimilar TNM(1.5)-Ti6242 will arise. As for dissimilar TNM-Ti64 preheated to 400 °C (Figure 50 (c)), the resulting microstructure in dissimilar TNM(1.5)-Ti6242 joints is martensitic with fine needles (Figure 50 (j)). Thus, the phase transformation from β to α/α_2 could take place and a crack-free TNM(1.5)-Ti6242 joint with a preheating temperature of 400 °C was generated (Figure 44 (k)).

With a preheating temperature of 600 °C a martensitic microstructure with fine needles also evolves in the dissimilar TNM-Ti6242 FZ (Figure 50 (e), (h)). The distinct microstructural change from the preheating temperatures of 400 °C to 600 °C of dissimilar TNM-Ti6242 joints (Figure 50 (g), (h)), supports the hypothesis that with the preheating temperature of 400 °C the phase transformation from $\beta \rightarrow \alpha/\alpha_2$ is suppressed. Moreover, for preheating temperatures of 600 °C and higher, the cooling rate for dissimilar TNM-Ti64, dissimilar TNM-Ti6242 with and without filler wire seems to be sufficiently low for the phase transformation $\beta \rightarrow \alpha/\alpha_2$ (Figure 50 (b), (e), (f), (i), (k), (l)).

As for 600 °C, the FZ of the dissimilar TNM-Ti64 joint, dissimilar TNM-Ti6242 with and without Ti6242 filler wire preheated to 800 °C exhibits a martensitic microstructure (Figure 50 (b), (f), (i)). As additional material has to be molten, the finer martensitic microstructure of the dissimilar TNM-Ti6242 joint welded with filler wire (Figure 50 (i)) compared to the dissimilar TNM-Ti6242 welded autogenously (Figure 50 (f)), each preheated to 800 °C, can be attributed to a higher cooling rate for the joint with filler wire. With an increasing preheating temperature the cooling rate decreases (Figure 42 (a)), which explains the change from a martensitic microstructure to a lamellar microstructure for dissimilar TNM(1.5)-Ti6242 joints with a preheating temperature of 600 °C and 800 °C, respectively (Figure 50 (k), (l)).

From the results of the microstructure analysis, the similar TNM joints and the fast ordering process $\alpha \rightarrow \alpha_2$, the α_2-phase can be assumed in the FZ of dissimilar TNM joints with an acicular microstructure (Figure 50). The grain size of dissimilar TNM joints increases with increasing preheating temperature (Figure 50, Figure 51 (a)). The significantly larger grain size in dissimilar TNM-Ti6242 joint preheated to 400 °C can be explained by the presence of β/β_O grains (Figure 50 (d), Figure 51 (a)). Nevertheless, the grain aspect ratio for all dissimilar TNM joints is constantly around 0.35 (Figure 51 (b)). Hence, a continuous grain growth with increasing preheating temperature can be assumed.

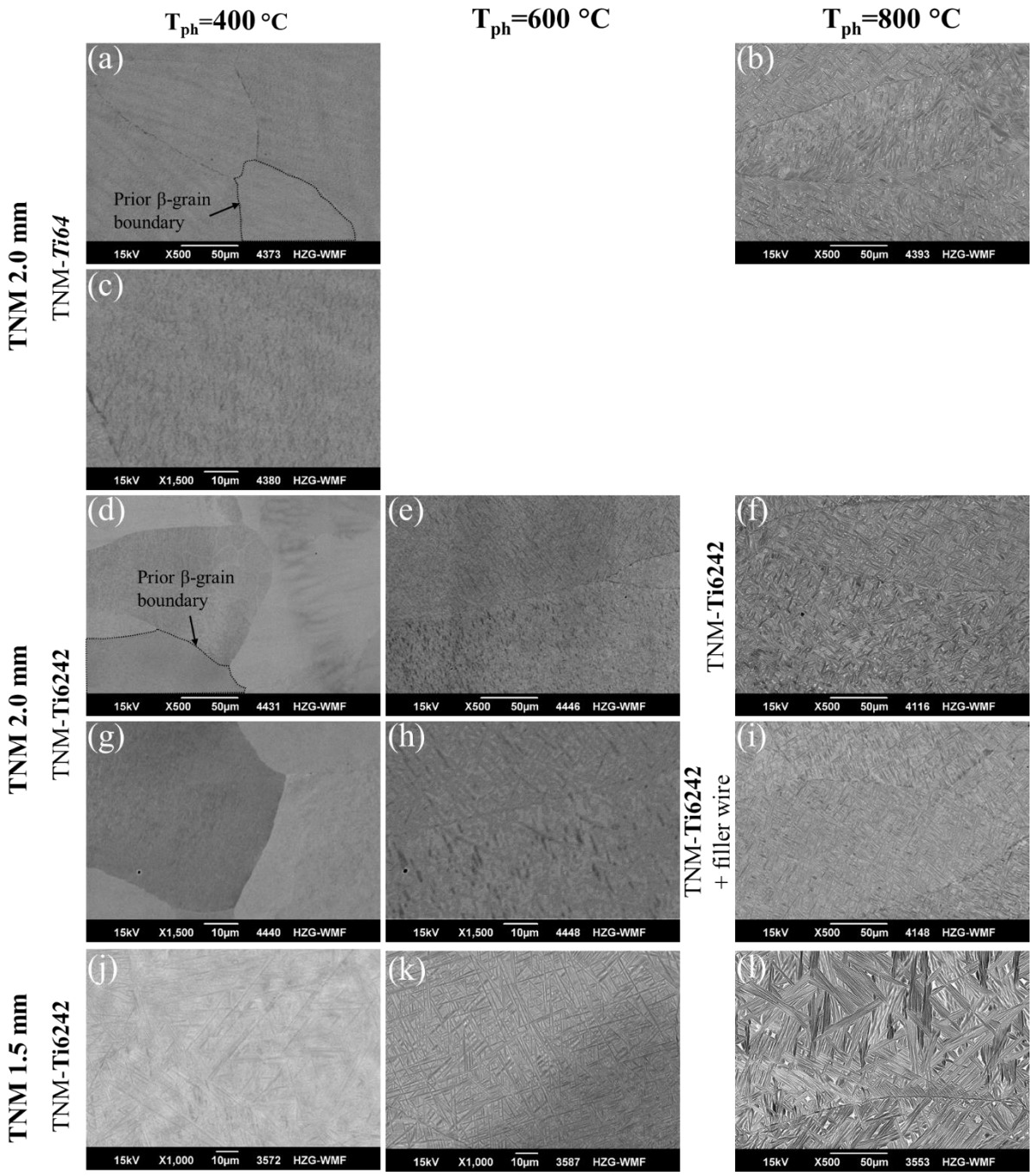

Figure 50: SEM images of FZ of dissimilar TNM joints with different preheating temperatures, Ti-alloy joining partners and sheet thicknesses welded with P=4.5 kW, v=3 m/min. Dotted lines: Exemplarily prior β-grain boundaries.

As the grain size of dissimilar TNM-Ti64 preheated to 400 °C and dissimilar TNM-Ti6242 preheated to 600 °C are alike (Figure 51 (a)), it seems that the massive phase transformation from β to α_2 occurs close to these preheating temperatures. For 2 mm thich TNM sheets, grain sizes at preheating temperatures of 800 °C are the smallest for dissimilar TNM-Ti6242 joints welded with filler wire, and largest for TNM-Ti64 joints (Figure 51 (a)). Considering the higher long-term service temperature of Ti6242 [3], the grain size difference of 5.49 µm and 7.51 µm for dissimilar TNM-Ti6242 and TNM-Ti64 joint respectively could be explained. Moreover, the preheating temperature of 600 °C for

dissimilar TNM(1.5)-Ti6242 joints, where a significant grain growth occurs (Figure 51 (a)), is above the Ti6242 long-term service temperature, which is between 425 °C and 450 °C [2,3].

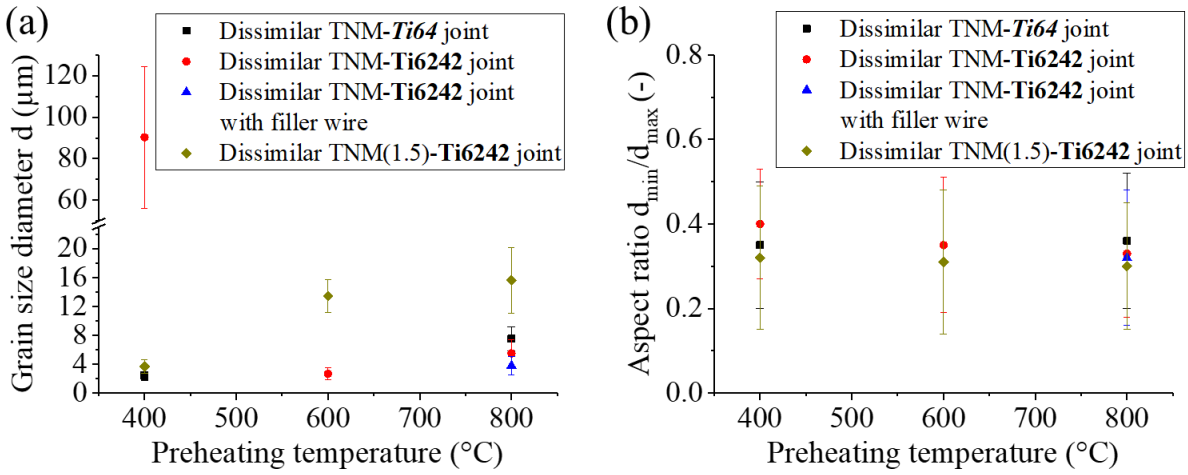

Figure 51: Influence of the preheating temperature on (a) the grain size and (b) the aspect ratio of different dissimilar TNM joints. P=4.5 kW, v=3 m/min.

The microstructure at the Ti6242 FL is shown exemplarily for dissimilar TNM-Ti6242 joints without and with filler wire preheated to 800 °C (Figure 52). Both HAZ microstructures are martensitic and a continuous transition between the HAZ and the FZ is present. Consequently and in contrast to the inhomogeneous transition at the TNM FL (Figure 48 (a), (d)), the theoretical cooling rates should be sufficiently low for the development of a homogeneous microstructure transition at the Ti6242 FL. Moreover, this is supported by the growth of needles from the Ti6242 HAZ into the FZ (Figure 52), which indicates heteroepitaxial growth at the Ti6242 FL. In the FZ of the dissimilar TNM-Ti6242 joint exemplarily the growth of needles from a prior β-grain boundary is exhibited (Figure 52 (a), red ellipse). Hence, a classical Ti-alloy needle growth mechanism [2,3] also occurs in dissimilar TNM joints.

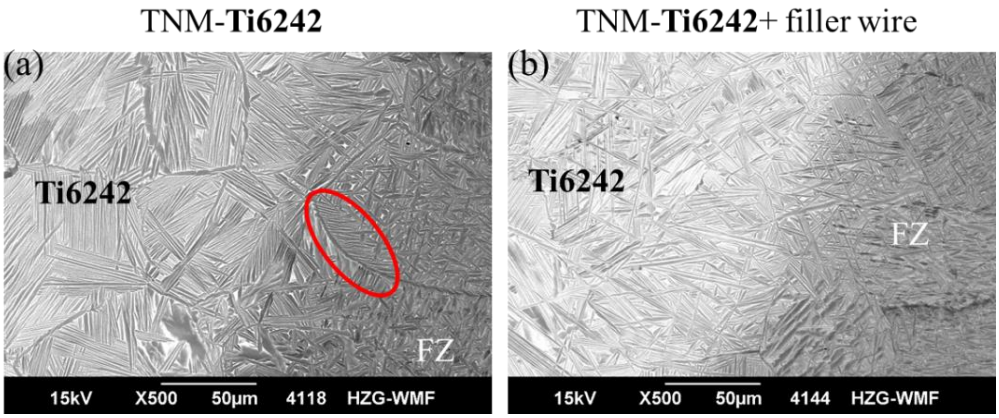

Figure 52: SEM images of FL on Ti6242 side of dissimilar (a) TNM-Ti6242 and (b) TNM-Ti6242 joint with filler wire. (a) P=4.5 kW, v=3 m/min, T_{ph}=800 °C. (b) P=4.5 kW, v=3 m/min, v_w~3.6 m/min, T_{ph}=800 °C. Red ellipse in (a): Exemplarily growth of needles from prior β-grain boundary

TNM is the more crack sensitive material [2,3,71] and has a higher thermal conductivity than the Ti-alloys (Table 3). Hence, the highest possibility for an unequal microstructure and phase transition of the dissimilar TNM joints occurs at the TNM FL. Moreover, the cross-section have revealed a seam at the TNM FL (Figure 48 (a), (d)). A continuous seam emerges for all dissimilar TNM joints with a martensitic microstructure in the FZ and a preheating temperature lower than 800 °C (Figure 53 (a), (d), (g), (h)). This seam could be the result of a higher cooling rate at the TNM side, due to the higher thermal conductivity. Therefore, a different microstructure evolves and altering phases could develop at the TNM FL. As the microstructures in the FZ for dissimilar TNM-Ti64 and TNM-Ti6242 joints with a preheating temperature of 400 °C differ (Figure 50 (c), (g)), the total FZ of the dissimilar TNM-Ti6242 could be seen as the evolving seam (Figure 53 (c)).

A comparable seam, as for the dissimilar TNM-Ti64 and TNM(1.5)-Ti6242 joint preheated to 400 °C (Figure 53 (a), (g)), is developed for the dissimilar TNM-Ti6242 joint with a preheating temperature of 600 °C (Figure 53 (d)). Hence, due to the differing theoretical cooling rates and temperature evolutions (Figure 23, Figure 42), the sheet thickness and the joining partner influence the development of the seam. Despite the continuous seam in the dissimilar TNM(1.5)-Ti6242 joint preheated to 600 °C, close to the TNM HAZ some needles are growing into the seam (Figure 53 (h)).

Significant differences in the seam for the dissimilar TNM joints are observed with preheating temperatures of 800 °C (Figure 53 (b), (e), (f), (i)). In spite of the coarsening of the martensitic microstructure in the FZ, a continuous seam is present for dissimilar TNM-Ti64 joints preheated to 800 °C (Figure 53 (b)). Moreover, the seam width is comparable to that of the dissimilar TNM-Ti64 joint preheated to 400 °C (Figure 53 (a)). In contrast, altering seams are visible for dissimilar TNM(1.5)-Ti6242, dissimilar TNM-Ti6242 joints with and without filler wire (Figure 53 (e), (f), (i)). The seam of dissimilar TNM-Ti6242 and TNM(1.5)-Ti6242 joint preheated to 800 °C are penetrated with needles (Figure 53 (e), (i)). Nevertheless, no continuous microstructural change occurs at the TNM FL. Furthermore, small needles within the seam of the dissimilar TNM(1.5)-Ti6242 joint (Figure 53 (i)) could indicate that at higher preheating temperatures, a phase transformation of the whole seam could take place. Chemical composition differences of the dissimilar TNM-Ti64 joint and the dissimilar TNM-Ti6242 joint, could explain the thermal stability of the dissimilar TNM-Ti64 joint seam (Figure 53 (b)). Minor chemical composition differences for dissimilar TNM-Ti6242 joints with and without filler wire at the preheating temperature of 800 °C are assumed. Hence, a potentially higher cooling rate by the use of filler wire could lead to the continuous seam of the dissimilar TNM-Ti6242 joint with filler wire in contrast to the penetrated dissimilar TNM-Ti6242 joint seam without filler wire (Figure 53 (e), (f)). The continuous seam of the dissimilar TNM-Ti6242 joint with filler wire preheated to 800 °C is comparable to the seams of dissimilar TNM-Ti6242 joints with a preheating temperature lower than 800 °C (Figure 53 (d), (g), (h)). This together with the high thermal conductivity of TNM (Table 3) leads to the assumption that the seam could be retained β/β_O-phase resulting from the high cooling rate at the TNM FL. Concluding, the preheating temperature, thus the cooling rate and temperature gradient at the FL, influences the microstructure of the TNM FL significantly.

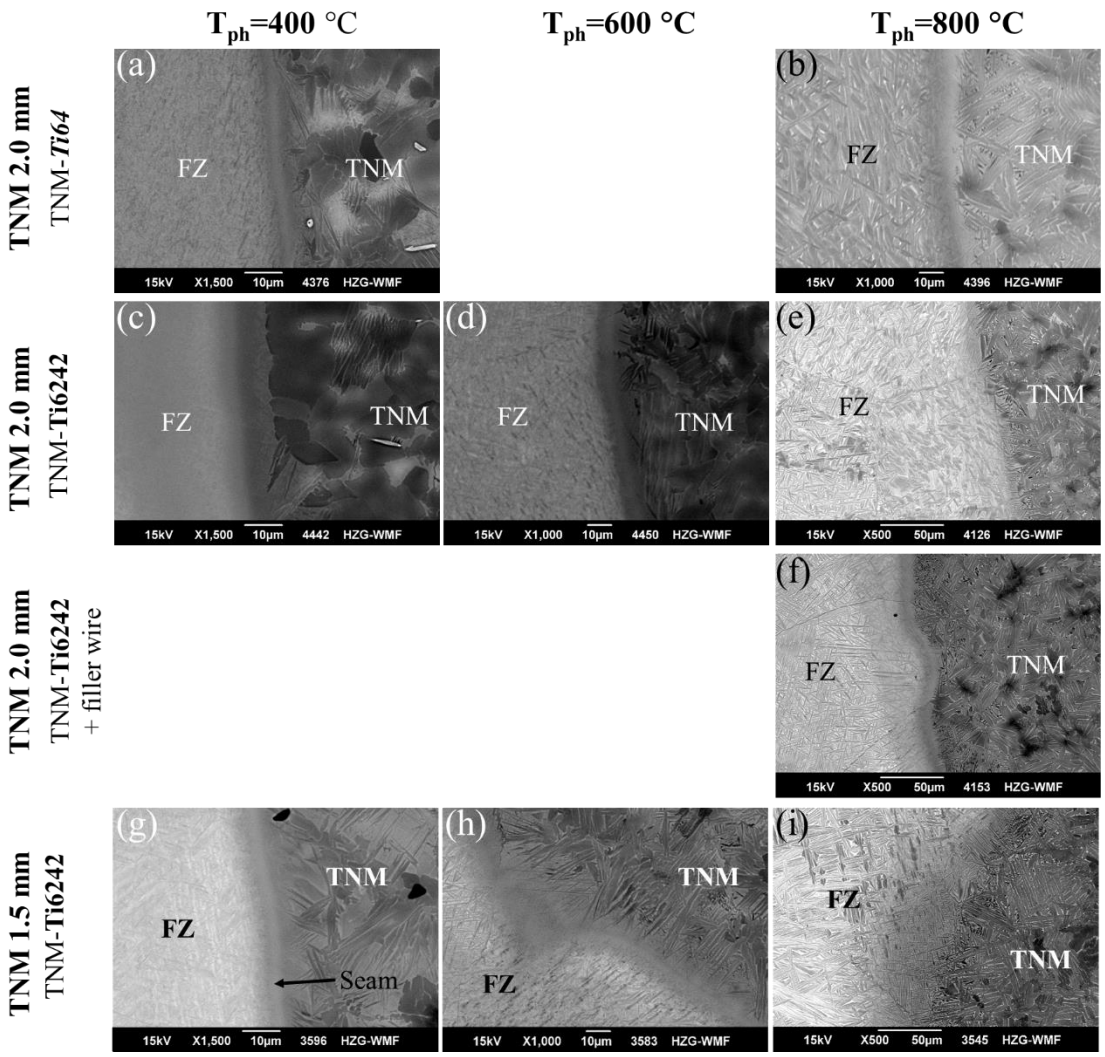

Figure 53: SEM image of FL on TNM side of dissimilar TNM joints with different preheating temperatures, Ti-alloy joining partners and sheet thicknesse welded with P=4.5 kW, v=3 m/min.

5.2.4. Chemical analysis

Chemical analysis by EDX were utilized to examine the chemical composition and thus the mixing behavior in terms of segregations for the dissimilar joints. Moreover, thereby atom migration processes were studied. The chemical analysis also enabled the verification if the α- or α_2-phase evolved in the FZ. Besides, the influence of the preheating temperature, TNM sheet thickness and use of Ti6242 filler wire on the chemical composition were examined.

To verify the assumption that the seam consists of the β/β_O-phase, EDX point analysis in the TNM HAZ, the seam and TNM FZ were performed (Figure 53 (g)). The results are listed in Table 14. From literature it is known that Nb and Mo are β-stabilizing elements [2]. Compared to the FZ, the seam is enriched in Nb, supporting the hypothesis of the β/β_O-phase containing seam. The chemical composition of the FZ corresponds to the α_2-phase.

Table 14: Average of three EDX point analysis in the HAZ TNM, seam and FZ of Figure 53 (g) [222]. Dissimilar TNM(1.5)-Ti6242 joint. P=4.5 kW, v=3 m/min, T_{ph}=400 °C, TNM t_S=1.5 mm.

Zone	**Al-K (wt .-%)**	**Sn-L (wt.-%)**	**Mo-L (wt.-%)**	**Zr-L (wt.-%)**	**Nb-L (wt.-%)**	**Ti-K (wt.-%)**
BM TNM	29.85	-	3.09	-	9.36	-
HAZ TNM	26.95	0.06	3.53	0.12	9.14	60.19
Seam	23.05	0.30	2.95	0.97	7.57	65.17
FZ	12.10	1.74	2.69	3.33	3.08	77.07

The overall chemical composition change is exemplarily shown for dissimilar Ti64-Ti6242, TNM-Ti64 and TNM-Ti6242 joints in Figure 54, which were welded at RT and 800 °C, respectively. For the dissimilar Ti64-Ti6242 joint the Ti amount continually decreases from the Ti64 side to the Ti6242 side (Figure 54 (d)). Representing a mixture of the chemical composition of both Ti-alloys (Table 2), the Al content in the FZ stays constant (Figure 54 (d)), while the minor alloying element amount changes abruptly (Figure 54 (g)). Alloying elements of each joining partner are also detected in the HAZ of the dissimilar Ti64-Ti6242 joint, hence short-term diffusion controlled migrations took place. For the dissimilar TNM-Ti64 and TNM-Ti6242 joints with a preheating temperature of 800 °C, major and minor alloying elements change abrupt at the FL (Figure 54 (e), (f), (h), (i)). Changes in the chemical composition of TNM alloys, particularly of the Al content, can lead to differing mechanical properties [2,7]. Therefore, a gradual change, especially of the major alloying element Al, within the FZ would be more preferential. In spite of the fast LBW process, thus a high cooling rate, diffusion controlled atom migrations also take place in the HAZ of dissimilar TNM joints, since in both cases alloying elements of the joining partner are detected in the HAZ (Figure 54 (h), (i)). Due to the abrupt change of the chemical composition, the mechanical properties could be influenced and the dissimilar joint can be seen as a three-component system.

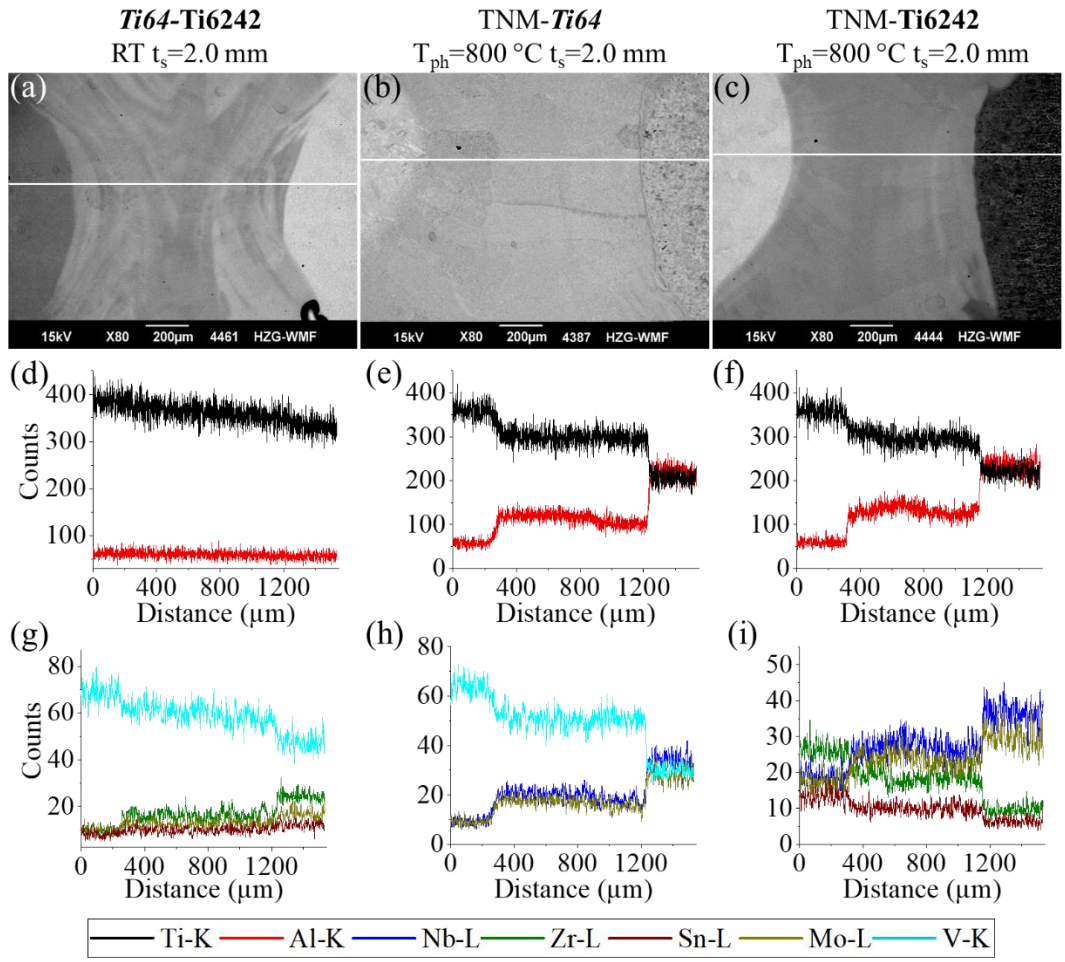

Figure 54: (a)-(c) SEM images of position of respective EDX line analysis welded with P=4.5 kW, v=3 m/min and line scan position (white line) (a) Dissimilar Ti64-Ti6242 joint RT with EDX line analysis of (d) major and (g) of minor alloying elements of line scan position in (a). (b) Dissimilar TNM-Ti64 joint preheated to T_{ph}=800 °C with EDX line analysis of (e) major and (h) of minor alloying elements of line scan position in (b). (c) Dissimilar TNM-Ti6242 joint preheated to T_{ph}=800 °C with EDX line analysis of (f) major and (i) of minor alloying elements of line scan position in (c). Minor alloying element EDX line analysis smoothened with 5 points averaged adjacent function.

The mixture in the FZ of dissimilar Ti64-Ti6242 joints is further investigated by EDX micro-area analysis close to the Ti64 side, in the FZ center and close to the Ti6242 side (Table 15). The maximum of the acceptable deviation is taken from the corresponding Ti64 and Ti6242 datasheets [110,111]. In case of the same alloying element, the smaller limit is selected (Table 2). The obtained results show that only the deviation of the Mo content is with a maximal difference of 0.29 wt.-% slightly above the acceptable deviation. Nevertheless, considering measurement inaccuracies [214], a homogeneous mixture in the FZ of dissimilar the Ti64-Ti6242 joint is obtained.

Table 15: EDX micro-area analysis of dissimilar Ti64-Ti6242 at different positions in the FZ and welded with P=4.5 kW, v=3 m/min.

Position	**Al-K (wt.-%)**	**V-K (wt.-%)**	**Sn-L (wt.-%)**	**Mo-L (wt.-%)**	**Zr-L (wt.-%)**	**Ti-K (wt.-%)**
Maximal acceptable deviation (wt.-%) of Ti64 and Ti6242	0.5 [111]	0.5 [110]	0.25 [111]	0.25 [111]	0.5 [111]	-
FZ close to Ti64	6.75	1.40	0.95	1.24	1.99	87.67
FZ center	6.75	1.41	0.97	1.24	2.00	87.63
FZ close to Ti6242	6.62	1.59	0.91	0.95	1.89	88.04

The overall mixture in the FZ of dissimilar TNM-Ti6242 joints is investigated analog (Figure 55 Moreover, for the ideal chemical mixture of the dissimilar TNM-Ti6242 joints, a molten amount of the joining partner in the FZ according to the sheet thickness is assumed. Thus, with the assumption of an accurate positioning of the laser beam, equal melting and mixing of both materials, for dissimilar TNM-Ti6242 joints a mixture of 50:50 (green open top triangle) and for dissimilar TNM(1.5)-Ti6242 joints of 25:75 (red open circle) is supposed (Figure 55). The corridor of gradual composition change is indicated by the grey area and the FZ by the turquoise area. As Al is an α-stabilizing element, Nb and Mo are β-phase stabilizers and Sn as well as Zr have a neutral influence on Ti-alloy phase diagrams [2], a particular focus is on the Al, Nb and Mo content.

The Al content for all dissimilar TNM-Ti6242 joints is slightly below the ideal mixture (Figure 55 (a), green solid top triangle, blue solid bottom triangle). The maximum acceptable Al deviation for Ti6242 is 1 wt.-% and for TNM 1.4 wt.-% [111,112]. The decreased Al content close to the Ti6242 BM for dissimilar TNM-Ti6242 joints with filler wire, leads to a maximum deviation of 1.36 wt.-%, thus slightly above the acceptable deviation. Utilizing the maximum acceptable deviation of TNM and Ti6242 at each measurement point, the overall mixture in the FZ of dissimilar TNM-Ti6242 joints is homogeneous. For dissimilar TNM(1.5)-Ti6242 joints the Al content close to the TNM increases and hence is with 1.46 wt.-% narrowly above the deviation (Figure 55 (a), red solid circle).

Nb contents are below the ideal mixture (Figure 55 (b)). Utilizing the deviation in each measurement point, the detected Nb content is within the deviation for dissimilar TNM-Ti6242 joints welded with and without filler wire. The highest decrease of Nb can be seen for dissimilar TNM(1.5)-Ti6242 joints close to the Ti6242 side (Figure 55 (b), red solid circle).

In general, the Mo amount is higher than for the ideal mixture, but nevertheless within deviation limits (Figure 55 (c)). The Mo content of the dissimilar TNM(1.5)-Ti6242 joint is even within the corridor of gradual chemical composition change (Figure 55 (c), red solid circle). Utilizing the deviations of the BM, all EDX micro-area analysis of the Mo content are within the acceptable deviation (Figure 55 (c)).

Possibly due to measurement inaccuracies, all Zr values are above the ideal mixture (Figure 55 (d)). Comparable to the Zr content of the dissimilar TNM(1.5)-Ti6242 joint, the Zr content close to the Ti6242 BM of the dissimilar TNM-Ti6242 joints with filler wire is higher and not within the acceptable deviation. This could be caused by measurement inaccuracies or by Ti6242 dominating the FZ. For the Sn amount in the FZ, all values are above the ideal mixture, especially for the dissimilar TNM(1.5)-Ti6242 joint (Figure 55 (e) , red solid circle). Nevertheless, all values are within the acceptable deviation in each measurement point.

Consequently, taking into account EDX measurement inaccuracies [214], the overall mixture of the dissimilar TNM-Ti6242 joint welded with and without filler wire as well as the autogenously welded TNM(1.5)-Ti6242 joint is homogeneous.

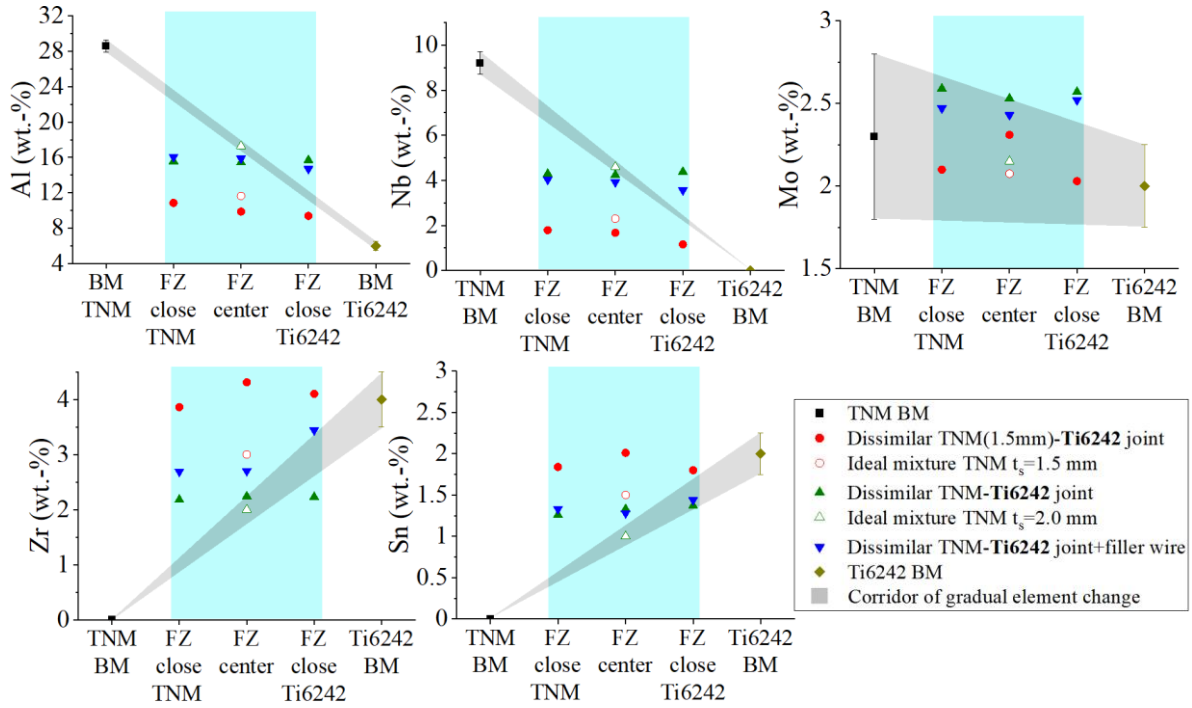

Figure 55: EDX micro-area analysis of different dissimilar TNM-Ti6242 joints at differeing FZ positions welded with P=4.5 kW, v=3 m/min, T_{ph}=800 °C. Ideal chemical composition of the BMs with acceptable deviation TNM BM (black solid square) and Ti6242 BM (yellow solid diamond) as well as chemical composition of dissimilar joints dissimilar TNM(1.5)-Ti6242 (red solid circle), dissimilar TNM-Ti6242 (green solid top triangle), dissimilar TNM-Ti6242 with Ti6242 filler wire v_w~3.6 m/min (blue solid bottom triangle). Ideal mixture dissimilar TNM(1.5)-Ti6242 (red open circle) and ideal mixture dissimilar TNM-Ti6242 (green open top triangle). Blue area corresponds to the FZ. Grey area corresponds to the corridor of gradual element change. (a) Al content. (b) Nb content. (c) Mo content. (d) Zr content. (e) Sn content.

Comparing the chemical compositions of dissimilar TNM-Ti6242 joints with different preheating temperatures in the FZ center (Table 16), reveals similar chemical compositions for joints preheated to 600 °C and 800 °C. This is consistent with the similar evolving microstructure for these preheating temperatures (Figure 50 (e), (f)). In contrast, the higher amount of Nb and Al, as well as the lower amount of Zr and Sn indicate the presence of a different phase at the preheating temperature of 400 °C. Moreover, the higher Nb content supports together with the microstructure evolution (Figure 50 (d)), the hypothesis that the phase transformation from β to α_2 is suppressed for the preheating temperature of 400 °C.

Table 16: Chemical composition of dissimilar TNM-Ti6242 joints in FZ center dependent on preheating temperature obtained by EDX micro-area analysis. P=4.5 kW, v=3 m/min.

Preheating temperature T_{ph} [°C]	**Al-K [wt.-%]**	**Sn-L [wt.-%]**	**Mo-L [wt.-%]**	**Zr-L [wt.-%]**	**Nb-L [wt.-%]**	**Ti-K [wt.-%]**
400	19.92	0.78	2.82	1.50	6.15	68.83
600	15.44	1.33	2.53	2.24	4.24	74.22
800	15.13	1.40	2.41	2.83	3.68	74.55

The occurrence of microsegregations in the dissimilar joint FZ were investigated by EDX line analysis, as these can lead to local altering mechanical properties. Furthermore, the influence of the preheating temperature on microsegregations was investigated for dissimilar TNM joints.

Regarding the dissimilar Ti64-Ti6242 joint welded at RT no microsegregations are detected (Figure 56 (a), (d), (g)). For dissimilar TNM-Ti64 and TNM-Ti6242 joints preheated to 400 °C microsegregations emerge (Figure 56 (b), (c), (e), (f), (h), (i)). More distinct for the dissimilar TNM-Ti6242 joint than the TNM-Ti64 joint, which could be explained by the higher theoretical cooling rate of Ti6242 (Figure 42) and the different evolving microstructures (Figure 50 (a), (d), Figure 56 (b), (c)). Minor microsegregations of Ti, Al, Nb and Mo are detected for dissimilar TNM-Ti64 joints (Figure 56 (e), (h)). The bright area of the dissimilar TNM-Ti6242 joint is Ti enriched and Al depleted (Figure 56 (f)). Moreover, minor microsegregations of Nb and Zr are present (Figure 56 (i)).

Concluding, due to the minor alloy differences of Ti64 and Ti6242 no microsegregations in the FZ center of dissimilar Ti64-Ti6242 joints occur. In contrast, the compositional difference of TNM and the Ti-alloys result in microsegregations of major and minor elements in the FZ for dissimilar TNM joints.

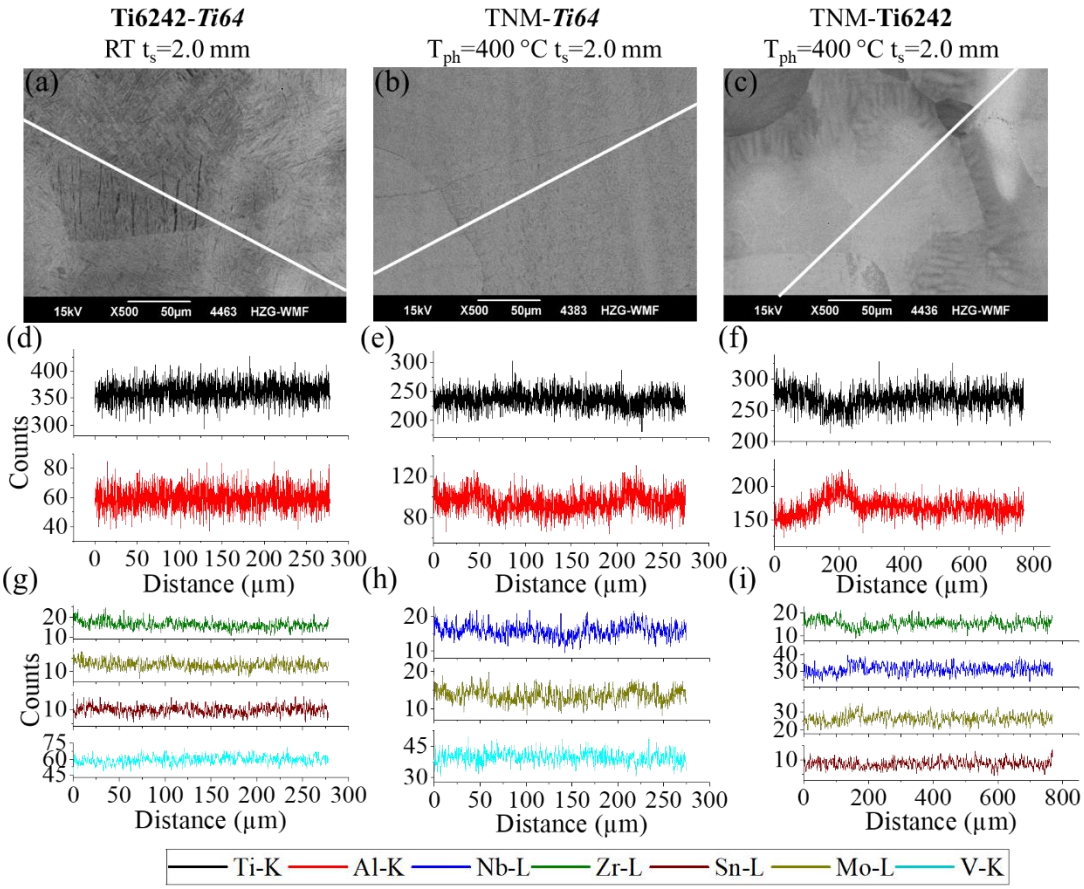

Figure 56: (a)-(c) SEM images of position of respective EDX line analysis welded with P=4.5 kW, v=3 m/min. Line scan position (white line). (a) Dissimilar Ti64-Ti6242 joint RT with EDX line analysis of (d) major and (g) of minor alloying elements of line scan position in (a). (b) Dissimilar TNM-Ti64 joint preheated to T_{ph}=400 °C with EDX line analysis of (e) major and (h) of minor alloying elements of line scan position in (b). (c) Dissimilar TNM-Ti6242 joint preheated to T_{ph}=400 °C with EDX line analysis of (f) major and (i) of minor alloying elements of line scan position in (c). Minor alloying element EDX line analysis smoothened with 5 points averaged adjacent function.

In contrast to the dissimilar TNM-Ti64 joint preheated to 400 °C (Figure 56 (b), (e), (h)) no microsegregations in the FZ center with a preheating temperature of 800 °C emerge (Figure 57 (a), (d), (g)). Therefore, the cooling rate seems to be sufficiently low for diffusion controlled atom migrations to homogenize chemical composition differences. For dissimilar TNM-Ti6242 joints preheated to 800 °C microsegregations of all elements are detected (Figure 57 (e), (h)). The dark area in the upper left corner is enriched in Al, Nb and Mo, while being depleted in Ti, Zr and Sn (Figure 57 (b), (e), (h)). Thus, the cooling time is too short and insufficiently for diffusion controlled homogenization to compensate chemical concentration differences. For dissimilar TNM-Ti6242 joints welded with filler wire at 800 °C microsegregations of all elements are detected (Figure 57 (f), (i)). As for the dissimilar TNM-Ti6242 joint in the brighter area Ti, Zr and Sn is enriched, while Al, Nb and Mo is depleted (Figure 57 (c), (f), (i)). The darker areas are enriched in Al, Nb and Mo. The filler wire could also influence the fluid dynamics of the melt pool. Thus the development of microsegregations could be supported.

Hence, with the applied deviations of the BM and measurement inaccuracies, the EDX micro-area analysis have verified that the overall mixture in the dissimilar joints is homogeneous (Figure 55).

Nevertheless, the EDX line analysis revealed microsegregations in the FZ center of the dissimilar TNM joints (Figure 56, Figure 57).

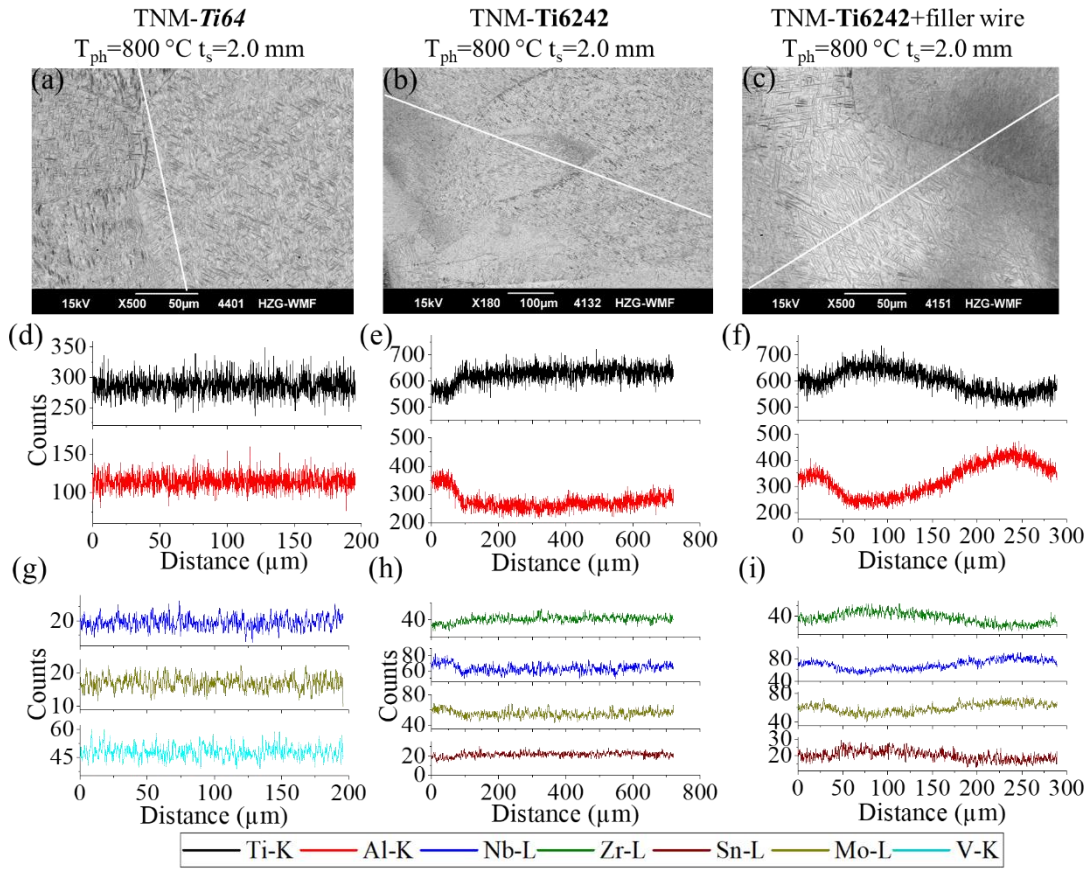

Figure 57: (a)-(c) SEM images of position of respective EDX line analysis welded with P=4.5 kW, v=3 m/min, T_{ph}=800 °C. and line scan position (white line). (a) Dissimilar TNM-Ti64 joint with EDX line analysis of (d) major and (g) of minor alloying elements of line scan position in (a). (b) Dissimilar TNM-Ti6242 joint with EDX line analysis of (e) major and (h) of minor alloying elements of line scan position in (b). (c) Dissimilar TNM-Ti6242 joint with Ti6242 filler wire, v_w~3.6 m/min, with EDX line analysis of (f) major and (i) of minor alloying elements of line scan position in (c). Minor alloying element EDX line analysis smoothened with 5 points averaged adjacent function.

5.2.5. Phase analysis

The phase analysis at characteristic weld seam positions is performed with the EBSD method to investigate the phase evolution in the dissimilar joints and after the PWHT. As the EBSD method cannot distinguish between certain crystallographically related phases (Chapter 2), XRD measurements are carried out for selected dissimilar TNM joints. Moreover, together with the microstructure analysis (Chapter 5.2.3) the obtained results of the phase analysis are correlated to the crack formation (Chapter 5.2.2.).

Referring to the results of the phase maps obtained by EBSD, the FZ of dissimilar Ti64-Ti6242 joints consists of the α-phase as the FZ of similar Ti6242 joints (Figure 38 (a), (b), Figure 58 (b)). Moreover, the α-phase is the major phase in both HAZs (Figure 58 (a), (c)). Besides, as a minor phase β is present. For demonstrating the β-stabilizing strength of an alloying element, the Mo-equivalent after [2] can be utilized. The Mo-equivalent for Ti64 is 2.68 and for Ti6242 2.0, explaining the higher β-phase content in the Ti64 HAZ compared to the Ti6242 HAZ (Figure 58 (a), (c)).

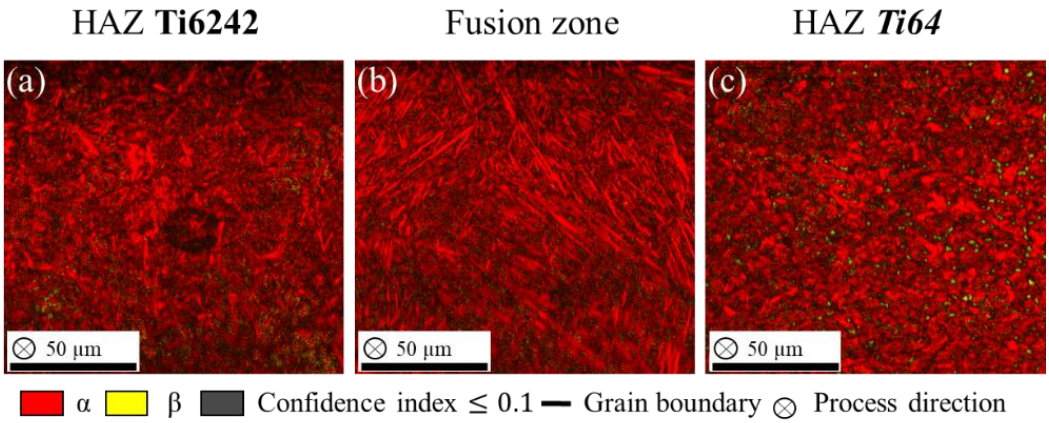

Figure 58: Phase maps of a dissimilar Ti64-Ti6242 joint welded with P=4.5kW, v=3.0 m/min, LE=90 MJ/m. α-red. β-yellow. Confidence index $\leq$ 0.1-grey. Grain boundary-black.

From the Calphad phase diagram (Figure 2) no information concerning the phase evolution of the dissimilar TNM joints can be deduced. Due to the significantly altering microstructural evolution in the FZ and at the TNM FL (Figure 50, Figure 53), for dissimilar TNM joints the focus of the phase analysis by the EBSD method is on these two regions.

Except for the dissimilar TNM-Ti6242 joint preheated to 400 °C, all other dissimilar TNM joint FZ consist of the α_2-phase (Figure 59). In the FZ of dissimilar TNM-Ti6242 joints preheated to 400 °C the β/β_O-phase is present (Figure 59 (c)). Moreover, from the shown phase maps, this joint is the only joint with a crack (Figure 44 (d)). Therefore, comparable to the findings for similar TNM joints (Figure 39), the presence of the β/β_O-phase as a block in the FZ of dissimilar TNM joints results in the crack formation (Figure 59). Considering the very fine microstructure (Figure 50 (a), (c)), a just occurred massive phase transformation from β to α_2 in the dissimilar TNM-Ti64 joint preheated to 400 °C can be assumed (Figure 59 (a)). This also explains the crack-free joint compared to the dissimilar TNM-Ti6242 joint (Figure 44 (a), (d)). Even so Ti6242 has with 2.0 a lower Mo-equivalent than Ti64, only in the dissimilar TNM-Ti6242 the β/β_O-phase is present. Hence, the dissimilar TNM-Ti6242 should have experienced a faster cooling process, which is supported by the theoretical considerations (Figure 42). As the phase maps here are given with the image quality information, black bands are visible in the dissimilar TNM-Ti6242 joint with β/β_O-phase in the FZ (Figure 59 (c). These indicate locations of defect densities probably caused by a higher cooling rate after the peak temperature and the temperature evolution (Figure 42 (b)). Thus, higher thermally induced stresses in the FZ compared to the other dissimilar TNM joints could be obtained (Figure 59), which could result in the crack formation (Figure 44). Due to the sufficient independent slips systems for plastic deformation of the β-phase [2,7], obtained stresses by the high defect density could be compensated, while this is improbable for the in TNM sheets until fracture elastically deforming β_O-phase [85]. Besides, as the β_O-phase is present in TNM at RT [102,103] and the ordering temperature $\beta \rightarrow \beta_O$ is between 1175 °C to 1215 °C [13,108], the formation of the β_O-phase cannot be excluded. Especially, as phase maps obtained by EBSD cannot differentiated between β- and β_O-phase. Therefore, the crack formation in the dissimilar TNM-Ti6242 joint preheated to 400 °C (Figure 44 (d)) indicates the presence of the β_O-phase. Depending on the cooling rate the β_O-phase can transform to the ω_O-, ω''- or ω'-phase at temperatures below 950 °C and since the mentioned phases are related to the β_O-phase [88,89,91,95], their presence cannot be excluded.

A lower cooling rate due to the thinner TNM sheet is feasiable, as the dissimilar TNM(1.5)-Ti6242 joint preheated to 400 °C is crack-free (Figure 44 (k)) and the FZ consisting of the α_2-phase (Figure 59 (g)).

For a preheating temperature of 600 °C the phase transformation from β to α_2 also emerged for the dissimilar TNM-Ti6242 joint (Figure 59 (d)). Due to the smaller sheet thickness the needles in the dissimilar TNM(1.5)-Ti6242 joint appear longer and broader than in the dissimilar TNM-Ti6242 joint (Figure 59 (d), (h)). In contrast to similar TNM joints with a preheating temperature of 800 °C (Figure 38 (c)), no γ-phase evolves in the FZ of all dissimilar TNM joint configurations (Figure 59 (b), (e), (f), (i)). Due to the high cooling rates during LBW, supersaturated α_2-phase could have evolved comparable to the first heat treatment step for TNM [13,103]. If this is the case, the supersaturated α_2-phase could transform in γ-phase by a heat treatment.

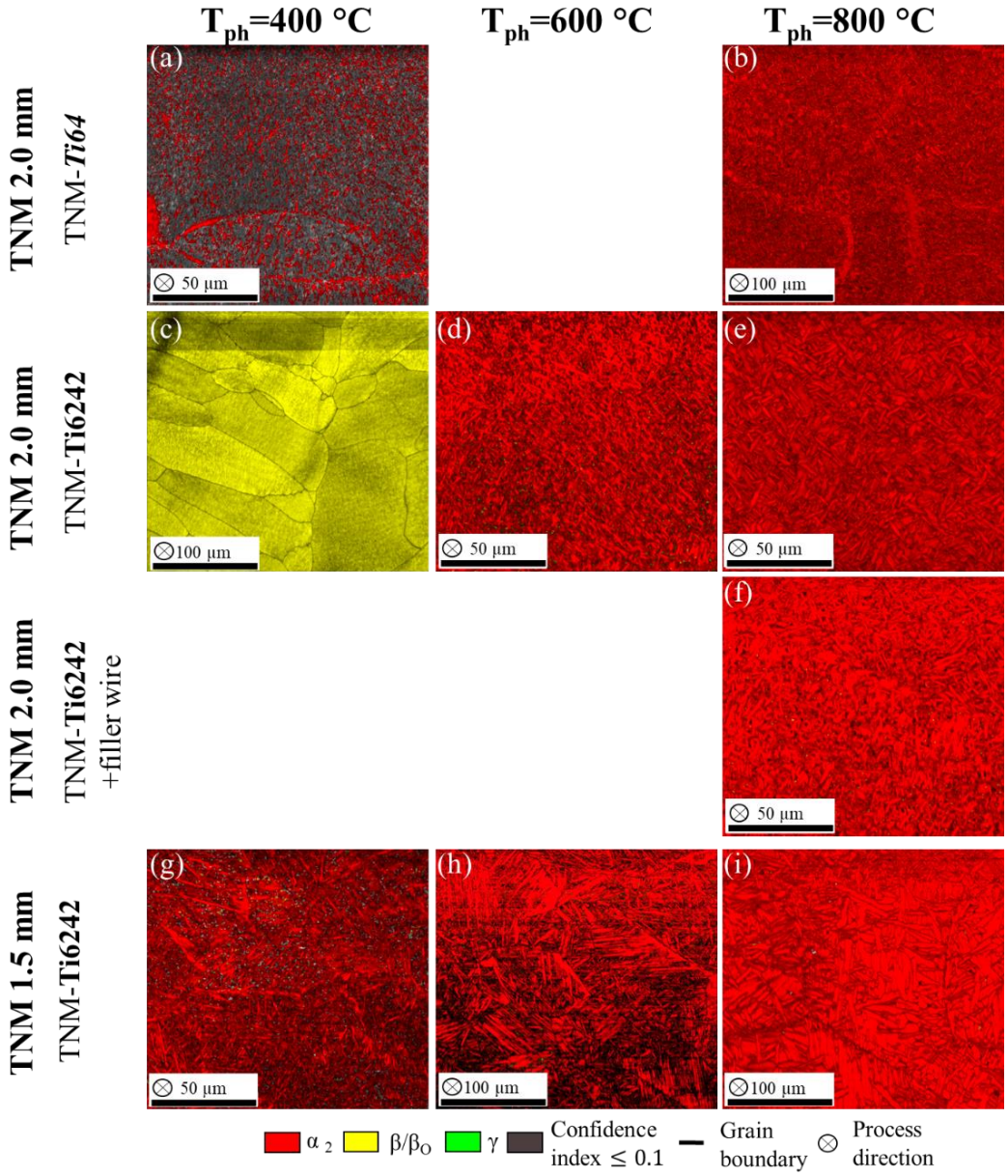

Figure 59: Phase maps of dissimilar TNM joint FZs with different preheating temperatures, Ti-alloy joining partners and sheet thicknesses welded with P=4.5 kW, v=3 m/min. α_2-red. β/β_O-yellow. γ-green. Confidence index ≤ 0.1-grey. Grain boundary-black.

At the FL the highest cooling rates develop [117,155], therefore the phase transformation from β to α_2 can be suppressed. Hence, at most dissimilar TNM FLs a continuous β-phase related seam emerges (Figure 60). Besides, for the dissimilar TNM-Ti6242 joints preheated to 400 °C, this explains the higher defect density at the FL compared to the FZ center, which are indicated by the black layer bands (Figure 59 (c), Figure 60 (c)). Due to the high cooling rate of the FZ center and the resulting β/β_O-phase in the FZ of the dissimilar TNM-Ti6242 preheated to 400 °C (Figure 59 (c)), the FZ can be seen as the β-phase related seam (Figure 60 (c)). Moreover, the β_O-phase in TNM forms a semi-coherent interface with the α_2-phase [104], which could be a further influencing factor for the higher defect density. Based on EDX point analysis (Table 14) and the phase maps utilizing EBSD (Figure 60 (g)), it can be stated, that the seam at the TNM FL in the SEM images corresponds to the β-phase related seam (Figure 53 (g)). As the thinner TNM sheet leads to the α_2-phase development in the FZ of the dissimilar TNM(1.5)-Ti6242 joint preheated to 400 °C (Figure 59 (g)), at the FL a continuous related β-phase seam is present (Figure 60 (g)). Therefore, a continuous β-phase related seam is expected for dissimilar TMN-Ti6242 joints at higher preheating temperatures.

As expected the continuous β-phase related seam develops for dissimilar TNM-Ti6242 joints with a preheating temperature of 600 °C (Figure 60 (d)). A continuous β-phase related seam is still present for a preheating temperature of 800 °C for the dissimilar TNM-Ti64 joint and the dissimilar TNM-Ti6242 joint with filler wire (Figure 60 (b), (f)), while for the dissimilar TNM-Ti6242 joint and the dissimilar TNM(1.5)-Ti6242 joint the seam is penetrated with α_2 needles (Figure 60 (e), (i)). Hence, for the dissimilar joints with the penetrated β-phase related seam, the preheating temperature is sufficiently high and the cooling rate appropriately low, for diffusion controlled phase transformations. Moreover, a higher amount of the γ-phase is detected in the TNM HAZ with the penetrated β-phase related seam (Figure 60 (e), (i)). Compared to the dissimilar TNM-Ti64 joint preheated to 400 °C (Figure 60 (a)), some α_2 needles occur close to the TNM HAZ for the preheating temperature of 800 °C (Figure 60 (b)). Nevertheless, the widths of the β-phase related seam is similar and for both preheating temperatures continuous. The thermal stability of the β-phase related seam of the dissimilar TNM-Ti64 joint compared to the dissimilar TNM-Ti6242 joint can be explained by the higher Mo-equivalent of Ti64 compared to Ti6242 with 2.68 to 2.0, respectively. As the β-phase related seam is continuous for dissimilar TNM-Ti6242 with filler wire preheated to 800 °C and comparable to that of dissimilar TNM-Ti6242 preheated to 600 °C (Figure 60 (d), (f)), similar cooling rates at the TNM FL should develop. Besides, the discontinuous microstructural change also a discontinuous phase change at the TNM FL emerges (Figure 53, Figure 60).

Concluding, if the FZ consists of α_2, a β-phase related seam at the TNM FL has no detrimental effect on the crack formation of dissimilar TNM joints. Nevertheless, the β-phase related seam could reduce the tensile properties as a continuous β_O seam at TNM colony boundaries is detrimental to the RT ductility, the fracture toughness and creep properties [105–107]. Furthermore, once a microcrack is formed in the β_O-phase, the crack propagates in the brittle phase [106]. On the other hand, the β_O-phase at colony boundaries has a strengthening effect at RT and suppresses grain growth [13]. Moreover, as for the FZ of the dissimilar TNM-Ti6242 joint preheated to 400 °C, the presence of the $\omega_{O,}$ ω'' or ω'-phase in the seam cannot be excluded [88,89,91,95].

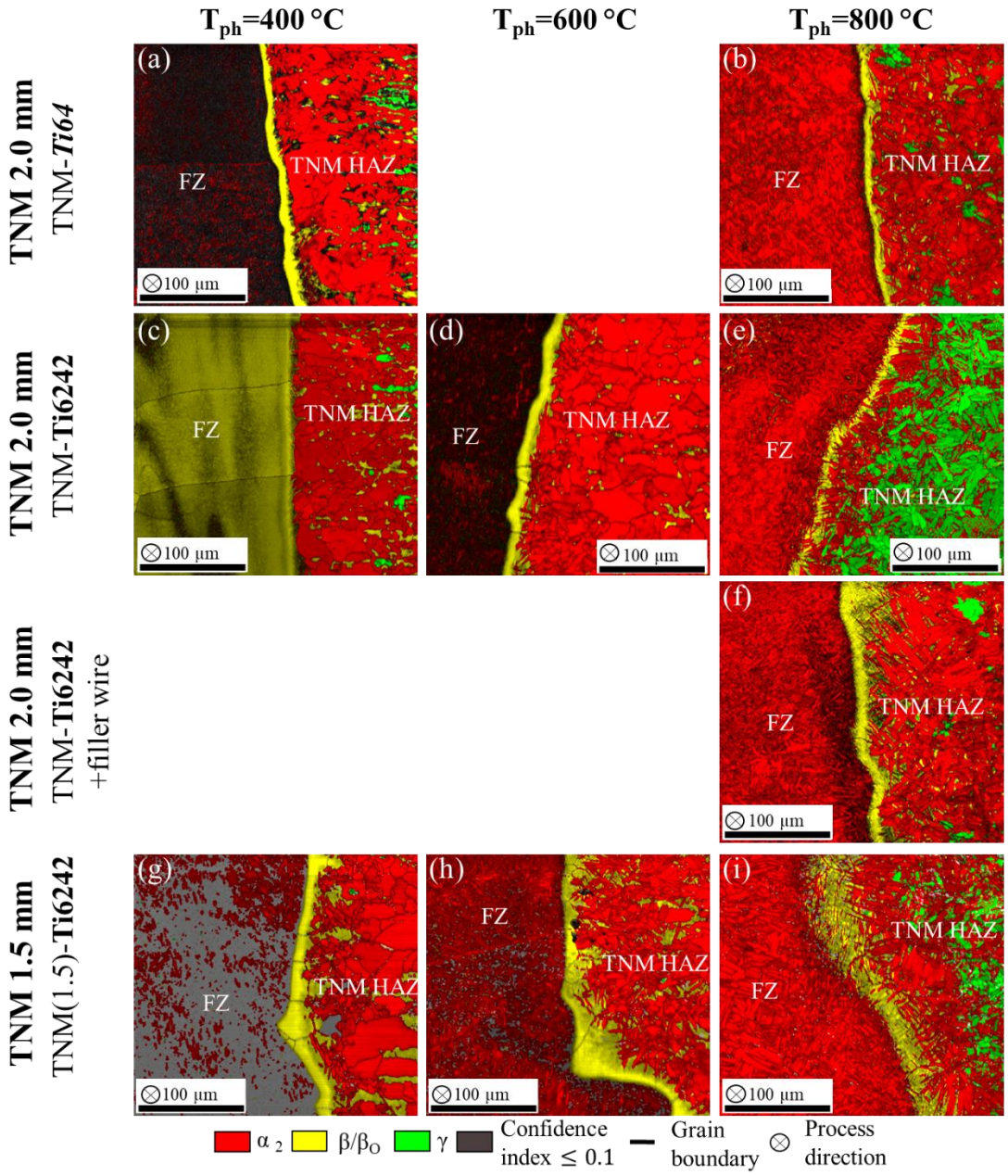

Figure 60: Phase maps of dissimilar TNM joint FLs with different preheating temperatures, Ti-alloy joining partners and sheet thicknesses welded with P=4.5 kW, v=3 m/min. α_2-red. β/β_O-yellow. γ-green. Confidence index ≤ 0.1-grey. Grain boundary-black.

If not stated differently in the further analysis dissimilar TNM joints with a TNM sheet thickness of 2.0 mm were analyzed. As the microstructure of as-welded and post weld heat-treated (1290 °C for 1 h) dissimilar TNM-Ti6242 joints with filler wire preheated to 800 °C changed significantly (Figure 48 (a), (c)), phase analysis by the EBSD method were utilized to investigate the evolving phases (Figure 61). Comparable to typical TNM heat-treatments [13,65], in the TNM HAZ of the heat-treated dissimilar TNM-Ti6242 joint α_2-γ domains occur (Figure 61 (b)). The FZ consists of the α_2-, β/β_O-phase and close to the TNM FL even γ needles evolve. In contrast to the expectation that the PWHT enables the phase transformation $\beta/\beta_O \rightarrow \alpha_2$, a high amount of β/β_O-phase in the TNM close to the FZ is detected. Nevertheless, the retained β/β_O-phase is penetrated with α_2 needles. As the amount of α_2 needles

increases in the OM image and the phase map (Figure 48 (c), (f), Figure 61 (b)), the bright seam in the OM image should correspond to the area at the FL with an increased β/β_O-phase amount. Both heat-treatment temperatures are inadequate for dissimilar TNM-Ti6242 joints, since a Ti6242 PWHT temperature of 950 °C insignificantly changes the microstructure in the FZ (Figure 48 (b)) and a TNM PWHT temperature of 1290 °C results in a massive grain growth on the Ti6242 side as well as a high amount of retained β/β_O-phase (Figure 48 (c), Figure 61 (b)). Furthermore, the evolution of the γ-phase in the FZ center seems to be improbable. Hence, to adjust the evolving microstructure and phases at the TNM FL, the preheating of the weld coupons for LBW seems to be preferable (Figure 53, Figure 60).

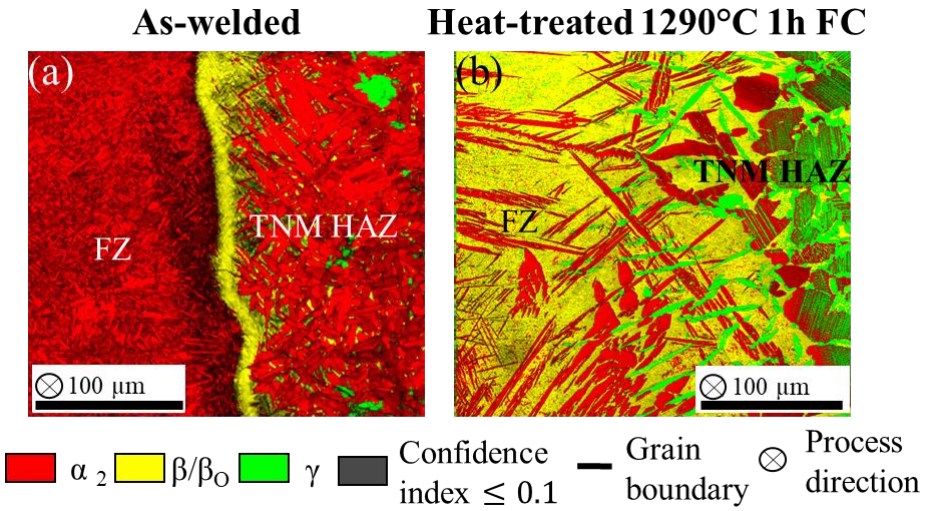

Figure 61: Phase maps of dissimilar TNM-Ti6242 joint FL with Ti6242 filler wire welded with P=4.5 kW, v=3 m/min, v_w~3.6 m/min, T_{ph}=800 °C, t_s=2.0 mm. α_2-red. β/β_O-yellow. γ-green. Confidence index ≤ 0.1-grey. Grain boundary-black. (a) As-welded and (b) heat-treated at 1290 °C for 1 h FC.

Studying the evolution of the β-phase related seam and the growth mechanism at the TNM FL, the phase orientation map of β/β_O-phase for dissimilar TNM joints preheated to 400 °C is utilized (Figure 62). Despite the differing joining partners, heteroepitaxial growth occurs at the TNM FL, as β/β_O grains with the same orientation at TNM FL are detected (Figure 62).

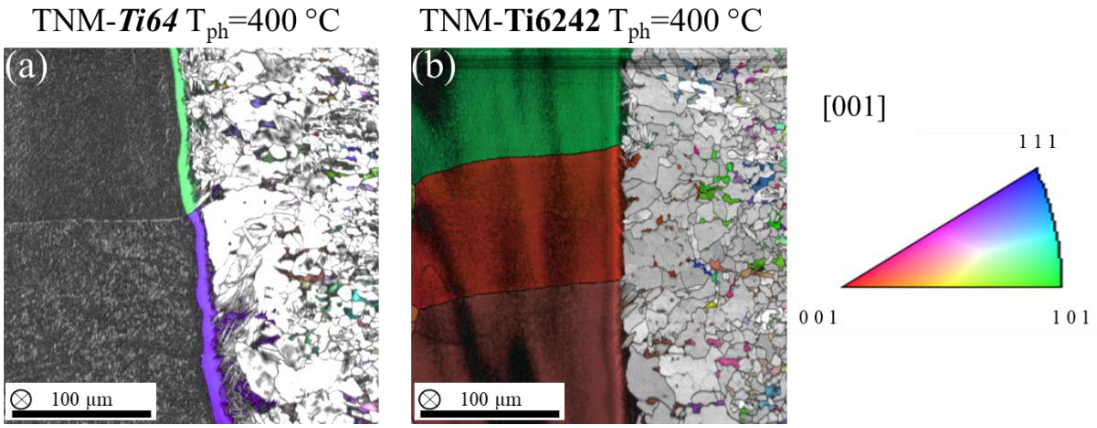

Figure 62: β/β_O-phase orientation maps of (a) dissimilar TNM-Ti64 and (b) dissimilar TNM-Ti6242 joints welded with P=4.5 kW, v=3 m/min, T_{ph}=400 °C, t_s=2.0 mm.

Due to the close crystallographic relationship between the β-, β_O-, ω_O-, ω''- and ω'-phase EBSD cannot differentiate between these phases (Chapter 2.2). Therefore, to verify if the β_O- or a ω_O-phase type is formed, XRD measurements are utilized (Figure 63).

FThe formation of a ω_O-phase type is indicated by the peak close to 22° (Figure 63 (a), blue top triangle). The slightly differing peak position could be the result of an incomplete phase transformation and varying lattice parameters. Due to the formation of ω_O-phase type particles and the high defect density (Figure 59 (c), Figure 60 (c)), a small peak broadening at the characteristic double peak position of the ω_O-phase is detected for the dissimilar TNM-Ti6242 joint preheated to 400 °C (Figure 63 (b)). The incomplete phase transformation could be caused by the high cooling rate. The ω_O-phase precursor ω'' is known to form for cooling rates $\geq$100 K/min [93]. Furthermore, locations of high defect density are detected in the image quality of EBSD measurements (Figure 59 (c), Figure 60 (c)) and the ω_O-phase has been reported to nucleate at point defects [97]. The ω_O-phase type could lead to embrittlement [99], and the locations of high defect density indicate high thermally induced stresses. Moreover, the formation of a ω_O-phase type is further supported as Nb segregations increases the growth rate of the ω_O-phase [92] and the Nb content in the FZ for dissimilar TNM-Ti6242 joint preheated to 400 °C is higher than for 600 °C (Table 16). In contrast, a peak broadening in the XRD results is absent in the dissimilar TNM-Ti6242 joint preheated to 600 °C (Figure 63 (d)). A sharper peak at this position and consistently to the phase maps and EDX micro-area analysis the α_2-phase is detected (Table 16, Figure 59 (d), Figure 63 (d) red square). Nevertheless, a small peak close to the 22° ω_O-phase position is present for the dissimilar TNM-Ti6242 joint preheated to 600 °C (Figure 63 (c)). With the results of the XRD measurements, it can be assumed that the crack formation in the dissimilar TNM-Ti6242 joint preheated to 400 °C could be due to the ω_O-phase type presence and the high defect density.

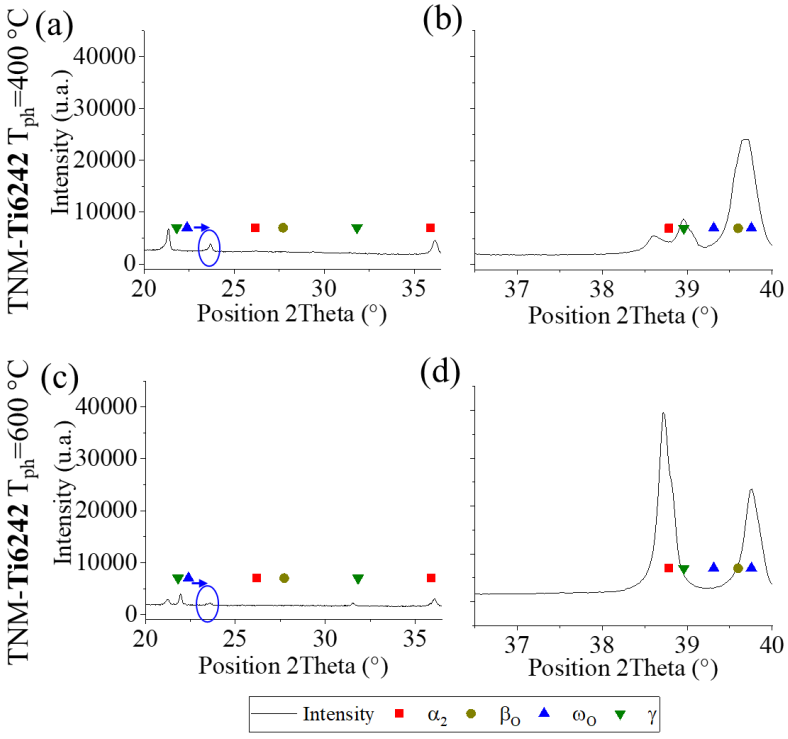

Figure 63: XRD measurements of (a)-(b) dissimilar TNM-Ti6242 joint FZ preheated to T_{ph}=400 °C, t_s=2.0 mm, (c)-(d) dissimilar TNM-Ti6242 joint FZ preheated to T_{ph}=600 °C and welded with P=4.5 kW, v=3 m/min, v_w~3.6 m/min, t_s=2.0 mm.

5.2.6. Microstructure measurements

The influence of the evolving microstructure, chemical composition and phases on the local mechanical properties were investigated by microhardness measurements. From literature it is known, that a link between the microhardness and crack-free similar TiAl-alloy joints exists [37]. Therefore, the question arises, if difference between the maximum microhardness values in the FZ between dissimilar TNM-Ti64 and TNM-Ti6242 joints occurs, which would correspond to the different phase evolutions (Chapter 5.2.5).

For dissimilar Ti64-Ti6242 joints the average microhardness in the FZ of 403±10 HV0.3 (green triangle) lies between the average microhardness values of the similar Ti64 and Ti6242 joints with 375±10 HV0.3 (black square) and 416±5 HV0.3 (red circle), respectively (Figure 64). Furthermore, a slight microhardness decrease from the Ti6242 to the Ti64 side is observed. In the FZ close to the Ti64 side a small microhardness plateau emerges. Nevertheless, the total microhardness scatter is 25 HV0.3 and referred to the average FZ microhardness less than 7 %.

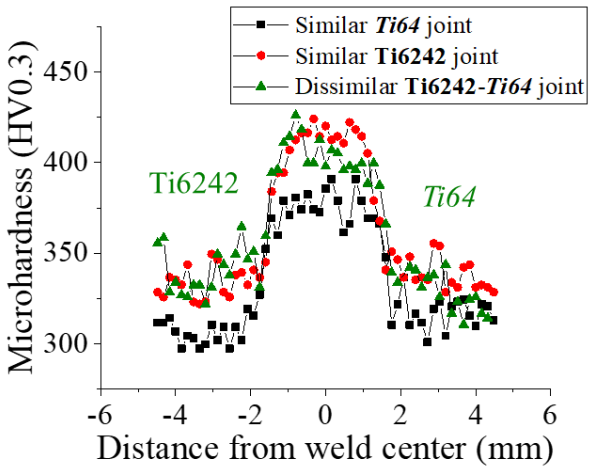

Figure 64: Microhardness profil of similar Ti64, Ti6242 and dissimilar Ti64-Ti6242 joints welded with P=4.5 kW, v=3 m/min.

Typical for all dissimilar TNM joints a characteristic microhardness increase from the BM to the FZ is measured (Figure 65). The average microhardness in the FZ decreases from 562±37 HV0.3, 506±32 HV0.3 to 438±56 HV0.3 for preheating temperatures of 400 °C (black square), 600 °C (red circle) and 800 °C (green triangle), respectively (Figure 65 (a)). To correlate the microhardness values to the evolving phases, the following points have to be considered. The ordering process from β to β_O-phase is very fast [223] and the evolution of a ω_O-phase type for a preheating temperature of 400 °C is indicated (Figure 63 (a)). Moreover, the hardness value of β_O-phase is higher than for globular α_2 [79] and for β_O+ω_O-phase even higher than for α_2 lamellas with a size between 1 and 2 µm [91,98]. Thus, the significantly higher microhardness value of the dissimilar TNM-Ti6242 joint preheated to 400 °C compared to 600 °C could be the result of the indicated presence of the ω_O-type phase in the FZ and the high defect density (Figure 59 (c), Figure 63 (a)). The microhardness value of dissimilar TNM-Ti6242 joints preheated to 800 °C (green triangle) has a value in the range for the joint preheated to 600 °C (red circle) (Figure 65 (a)). In the FZ on the Ti6242 side of the dissimilar TNM-Ti6242 joint preheated to 800 °C (green trinagle), the value decreases significantly from 528 HV0.3 to 394 HV0.3 (Figure 65(a)),

which can be attribute to microsegregations (Figure 57 (b), (e), (h)) and possibly slightly altering microstructures close to the respective FL (Figure 52 (a), Figure 53 (e)).

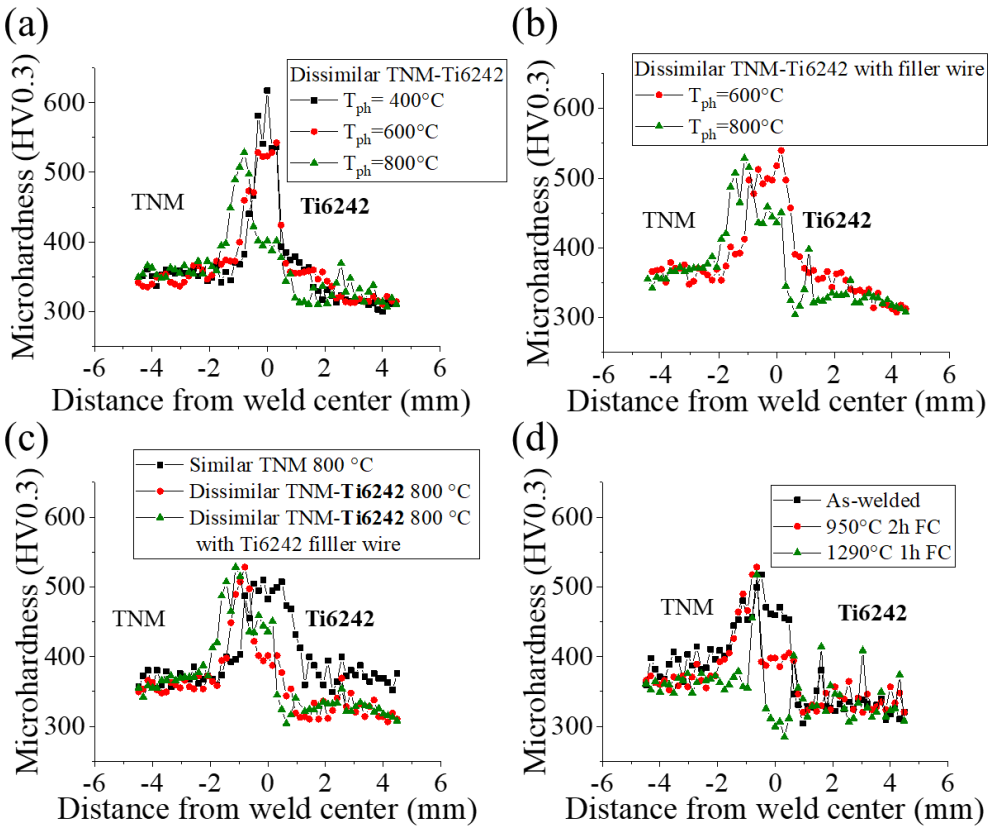

Figure 65: Microhardness measurement of dissimilar TNM-Ti6242 joints welded with P=4.5 kW, v=3 m/min. (a) Influence of preheating temperature. (b) Influence of Ti6242 filler wire v_w~3.6 m/min with different preheating temperatures. (c) Comparison of similar TNM, dissimilar TNM-Ti6242 and dissimilar TNM-Ti6242 joints with filler wire v_w~3.6 m/min. All joints preheated to T_{ph}=800 °C. (d) Influence of post-weld heat treatment. As-welded: P=4.5 kW, v=3 m/min, v_w~3.6 m/min, T_{ph}=800 °C.

As for the dissimilar TNM-Ti6242 joints without filler wire, the average microhardness of the dissimliar TNM-Ti6242 joints with filler wire decreases with the preheating temperature 600 °C (red open circle) and 800 °C (green open triangle) from 504±19 HV0.3 to 468±36 HV0.3, respectively (Figure 65 (b)). Thus, the use of filler wire with a preheating temperature of 600 °C has no influence on the average microhardness in FZ (Figure 65 (b)). Comparable to the behavior of the TNM-Ti6242 joints without filler wire preheated to 800 °C (green solid triangle), the microhardness in the FZ of dissimilar TNM-Ti6242 joints with filler wire (green open triangle) decreases from the TNM to the Ti6242 side and a microhardness plateau closer to the Ti6242 is presented (Figure 65 (b)). Reasons for this plateau can be the microsegregations (Figure 57 (c), (f), (i)) and different cooling behaviors of the FZ influenced by the thermophysical properties of the closer joining material.

For the PWHT dissimilar TNM-Ti6242 joints with filler wire preheated to 800 °C were utilized. The average microhardness values of the as-welded (black square), PWHT with 950 °C (red circle) and PWHT with 1290 °C (green triangle) dissimilar joints are 471±21 HV0.3, 430±54 HV0.3 and 345±78 HV0.3, respectively (Figure 65 (d)). Thus, for both PWTHs the average microhardness values and the values of the microhardness plateau close to the Ti6242 side decrease with increasing preheating

temperature. This indicates the activation of diffusion controlled atom migrations and grain growth. As the typical TNM heat-treatment temperature of 1290 °C is significantly higher than the β-transus temperature of Ti6242 with 995 °C, the microstructure in the FZ and the Ti6242 coarsened largely (Figure 48 (c), (f)). Thereby, the major microhardness decrease close to the Ti6242 is explained. Despite the increased scatter after PWHT, the BM microhardness values of as-welded and post weld heat-treated dissimilar TNM-Ti6242 joints with filler wire are comparable. However, some microhardness values in the FZ close to the Ti6242 side are lower than the BM microhardness, emphasizing that no second phase, which could enable the pinning effect against grain growth, is present. In the FZ on the TNM side comparable values as for the as-welded joint are measured. This leads to a sharp microhardness gradient, especially for a PWHT temperature of 1290 °C. The peak microhardness value in the FZ close to the TNM side of the joint heat-treated at 1290 °C can be explained by the presence of the β/β_O-phase penetrated with α_2-needles (Figure 61 (b), Figure 65 (d)).

Due to the different grain sizes in the α_2-phase consisting FZ (Figure 51, Figure 59) and comparable to dissimilar TNM-Ti6242 joints, the average microhardness values in the FZ of dissimilar TNM-Ti64 joints falls from 532±27 HV0.3 via 505±17 HV0.3 to 449±18 HV0.3 for the preheating temperatures of 400 °C (black square), 600 °C (red circle) and 800 °C (green triangle), respectively (Figure 66 (a)). For the preheating temperature of 800 °C (green triangle), the microhardness decreases in the FZ from the TNM side to the Ti64 side is most significantly. As for dissimilar TNM-Ti6242 joints, welded at the same preheating temperature, a microhardness plateau is present close to the Ti64 side (Figure 65 (a), Figure 66 (a)), which could be due to the slightly different chemical compositions and microstructures in the FZ. The average microhardness in the FZ of similar Ti64-Ti64 (black square), similar TNM-TNM (red circle) and dissimilar TNM-Ti64 (green triangle) joints are 375±9 HV0.3, 489±17 HV0.3 and 447±19 HV0.3, respectively (Figure 66 (b)). Therefore, the microhardness values in the FZ of the dissimilar TNM-Ti64 joint is between the microhardness of the similar joints.

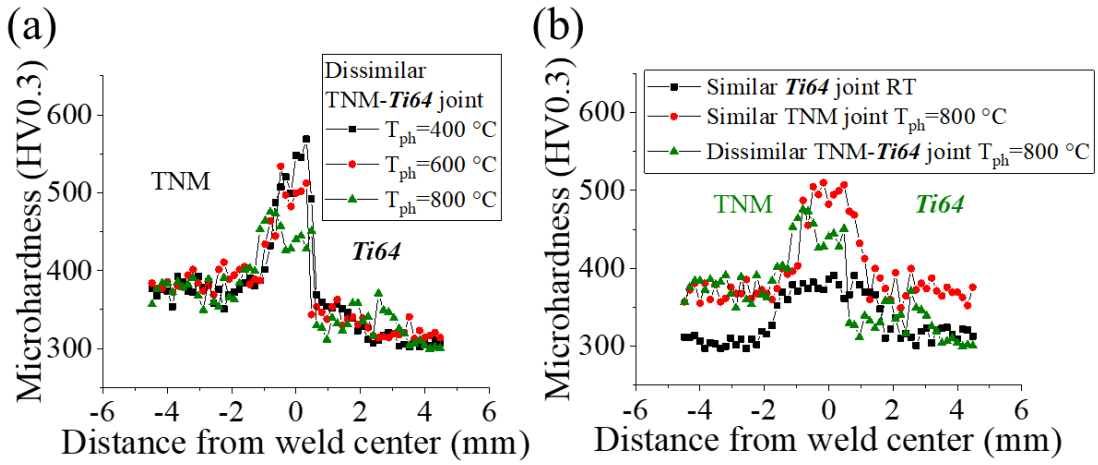

Figure 66: Microhardness measurement of dissimilar TNM-Ti64 joints welded with P=4.5 kW, v=3 m/min. (a) Influence of preheating temperature. (b) Comparison of similar Ti64 RT, similar TNM and dissimilar TNM-Ti64 joints. Similar TNM and dissimilar TNM-Ti64 joints preheated to T_{ph}=800 °C.

The indicated ω_O-type phase presence in the FZ of dissimilar TNM-Ti6242 joints preheated to 400 °C together with the high defect density (Figure 59, Figure 60, Figure 63) explains the significantly higher

peak microhardness values of 618 HV0.3 for the TNM-Ti6242 joint (red circle) compared to 569 HV0.3 for the TNM-Ti64 joint (black square) both preheated to 400 °C (Figure 67 (a)). Moreover, this also influences the average microhardness value in the FZ with 562±37 HV0.3 and 532±27 HV0.3, respectively (Figure 67 (b)). The average microhardness in the FZ decreases with the preheating temperature (Figure 67 (b)). As the same major α_2-phase for preheating temperatures higher than 400 °C is present (Figure 59) and the grain sizes are in a similar range (Figure 51), average microhardness differences for the dissimilar TNM joints are insignificantly. At preheating temperatures of 800 °C, average microhardness values of dissimilar TNM-Ti6242 (red circle) and dissimilar TNM-Ti64 joints (black square) are 438±56 HV0.3 and 449±18 HV0.3, respectively (Figure 67 (b)).

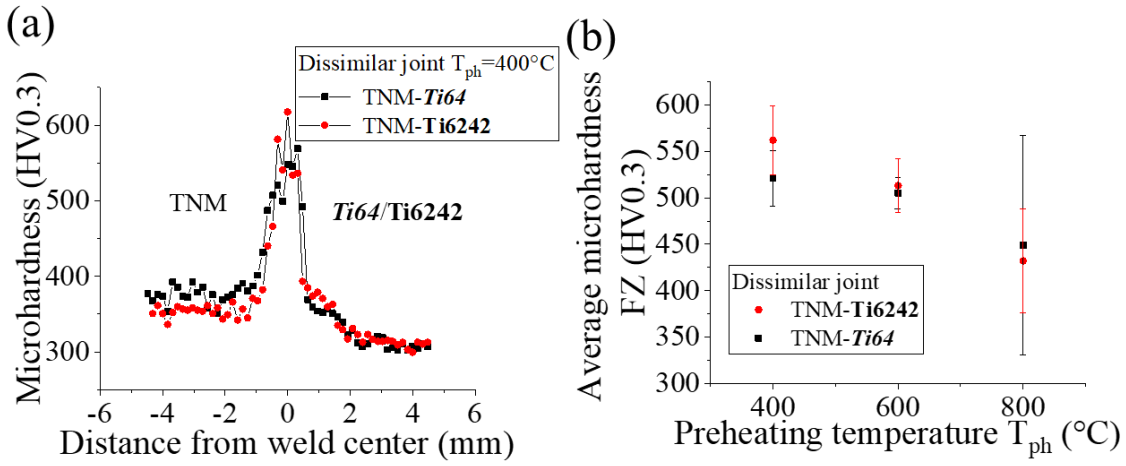

Figure 67: Comparison of microhardness measurement of dissimilar TNM-Ti64 and TNM-Ti6242 joints welded with P=4.5 kW, v=3 m/min. (a) Comparison of microhardness profiles preheated to T_{ph}=400 °C. (b) Comparison of average microhardness in FZ in dependence on the preheating temperatures.

5.3. Mechanical properties of similar and dissimilar joints

From selected LBW parameter sets, tensile specimens were processed to evaluate the influence of the evolving microstructure and phase on the tensile properties. On this behalf, for the first time similar Ti6242 joints manufactured by LBW were tested at 425 °C. Tensile results of the BM and similar joints were utilized as references for the dissimilar joints. The focus of the dissimilar TNM joints was on dissimilar TNM-Ti6242 joints and the influence of the evolving β-phase related seam on the tensile properties. As machining is an additional process step, tensile samples were first tested in the as-welded state. In case of inferior tensile properties machined tensile specimens were utilized to verify if the inferior tensile properties are due to surface roughness, weld seam imperfections or the joint properties.

5.3.1. Similar joints

Similar joints were tested at RT and their respective long-term service temperature to obtain the joint tensile properties. The fracture position was identified by visual inspection and macro camera images. Furthermore, for similar TNM joints the fracture surface was examined by SEM to attain a deeper knowledge concerning the fracture cause.

No tensile studies are available for LBW welded similar Ti6242 joints examined at 425 °C, the long-term service temperature of Ti6242 [3] (Chapter 3.5.1.). Therefore, exemplarily the characteristic tensile test curve profiles for the Ti6242 BM and two as-welded similar Ti6242 joints tested at RT and

425 °C are displayed in Figure 68. At RT necking emerges at a lower elongation for the similar Ti6242 joint welded with the higher line energy of 150 MJ/m (red curve) (Figure 68 (a)), which resulted in larger prior-β grains and a coarser martensitic microstructure (Figure 29 (e), Figure 34 (a)). This is in accordance to the results from literature, where Ti-alloys possessing coarser lamellas generally exhibit a lower strength and ductility [2]. The tensile curve of the similar Ti6242 joint welded with a lower line energy of 52.5 MJ/m (green curve), exhibiting a finer martensitic microstructure, larger underfill and slightly increased average microhardness (Figure 29 (h), Figure 34 (d)), is almost comparable to the BM curve (Figure 68 (a)). The average mechanical properties of the similar Ti6242 joint at RT with the higher line energy of 150.0 MJ/m and the lower line energy of 52.5 MJ/m reaches 98 % and 99 % of the tensile strength, 91 % and 93 % of the yield strength, 85 % and 95 % of the fracture elongation of the Ti6242 BM, respectively (Figure 68 (c), (d), (e)). At the testing temperature of 425 °C, the similar Ti6242 joint tensile curves are in the range of the BM tensile test curve (Figure 68 (b)). Comparable to necking, the decreased fracture elongation of the similar Ti6242 joint welded with the higher line energy of 150 MJ/m can be attributed to the coarser lamellas. As the fracture originates in both similar Ti6242 joints in the BM, the increased microhardness in the FZ of the weld seams acts as a shield against failure [31] and the differences in mechanical properties should be attributed to scatter.

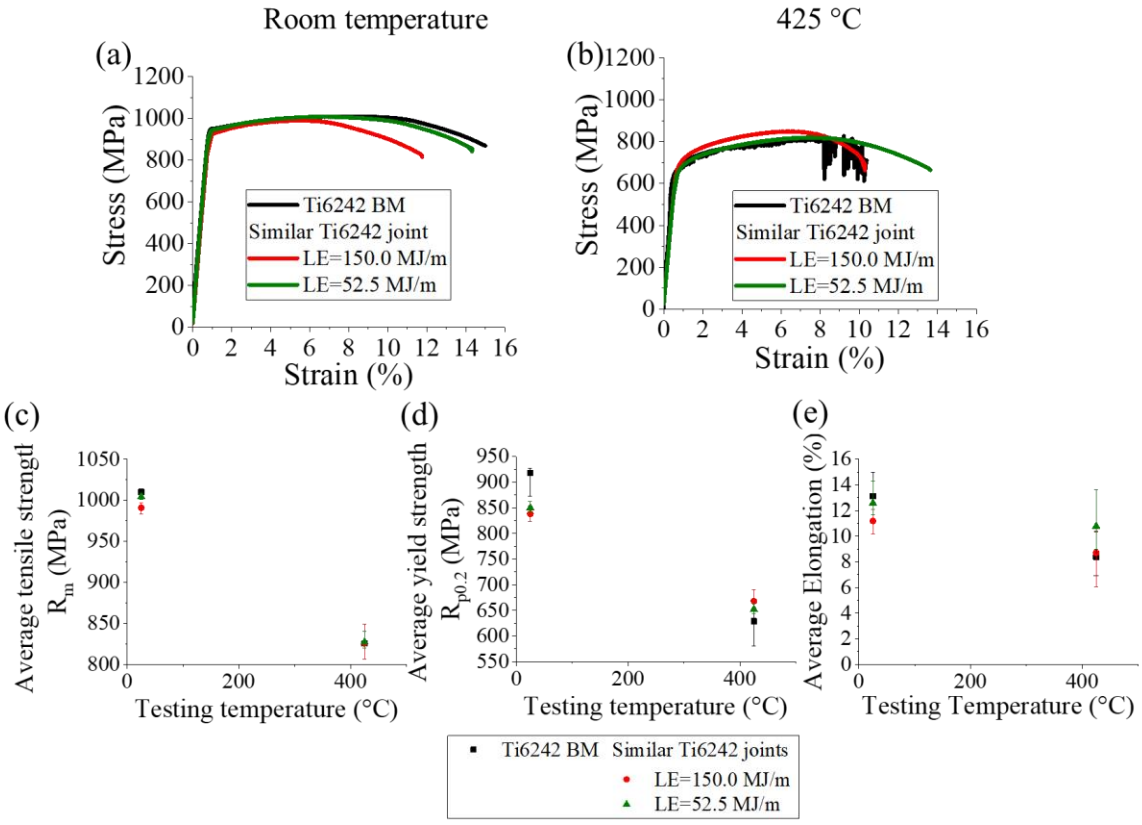

Figure 68: Exemplary tensile test curves of Ti6242 BM (black) and as-welded similar Ti6242 joints tested at (a) RT and (b) 425 °C. Average (c) tensile strength, (d) yield strength and (e) fracture elongation with maximum and minimum value of Ti6242 BM and as-welded similar Ti6242 joints dependent on the test temperature. Welding parameters (red): P=1.75 kW, v=0.7 m/min, LE=150.0 MJ/m. Welding parameters (green): P=3.50 kW, v=4.0 m/min, LE=52.5 MJ/m.

Comparable to the results at RT, at 425 °C the fracture position in the similar Ti6242 joints is located in the Ti6242 BM. Post-processing in terms of machining is not mandatory for similar Ti6242 joints to achieve tensile mechanical properties of Ti6242 BM, since ductile fracture in the BM occurred for as-welded similar Ti6242 joints at both testing temperatures. Being within deviation or close by, minor differences of mechanical properties at RT and insignificant differences at 425 °C between the as-welded similar Ti6242 joints emerge (Figure 68 (c), (d), (e)). Furthermore, the mechanical properties of Ti6242 BM and as-welded similar joints decrease with increasing testing temperature (Figure 68 (c), (d), (e)).

As post-processing is increasing the costs of a part, similar TNM joints were tested in the as-welded state (Figure 69, red). Moreover, only tensile tests with bead-on-plate TNM welds and one study with CO_2 laser beam welded similar TNM joints have been reported in literature [51,52]. At RT, for as-welded samples fracture occurred in the elastic regime so that BM values were not reached (Figure 69 (a), red line). Comparable to as-cast TNM samples, the average elongation is below 0.5 % [77] (Figure 69 (e), red circle). With an average tensile strength of 385 MPa and a maximum tensile strength of 545 MPa (Figure 69 (c), red circle), the as-cast TNM tensile strength of 600-710 MPa was not reached [77]. It should be pointed out that as-cast specimens could have been machined, since specimens were prepared according to ASTM Standard E8 [77]. In case of the as-welded similar TNM joints, possible reasons for the decrease of the mechanical properties are a sheet offset, rolling grooves and other weld seam irregularities. Mechanical properties of similar TNM joints were significantly improved by grinding the surface subsequent to LBW (Figure 69 (a), green curve, (c), (d), (e), green triangle). Fracture for grinded samples emerged in the plastic regime. Consequently, post-processing in terms of grinding is mandatory for similar TNM joints. As TNM is sensitive to changes in the thermomechanical history, the scatter of the average tensile strength, yield strength and fracture elongation of the TNM BM and the grinded similar TNM joint can be explained by the different microstructures of the tested TNM BM and the TNM weld coupon material (Figure 41 (b), (c), Figure 69 (c)-(e)). Depending on the chemical composition and microstructure the reported yield strength of TNM at RT lies between 680 MPa and 950 MPa [13]. The average yield strength of the grinded similar TNM joint is 825 MPa, which is within the reported range. In contrast to RT, at 800 °C the as-welded TNM joint fractures in the plastic regime (Figure 69 (b)). Due to the increased testing temperature the influence of a possible sheet offset, rolling grooves and other weld seam irregularities on the deformation is lower. The average tensile strength of the as-welded similar TNM joint tested at 800 °C is 376 MPa, which is close to the yield strength of 317 MPa. The reported tensile strength for CO_2 laser beam welded similar joints of casted and extruded TNM tested at 700 °C was between 296 MPa and 740 MPa [52]. The reported yield strength range at 800 °C lies between 450 MPa and 650 MPa [13]. Hence, the reduced tensile and yield strength seems not only to be attributed to the different microstructures of the TNM BM for tensile tests conducted at 800 °C, but could also be related to the fracture position. The yield and tensile strength of the TNM BM and the similar TNM joints decreases with testing temperature (Figure 69 (c), (d)). As the brittle-to-ductile temperature is exceeded, the average fracture elongation of the TNM BM and similar TNM joints is significantly increased at 800 °C to 4.5 % and 10 %, respectively (Figure 69 (e)).

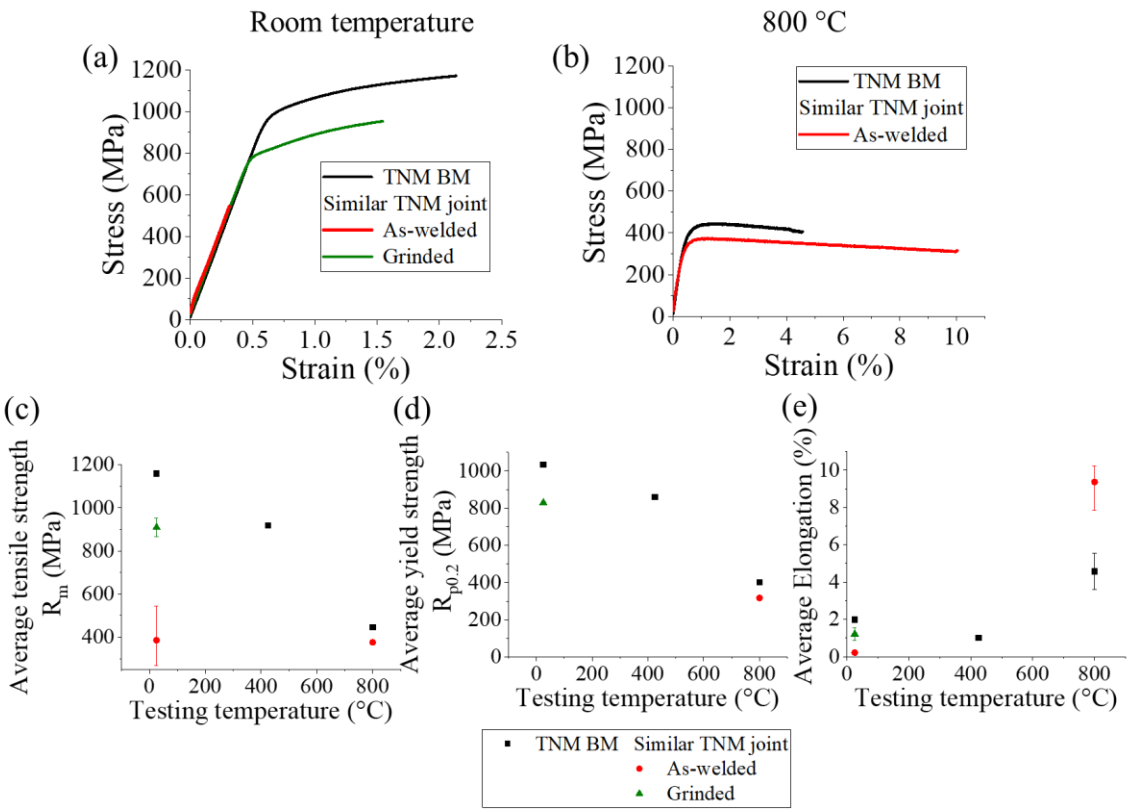

Figure 69: Exemplary tensile test curves of TNM BM (black), as-welded (red) and grinded (green) similar TNM joints tested at (a) RT and at (b) 800 °C. Average (c) tensile strength, (d) yield strength and (e) fracture elongation with maximum and minimum value of TNM BM, as-welded and grinded similar TNM joints dependent on the test temperature. Welding parameters: P=4.5 kW, v=3 m/min, T_{ph}=800 °C.

Fracture of as-welded and grinded similar TNM joints originated either in the TNM BM or the FZ at RT (Figure 70). Furthermore, a competition process between both positions seem to take place, as TiAl is sensitive to surface defects [219]. Therefore, the increased microhardness in the similar TNM joint FZ (Figure 41 (f)) could not totally prevent fracture in or closely to the mainly α_2-phase consisting FZ, since the deformation potential of the α_2-phase compared to the γ-phase is restricted to certain orientations [85]. Another possible reason for the fracture in the TNM BM of as-welded similar TNM joints and in the FZ of grinded similar TNM joints are grooves by the manufacturing process (Figure 70 (a), (b), (d)). For as-welded similar TNM joints the fracture in the FZ could be sheet-off set, rolling grooves and weld seam imperfections (Figure 70 (c)). For as-welded similar TNM joints tested at 800 °C, the fracture also occurs in the FZ close to the FL. Thus, comparable to the results at RT, the increased microhardness in the FZ no longer acts as a shielding effect as the deformation behavior of α_2 is restricted to certain orientations. This also could explain the reduced yield strength of the as-welded similar TNM joints tested at 800 °C compared to the reported values in literature.

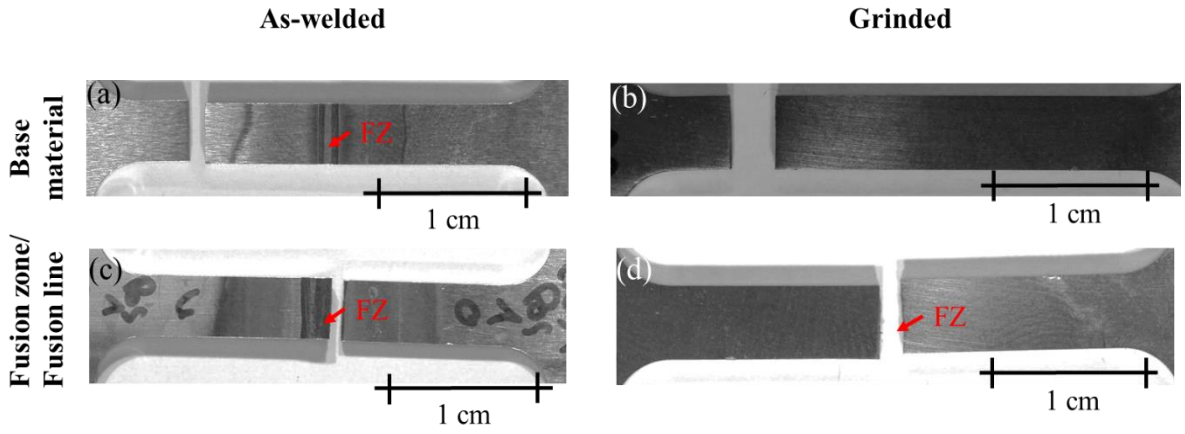

Figure 70: Fracture position of similar TNM joints tested at RT and welded with P=4.5 kW, v=3 m/min, T_{ph}=800 °C. (a), (b) Fracture in BM. (c), (d) Fracture at FZ or FL.

The fracture surfaces are further analyzed by SEM images of the as-welded similar TNM joints fractured in the FZ close to the FL at RT and 800 °C (Figure 71 (a), (b)). The same analysis is conducted for the grinded similar TNM joint tested at RT (Figure 71 (c)). The smoother surface at the corner and edges of the as-welded similar TNM joint indicated a surface defect, which could be a crack nucleus (Figure 71 (a), (b)). Therefore, the mechanical properties of the as-welded joints are influenced by these kinds of irregularities. In contrast, the corners and edges of the grinded similar TNM joint specimens are smooth and hence the measured mechanical properties are the true material-joint properties (Figure 71 (c)).

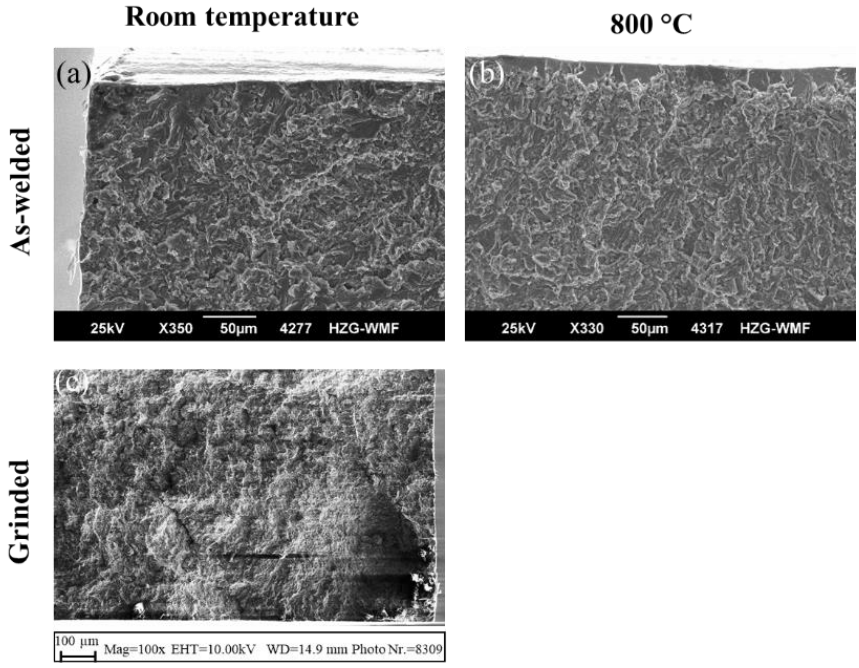

Figure 71: Fracture surface of (a), (b) as-welded and (c) grinded similar TNM tensile specimens tested at (a), (c) RT and (b) 800 °C and welded with P=4.5 kW, v=3 m/min, T_{ph}=800 °C.

5.3.2. Dissimilar joints

Dissimilar TNM-Ti6242 joints were tested at RT and their respective BM long-term service temperature. To gain further knowledge about the influence of the microstructure and phase on the fracture behavior, OM and SEM images as well as the EBSD method were used.

Exemplarily tensile test curves of as-welded dissimilar TNM-Ti6242 joints welded with (blue) and without filler wire (green) were tested at RT, 425 °C and 800 °C and compared to the BM results (Figure 72).

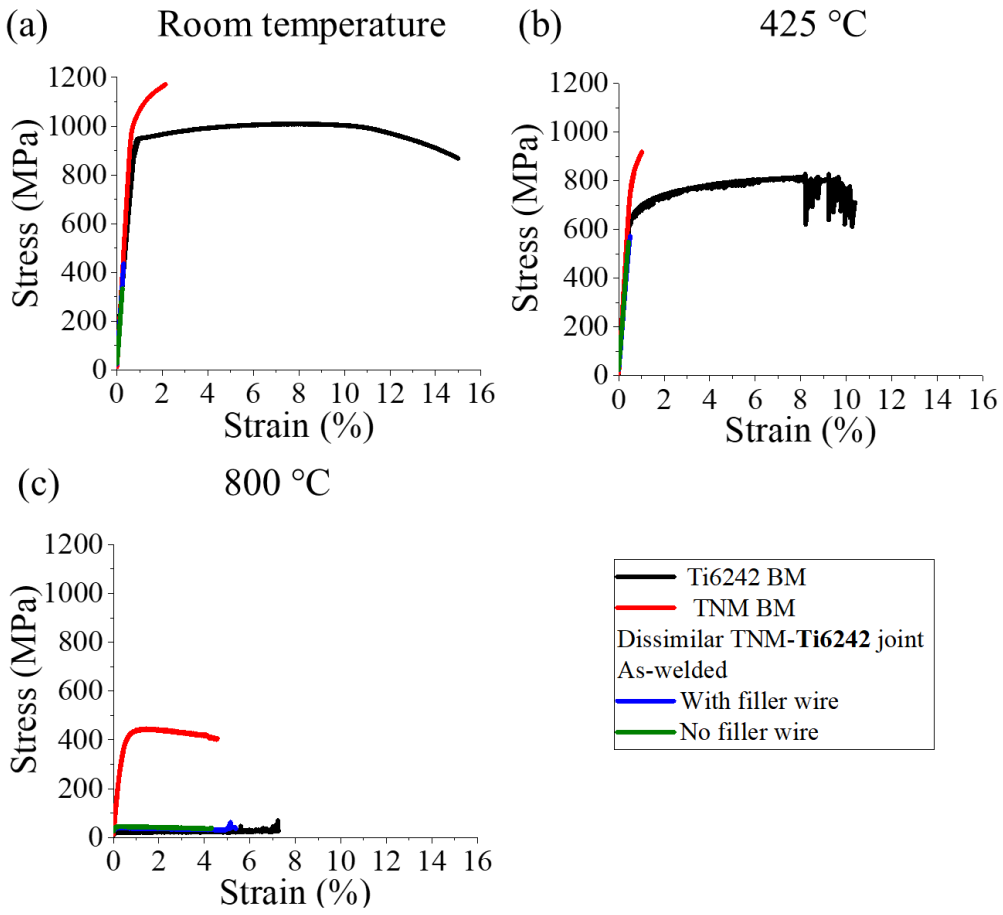

Figure 72: Comparison of exemplary tensile test curves of Ti6242 BM (black line), TNM BM (red line), as-welded dissimilar TNM-Ti6242 joints welded without (green line) and with filler wire (blue line) at (a) RT, (b) 425 °C and (c) 800 °C. Welding parameters without filler wire: P=4.5 kW, v=3 m/min, T_{ph}=800 °C. Welding parameters with filler wire: P=4.5 kW, v=3 m/min, v_w~3.6 m/min, T_{ph}=800 °C.

For tests at RT and 425 °C the mechanical properties of the as-welded dissimilar TNM-Ti6242 joints are significantly below the values of TNM and Ti6242 BM (Figure 72 (a), (b)) and consistently fracture occurs in the elastic regime. Nevertheless, the tensile strength at 425 °C is higher than at RT. Even though 425 °C is below the brittle-to-ductile temperature of TNM, the TNM deformation could be slightly increased and the contribution of the Ti6242 side to the elastic deformation of the dissimilar TNM-Ti6242 joint should be higher. Comparable to the as-welded similar TNM joints, the fracture position of the dissimilar TNM-Ti6242 joints are in the TNM BM or at the FL on the TNM side. Due to the higher fracture mechanical geometry factor, surface cracks are directly critical after formation and lead to a reduced ductility [219]. Furthermore, stepwise X-ray tomography revealed that internal

cracks are already formed at plastic strains of 0.1 % [219]. Comparable to similar TNM joints, the sheet offset, rolling grooves or other weld seam imperfections could be responsible for the fracture in the elastic regime. The hypothesis of reduced tensile properties due to surface irregularities is further supported, as for higher temperatures the failure of tensile samples was found to be the result of the formation and growth of surface cracks [219]. Moreover, the fracture position at the FL on the TNM side indicates an influence of the detected seam on the mechanical properties (Figure 60 (e), (f)). The mechanical properties of dissimilar TNM-Ti6242 joints tested at 800 °C deteriorate significantly, as the temperature is much higher than the long-term service temperature of Ti6242 (Figure 72 (c)). At that test temperature, the ductile fracture emerged on the Ti6242 side and the maximum of the mechanical properties of the Ti6242 BM were reached. Consequently, the long-term service temperature of the dissimilar TNM-Ti6242 joint is restricted to 425 °C.

The fracture surface and position of the as-welded dissimilar TNM-Ti6242 joint welded with filler wire and tested at 425 °C were further investigated by SEM and EBSD (Figure 73). The crack initiated at the edge of the sample surface (Figure 73 (a), (b), white arrows).

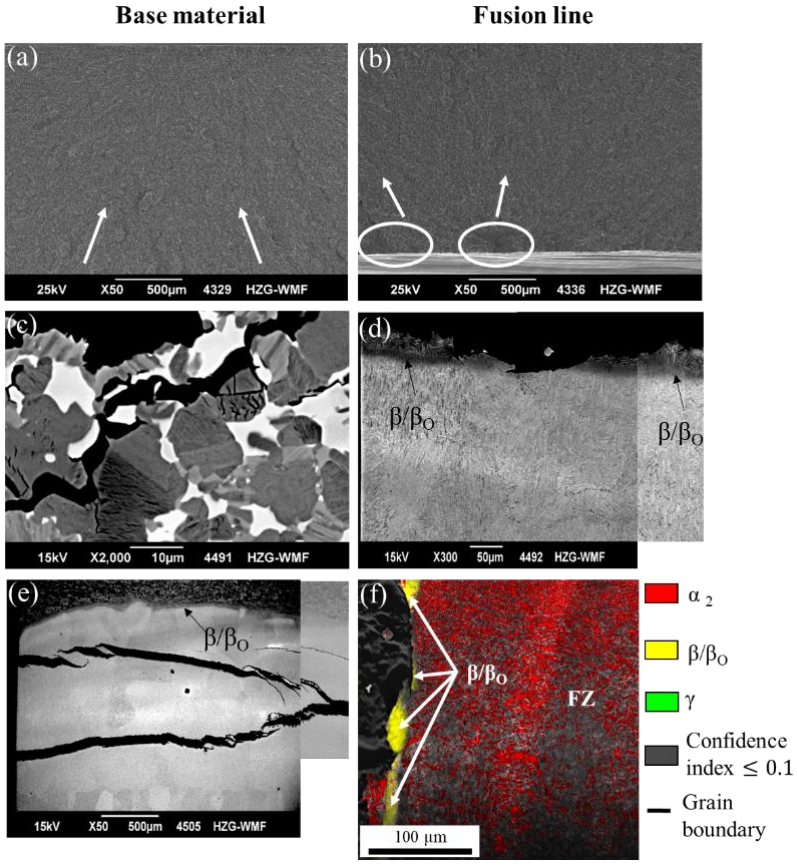

Figure 73: Fracture analysis of as-welded dissimilar TNM-Ti6242 joints welded with filler wire after tensile testing at 425 °C with different fracture positions and welded with P=4.5 kW, v=3 m/min, v_w~3.6 m/min, T_{ph}=800 °C. (a)-(e) SEM images with fracture position in the (a), (c), (e) BM and (b), (d), (f) at FL. White arrows in (a) and (b) indicate schematic crack growth direction. White ellipses in (b) area with smoother surface. (f) Phase map of SEM image in (d). α_2-red. β/β_O-yellow.γ-green. Confidence index ≤ 0.1-grey. Grain boundary-black.

For the dissimilar TNM-Ti6242 joint welded with filler wire and the fracture position at the FL, a considerable smoother sample surface at the edge is detected (Figure 73 (b), white ellipse). Hence, comparable to similar as-welded TNM joints, the sheet offset, rolling grooves or other weld seam imperfections seem to influence the mechanical properties of the as-welded dissimilar TNM-Ti6242 joint welded with filler wire. The fracture in the TNM BM for dissimilar TNM-Ti6242 joints with filler wire is along the phase boundaries, as well as inter- and trans-lamellar (Figure 73 (c)). Despite the fracture in the TNM BM, cracks in the FZ close to the TNM side were detected (Figure 73 (e)). The comparable tensile strength values of 532 MPa and 572 MPa for the fracture position in the BM and at the FL, respectively, further supports the hypothesis of a competition process between these fracture positions. The crack in the FZ is perpendicular to the loading direction and crack branching occurs (Figure 73 (e)). In contrast to Ti6242 joints [31], the increased microhardness in the FZ (Figure 65 (c)) does not provide a shielding effect and could only partly inhibit fracture in the FZ (Figure 73 (e)), since the deformation behavior of the α_2-phase is restricted to certain orientations [85]. Furthermore, as different phases with different deformation mechanisms evolve in the FZ, at the FL and in the BM strain restrictions could emerge. As crack positions vary and these are not linked to segregations [219], crack formation due to microsegregations in the FZ could be excluded (Figure 57 (c), (f), (i)). The hypothesis that the β-phase related seam influences the fracture at the FZ is verified by the SEM image and phase map (Figure 73 (d), (f)). The β-phase related seam is partly broken, indicating that a continuous seam is detrimental. As the β_O-phase -α_2-phase interface is semi-coherent [104], stress concentrations could be redistributed and peak stresses could develop. Moreover, once a crack is initiated in the β_O-phase, the crack can progress straightforward [106] and crack tips terminating in the β_O-phase are always sharp [219].

As grinding resulted in a significant improvement of the mechanical properties of similar TNM joints, further tensile tests with grinded dissimilar TNM-Ti6242 joints were conducted. 425 °C is the maximum service temperature of the dissimilar joints (Figure 72). Therefore, grinded dissimilar TNM-Ti6242 joints were tested at 425 °C (Figure 74). Tensile test curves are exemplarily shown for the TNM BM, the as-welded and grinded dissimilar TNM-Ti6242 joints (Figure 74 (a)). Through grinding, the mechanical properties of the dissimilar TNM-Ti6242 joint with (blue) and without filler wire (green), thus with continuous and discontinuous seam, improved significantly. Moreover, fracture occurs in the plastic regime. The grinded dissimilar TNM-Ti6242 joint welded with filler wire (blue dashed line) fractured at an elongation comparable to that of TNM BM. Hence, indicating a fracture connected to the TNM side, possibly due to the β-phase related seam along the FL (Figure 60). The fracture elongation of the grinded dissimilar TNM-Ti6242 joint welded without filler wire (green dashed line) is even higher. Thus, the fracture position and cause have to be further investigated. The average fracture elongation of the grinded dissimilar TNM-Ti6242 joint welded with and without filler wire reaches 36 % and 164 % of the TNM BM value (Figure 74 (b)). Thus, by grinding the dissimilar TNM-Ti6242 joints the average elongation increased in both configurations, especially for joints welded without filler wire. The significantly increased average elongation for the dissimilar TNM-Ti6242 joint could be due to the α_2 penetrated β-phase related seam. By the penetration of the β-phase related seam with α_2-needles and the fact that deformation can occur for certain α_2-phase orientations [85], local stress peaks could be relieved and the average elongation increased.

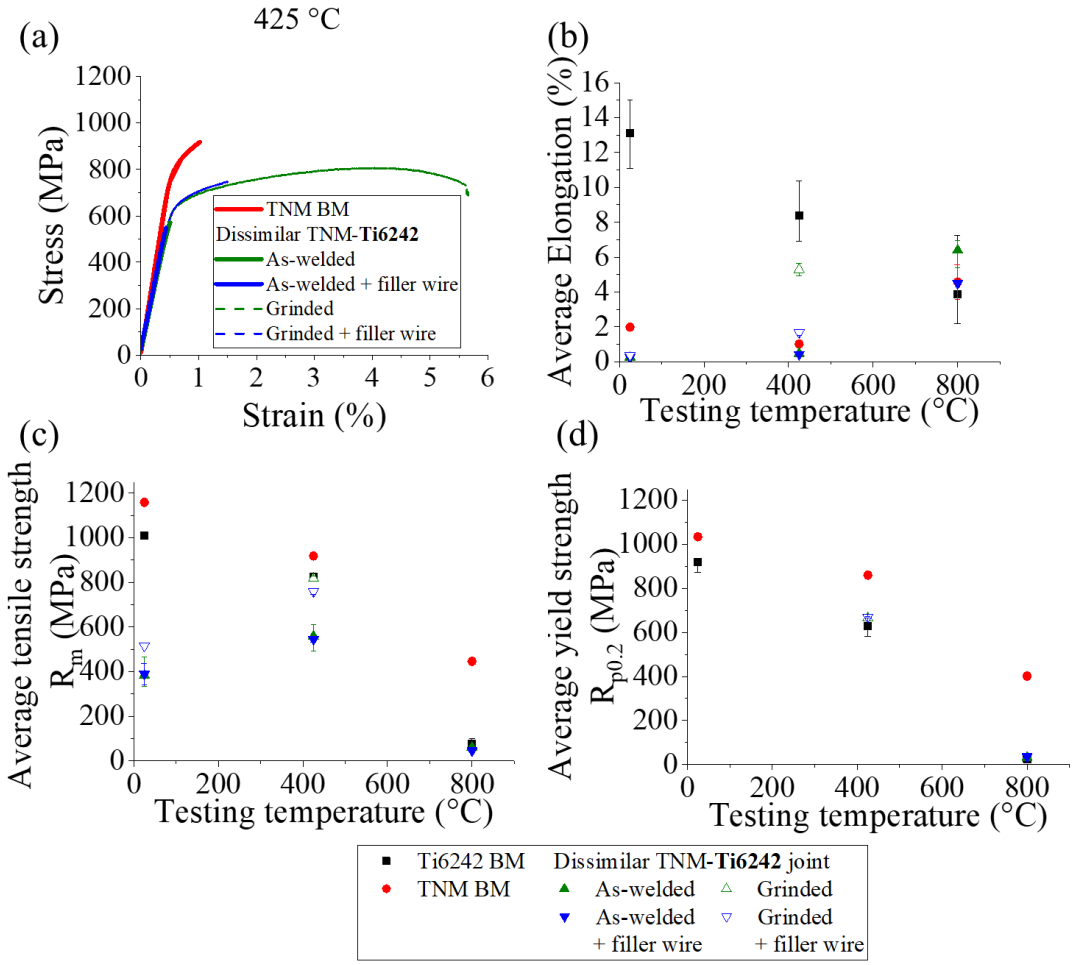

Figure 74: (a) Exemplary tensile test curves of TNM BM (red), as-welded (solid line) and grinded (dashed line) dissimilar TNM-Ti6242 joints welded with (blue) and without (green) filler wire. Average (b) elongation, (c) tensile strength and (e) yield strength with maximum and minimum value of Ti6242 BM (black), TNM BM, as-welded and grinded dissimilar TNM-Ti6242 joints welded with and without filler wire dependent on the test temperature. Welding parameters without filler wire: P=4.5 kW, v=3 m/min, T_{ph}=800 °C. Welding parameters with filler wire: P=4.5 kW, v=3 m/min, v_w~3.6 m/min, T_{ph}=800 °C.

At RT the grinded dissimilar TNM-Ti6242 joint welded with filler wire (blue open bottom triangle) exhibits a fracture elongation value of the as-welded dissimilar TNM-Ti6242 joints (green solid top triangle). This could be due to the seam hindering the relieve of local stress peaks, the reduced slip systems, the semi-coherent interface of β_O- to α_2-phase [104] and strain restrictions [85]. Nevertheless, the RT tensile strength of the grinded dissimilar TNM-Ti6242 joint welded with filler wire (blue open bottom triangle) is slightly improved compared to the as-welded joints (blue solid bottom triangle) (Figure 74 (c)). Moreover, the tensile strength of grinded dissimilar TNM-Ti6242 joints tested at 425 °C (green/blue open top/bottom triangle) almost reaches the Ti6242 BM values (black square) (Figure 74 (c)). Due to the α_2-phase penetrated β-phase related seam, the tensile strength of grinded dissimilar TNM-Ti6242 joints welded without filler wire (green open top triangle) could be slightly higher than for the grinded dissimilar TNM-Ti6242 joint welded with filler wire (blue open bottom triangle) (Figure 74 (c)). For very low fracture elongations (Figure 74 (b)), the yield strength at RT and 425 °C cannot be determined (Figure 74 (d)). In contrast, both grinded dissimilar TNM-Ti6242 joints reach the yield strength of the Ti6242 BM at 425 °C (green/blue open top/bottom triangle) (Figure 74 (d)).

Hence, grinding is also mandatory for the dissimilar TNM-Ti6242 joints. It is indicated that the continuous seam is still detrimental to the RT mechanical properties. Moreover, the α_2-phase penetrated β-phase related seam seems to be beneficial for the mechanical properties of grinded dissimilar TNM-Ti6242 joints.

To investigate the influence of the seam further, the fracture position of the grinded dissimilar TNM-Ti6242 joints tested at 425 °C was analyzed (Figure 75).

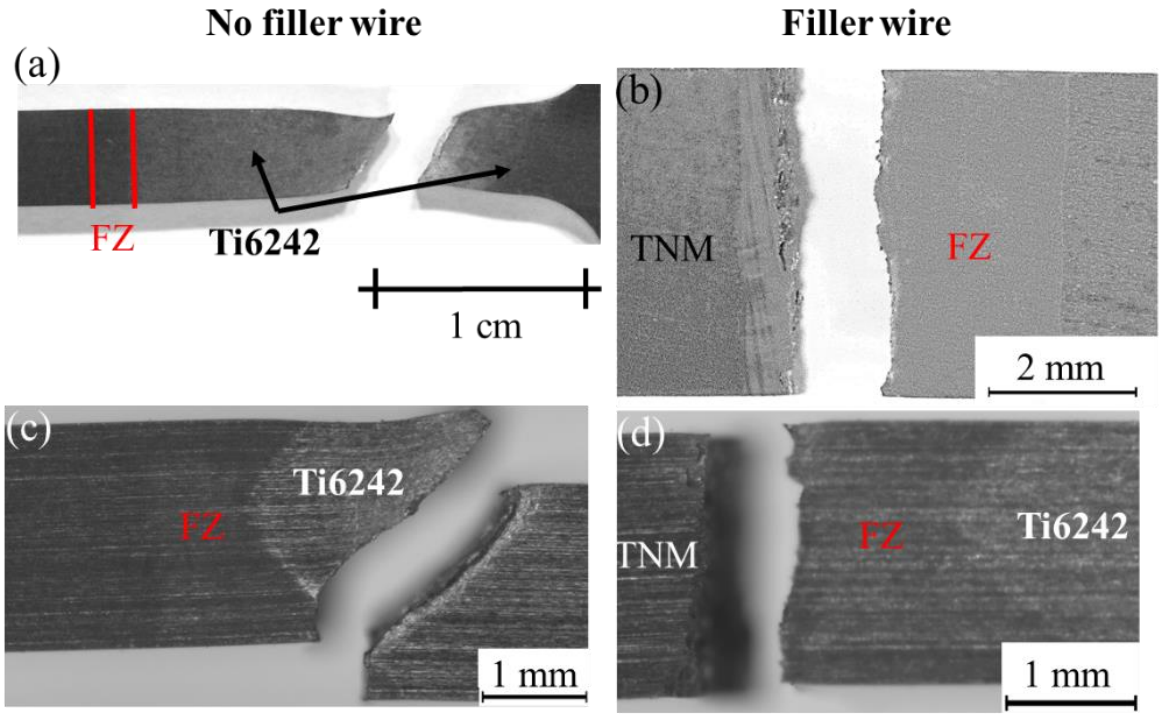

Figure 75: Fracture position of grinded dissimilar TNM-Ti6242 joints welded (b), (d) with and (a), (c) without filler wire tested at 425 °C. Welding parameters: P=4.5 kW, v=3 m/min, v_w~3.6 m/min, T_{ph}=800 °C.

As indicated by the different fracture elongations, the fracture positions of the grinded dissimilar TNM-Ti6242 joints welded with and without filler wire differ. Without filler wire the fracture originated on the Ti6242 side (Figure 75 (a), (c)), either in the Ti6242 BM (Figure 75 (a)) or in the Ti6242 BM and partly in the FZ (Figure 75 (c)). Thus, the stresses are relieved by plastic deformation of the Ti6242 BM. Consequently, the deformation is conducted by the Ti6242 side of the grinded dissimilar TNM-Ti6242 joint welded without filler wire. As the tensile strength of the Ti6242 BM at 425 °C is lower than the TNM BM tensile strength (Figure 74 (c)), fracture occurred at the Ti6242 side of the dissimilar joint. In contrast, as an X-shaped weld seam in dissimilar TNM-Ti6242 joints welded with filler wire emerge (Figure 46 (h)), a broken seam in the grinded dissimilar TNM-Ti6242 joint welded with filler wire could be responsible for the fracture of the FZ close to the TNM side (Figure 75 (b), (d)). Supporting this hypothesis further is the partly broken continuous seam in the as-welded dissimilar joint (Figure 73 (f)). Another possibility is that the β-phase related seam hinders the stress concentrations, peak stresses evolve close to the FL, which cannot be reduced by deformation on the TNM side. As the hardness of the β/β_O-phase is higher than of the α_2-phase with a lamellar size of 1-2 µm [98], and the hardness further increases by the presence of the ω_O-phase [91], the β-phase related seam is expected

to have a higher tensile strength than the FZ consisting of the α_2-phase. Nevertheless, the fracture of the FZ close to the FL could be the result of sharp crack tips in the β_O-phase [219] and straightforward propagating cracks in β/β_O-phase [106]. Cracks in the FZ close to the β-phase related seam could be responsible for the fracture, since for as-welded dissimilar TNM-Ti6242 joints welded with filler wire these have been detected (Figure 73 (e)). Moreover, weld seam irregularities could initiate the crack formation.

The fracture position at the FL of the grinded dissimilar TNM-Ti6242 joint welded without filler is further investigated by SEM images (Figure 76). The Ti6242 fracture surfaces show a honeycomb structure typical for ductile deformation (Figure 76 (a)). In contrast, the fracture surface in the FZ is considerable smoother and terrace structures occur. Furthermore, as porosity was found to be detrimental on the tensile properties of similar Ti6242 joints at RT [32], a micropore close to the FL of the Ti6242 side and the weld seam root, with a pore diameter of 11 µm (Figure 76 (b)), could have caused the partly fracture in the FZ.

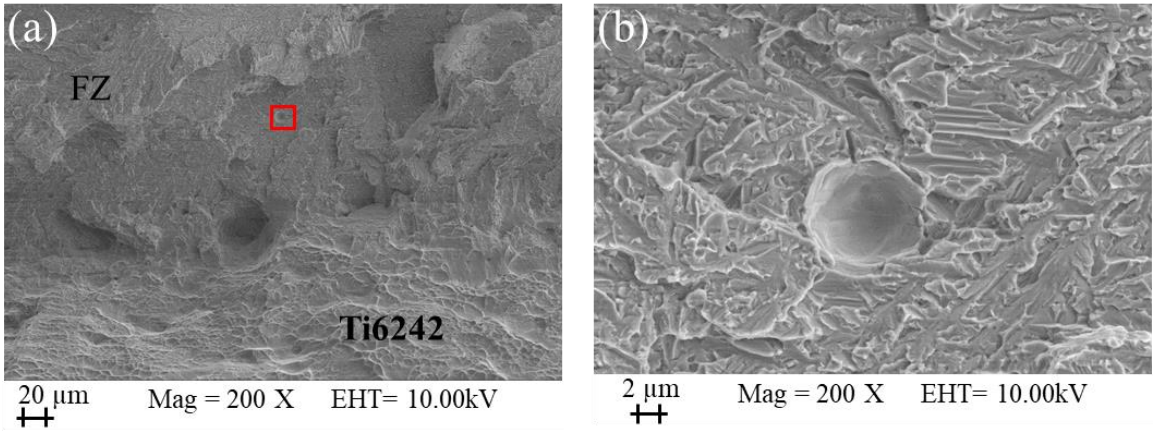

Figure 76: Fracture analysis by SEM of the dissimilar TNM-Ti6242 joint with the fracture position in the FZ and Ti6242 BM tested at 425 °C of Figure 75 (c) welded with P=4.5 kW, v=3 m/min, T_{ph}=800 °C. (a) Overview of fracture surface. (b) Close-up of red square in (a).

Summing up, grinding the surfaces of similar and dissimilar TNM joints is mandatory to obtain the material properties. Furthermore, a continuous seam is detrimental on the tensile properties. In contrast, by a discontinuous seam a higher tensile strength, fracture elongation and a favorable fracture position on the Ti6242 side of the dissimilar TNM-Ti6242 joint are achieved.

6. Comparison of dissimilar joints by laser beam welding and laser metal deposition

As similarities between LBW, laser metal wire deposition (LMwD) and laser metal powder deposition (LMpD) occur (Chapter 3.2), the investigation in terms of knowledge transferability from LBW to the two LMD processes is justified. Thereby, the present thesis is extended and the relevance of the gained knowledge by LBW is emphasized. For this purpose, in this chapter it is verified to what extent the gained knowledge of the previous chapters concerning the microstructure and phase evolution as well as crack formation for dissimilar joints can be transferred from LBW to the two LMD processes.

Due to the differing preferred laser modes, keyhole mode for LBW and conduction mode with a defocused laser beam for LMD [58], some theoretical considerations have to be taken into account. To consider the different laser modes and laser-optic systems used for LBW, LMwD and LMpD, a scaling factor for the laser power is introduced. This scaling factor is the ratio of the utilized laser beam diameter and the focused laser beam diameter. In this estimation, the different heat conduction directions (Figure 10) as well as shielding effects by the metal-vapor cloud, laser irradiation scattering and reflection at the filler material are neglected. To determine whether the 2D or 3D Rosenthal equation is suitable for calculating the theoretical cooling rate for the LMD processes, τ is calculated according to Equation 8 (Figure 77 (a), Chapter 3.3). For $\tau<0.6$ the 2D Rosenthal equation and for $\tau>0.9$ the 3D Rosenthal equation is considered (Chapter 3.3). For the LMwD process the 2D Rosenthal equation can be utilized, while for the LMpD process most values are in the intermediate or 3D Rosenthal regime. Applying the second criteria for choosing the Rosenthal equation, that the lower calculated value should be taken, the theoretical cooling rates by the 2D and 3D Rosenthal equation are calculated for the LMpD process, (Figure 77 (b)). Only for very small energy per surface values (Equation (4)), the theoretical cooling rate of the 3D Rosenthal equation is lower than for the 2D Rosenthal equation. Therefore, it is valid to utilize the 2D Rosenthal equation for the LMpD process and enabling the comparison of the three processes.

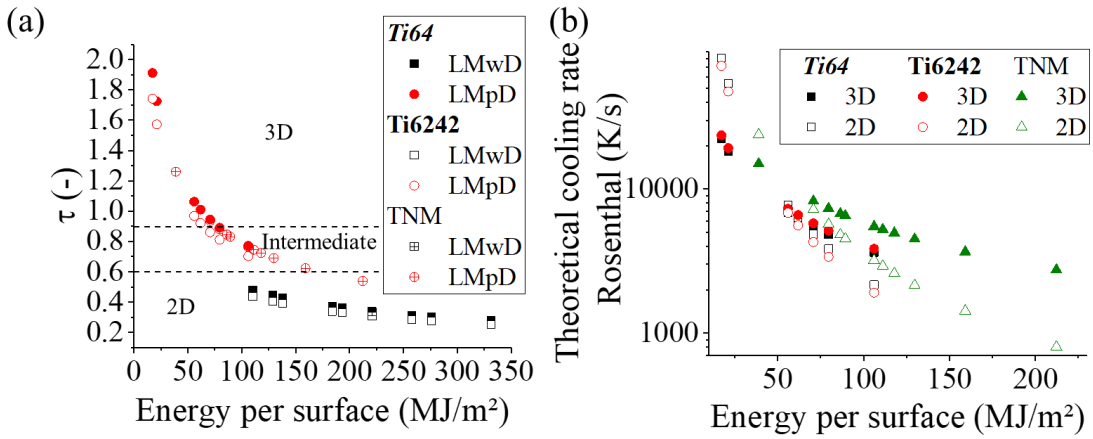

Figure 77: (a) Evaluation of appropriate Rosenthal equation for LMwD and LMpD with different utilized energies per surface and materials by equation (8). (b) Theoretical cooling rates according to the 2D and 3D Rosenthal equation (6), (7) for LMpD and different Ti-alloys depending on the energy per surface.

Concerning the LMD processes, to obtain a sufficient bonding between substrate and deposited layer, the development of a dilution zone, the FZ part located in the substrate, is mandatory. Besides, the theoretical cooling rate, the surface-to-volume ratio (A/V-ratio) can be applied to differentiate between the three processes. As the surface for LBW the toe and root surface, for LMwD the filler wire surface and for LMpD the particle surface is utilized. The volume utilized in the calculation of the A/V-ratio is the same in all processes and equals 0.5 mm^3. For a typical LBW weld seam width of 1.8 mm the A/V-ratio is 1 m^{-1}. The Ti6242 filler wire diameter is 0.8 mm and thus the A/V-ratio 5 m^{-1}. Calculating the A/V-ratio for the LMpD process the two different powder grain size distributions for Ti6242 powder and TNM powder have to be considered. Hence, the A/V-ratio is 200 m^{-1} and 100 m^{-1} for Ti6242 and TNM powder, respectively. Comparable energy amounts for melting, theoretical cooling rates, microstructures, probability of alloy element vaporization and microhardness values are expected for LBW and LMwD, as these have A/V-ratios in the same order of magnitude. In contrast, due to the one order of magnitude higher A/V-ratio for LMpD, smaller energy amounts for melting, a higher theoretical cooling rate, a finer microstructure, a higher probability for alloy element vaporization and higher microhardness values could occur.

6.1. Transferability from dissimilar Ti-Ti-alloy joints to depositions

In a first step, the transferability to dissimilar Ti-Ti-alloy joints was evaluated. As the thermophysical properties are close by (Table 3) and no cracks or a second phase at the interface of dissimilar LBW Ti64-Ti6242 joints were detected (Chapter 5.2.), no major challenges regarding the transferability of the evolving microstructures and phases were expected.

6.1.1. Process characteristics, laser metal deposition characteristics and microstructure analysis

The three laser-based processes were compared by their laser power, process velocity and theoretical cooling rate to classify the processes and attain a sustained expectation concerning the transferability. LMD characteristics were analyzed by radiography and cross-section images. Cross-section characteristics as FZ, HAZ size and the FZ/HAZ ratio were utilized to compare the processes further.

For a first simple classification of the processes the laser power and process velocity of crack- and macropore-free parameter sets are displayed (Figure 78 (a)). Laser defocusing and the filler material amount of LMD processes are neglected. Typical laser powers of LBW and LMwD are in the same range, which corresponds to the same order of magnitude of the A/V-ratio. As the LMwD process is executed in the conduction mode, hence defocusing, smaller process velocities can be applied. Due to the smaller powder grain size compared to the filler wire diameter and the higher A/V-ratio, to deposit Ti6242 powder smaller laser powers are necessary. The process velocities of LMwD and LMpD are in the same range, as the conduction mode by a defocused laser was utilized. As a correlation between the energy per surface and the theoretical cooling rate exists, the theoretical cooling rate decreases with increasing energy per surface values (Figure 78 (b)). For LMpD the theoretical cooling rate is higher and the energy per surface smaller than for the other two processes. This corresponds to the higher A/V-ratio. Despite the different laser modes, LBW and LMwD have similar theoretical cooling rates and energy per surface values. Hence, for LBW and LMwD comparable microstructures and phases are assumed to evolve, while a finer microstructure or even a different phase could evolve in the LMpD

process. Furthermore, due to different microstructures or phases, the local mechanical properties could differ.

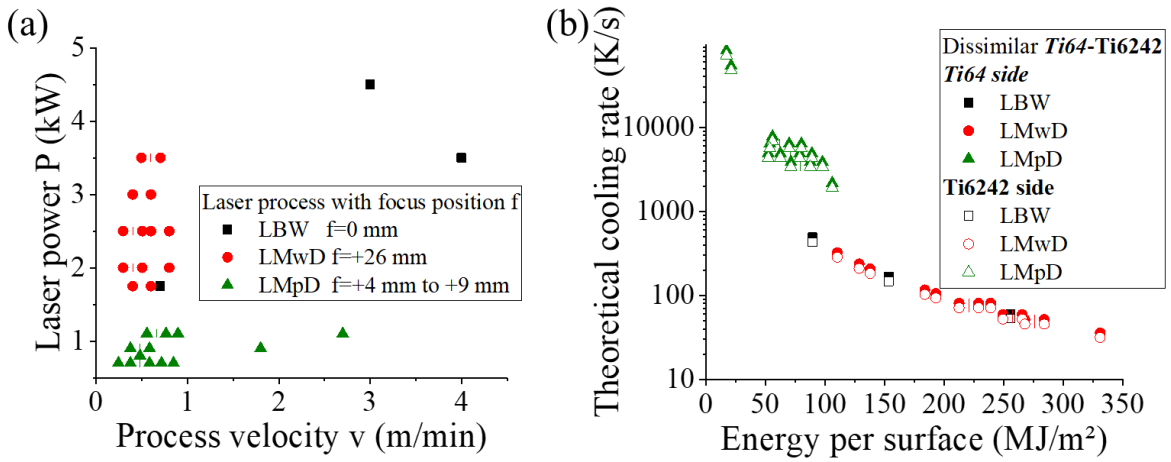

Figure 78: (a) Laser power and process velocity of crack- and macropore-free LBW, LMwD and LMpD parameter sets of dissimilar Ti64(s)-Ti6242(w/p) joints and depositions. (b) Theoretical cooling rates according to the 2D Rosenthal equation (6) calculated with the effective laser power and correlated to the energy per surface values of dissimilar Ti64(s)-Ti6242(w/p) joints and depositions.

Typical defects of Ti-alloy depositions with the parameter sets of Table 17 are shown in Figure 79. Macropores and line porosity can emerge in LMwD with pore sizes between 0.17 mm and 1.0 mm (Figure 79 (a)). These results are comparable to the results for the similar Ti6242 joints welded with filler wire, for which pore sizes between 0.13 mm and 0.97 mm were detected. Here, porosity is predominantly formed due to high power intensities [142,147], which leads to overheating of the melt and entrapping of pores. Thus, the same pore formation mechanism for LBW and LMwD can be assumed. As the amount of porosity increases at the end of the deposition, pore formation due to overheating is the most likely mechanism. Macropore- and line porosity-free dissimilar Ti64-Ti6242 joints and LMwD depositions were only achieved for decreased line energies or laser powers (Figure 79 (g), (f), (i)). Hence, pore formation because of oxidized Ti6242 filler wire can be excluded. Another typical defect of LMwD is that caused by a too high filler wire velocities for the utilized laser power and process velocity, the filler wire no longer can be molten, is fed to a solidified melt pool and fractures (Figure 79 (d)). In contrast to LMwD, no macropores in LMpD depositions are detected (Figure 79 (b), (e), (h)). In spite of the good weldability of Ti-alloys [71], for a few similar Ti-alloy LMpD depositions cracks emerged (Figure 79 (h)). The crack is located in an area with decreased amount of deposited material, indicating a higher cooling rate compared to the surrounded deposit. Therefore, it can be assumed that the different cooling rates lead to stresses in the deposit, which resulted in crack formation. Consequently, a uniform feeding rate is essential for a homogeneous outer appearance and the deposition of a sound layer.

Table 17: Parameter sets of investigated radiography images of dissimilar Ti-Ti-alloy depositions. LMwD: f=+26 mm. LMpD: f=+8 mm, N_{gas}=4 l/min.

Parameter set	Process	P (kW)	v (m/min)	v_w (m/min)	R (rpm)	Cgas (l/min)
5	LMwD	3.5	0.6	6.0	-	-
6		4.0	0.6	12.0	-	-
7		2.0	0.4	2.5	-	-
8		3.0	0.4	2.5	-	-
11	LMpD	1.1	0.66	-	2	2
12		1.1	0.66	-	4	2
13		0.7	0.48	-	6	5

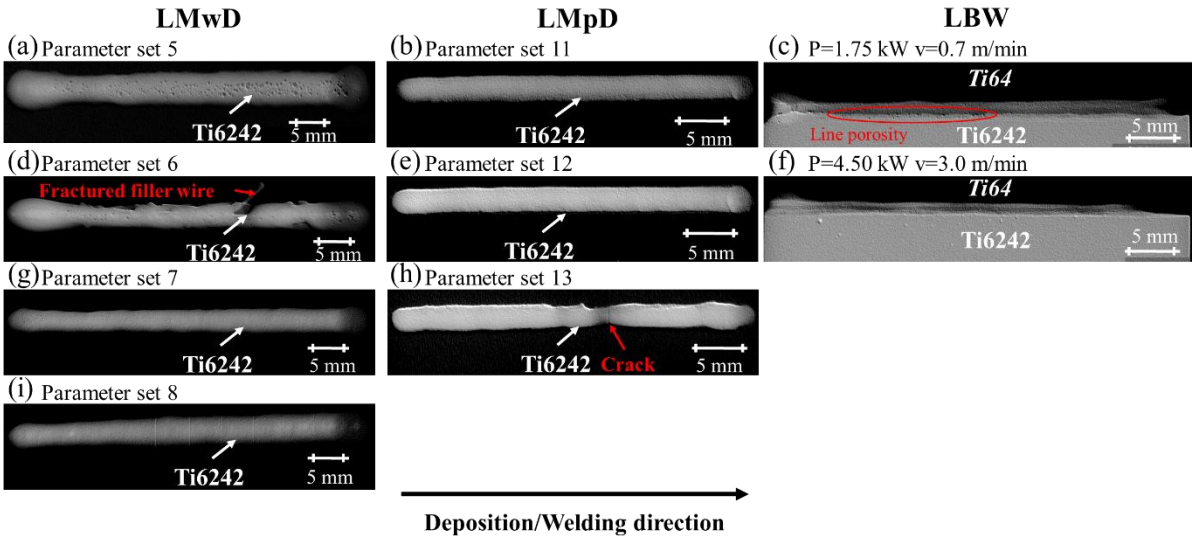

Figure 79: Radiography images of (a), (d), (g), (i) LMwD and (b), (e), (h) LMpD dissimilar Ti64(s)-Ti6242(w/p) depositions and (c), (f) LBW dissimilar Ti64-Ti6242 joints.

Comparing the cross-sections obtained by the parameter sets of Table 18, different evolving FZ shapes and microstructures, especially prior β-grain sizes, are revealed (Figure 80). For the LMwD process only one shape evolves, while three characteristic shapes can evolve for the LMpD process (Figure 80). The LMpD flat shape has the largest contact angle 141° and highest dilution (Figure 80 (d)). In contrast, the LMpD droplet has the smallest contact angle 81°, greatest height and the maximum width does not correspond to the width at the substrate (Figure 80 (e)). Thus, the danger for a lack of bonding arises. Between these two shapes, a LMpD half-circle shape with a medium contact angle can evolve (Figure 80 (f)). In the LBW process the length growth of the prior β-grains is restricted at the center line as these encounter each other there (Figure 10). Comparing the prior β-grain width and length of the three processes, as expected from the theoretical cooling rates (Figure 78 (b)), the average prior β-grain width of the LBW and LMwD processes overlap (Table 19). Furthermore, despite of the smaller theoretical cooling rates for LMpD compared to LBW (Figure 78 (b)), some overlap between the prior β-grain size of the LBW and LMpD process occurs for similar energy per surface values (Table 19). Hence, the influence of the energy per surface value should not be neglected. Due to a certain cooling effect of the

shielding and powder carrier gas, higher cooling rates could be obtained in the outer half of the deposition, leading to the smaller prior β-grains for LMwD and LMpD at this position (Figure 80 (b), (d), (e)). Moreover, for LMpD the powder particles also could have been molten shortly before solidification.

Table 18: Parameter sets of investigated cross-sections of dissimilar Ti-Ti-alloy depositions. LMwD: f=+26 mm. LMpD: f=+8 mm, N_{gas}=4 l/min.

Parameter set	Process	P (kW)	v (m/min)	v_w (m/min)	R (rpm)	Cgas (l/min)
7	LMwD	2.0	0.4	2.5	-	-
9		1.75	0.6	2.5	-	-
10		3.5	0.6	3.5	-	-
11	LMpD	1.1	0.66	-	2	2
14		1.1	0.66	-	6	3
15		0.9	2.7	-	6	3

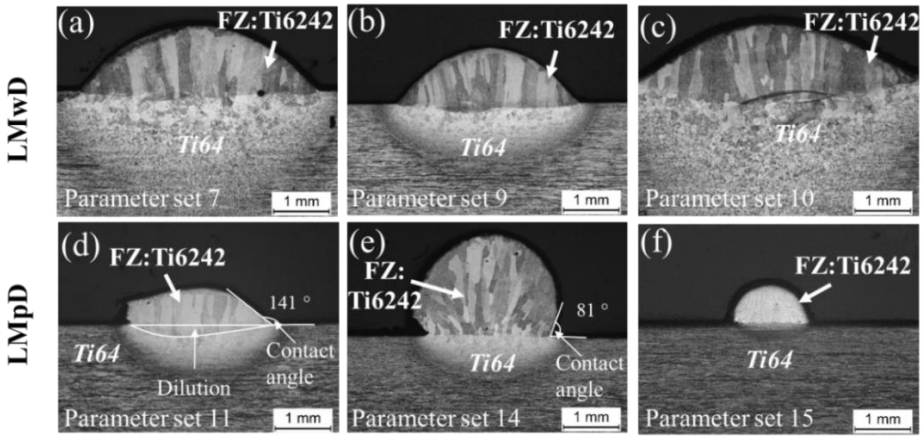

Figure 80: Cross-sections of (a)-(c) LMwD and (d)- (f) LMpD dissimilar Ti64(s)-Ti6242(w/p) deposition.

Table 19: Prior β-grain sizes of investigated dissimilar Ti64-Ti6242 joints and depositions of Figure 45 and Figure 80.

Process	Prior β-grain width (mm)	Prior β-grain length (mm)
LBW	0.06-0.16	0.2-0.55
LMwD	0.12-0.17	0.64-0.87
LMpD	0.05-0.1	0.32-0.5

The area of the FZ and the HAZ are measured in the cross-sections to further compare the processes. Here, the amount of filler material fed in the LMD process is included in the measured area of the FZ. Due to smaller deposition rates for LMpD [58], the area of the FZ is smaller than for LBW and LMwD (Figure 81 (a)). Nevertheless, for energy per surface values between 75 MJ/m^2 and 150 MJ/m^2, a section with similar FZ sizes emerge, indicating comparable filler material amounts fed to the melt pool. Despite the possibility in LBW to conduct heat in two directions and the limitation in LMD to one direction (Figure 10), the HAZ of the LMpD process is smaller than for the LBW and LMwD process

(Figure 81 (b)). This can be attributed to the smaller laser powers utilized in LMpD (Figure 78 (a)). The ratio of total FZ and total HAZ can be seen as an indicator for the effectiveness of the utilized process (Figure 81 (c)). As the LMpD process has the highest ratios, the energy input seems to be most effectively utilized to melt the powder and build-up the deposition.

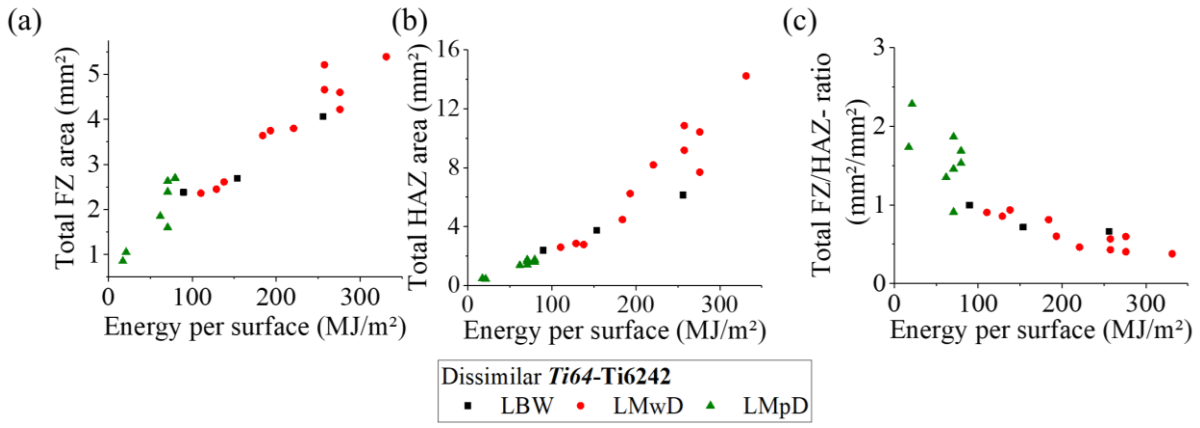

Figure 81: Correlation of dissimilar Ti-Ti-alloy joint and deposition characteristics to corresponding energy per surface values. (a) Total FZ. (b) Total HAZ. (c) Ratio of total FZ to total HAZ.

For further microstructural analysis, SEM images are utilized (Figure 82). Due to the comparable theoretical cooling rates of LBW and LMwD (Figure 78 (b)) and the knowledge regarding the LBW microstructural development (Figure 82 (e)), a martensitic microstructure for the LMwD sample is expected. As LMpD encounters the highest theoretical cooling rates (Figure 78 (b)), probably an even finer martensitic microstructure can be attained. SEM images of the FZ reveal a martensitic microstructure for all three processes (Figure 82). The overall size of the needles seems to be comparable, with slightly more areas with broader needles for the LMwD than the LMpD process (Figure 82 (a), (b) red ellipse, (c), (d)). These could be the result of the lower theoretical cooling rates of the LMwD process. The major and minor axis of the evolving martensitic microstructure of the investigated dissimilar Ti64(s)-Ti6242(p/w) depositions are displayed in Table 20. Thus, as excepted the LMpD microstructure is finer than for LMwD.

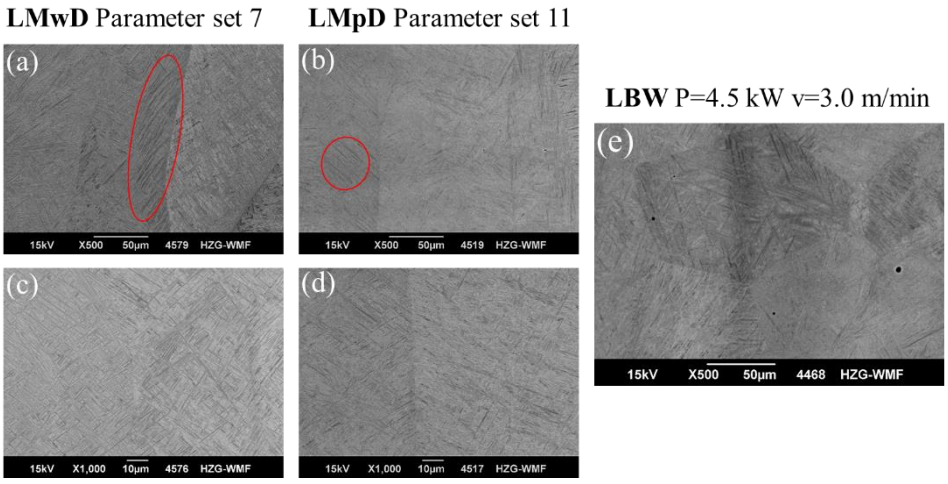

Figure 82: SEM images of FZs of (a), (c) LMwD, (b), (d) LMpD dissimilar Ti64(s)-Ti6242(w/p) depositions and (e) LBW dissimilar Ti64-Ti6242 joint. Red ellipse: Exemplry areas with broader needles.

Table 20: Grain diameter major and minor axis of dissimilar Ti64(s)-Ti6242(p/w) depositions of Figure 82 (a)-(d) obtained by the EBSD method.

Process	**Grain diameter major axis d_{max} (µm)**	**Grain diameter minor axis d_{min} (µm)**
LMwD	8.17±2.52	1.39±0.37
LMpD	4.31±1.58	1.15±0.31

As supposed from the LBW dissimilar Ti64-Ti6242 joints (Figure 83 (c), (f)), no seam along the FL, thus the dissimilar interface, is formed in the LMwD and LMpD process (Figure 83 (a), (b)). Vortexes emerge in the FZ close to the Ti64 substrate, indicating the mixture of the two alloys and possible segregations. Similar to the LBW process (Figure 83 (c), (f)), prior β-grains belong to the FZ and HAZ are present (Figure 83 (a), (b)), indicating heteroepitaxial growth for both LMD processes. Needles are even growing across the FL (Figure 83 (d), (e), red ellipse). Thus, it can be concluded that the growth mechanism at the interface is in the given cases independent of the laser mode, the process and consequently dominated by the two joined alloys.

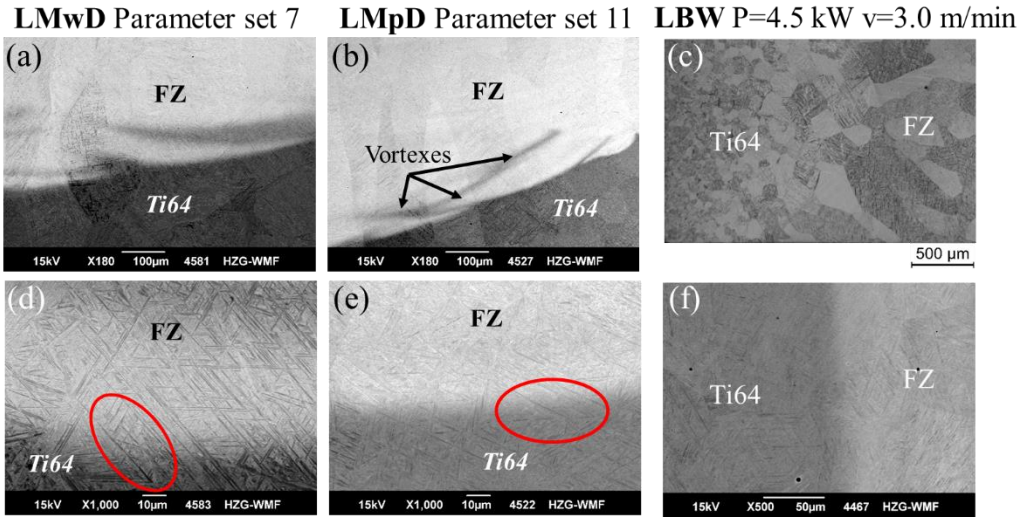

Figure 83: SEM images of FLs of (a), (d) LMwD and (b), (e) LMpD dissimilar Ti64(s)-Ti6242(w/p) depositions. (c) OM and (f) SEM image of FL Ti64 side of LBW dissimilar Ti64-Ti6242 joint. Red ellipse: Expemplary positions of needle grwoth across the FL.

6.1.2. Chemical analysis, phase analysis and microhardness measurements

As the dilution zone was smaller for the LMD processes than for LBW, the degree of mixing of the differing alloys is expected to be lower for the LMD processes (Figure 45, Figure 80). Therefore, for the LMD processes a chemical composition closer to the filler material should be obtained. Moreover, comparable to the dissimilar LBW Ti64-Ti6242 joints no segregations should occur (Figure 56 (d), (g)). Due to the comparable microstructures (Figure 82), the α-phase should be presented in the FZ of the depositions. The theoretical cooling rate for the LMpD process was found to be higher than for the other two processes (Figure 78 (b)), consequently the microhardness values in the FZ of dissimilar Ti-Ti-alloy deposition by LMpD could be reasonably higher.

Results of the EDX line analysis for the LMD depositions are displayed in Figure 84. Comparable to the LBW dissimilar Ti64-Ti6242 joints, the EDX line analysis of the dissimilar Ti64(s)-Ti6242(w/p)

depositions reveal an abrupt change at the FL for the minor alloying elements Zr, Mo, Sn and V (Figure 84 (c), (f), (i)). Due to the substrate-deposition set-up for LMwD and LMpD (Figure 10), only one chemical composition change at FL is present (Figure 84 (c), (f)), while two were identified for the LBW dissimilar Ti64-Ti6242 joint (Figure 84 (i)). Furthermore, as a certain dilution for LMD with the Ti64 substrate occurs, mixing between the two alloys has to take place. For the LBW process, sections of the two weld coupons are molten and the FZ can be regarded as the mixing zone. In contrast, in LMD only a small part of the substrate is molten, and the missing of the second chemical composition change can be seen as an indicator for a smaller mixing zone of Ti64 and Ti6242 in the LMD processes. Consequently, the FZ composition of the LMwD and the LMpD deposition should be closer to the chemical composition of the Ti6242 filler material.

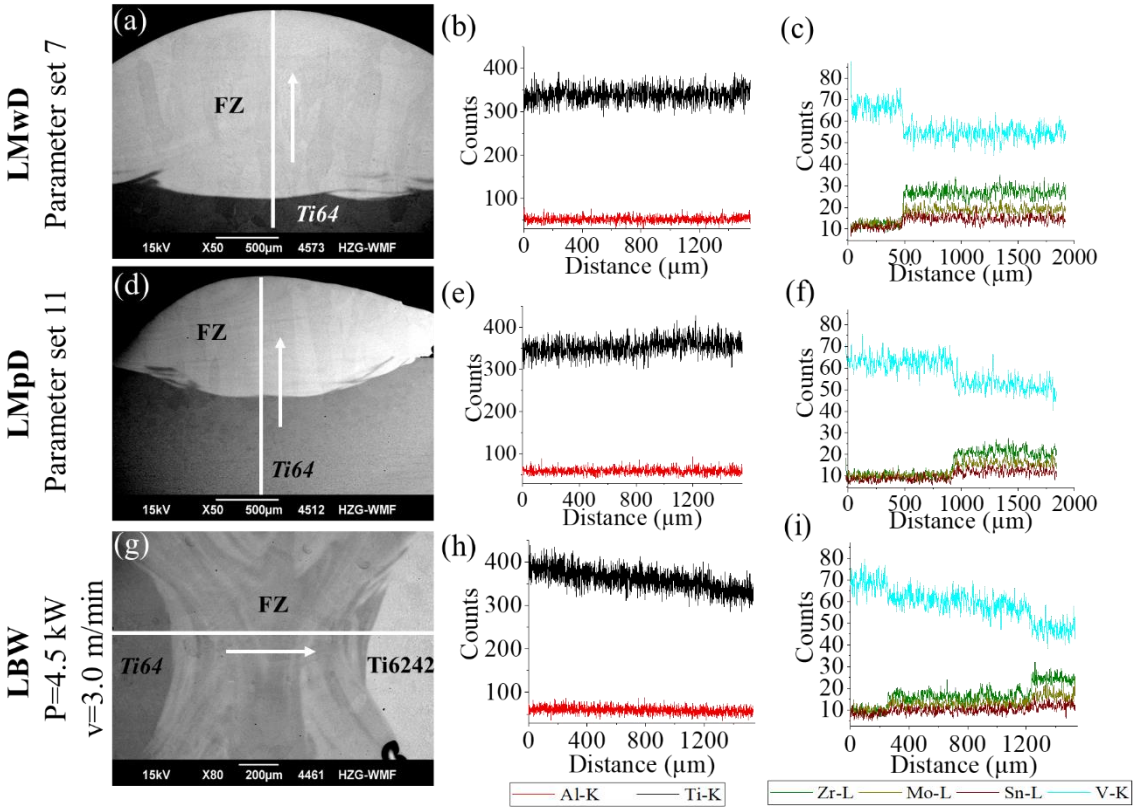

Figure 84: (a), (d), (g) Overview SEM images of position of respective EDX line analysis with schematic measurement direction (white arrow) and line scan position (white line). (a) LMwD dissimilar Ti64(s)-Ti6242(w) deposition with EDX line analysis of (b) major and (c) of minor alloying elements of line scan position in (a). (d) LMpD dissimilar Ti64(s)-Ti6242(p) deposition with EDX line analysis of (e) major and (f) of minor alloying elements of line scan position in (b). (g) LBW dissimilar Ti64-Ti6242 joint with EDX line analysis of (h) major and (i) of minor alloying elements of line scan position in (g). Minor alloying EDX line analysis smoothened with 5 points averaged adjacent function.

To analyze the overall mixture in the FZ center, FZ close to the substrate or joining partners, EDX micro-area analysis were performed (Figure 85). Comparable to LBW (red circle), for the LMwD (green top triangle) and LMpD (blue bottom triangle) dissimilar Ti64-Ti6242 depositions the Al content is constant, as both joining partners contain the same Al amount (Figure 85 (a)). For the LMwD process the Al content is even within the acceptable deviation limits (Table 2, Figure 85 (a)). Therefore, no distinct Al loss due to vaporization occurred. In contrast to the depletion of Mo for dissimilar Ti64-Ti6242 LBW joints, the measured Mo content for LMwD and LMpD are close to the BM values (Table

2, Figure 85 (b)). This supports the hypothesis of a decreased mixing of Ti64 and Ti6242 in FZ during the LMD processes. The FZ of the LBW joint is the equal mixture of the two joining partners, as the measured EDX values for Zr, Sn and V are between the Ti64 and Ti6242 BM values (Figure 85 (c)-(e)). Taking into account the measurement accuracy of the EDX analysis against standards, the measurement accuracy is about 1 % and the detection sensitivity of 0.1 % for elements with an atomic number greater than 10 [214]. Hence, the Zr and Sn content of the LMwD and LMpD sample are within the deviation of the Ti6242 value (Figure 85 (c), (d)). Moreover, respecting the detection sensitivity, the LMpD FZ contains a minor amount of V, while the LMwD FZ is V-free (Figure 85 (e)). The detected V content and the lower Zr content of the LMpD deposition could be explained by the different dilution to total FZ values of 0.12 and 0.26 for the LMwD and LMpD sample, respectively. Due to the higher ratio for LMpD, more Ti64 is molten during the LMpD deposition and the FZ contains V. Overall, it can be stated that by utilizing the LMwD and LMpD process, the mixing of the two joining partners is minimalized. Hence, the FZ of LMwD and LMpD should have the material properties close to the Ti6262 BM.

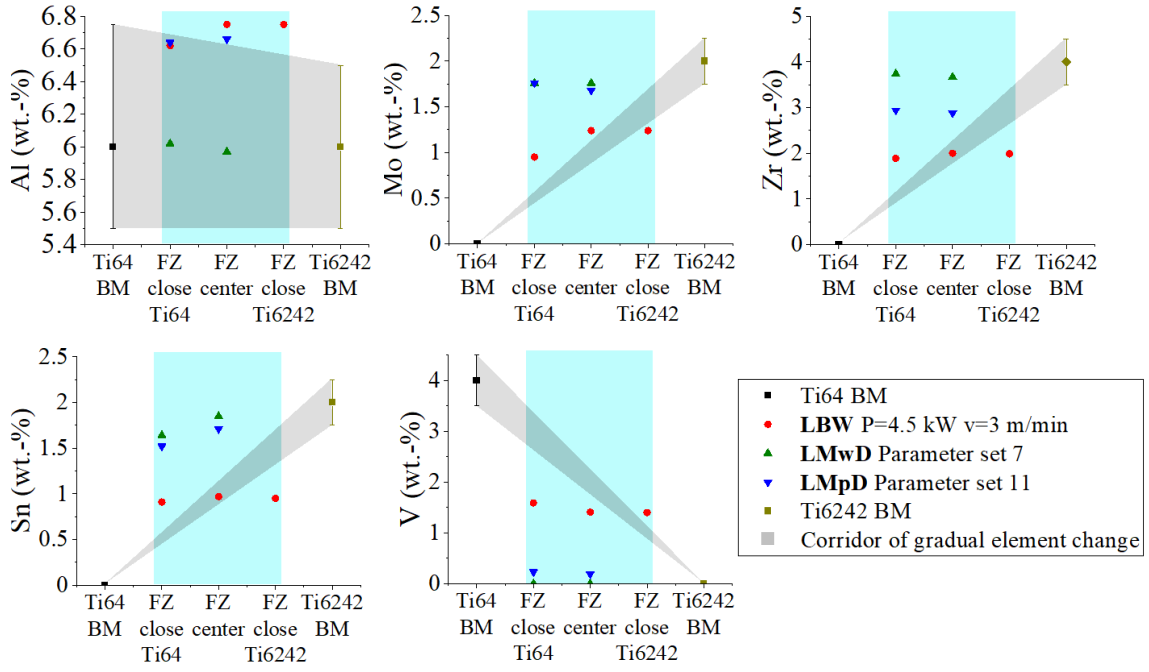

Figure 85: EDX micro-area analysis of dissimilar Ti64-Ti6242 joint and depositions. Ideal chemical composition of the BMs with acceptable deviation Ti64 BM (black square) and Ti6242 BM (yellow diamond) as well as chemical composition of dissimilar LBW Ti64-Ti6242 joint (red circle), dissimilar LMwD Ti64(s)-Ti6242(w) (green top triangle) and dissimilar LMpD Ti64(s)-Ti6242(p) (blue bottom triangle) deposition. Blue area corresponds to the FZ. Grey area corresponds to the corridor of gradual element change. (a) Al content. (b) Mo content. (c) Zr content. (d) Sn content. (e) V content.

As indicated by the chemical composition in the FZ and SEM images (Figure 84 (a), (d), Figure 85) and comparable to the results of the LBW dissimilar Ti64-Ti6242 joint (Figure 86 (g), (h), (i)), no microsegregations are detected in the LMwD and LMpD sample in the FZ center (Figure 86 (a)-(f)). Hence, the overall mixing in the FZ is homogeneous and the brightness differences are due to different grain orientations.

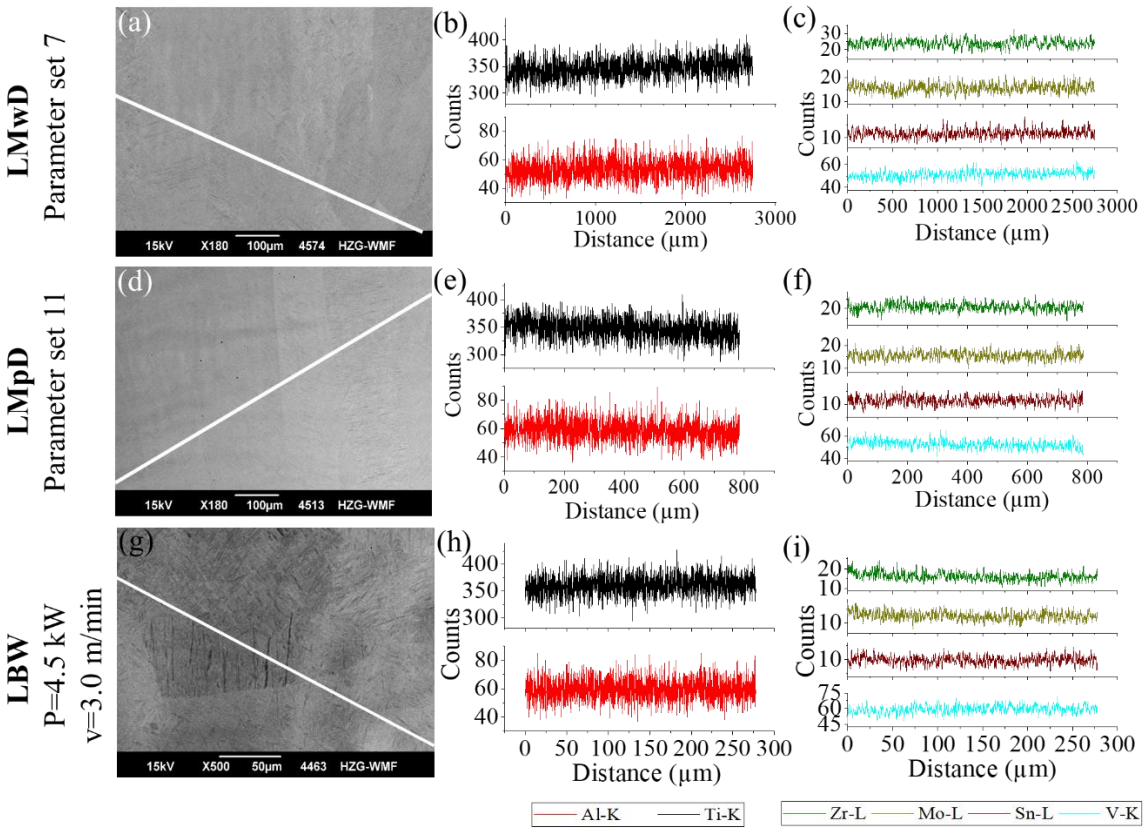

Figure 86: (a), (d), (g) Overview SEM images of position of respective EDX line analysis with schematic measurement direction (white arrow) and line scan position (white line). (a) LMwD dissimilar Ti64(s)-Ti6242(w) deposition with EDX line analysis of (b) major and (c) of minor alloying elements of line scan position in (a). (d) LMpD dissimilar Ti64(s)-Ti6242(p) deposition with EDX line analysis of (e) major and (f) of minor alloying elements of line scan position in (b). (g) LMB dissimilar Ti64-Ti6242 joint with EDX line analysis of (h) major and (i) of minor alloying elements of line scan position in (g). Minor alloying EDX line analysis smoothened with 5 points averaged adjacent function.

In contrast, in the FZ close to the Ti64 substrate of the LMwD and LMpD dissimilar Ti64(s)-Ti6242(w/p) depositions, vortexes emerge (Figure 87). The vortexes could be the result of the Ti64 substrate melting process or differing grain orientations. As known from LBW, the highest temperature gradient occurs at the FL [117], which leads to a fast solidification process and could inhibit homogenous mixing close to the Ti64 substrate. Therefore, the development of vortexes, due to the alloying mixing process seems to be most feasible.

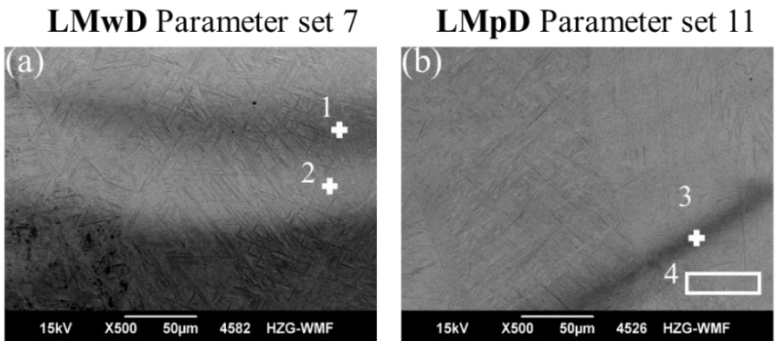

Figure 87: Positions of EDX point and micro-area analysis at FL of dissimilar (a) LMwD and (b) LMpD Ti64(s)-Ti6242(w/p) depositions.

To verify this assumption, in areas of differing brightness in the SEM images (Figure 87), EDX point and micro-area analysis were conducted and results are shown in Table 21. In all measurements the different alloying elements of Ti64 and Ti6242 are detected, but different chemical compositions are obtained. Consistently for LMwD and LMpD, in the brighter areas in SEM images the Ti6242 alloying elements Mo, Zr and Sn are enriched, while V is depleted (Figure 87 Position 2 and 4, Table 21). In contrast, in the darker areas V, a Ti64 element, is enriched and the Ti6242 alloying elements depleted (Figure 87 Position 1 and 3, Table 21). Therefore, the evolving vortexes at the interface are the result of the alloy mixing process and not due to different grain orientations.

Table 21: Results of EDX point and micro-area analysis at FL of dissimilar Ti64(s)-Ti6242(w/p) depositions of positions in Figure 87.

Position	**Al-K [wt.- %]**	**V-K [wt.- %]**	**Sn-L [wt.- %]**	**Mo-L [wt .-%]**	**Zr-L [wt .-%]**	**Ti-K [wt.- %]**
1	6.43	1.79	0.64	0.78	1.59	88.77
2	6.15	0.81	1.47	1.38	2.8	87.38
3	6.71	1.8	0.86	0.94	1.36	88.33
4	6.72	0.27	1.75	1.97	3.02	86.26

Exemplarily, the evolving phases in the FZ and at the FL of the LMD processes were identified by phase maps utilizing EBSD (Figure 88 (a), (b), (d), (e)).

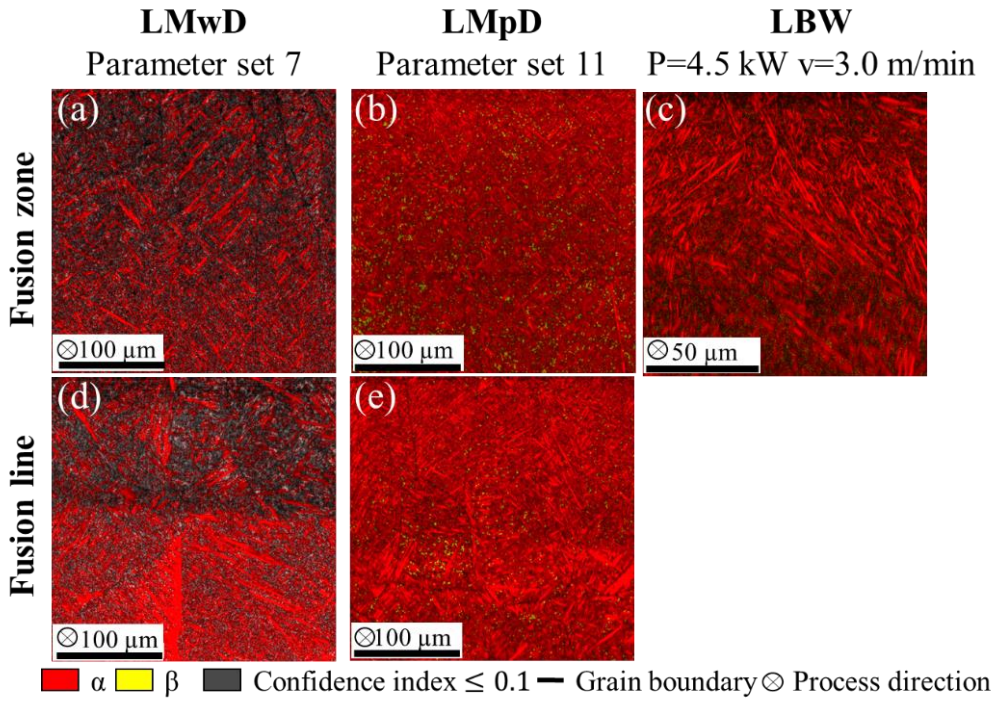

Figure 88: Phase maps of the (a)-(c) FZ and (d)-(e) FL of (a), (d) LMwD, (b), (e) LMpD dissimilar Ti64(s)-Ti6242(w/p) depositions and (c) LBW dissimilar Ti64-Ti6242 joint. α-red. β-yellow. Confidence index≤0.1-grey. Grain boundary-black.

Referring to the theoretical cooling rates, LBW and LMwD dissimilar Ti64-Ti6242 joints and deposition should consist of the same phases (Figure 78 (b)). In all three processes the α-phase is the

main phase in the FZ (Figure 88 (a), (b), (c)). Thus, the cooling rate is sufficiently low for the phase transformation from β to α. Nevertheless, with 6.5 % the retained β-phase amount is highest for the LMpD deposition, compared to 0.4 % for LBW and 1.7 % for LMwD. This can be attributed to the higher cooling rates in the LMpD process, while the cooling rates of the LBW and LMwD process seem to be comparable. Furthermore, consistent with the difference in theoretical cooling rates of the processes (Figure 78 (b)), the martensitic microstructure is finer for the LMpD process compared to the LBW and LMwD process (Figure 88 (a), (b), (c)). As indicated by the SEM images (Figure 83), the phase maps verify that no seam at the FL occurs (Figure 88 (d), (e)).

The FZ microhardness values of the dissimilar Ti64-Ti6242 depositions, generated by the parameter sets in Table 22, are displayed in Figure 89. As all FZs mainly consist of the α-phase (Figure 88), the influence of the α-phase on differing microhardness in the FZ should be insignificant. Due to the minimized mixing of Ti64 and Ti6242 in the FZ by the LMD processes (Figure 85), microhardness values closer to the similar Ti6242 joint FZ microhardness values are anticipated. Moreover, the microstructure of the LMpD depositions is finer than for LMwD (Figure 82, Table 20, Figure 88), which could lead to higher microhardness values for LMpD. Exemplarily, microhardness profiles for LMwD and LMpD are displayed in Figure 89 (a). The characteristic microhardness increase from BM to HAZ is absent for the LMwD utilizing parameter set 7 (Figure 89 (a), black square), due to the combination of the parameter set and the utilization of a thin sheet. In contrast, resulting from the smaller HAZ of LMwD depositions (Figure 80 (b), red circle), the characteristic microhardness increase is observed (Figure 89 (a), red circle). Comparable for the LMpD deposition the characteristic microhardness increase is also measured (Figure 89 (a), green/blue top/bottom triangle).

Correlating the average microhardness in the FZ to the energy per surface, in each process the general trend of a decreasing microhardness in the FZ with increasing energy per surface is observed (Figure 89 (b)). Due to different filler material amounts and hence microstructures, differing average microhardness values in LMD structures deposited with the same energy per surface values are obtained. As energy per surface values are lowest and consequently higher cooling rates emerge for LMpD depositions, the average microhardness values in the FZ are highest. Moreover, the LMpD values seem to be close to the microhardness values of the LBW similar Ti6242 joint FZ values welded with the smallest energy per surface. Despite the minimized mixer for the LMwD depositions, this is not always the case for these values. As both LMD processes exhibit the same major phase in the FZ (Figure 88 (a), (b)) and the chemical compositions are comparable (Figure 85), the influence of thediffering microstructure on the development of the microhardness value in the FZ seems to be higher than the alloy mixing influence.

Table 22: Parameter sets of investigated microhardness measurements of dissimilar Ti-Ti-alloy depositions. LMwD: f=+26 mm. LMpD: f=+8 mm, N_{gas}=4 l/min.

Parameter set	Process	P (kW)	v (m/min)	v_w (m/min)	R (rpm)	Cgas (l/min)
7	LMwD	2.0	0.4	2.5	-	-
9		1.75	0.6	2.5	-	-
11	LMpD	1.1	0.66	-	2	2
12		1.1	0.66	-	4	2

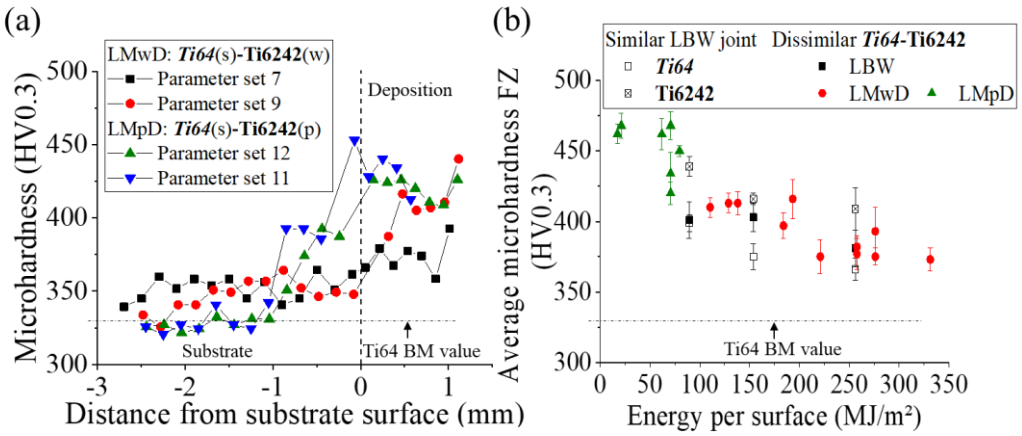

Figure 89: (a) Microhardness profiles of LMwD and LMpD dissimilar Ti64(s)-Ti6242(w/p) depositions. (b) Average microhardness values in the FZ of similar Ti64 (open square), Ti6242 (open cross square) and dissimilar Ti64-Ti6242 LBW joints (black solid square), Ti64(s)-Ti6242(w/p) LMwD (red circle) and LMpD (green triangle) deposition correlated to the energy per surface.

6.2. Transferability from dissimilar TiAl-Ti-alloy joints to deposition

As for LMwD no TNM filler wire is available, for the dissimilar LMwD TNM-Ti-alloy depositions TNM was utilized as a substrate. In contrast, for LMpD TNM powder was deposited on a Ti64 substrate (Chapter 4.3). Due to the possibility to decrease the crack-sensitivity of the dissimilar TNM joints by the choice of the joining partner (Figure 44), the question arises, if it is possible to obtain crack-free LMpD TNM-Ti64 depositions at RT. Furthermore, preheating of the substrate, especially of a thin sheet, could change its optimized initial microstructure. For this reason, it would be advantageous to avoid preheating. As the evolving β-phase related seam at the TNM FL of dissimilar LBW TNM-Ti6242 joints was crucial for the mechanical properties (Chapter 5.3), the focus of this chapter is on the interface evolution at the FL.

6.2.1. Process characteristics, laser metal deposition characteristics and microstructure analysis

Theoretical considerations are utilized to classify the processes. Laser metal deposition characteristics are tried to be correlated to the crack formation. Due to the evolving β-phase related seam at the interface of dissimilar LBW TNM joints the evolving microstructure was examined in depth at this position. Besides, an evolving seam at the interface was excepted for the LMD processes.

The theoretical cooling rates of the dissimilar LMwD depositions and LBW joints appear to be in the same range (Figure 90 (a)). Compared to the other two processes, all investigated theoretical LMpD cooling rates have values an order of magnitude higher. Consequently, comparable microstructural and phase evolution at the FL interface are expected for LBW and LMwD, while for LMpD these could

differ. As the highest theoretical cooling rates occur, the highest crack tendency is assumed for LMpD depositions. Due to the correlation between the energy per surface and the theoretical cooling rate, the tendency for crack formation of LMpD dissimilar TNM(p)-Ti64(s) depositions at RT decreases with increasing energy per surface and thus decreasing theoretical cooling rate (Figure 90 (b)). Furthermore, comparable to LBW (Figure 23), no general theoretical threshold cooling rate is obtained, but a transition range for theoretical cooling rates between crack-free depositions and depositions with cracks emerges (Figure 90 (b)).

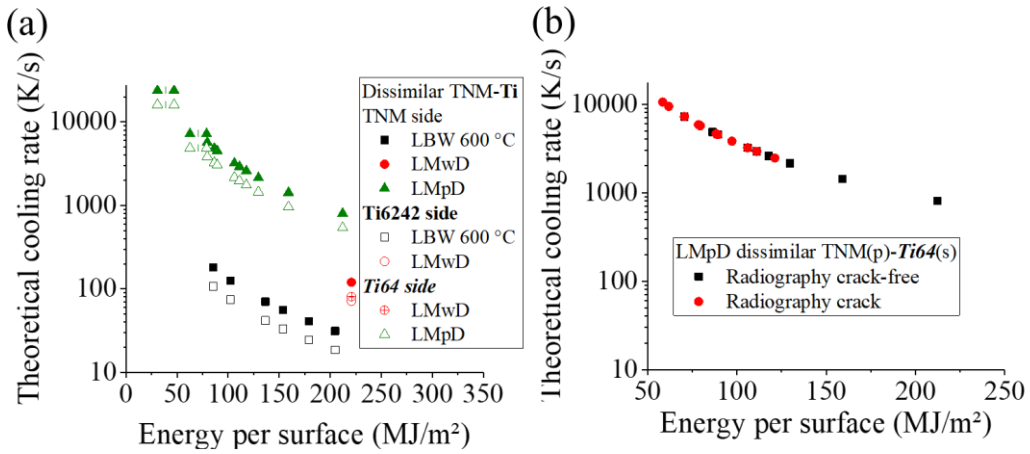

Figure 90: (a) Theoretical cooling rate according to 2D Rosenthal equation (6) with the effective laser power and correlated to the energy per surface values of LBW, LMwD and LMpD dissimilar TNM-Ti-alloy joints and depositions. (b) Crack formation depending on the theoretical cooling rate according to 2D Rosenthal equation (6) and the energy per surface for the TNM side.

Exemplarily radiography images of LMwD and LMpD depositions, which were generated with the parameter sets in Table 23, are presented in Figure 91. For the dissimilar LMwD TNM(s)-Ti6242(w) deposition the same parameter set as for dissimilar Ti64(s)-Ti6242(w) depositions with no macroporosity was utilized. Only at the end of the deposition, a crack is detected for processing at RT (Figure 91 (a)). Due to the acceleration and deceleration at the start and end of a deposition, the LMD process is not stable and these parts are excluded in the deposition assessment. Therefore, in the following the dissimilar TNM(s)-Ti6242(w) deposition is regarded as crack-free. Due to the 0.2 mm larger filler wire diameter for Ti64, a decreased heat input into the substrate and hence an increased cooling rate can be expected. This could lead to the cracks in the dissimilar LMwD TNM(s)-Ti64(w) deposition with the same parameter set as for the other LMwD deposition (Figure 91 (d)). A negative influence of Ti64 as a joining partner is improbable, since the crack-free LBW dissimilar TNM-Ti64 joint was obtained at a lower preheating temperature than the crack-free LBW dissimilar TNM-Ti6242 joints (Figure 91 (c), (f)). For LMpD at RT even crack-free dissimilar TNM(p)-Ti64(s) deposition are achieved (Figure 91 (b), (e)). Nevertheless, due to the known TiAl crack-sensitivity (Chapter 3.4.), cracks also emerge in LMpD TNM(p)-Ti64(s) depositions (Figure 91 (g)).

Table 23: Parameter sets for dissimilar TNM-Ti-alloy depositions. LMwD: f=+26 mm. LMpD: f= +8 mm, N_{gas}=4 l/min.

Parameter set	Process	P (kW)	v (m/min)	v_w (m/min)	R (rpm)	Cgas (l/min)
7 (same as for Ti-Ti-alloy depositions)	LMwD	2.0	0.4	2.5	-	-
11 (same as for Ti-Ti-alloy depositions)	LMpD	1.1	0.66	-	2	2
17		0.9	0.48	-	3	3
18		1.1	0.36	-	3	2
19		1.1	1.2	-	1	2

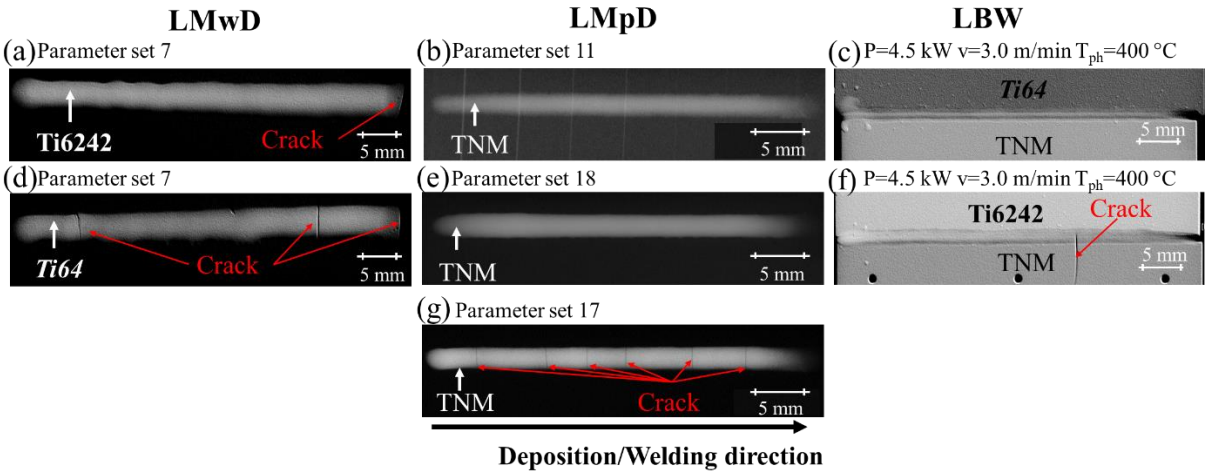

Figure 91: Radiography images of (a), (d) LMwD dissimilar TNM(s)-Ti-alloy(w) and (b), (e), (g) LMpD dissimilar TNM(p)-Ti64(s) depositions. (a) LMwD dissimilar TNM(s)-Ti6242(w) deposition. (d) LMwD dissimilar TNM(s)-Ti64(w) deposition. LBW dissimilar (c) TNM-Ti64 and (f) TNM-Ti6242 joint.

Cross-sections of dissimilar LMD TNM-Ti-alloy depositions, obtained with parameter sets in Table 23, are shown in Figure 92. Comparing dissimilar LMwD TNM(s)-Ti64(w) and TNM(s)-Ti6242(w) depositions generated with the same parameter set (Figure 92 (a), (d)), a smaller dilution and HAZ are present for the Ti64 wire deposition (Figure 92 (a)). This should be attributed to the larger wire diameter, the higher material amount deposited and thus a reduced heat input into the substrate. As for dissimilar Ti64(s)-Ti6242(w) depositions prior β-grains are revealed in both dissimilar joints. For the same LMwD parameter set the prior β-grain size of dissimilar Ti64(s)-Ti6242(w), TNM(s)-Ti6242(w) and TNM(s)-Ti64 (w) depositions are presented in Table 24. Thus, changing the substrate influences insignificantly the prior β-grain size in the FZ.

For dissimilar LMpD TNM(p)-Ti64(s) depositions, two differing microstructures are obtained, (Figure 92 (b), (c), (e), (f)). Prior β-grains could be assumed in the dissimilar TNM(p)-Ti64(s) deposition of Figure 92 (b) and (f). In contrast, needles could emerge in the other LMpD microstructure type (Figure 92 (c), (e)). The occurrence of the two microstructure types could be the result of the different depositionamounts, which could influence the cooling rate. Moreover, even for comparable microstructures, the shape of the LMpD dissimilar deposition is no indicator for a crack-free deposition (Figure 92 (c), (e)).

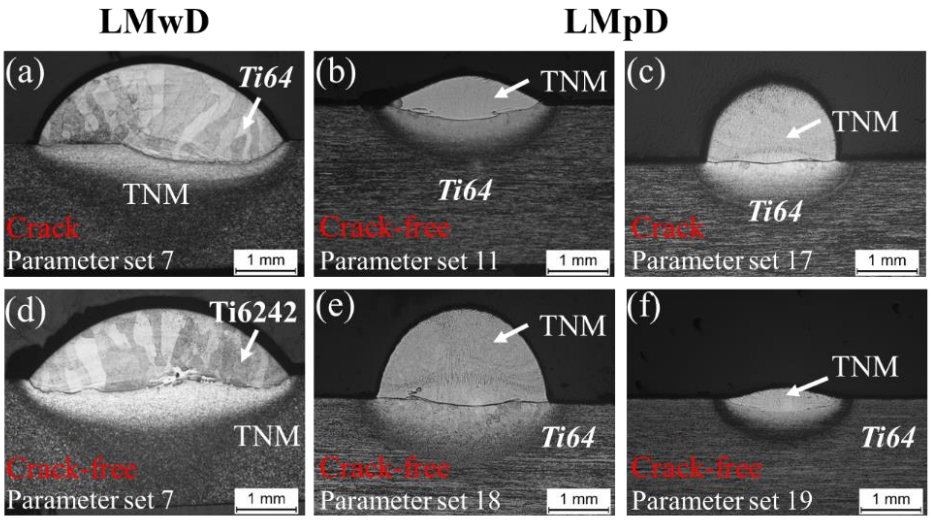

Figure 92: Cross-sections of (a), (d) LMwD dissimilar TNM(s)-Ti-alloy(w) and (b), (c), (e), (f) LMpD dissimilar TNM(p)-Ti64(s) depositions. (a) LMwD dissimilar TNM(s)-Ti64(w) deposition. (d) LMwD dissimilar TNM(s)-Ti6242(w) deposition.

Table 24: Prior *β*-grain size of dissimilar LMwD Ti-Ti-alloy and TNM-Ti-alloy depositions generated with parameter set 7.

Deposition	**Prior *β*-grain width (mm)**	**Prior *β*-grain length (mm)**
Ti64(s)-Ti6242(w)	0.14±0.02	0.74±0.33
TNM(s)-Ti6242(w)	0.18±0.07	0.77±0.20
TNM(s)-Ti64(w)	0.2±0.07	0.84±0.20

The size of the total FZ and total HAZ is measured to further examine the cross-sections (Figure 93 (a), (b)). Due to the limited number of LMwD dissimilar TNM depositions, no conclusion can be drawn if similar FZ sizes compared to the other processes can be achieved. For the applied parameter set, it seems that the energy per surface was barely high enough to melt the Ti64 filler wire with the larger diameter and minor differences in FZ size for LMwD were attained (Figure 93 (a), red circle). As expected the smallest FZ sizes could be achieved by LMpD (green triangle). The smallest filler material amounts can be supplied by this process, and hence FZ sizes can vary. In contrast, the variation of the FZ size for LBW dissimilar TNM-Ti6242 joints preheated to 600 °C is insignificant (black square). Nevertheless, for energy per surface values between 75 MJ/m^2 and 200 MJ/m^2, similar FZ sizes are achieved by LMpD and LBW. Moreover, LMpD depositions with cracks seem to have larger FZ (green open triangle) compared to crack-free LMpD depositions (green solid triangle) with a similar energy per surface value. The smallest HAZ sizes occur for LMpD depositions (Figure 93 (b), green triangle). Comparing LMpD depositions with similar energy per surface values, the crack probability seems to be higher for LMpD depositions with smaller HAZs (green open triangle). This indicates that the heat input into the substrate could be an important factor to obtain crack-free depositions. The hypothesis is further supported by the LMwD depositions, where a crack is detected for the TNM(s)-Ti64(w) deposition with the smaller HAZ size (red open circle), while the TNM(s)-Ti6242(w) deposition with the larger HAZ is crack-free (red solid circle). Consequently, the crack formation could be the result of higher thermally induced stresses for smaller HAZs, since the heat input into the substrate is smaller and a higher temperature difference between FZ and substrate could develop.

The ratio of the total FZ-HAZ surface is displayed in Figure 93 (c). For LBW dissimilar TNM-Ti6242 joints preheated to 600 °C, the influence of the energy per surface values on the measured characteristics and the variation of the ratio is insignificant (Figure 93). In contrast, as indicated by the differing HAZs of the LMD depositions (Figure 93 (b)), if less energy is absorbed by the substrate with regard to the FZ size, hence for higher ratios, the tendency for crack formation of depositions with similar energy per surface values is increased (Figure 93 (c), red/green open circle/triangle).

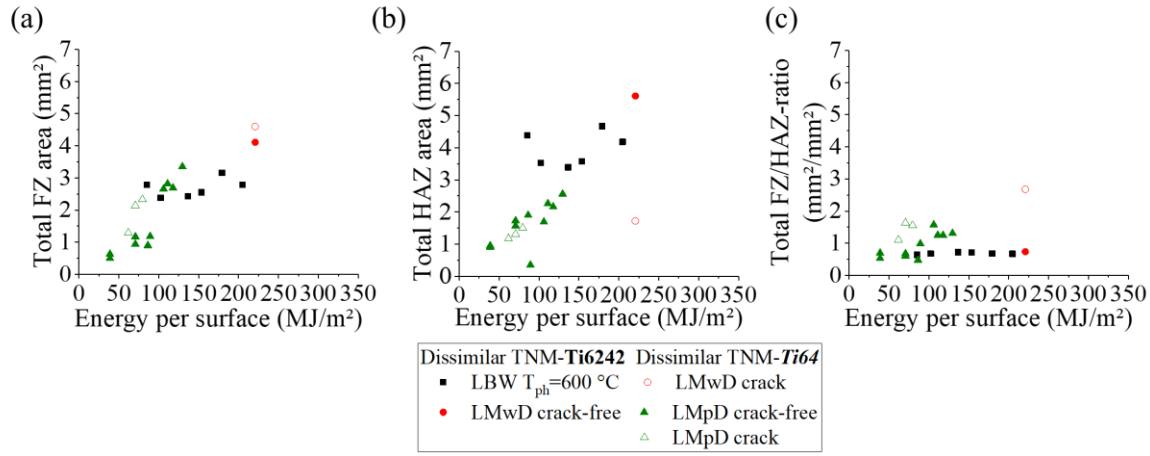

Figure 93: Correlation of dissimilar TNM-Ti-alloy joint and deposition characteristics to corresponding energy per surface values for. (a) Total FZ. (b) Total heat-affected-zone. (c) Ratio of total FZ to total HAZ.

Table 25 displays the utilized parameter sets for the cross-sections in Figure 94. Examining the microstructure at the FL, LMwD depositions show a brighter area at the interface (Figure 94 (a), (e)), which could correspond to the β-phase related seam found in the dissimilar LBW TNM-Ti64 joint (Figure 94 (d)). Despite the crack in the LMwD dissimilar TNM(s)-Ti64(w) (Figure 91 (d)), the brighter area does not appear broader than for the crack-free dissimilar TNM(s)-Ti6242(w) deposition (Figure 94 (a), (e)). Therefore, the heat input into the substrate could be more crucial for crack-free LMwD depositions than the interface evolution (Figure 93 (b), (c), Figure 94 (a), (e)). As for LMwD, the brighter area in LMpD depositions could be a β-phase related seam (Figure 94 (b), (c), (f)). For the dissimilar LMpD TNM(p)-Ti64(s) two different FL microstructures seem to develop (Figure 94 (b), (c), (f), (g)). In spite of the microstructural differences, heteroepitaxial growth is observed in all LMpD dissimilar TNM(p)-Ti64(s) depositions as prior β-grains belonging to the HAZ and FZ are present (Figure 94 (b), (c), (f), (g), red ellipse). A grain-like microstructure with no needles in the FZ is observed (Figure 94 (b), (g)), leading to the hypothesis that the phase transformation from β to α_2 could have been suppressed. Comparable to the dissimilar LBW TNM-Ti6242 joint preheated to 400 °C (Figure 94 (h)), in Figure 94 (g), with the grain-like microstructure, no bright area at the interface occurs. This further supports the hypothesis that the phase transformation from β to α_2 could have been suppressed and the FZ corresponds to the related β-phase. The second microstructure type reveals needles in the FZ (Figure 94 (c), (f)), indicating a sufficiently low cooling rate for the phase transformation from β to α_2. The needles evolve for the half-circle shape with high total FZ/HAZ ratios of 1.31 and 1.55. Despite similar microstructures and deposition shapes, crack-free and cracked LMpD dissimilar TNM(p)-Ti64(s) depositions are obtained (Figure 92 (c), (e), Figure 94 (c), (f)). As the total FZ/HAZ ratios for comparable energy per surface values of the LMpD dissimilar TNM(p)-Ti64(s) deposition with cracks

is higher than for the ones without cracks, the importance of the heat input into the substrate for crack-free depositions is further strengthened.

Table 25: Parameter sets for dissimilar TNM-Ti-alloy depositions. LMwD: f=+26 mm. LMpD: f= +8 mm, N_{gas}=4 l/min.

Parameter set	Process	P (kW)	v (m/min)	v_w (m/min)	R (rpm)	Cgas (l/min)
7 (same as for Ti-Ti-alloy depositions)	LMwD	2.0	0.4	2.5	-	-
11 (same as for Ti-Ti-alloy depositions)	LMpD	1.1	0.66	-	2	2
17		0.9	0.48	-	3	3
18		1.1	0.36	-	3	2
19		1.1	1.2	-	1	2

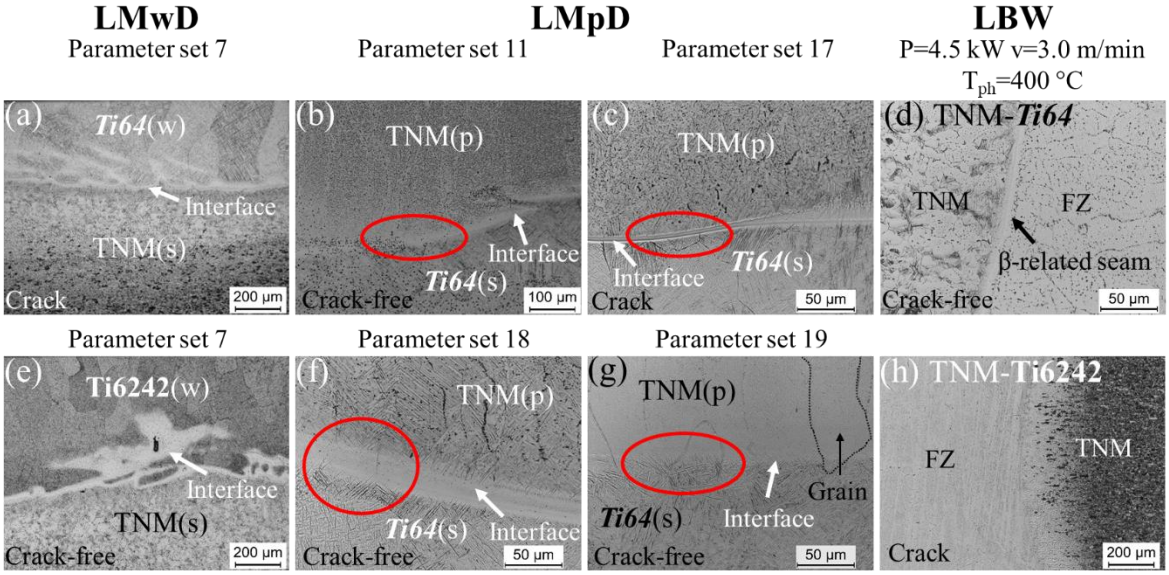

Figure 94: Cross-sections of (a), (e) LMwD dissimilar TNM(s)-Ti-alloy(w), (b), (c), (f), (g) LMpD dissimilar TNM(p)-Ti64(s) depositions, LBW dissimilar (d) TNM-Ti64 and (h) TNM-Ti6242 at the FL. Red ellipse: Exemplary region of heteroepitaxial growth. (a) LMwD dissimilar TNM(s)-Ti64(w) deposition. (e) LMwD dissimilar TNM(s)-Ti6242(w) deposition. Dissimilar LBW joints welded with the same parameter set.

SEM images are utilized to further examine the interface at the FL (Figure 95). These reveal for LMwD depositions comparable microstructures as for the LBW dissimilar TNM joints with a β-phase related seam (Figure 95 (a), (c), (d)). Thus, the hypothesis of an evolving β-phase related seam due to the comparable theoretical cooling rates is supported. Moreover, as the theoretical LMwD cooling rates are higher than for the LBW dissimilar TNM-Ti6242 joints (Figure 90 (a)), the β-phase related seam is continuous (Figure 95 (a), (d)). Heteroepitaxial growth is also found in the LMwD process as prior β-grains belonging to the HAZ and FZ occur (Figure 95 (d), red ellipse). As assumed based on the OM images, for the LMpD deposition, a grain-like microstructure in the FZ (Figure 95 (b)), comparable to the evolving microstructure of the LBW dissimilar TNM-Ti6242 joint preheated to 400 °C (Figure 95 (e), (f)), emerges. Thus, the brighter area at the interface of the LMpD deposition should be due to the

mixing behavior of the joining partners (Figure 95 (b)). In contrast to LBW dissimilar TNM-Ti-alloy joints (Figure 95 (c), (e), (f)), the crack formation of LMpD dissimilar TNM(p)-Ti64(s) depositions seems not to be associated with the evolving microstructure (Figure 94 (b), (c), (f), (g), Figure 95 (b)), which is connected to the phases evolution. Consequently, the crack formation for LMpD dissimilar TNM(p)-Ti64(s) should be due to the differing total FZ/HAZ ratios, thus heat inputs into the substrate (Figure 93 (c)).

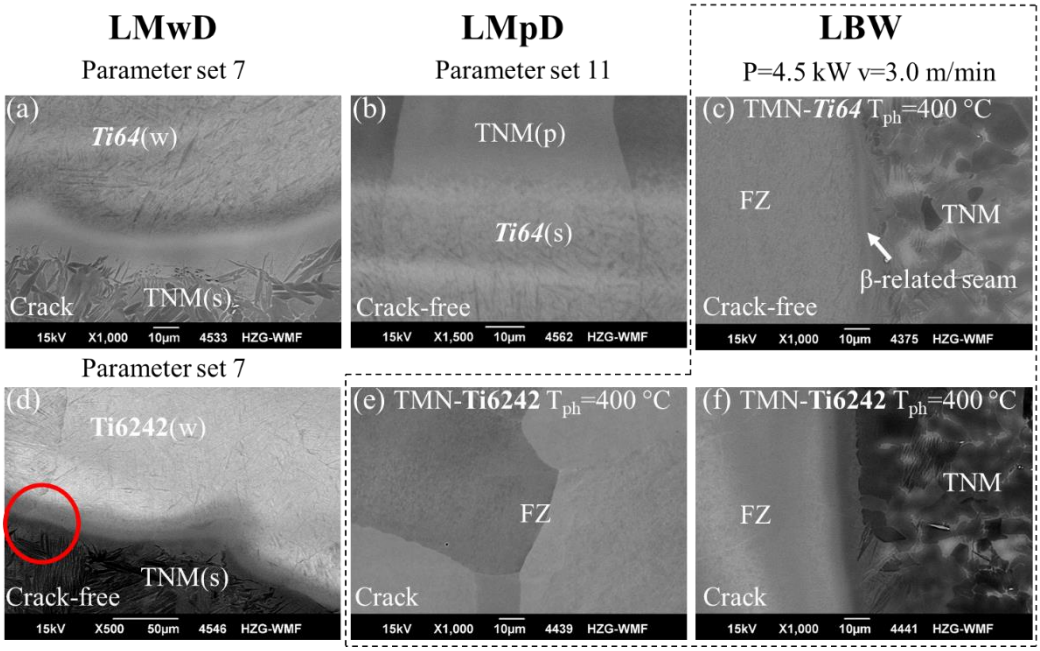

Figure 95: SEM images of (a), (d) LMwD dissimilar TNM(s)-Ti-alloy(w) and (b) LMpD dissimilar TNM(p)-Ti64(s) depositions at the FL. LBW dissimilar (c) TNM-Ti64, (f) TNM-Ti6242 joint at FL and (e) dissimilar TNM-TI6242 joint in FZ. Red ellipse: Exemplary region of heteroepitaxial growth. (a) LMwD dissimilar TNM(s)-Ti64(w) deposition. (d) LMwD dissimilar TNM(s)-Ti6242(w) deposition.

6.2.2. Chemical analysis, phase analysis and microhardness measurements

The chemical analysis of dissimilar Ti-Ti-alloy depositions exhibited a lower degree of mixing compared to the dissimilar Ti-Ti-alloy joints (Figure 85). Consistently, for dissimilar TNM-Ti-alloy depositions also a low degree of mixing was expected. From the microstructure analysis (Chapter 6.2.1.) and the knowledge from the dissimilar LBW TNM joints (Chapter 5.2), a β-phase related seam was anticipated for the LMD processes. As Ti-alloys were utilized as filler materials for the LMwD process, only the microhardness values of the dissimilar LBW TNM joints and dissimilar LMpD TNM depositions are compared with each other. As the theoretical cooling rates differ (Figure 90 (a)) and deposition shapes of the LMpD process were no indicator for crack-free depositions (Figure 92), the question arises whether at all comparable microhardness values occur. Moreover, if as stated in literature for similar LBW TiAl joints [37] and as hinted by the dissimilar TNM-Ti6242 joints (Figure 65 (a)), the microhardness values can be utilized as a crack indicator.

For the dissimilar LMpD TNM(p)-Ti64(s) deposition Figure 92 (b) showed one of the largest dilution zones. Consequently, the degree of mixing with the Ti64 substrate is one of the highest for the LMpD process. The chemical composition in the FZ of this dissimilar LMpD TNM(p)-Ti64(s) deposition investigated by EDX micro-area measurements is 71.73 wt.-% Ti, 19.44 wt.-% Al, 5.81 wt.-% Nb,

2.15 wt.-% Mo and 0.88 wt.-%°V. For the dissimilar TNM-Ti64 joint preheated to 400 °C, the detected vanadium content is 1.47 wt.-%. Hence, due to the low degree of alloy mixture, some microhardness values in the FZ of the dissimilar LMpD TNM(p)-Ti64(s) deposition could be closer to the similar TNM joint microhardness values in the FZ.

As excepted from the theoretical cooling rates, OM and SEM images at the FL of the LMwD dissimilar TNM(s)-Ti(w) depositions, a β-phase related seam evolves at the FL (Figure 96 (a), (e)). Thus, the knowledge of the phase evolution at the FL of LBW and LMwD dissimilar TNM joints are comparable and could be successfully transferred from LBW to LMwD. The utilized parameter sets are presented in Table 26. A smaller HAZ for LMwD dissimilar TNM(s)-Ti64(w) depositions than for the dissimilar TNM(s)-Ti6242(w) deposition emerges (Figure 93 (b)). Hence, a higher temperature gradient at the FL for LMwD dissimilar TNM(s)-Ti64(w) depositions is expected. However, as already assumed by the SEM images (Figure 95 (a), (d)), the β-phase related seam of the LMwD dissimilar TNM(s)-Ti64(w) deposition is not wider than for the dissimilar TNM(s)-Ti6242(w) deposition. Consequently, as the microstructure and phase evolutions at the interface are alike (Figure 94 (a), (e), Figure 95 (a), (d), Figure 96 (a), (e)), the cause for the crack formation in the LMwD dissimilar TNM(s)-Ti64(w) deposition compared to the crack-free LMwD dissimilar TNM(s)-Ti6242(w) could be attributed to the differing total FZ/HAZ ratios (Figure 93 (c)). Hence, the different heat inputs into the substrate seems to be crucial for crack-free depositions (Figure 93 (b)).

In contrast to the phase maps of LBW joints, where the dissimilar TNM-Ti6242 joint with a FZ consisting of a related β-phase is not crack-free (Figure 96 (h)), a crack-free LMpD TNM(p)-Ti64(s) deposition with a related β-phase in the FZ could be obtained (Figure 91 (b), Figure 96 (b)). As the theoretical cooling rates for LMpD are higher than for LBW (Figure 90 (a)), the FZ shapes and deposition lengths differ, different thermally induced stresses could evolve. Moreover, these differing thermally induced stresses could also develop, as the LMD FZ is only fixed to one side, the substrate, while the LBW FZ is fixed to two sides, the weld coupons (Figure 10). Indicating higher thermally induced stresses in the cracked LBW dissimilar TNM-Ti6242 joint consisting of the related β-phase, and supporting the hypothesis, are the locations of high defect density at the FL (Figure 96 (h), black layer bands). In contrast, for the crack-free LMpD dissimilar TNM(p)-Ti64(s) with the related β-phase in the FZ, no locations of high defect density are detected (Figure 96 (b)). Despite the phase transformation from β to α_2 and differing from the LBW dissimilar TNM-Ti64 joint (Figure 96 (d)), for the LMpD deposition cracks were detected (Figure 96 (c)). Moreover, differently to the LBW similar TNM joints (Figure 96 (g)), a related β-phase is detected as a block in the crack-free mainly α_2 containing LMpD deposition (Figure 96 (f)). The total FZ/HAZ ratios of the crack-free LMpD dissimilar TNM(p)-Ti64(s) depositions (Figure 96 (b), (f)) are with 0.68 and 1.31 lower than for the cracked LMpD deposition with 1.55 (Figure 96 (c)), leading to the assumption that different thermally induced stresses could evolve. This differing stresses than could result in differing probabilities for crack formation in LMpD depositions, as revealed for the transition range of the theoretical cooling rates (Figure 90 (b)). Nevertheless, the phase evolution at the interface for LBW and LMpD are comparable and thus as for the LMwD process, the powerful synergetic benefit of knowledge about the LBW process and the metallurgy could be successfully utilized for LMpD.

Table 26: Parameter sets of dissimilar TNM-Ti-alloy depositions investigated by the EBSD method. LMwD: f=+26 mm. LMpD: f= +8 mm, N_{gas}=4 l/min.

Parameter set	Process	P (kW)	v (m/min)	v_w (m/min)	R (rpm)	Cgas (l/min)
7 (same as for Ti-Ti-alloy depositions)	LMwD	2.0	0.4	2.5	-	-
11 (same as for Ti-Ti-alloy depositions)	LMpD	1.1	0.66	-	2	2
17		0.9	0.48	-	3	3
18		1.1	0.36	-	3	2

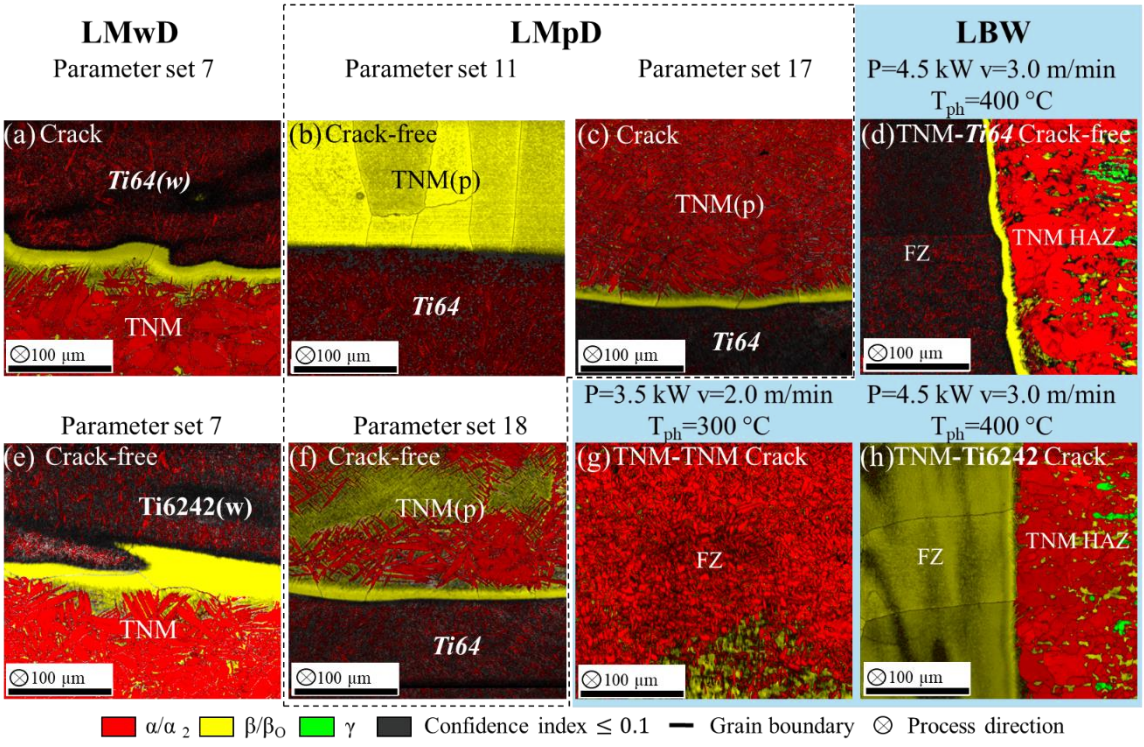

Figure 96: Phase maps of (a), (e) LMwD dissimilar TNM(s)-Ti-alloy(w) and (b), (c), (f) LMpD dissimilar TNM(p)-Ti64(s) depositions at the FL. (a) LMwD dissimilar TNM(s)-Ti64(w) deposition. (e) LMwD dissimilar TNM(s)-Ti6242(w) deposition. LBW (g) similar TNM(1.5), (d) dissimilar TNM-Ti64 and (h) TNM-Ti6242 joint. α/α_2-red. β/β_O-yellow. γ-green. Confidence index≤0.1-grey. Grain boundary-black.

Exemplarily, as for the crack-free LBW dissimilar TNM-Ti64 joint preheated to 400 °C with an α_2-phase consisting FZ, for the crack-free LMpD dissimilar TNM(p)-Ti64(s) depositions containing a FZ with a related β-phase, the characteristic microhardness increase in the FZ is observed in Figure 97 (a). Even so a β-phase related FZ is present in the LMpD deposition, the crack-free structures of the joint and deposition could be explained by the comparable microhardness values in the FZ. For the ω_O-phase type consisting FZ of the cracked LBW dissimilar TNM-Ti6242 joint, the average microhardness in the FZ with 562 HV0.3 and maximum microhardness with 599 HV0.3 (Figure 97 (b), black open square), is higher than for the crack-free dissimilar TNM-Ti64 joints preheated to 400 °C consisting of the α_2-phase with 521 HV0.3 and 551 HV0.3 (Figure 97 (b)), respectively. In contrast, despite the differing theoretical cooling rates, no significant average microhardness difference in the FZ between crack-free

LMpD dissimilar TNM(p)-Ti64 depositions and depositions with cracks can be measured (Figure 97 (b) solid and open green triangle). Even so, the degree of mixing for LMpD depositions is low, the average microhardness values in the FZ of similar TNM joints (red circle) are not closer to the LMpD values (solid and open green triangles) than the dissimilar TNM-Ti64 joint values (solid black square) (Figure 97 (b)). Thus, in contrast to LBW, for LMpD dissimilar TNM(p)-Ti64(s) depositions neither the phase evolution nor the microhardness is an indicator for the crack formation. The crack probability is effected by the heat input into the substrate, which is illustrated by the total FZ/HAZ ratio (Figure 93 (c)), and could influence the thermally induced stresses.

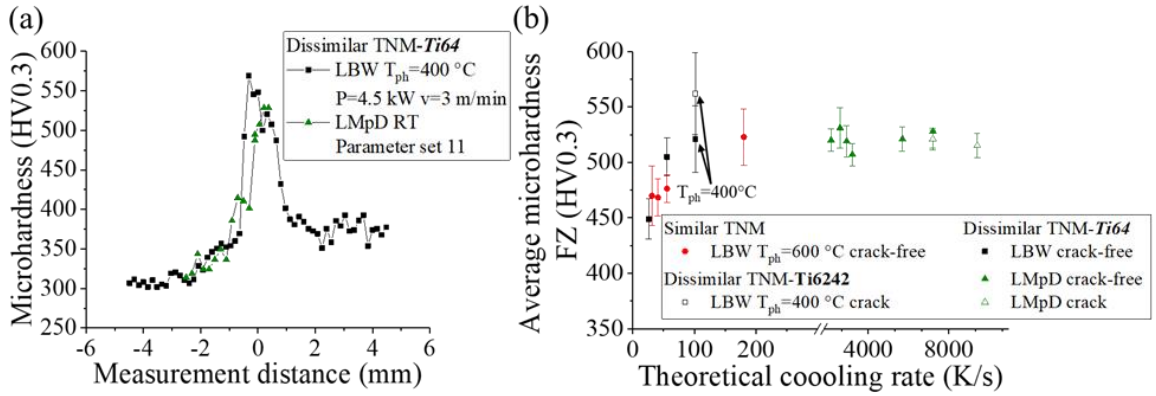

Figure 97: (a) Microhardness profiles of the LBW dissimilar TNM-Ti64 joint, and LMpD dissimilar TNM(p)-Ti64 deposition. (b) Average microhardness values in the FZ of LBW dissimilar TNM-Ti6242 joints, TNM-Ti64 joints , LMpD dissimilar TNM(p)-Ti64(s) depended on the theoretical cooling rate 2D Rosenthal equation (6) for TNM.

Summing up, the gained knowledge for LBW regarding the microstructure and phase evolution at the dissimilar interface could be successfully transferred to both LMD processes. In contrast, a limit of transferability for the crack formation is reached, since the crack formation cannot be correlated to the microstructure and phase evolution as in LBW. Differently to LBW microhardness values (Figure 65, Figure 67) and fusion welding literature [37,39], microhardness values of LMD depositions cannot be utilized as an indicator for crack formation. This could be the result of differing thermally induced stresses, due to different theoretical cooling rates, deposition amounts, shapes and lengths. The hypothesis is further supported by the differing amount of defect densities in the FZ of LBW and LMpD dissimilar TNM joints (Figure 96). For crack-free LMD depositions the heat input into the substrate and the total FZ/HAZ ratio seems to be crucial (Figure 93 (b), (c)).

7. Conclusion

Promising candidates to fulfill the increased requirements for lightweight constructions in aviation and space industry are γ-TiAl-alloys such as TNM. The application of γ-TiAl-alloys enables the use of Ti-based alloys up to a service temperature of 800 °C. However, due to their crack sensitivity, joining of these intermetallics is challenging. Preheating prior to fusion welding has shown to be an effective tool to obtain crack-free joints. Nevertheless, further knowledge regarding the microstructure-phase influence on the crack formation is necessary to gain a deeper understanding concerning the crack formation. Besides, the substitution of materials as well as the utilization of materials with differing mechanical properties in one part enables the effective use of the material and material savings. Due to the different thermophysical properties and chemical compositions, manufacturing one part with different local mechanical properties by joining two materials is challenging. However, as new design and weight saving possibilities emerge, dissimilar joints are requested by industry.

Aim of this thesis was the establishing of the technological and material science fundamentals for dissimilar Ti-Ti- and γ-TiAl-Ti-alloy joints by laser beam welding and laser metal deposition. Therefore, the three aviation approved alloys Ti64, Ti6242 and TNM were utilized. Each of these alloys' posses a different long-term service temperature. Focus of this thesis was on the more mature laser beam welding process to establish the fundamentals for dissimilar Ti-alloys and dissimilar TNM joints to gain a comprehensive knowledge regarding the microstructure-property relationship. Extending the thesis, the transferability of obtained knowledge by laser beam welding to laser metal deposition was investigated, considering especially the dissimilar interface. The results of the thesis are summarized according to the four objectives in chapter 1.2.:

1. Overlapping process windows of all three similar joints by laser beam welding were established by a feasibility study. Hence, despite the different thermophysical properties and chemical compositions, the parameter transfer was effective and the fundamental requirement to achieve dissimilar joints was obtained. Moreover, the process windows of the investigated dissimilar Ti-Ti- and TNM-Ti-alloys joints were within the similar joint process windows. Therefore, no additional measures for attaining dissimilar joints were necessary.
2. Crack-free dissimilar TNM-Ti-alloy joints were successfully obtained on a laboratory scale by preheating. The required preheating temperature was shown to be dependent on the TNM sheet thickness and the Ti-alloy joining partner. For crack-free similar TNM joints, the mandatory preheating temperature was 400 °C and 600 °C for a sheet thickness of 1.5 mm and 2.0 mm, respectively. Crack-free dissimilar TNM-Ti64 joints were obtained with a preheating temperature of 400 °C, while for crack-free dissimilar TNM-Ti6242 joints a preheating temperature of 600 °C was necessary. Moreover, theoretical considerations revealed that for each parameter set an individual theoretical cooling rate and no general theoretical threshold cooling rate for crack-free joints exists. Besides, the temperature gradient in the joint is also an important key for crack-free joints, which seems to be most effectively influenced by the preheating temperature. In addition to establishing the crack-free manufacturing process of dissimilar TNM joints, the effective use of Ti6242 filler wire to reduce the underfill in crack-free dissimilar TNM-Ti6242 joints was developed. The different necessary preheating temperatures for dissimilar TNM joints could be correlated to the evolving microstructure and phases. All crack-free joints exhibit a martensitic microstructure in the fusion zone and

consequently the phase transformation from a related β-phase to the α_2-phase is crucial to obtain crack-free similar and dissimilar TNM joints.

3. For similar and dissimilar joints, the investigation of the microstructure-phase evolution on the interface between fusion zone and heat-affected zone indicated epitaxial and heteroepitaxial growth, respectively. For dissimilar TNM joints, the phase constitution via the β-phase could be verified. Moreover, for high cooling rates the decomposition to a ω_O-phase type in the fusion zone, could be revealed. The indicated ω_O-phase type and the high defect density in the fusion zone resulted in the crack formation of the dissimilar TNM-Ti6242 joint preheated to 400 °C. Besides, dependent on the preheating temperature and the joining partner, a β-phase related seam at the fusion line on the TNM interface evolved. The β-phase related seam could not be removed by post-weld heat treatments utilizing typical TNM and Ti6242 heat treatment temperatures. An interruption of the otherwise continuous β-phase related seam by α_2 needles could be achieved by preheating the dissimilar TNM-Ti6242 joint to 800 °C. For the investigation of the mechanical properties, a suitable tensile sample manufacturing process and testing set-up for similar and dissimilar TNM sheet joints for high temperature tensile tests was successfully developed. Despite the effective reduction of the underfill by the utilization of Ti6242 filler wire in dissimilar TNM-Ti6242 joints, the notch sensitivity of TNM was still the dominant cause of failure for the as-welded dissimilar TNM-Ti6242 joints. Hence, grinding of tensile specimens was proven to be mandatory to obtain the tensile properties of similar and dissimilar TNM joints. Furthermore, as Ti6242 softens at the TNM long-term service temperature of 800 °C, the service temperature of dissimilar TNM-Ti6242 joints is restricted to 425 °C the long-term service temperature of Ti6242. Regarding the influence of the β-phase related seam on the tensile properties, a β-phase related seam penetrated with α_2 needles was beneficial for the tensile properties as the fracture elongation could be increased. Moreover, thereby the fracture position could be favorable changed from the TNM to the Ti6242 side. Consequently, the interface evolution is of vital importance for the resulting mechanical properties.
4. As the interface region of laser beam welded dissimilar TNM joints showed to be crucial for the mechanical properties, the transferability of knowledge from laser beam welding to wire- and powder-based laser metal deposition focused on this region. Heteroepitaxial growth was indicated for all processes. Showing the powerful synergistic benefit of the knowledge about laser beam welding and metallurgy, the microstructure and phase evolution at the dissimilar interface could be successfully transferred from laser beam welding to laser metal deposition. Nevertheless, and in contrast to laser beam welding, the crack formation could not be correlated to the evolving microstructure and phases. Thus, the limit of knowledge transferability was revealed. For crack-free dissimilar TNM depositions, a sufficient heat input into the substrate showed to be advantageous, since the thermally induced stresses seem to be of greater importance for laser additive manufactured depositions.

Therefore, by the present thesis the technological and material science fundamentals for dissimilar Ti-Ti- and γ-TiAl-Ti-alloy joints by laser beam welding and laser metal deposition were established. To scale-up the developed approach for crack-free dissimilar TNM joints, a larger preheating device could prove the effective use of large-scaled dissimilar TNM or Ti-Ti-alloy-TNM parts for example in aircraft engine exhaust linings or as a thermal protection shield in space industry.

8. Bibliography

[1] BDL-Bundesverband der Deutschen Luftverkehrswirtschaft, Klimaschutzreport 2017, 2017. https://doi.org/10.1017/CBO9781107415324.004.

[2] M. Peters, C. Leyens, Titan und Titanlegierungen, WILEY-VCH Verlag GmbH & Co. KGaA; Weinheim, Weinheim, 2002.

[3] R. Boyer, G. Welsch, E.W. Collings, Materials Properties Handbook: Titanium Alloys, ASM International, Materials Park, 1998.

[4] B. Sefer, Oxidation and Alpha–Case Phenomena in Titanium Alloys used in Aerospace Industry: Ti–6Al–2Sn–4Zr–2Mo and Ti–6Al–4V, Lulea University of Technology, 2014.

[5] B.P. Bewaly, S. Nag, A. Suzuki, M. Weimer, TiAl alloys in commerical aircraft engines, Mater. High Temp. 33 (2016) 549–559.

[6] H. Clemens, S. Mayer, Design, processing, microstructure, properties, and applications of advanced intermetallic TiAl alloys, Adv. Eng. Mater. 15 (2013) 191–215. https://doi.org/10.1002/adem.201200231.

[7] F. Appel, J.D.H. Paul, M. Oehring, Gamma Titanium Aluminide Alloys, WILEY-VCH Verlag GmbH & Co. KGaA, Weinheim, 2011.

[8] H. Clemens, W. Smarsly, Light-Weight Intermetallic Titanium Aluminides – Status of Research and Development, Adv. Mater. Res. 278 (2011) 551–556. https://doi.org/10.4028/www.scientific.net/AMR.278.551.

[9] T. Tetsui, Development of a TiAl turbocharger for passenger vehicles, Mater. Sci. Eng. A. 329–331 (2002) 582–588. https://doi.org/10.1016/S0921-5093(01)01584-2.

[10] H. Clemens, W. Smarsly, V. Güther, S. Mayer, Advanced intermetallic titanium aluminides, in: Proc. 13th World Conf. Titan., TMS (The Minerals, Metals & Materials Society), 2016: pp. 1189–1200.

[11] V. Güther, M. Achtermann, J. Klose, C. ROthe, I. Eulitz, Manufacturing and Properties of TiAl TNM sheet materials, in: Present. Titan. Eur. 2014, Sorrento Italy, n.d.

[12] E. Schwaighofer, M. Schloffer, T. Schmoelzer, S. Mayer, J. Lindemann, V. Guether, J. Klose, H. Clemens, Influence of Heat Treatments on the Microstructure of a Multi-Phase Titanium Aluminide Alloy, Pract. Metallogr. 49 (2012) 124–137. https://doi.org/10.3139/147.110142.

[13] E. Schwaighofer, H. Clemens, S. Mayer, J. Lindemann, J. Klose, W. Smarsly, V. Güther, Microstructural design and mechanical properties of a cast and heat-treated intermetallic multi-phase γ-TiAl based alloy, Intermetallics. 44 (2014) 128–140. https://doi.org/10.1016/j.intermet.2013.09.010.

[14] A. Bartels, H. Kestler, H. Clemens, Deformation behavior of differently processed γ-titanium aluminides, Mater. Sci. Eng. A. 329 (2002) 153–162. https://doi.org/10.1016/S0921-5093(01)01552-0.

[15] C. Koeppe, A. Bartels, H. Clemens, P. Schretter, W. Glatz, Optimizing the properties of TiAl sheet material for application in heat protection shields or propulsion systems, Mater. Sci. Eng. A. 201 (1995) 182–193. https://doi.org/10.1016/0921-5093(94)09754-2.

[16] S.L. Draper, D. Krause, B. Lerch, I.E. Locci, B. Doehnert, R. Nigam, G. Das, P. Sickles, B. Tabernig, N. Reger, K. Rissbacher, Development and evaluation of TiAl sheet structures for hypersonic applications, Mater. Sci. Eng. A. 464 (2007) 330–342. https://doi.org/10.1016/j.msea.2007.02.020.

[17] M. Abecassis, A. Köster, V.A. Esin, V. Chiaruttini, V. Maurel, Crack growth behavior in dissimilar welded Ti based alloys under biaxial fatigue loading, Int. J. Fatigue. 118 (2019) 209–224. https://doi.org/10.1016/j.ijfatigue.2018.09.013.

[18] C.T. Hsieh, C.Y. Chu, R.K. Shiue, L.W. Tsay, The effect of post-weld heat treatment on the notched tensile fracture of Ti-6Al-4V to Ti-6Al-6V-2Sn dissimilar laser welds, Mater. Des. 59 (2014) 227–232. https://doi.org/10.1016/j.matdes.2014.02.055.

[19] Z.-J. Xu, Y.-Z. Zhang, M.-K. Liu, X.-Y. Gong, Interface microstructure evolution and bonding strength of TC11/γ-TiAl bi-materials fabricated by laser powder deposition, Rare Met. (2014). https://doi.org/10.1007/s12598-014-0243-1.

[20] B. Dogan, X. Zheng, H. Bohm, Characterisation of diffusion bond TiAl-Ti 6242 joints, Mater. High Temp. 23 (2006) 179.

[21] X. Cai, D. Sun et al., Dissimilar joining of TiAl alloy and Ni based superalloy by laser welding technology using V-Cu composite interlayer.pdf, Opt. Laser Technol. 111 (2019) 205–213.

[22] K. Han, H. Wang, B. Zhang, Y. Li, T. Wang, Effect of thermal compensation on microstructure and mechanical properties of electron-beam welded joint for high-Nb containing TiAl/Ti600 alloys, Mater. Des. 131 (2017) 273–285. https://doi.org/10.1016/j.matdes.2017.05.092.

[23] R.R. Wang, G.E. Welsch, Joining titanium materials with tungsten inert gas welding, laser welding, and infrared brazing, J. Prosthet. Dent. 74 (1995) 521–530. https://doi.org/10.1016/S0022-3913(05)80356-7.

[24] A.M. Irisarri, J.L. Barreda, X. Azpiroz, Influence of the filler metal on the properties of Ti-6Al-4V electron beam weldments . Part I : Welding procedures and microstructural characterization, Vaccum. 84 (2010) 393–399. https://doi.org/10.1016/j.vacuum.2009.08.003.

[25] E.J. Kannatey-Asibu, Principles of Laser Materials Processing, John Wiley & Sons, Hoboken, New Jersey, 2009.

[26] C. Dawes, Laser welding, a practical guide, Abington Publishing, Cambridge, 1992.

[27] E. Akman, A. Demir, T. Canel, T. Sinmazçelik, Laser welding of Ti6Al4V titanium alloys, J. Mater. Process. Technol. 209 (2009) 3705–3713. https://doi.org/10.1016/j.jmatprotec.2008.08.026.

[28] G. Casalino, M. Mortello, S.L. Campanelli, Ytterbium fiber laser welding of Ti6Al4V alloy, J. Manuf. Process. 20 (2015) 250–256. https://doi.org/10.1016/j.jmapro.2015.07.003.

[29] Q. Yunlian, D. Ju, H. Quan, Z. Liying, Electron beam welding, laser beam welding and gas tungsten arc welding of titanium sheet, Mater. Sci. Eng. A. 280 (2000) 177–181. https://doi.org/10.1016/S0921-5093(99)00662-0.

[30] Z. Li, S.L. Gobbi, I. Norris, S. Zolotovsky, K.H. Richter, Laser welding techniques for titanium alloy sheet, J. Mater. Process. Technol. 65 (1997) 203–208. https://doi.org/10.1016/S0924-0136(96)02263-7.

[31] N. Kashaev, D. Pugachev, V. Ventzke, F. Fomin, I. Burkhardt, J. Enz, S. Riekehr, Microstructure and mechanical performance of autogenously fibre laser beam welded Ti-6242 butt joints, Mater. Sci. Eng. A. 694 (2017) 110–120. https://doi.org/10.1016/j.msea.2017.03.115.

[32] A. Chamanfar, T. Pasang, A. Ventura, W.Z. Misiolek, Mechanical properties and microstructure of laser welded Ti–6Al–2Sn–4Zr–2Mo (Ti6242) titanium alloy, Mater. Sci. Eng. A. 663 (2016) 213–224. https://doi.org/10.1016/j.msea.2016.02.068.

[33] J. Cao, J. Qi, X. Song, J. Feng, Welding and joining of titanium aluminides, Materials (Basel).

7 (2014) 4930–4962. https://doi.org/10.3390/ma7074930.

[34] M.C. Chaturvedi, Q. Xu, N.L. Richards, Development of crack-free welds in a TiAl-based alloy, J. Mater. Process. Technol. 118 (2001) 74–78. https://doi.org/10.1016/S0924-0136(01)00870-6.

[35] J. Liu, M. Dahmen, V. Ventzke, N. Kashaev, R. Poprawe, The effect of heat treatment on crack control and grain refinement in laser beam welded β-solidifying TiAl-based alloy, Intermetallics. 40 (2013) 65–70. https://doi.org/10.1016/j.intermet.2013.04.007.

[36] Q. Xu, M.C. Chaturvedi, N.L. Richards, The role of phase transformation in electron-beam welding of TiAl-based alloys, Metall. Mater. Trans. A Phys. Metall. Mater. Sci. 30 (1999) 1717–1726. https://doi.org/10.1007/s11661-999-0171-0.

[37] A. Hirose, Y. Arita, K.F. Kobayashi, Microstructure and crack sensitivity of laser-fusion zones of Ti-46 mol % Al-2 mol % Mo alloy, J. Mater. Sci. 30 (1995) 970–979. https://doi.org/10.1007/BF01178432.

[38] C. Guoqing, Z. Binggang, L. Wei, F. Jicai, Crack formation and control upon the electron beam welding of TiAl-based alloys, Intermetallics. 19 (2011) 1857–1863. https://doi.org/10.1016/j.intermet.2011.07.017.

[39] R.A. Patterson, P.L. Martin, B.K. Damkroger, L. Christodoulou, Titanium Aluminide : Electron Beam Weldability, Weld. Res. Suppl. (1990) 39–44.

[40] M.F. Arenas, V.L. Acoff, Analysis of gamma titanium aluminide welds produced by gas tungsten arc welding, Weld. J. (Miami, USA). 82 (2003) 110/S-115/S.

[41] Q. Qiu, Y. Wang, Z. Yang, X. Hu, D. Wang, Microstructure and mechanical properties of TiAl alloy joints vacuum brazed with Ti–Zr–Ni–Cu brazing powder without and with Mo additive, Mater. Des. 90 (2016) 650–659. https://doi.org/10.1016/j.matdes.2015.11.008.

[42] K. Saida, H. Ohnishi, K. Nishimoto, Laser brazing of TiAl intermetallic compound using precious brazing filler metals, Weld. World. 59 (2014) 9–22. https://doi.org/10.1007/s40194-014-0173-4.

[43] T. Tetsui, Effects of brazing filler on properties of brazed joints between TiAl and metallic materials, Intermetallics. 9 (2001) 253–260. https://doi.org/10.1016/S0966-9795(00)00129-1.

[44] G.Q. Wu, Z. Huang, C.Q. Chen, Z.J. Ruan, Y. Zhang, Superplastic diffusion bonding of γ-TiAl-based alloy, Mater. Sci. Eng. A. 380 (2004) 402–407. https://doi.org/10.1016/j.msea.2004.04.011.

[45] A.I.I. Ustinov, Y.V. V. Falchenko, A.Y.Y. Ishchenko, G.K.K. Kharchenko, T.V. V. Melnichenko, A.N.N. Muraveynik, Diffusion welding of γ-TiAl based alloys through nano-layered foil of Ti/Al system, Intermetallics. 16 (2008) 1043–1045. https://doi.org/10.1016/j.intermet.2008.05.002.

[46] M. Holmquist, V. Recina, B. Pettersson, Tensile and creep properties of diffusion bonded titanium alloy IMI 834 to gamma titanium aluminide IHI alloy 01A, Acta Mater. 47 (1999) 1791–1799. https://doi.org/10.1016/S1359-6454(99)00051-8.

[47] P.L. Threadgill, The prospects for joining titanium aluminides, Mater. Sci. Eng. A. 192–193 (1995) 640–646. https://doi.org/10.1016/0921-5093(94)03346-3.

[48] H. Duan, M. Koçak, K.-H. Bohm, V. Ventzke, Transient liquid phase (TLP) bonding of TiAl using various insert foils, Sci. Technol. Weld. Join. 9 (2004) 513–518. https://doi.org/10.1179/136217104225021850.

[49] L.C. Mallory, W.A. Baeslack, D. Phillips, Evolution of the weld heat-affected zone microstructure in a Ti-48AI-2Cr-2Nb gamma titanium aluminide, J. Mater. Sci. Lett. 13 (1994)

1061–1065. https://doi.org/10.1007/BF00277040.

[50] Y. Li, H. Wang, K. Han, X. Li, B. Zhang, Microstructure of Ti-45Al-8.5Nb-0.2W-0.03Y electron beam welding joints, J. Mater. Process. Technol. 250 (2017) 401–409. https://doi.org/10.1016/j.jmatprotec.2017.07.004.

[51] J. Liu, P. Staron, D. Schnubel, N. Schell, N. Huber, N. Kashaev, The cooling gradient and microstructure control in laser beam welded TiAl alloy asisted by temperature field simulation, 29th Congr. Int. Counc. Aeronaut. Sci. (2014) 1–10.

[52] GSI SLV München, Bericht 5155/11 IGF-Nr. 15.596 N DVS-Nr. 01.063 Entwicklung von Fügentechnologien für Leichtbauanwendungen mit schmiedbaren γ-Titanalumniden verbesserter Duktilität, 2011.

[53] B. Majumdar, R. Galun, A. Weisheit, L. Mordike, Formation of a crack-free joint between Ti alloy and Al alloy by using a high-power CO 2 laser, J. Mater. Sci. 32 (1997) 6191–6200.

[54] G. Casalino, M. Mortello, P. Peyre, Yb-YAG laser offset welding of AA5754 and T40 butt joint, J. Mater. Process. Technol. 223 (2015) 139–149. https://doi.org/10.1016/j.jmatprotec.2015.04.003.

[55] A.S. Ramos, M.T. Vieira, S. Simões, F. Viana, M.F. Vieira, Joining of Superalloys to Intermetallics Using Nanolayers, Adv. Mater. Res. 59 (2009) 225–229. https://doi.org/10.4028/www.scientific.net/AMR.59.225.

[56] S. Simões, F. Viana, A.S. Ramos, M.T. Vieira, M.F. Vieira, Reaction-assisted diffusion bonding of TiAl alloy to steel, Mater. Chem. Phys. 171 (2016) 73–82. https://doi.org/10.1016/j.matchemphys.2015.11.032.

[57] R. Jiang, R. Kleer, F.T. Piller, Predicting the future of additive manufacturing: A Delphi study on economic and societal implications of 3D printing for 2030, Technol. Forecast. Soc. Change. 117 (2017) 84–97. https://doi.org/10.1016/j.techfore.2017.01.006.

[58] T. Debroy, H.L. Wei, J.S. Zuback, T. Mukherjee, J.W. Elmer, J.O. Milewski, A.M. Beese, A. Wilson-heid, A. De, W. Zhang, Progress in Materials Science Additive manufacturing of metallic components – Process , structure and properties, Prog. Mater. Sci. 92 (2018) 112–224. https://doi.org/10.1016/j.pmatsci.2017.10.001.

[59] W.U.H. Syed, A.J. Pinkerton, L. Li, Combining wire and coaxial powder feeding in laser direct metal deposition for rapid prototyping, Appl. Surf. Sci. 252 (2006) 4803–4808. https://doi.org/10.1016/j.apsusc.2005.08.118.

[60] R.M. Miranda, G. Lopes, L. Quintino, J.P. Rodrigues, S. Williams, Rapid prototyping with high power fiber lasers, Mater. Des. 29 (2008) 2072–2075. https://doi.org/10.1016/j.matdes.2008.03.030.

[61] K. Richter, S. Orban, S. Nowotny, LASER CLADDING OF THE TITANIUM ALLOY TI6242 TO RESTORE DAMAGED BLADES, in: Proc. 23rd Int. Congr. Appl. Laser Electro-Optics 2004, 2004.

[62] X. Wu et al., Microstructures of laser-deposited Ti–6Al–4V, Mater. Des. 25 (2004) 137–144. https://doi.org/10.1016/j.matdes.2003.09.009.

[63] B. Baufeld, E. Brandl, O. Van Der Biest, Wire based additive layer manufacturing : Comparison of microstructure and mechanical properties of Ti – 6Al – 4V components fabricated by laser-beam deposition and shaped metal deposition, J. Mater. Process. Tech. 211 (2011) 1146–1158. https://doi.org/10.1016/j.jmatprotec.2011.01.018.

[64] S.M. Kelly, S.L. Kampe, Microstructural evolution in Laser-Deposited multilayer Ti6Al-4V build: Part I. Microstructural characterization, Metall. Mater. Trans. A. 35 (2004) 1861–1867.

https://doi.org/10.1007/s11661-004-0094-8.

[65] S.K. Rittinghaus, U. Hecht, V. Werner, A. Weisheit, Heat treatment of laser metal deposited TiAl TNM alloy, Intermetallics. 95 (2018) 94–101. https://doi.org/10.1016/j.intermet.2018.02.002.

[66] H.P. Qu, P. Li, S.Q. Zhang, A. Li, H.M. Wang, The effects of heat treatment on the microstructure and mechanical property of laser melting deposition γ-TiAl intermetallic alloys, Mater. Des. 31 (2010) 2201–2210. https://doi.org/10.1016/j.matdes.2009.10.045.

[67] I.N. Maliutina, H. Si-Mohand, R. Piolet, F. Missemer, A.I. Popelyukh, N.S. Belousova, P. Bertrand, Laser Cladding of γ-TiAl Intermetallic Alloy on Titanium Alloy Substrates, Metall. Mater. Trans. A. 47 (2016) 378–387. https://doi.org/10.1007/s11661-015-3205-9.

[68] M. Thomas, T. Malot, P. Aubry, Laser Metal Deposition of the Intermetallic TiAl Alloy, Metall. Mater. Trans. A. 48 (2017) 3143–3158. https://doi.org/10.1007/s11661-017-4042-9.

[69] H.P. Qu, H.M. Wang, Microstructure and mechanical properties of laser melting deposited γ-TiAl intermetallic alloys, Mater. Sci. Eng. A. 466 (2007) 187–194. https://doi.org/10.1016/j.msea.2007.02.073.

[70] E. Brandl, V. Michailov, B. Viehweger, C. Leyens, Deposition of Ti – 6Al – 4V using laser and wire , part II : Microstructural properties of single beads, Surf. Coat. Technol. 206 (2011) 1120–1129. https://doi.org/10.1016/j.surfcoat.2011.07.094.

[71] G. Schulze, Die Metallurgie des Schweißens, Eisenwerkstoffe-Nichteisenwerkstoffe, 4., Springer-Verlag, Berlin Heidelberg New York, n.d.

[72] G. Lütjering, J.C. Willams, Titanium, Springer-Verlag, Berlin Heidelberg New York, 2007.

[73] T. Ahmed, H.J. Rack, Phase transformations during cooling in α+β titanium alloys, Mater. Sci. Eng. A. A243 (1998) 206–211.

[74] W. Wallgram, T. Schm, L. Cha, G. Das, H. Clemens, F. Jeglitsch, Technology and mechanical properties of advanced y-TiAl based alloys, (n.d.) 1021–1030.

[75] B. Dogan, R. Wagner, P. Beaven, Fracture behavior of Ti-48.5Al-1Mn, Scr. Metall. Mater. 25 (1991) 773–778.

[76] B. Wittkowsky, M. Pfuff, B. Dogan, K.-H. Schwalbe, R. Wagner, Statistical treatment of fracture toughness in Ti-Al-Si-Nb alloys.pdf, Mater. Sci. Eng. (1994) 105–111.

[77] M.S. Dahar, S.A. Tamirisakandala, J.J. Lewandowski, Evolution of fatigue crack growth and fracture behavior in gamma titanium aluminide Ti-43.5Al-4Nb-1Mo-0.1B (TNM) forgings, Int. J. Fatigue. 111 (2018) 54–69. https://doi.org/10.1016/j.ijfatigue.2018.01.026.

[78] Y.W. Kim, Ordered intermetallic alloys, part III: Gamma titanium aluminides, Jom. 46 (1994) 30–39. https://doi.org/10.1007/BF03220745.

[79] M. Schloffer, F. Iqbal, H. Gabrisch, E. Schwaighofer, F.P. Schimansky, S. Mayer, A. Stark, T. Lippmann, M. Göken, F. Pyczak, H. Clemens, Microstructure development and hardness of a powder metallurgical multi phase y-TiAl based alloy, Intermetallics. 22 (2012) 231–240. https://doi.org/10.1016/j.intermet.2011.11.015.

[80] L. Cha, C. Scheu, H. Clemens, H.F. Chladil, G. Dehm, R. Gerling, A. Bartels, Nanometer-scaled lamellar microstructures in Ti-45Al-7.5Nb-(0; 0.5)C alloys and their influence on hardness, Intermetallics. 16 (2008) 868–875. https://doi.org/10.1016/j.intermet.2008.03.009.

[81] H. Clemens, P. Schretter, W. Glatz, Mikrostruktur und Eigenschaften von gamma-TiAl-Basislegierungen, Pract. Metallogr. 33 (1996).

[82] R. Hoppe, F. Appel, Deformation-induced internal stresses in multiphase titanium aluminide alloys, Acta Mater. 64 (2014) 169–178. https://doi.org/10.1016/j.actamat.2013.10.024.

[83] S. Djanarthany et al., Phase transformations in Ti3Al and Ti3Al+Mo aluminides, J. Mater. Res. 6 (1991) 969–986. https://doi.org/DOI: 10.1557/JMR.1991.0969.

[84] S. Mayer, M. Petersmann, F.D. Fischer, H. Clemens, T. Waitz, T. Antretter, Experimental and theoretical evidence of displacive martensite in an intermetallic Mo-containing γ-TiAl based alloy, Acta Mater. 115 (2016) 242–249. https://doi.org/10.1016/j.actamat.2016.06.006.

[85] P. Erdely, P. Staron, E. Maawad, N. Schell, H. Clemens, S. Mayer, Lattice and phase strain evolution during tensile loading of an intermetallic, multi-phase γ-TiAl based alloy, Acta Mater. 158 (2018) 193–205. https://doi.org/10.1016/j.actamat.2018.07.062.

[86] M.W. Rackel, A. Stark, H. Gabrisch, N. Schell, A. Schreyer, F. Pyczak, Orthorhombic phase formation in a Nb-rich γ-TiAl based alloy – An in situ synchrotron radiation investigation, Acta Mater. 121 (2016) 343–351. https://doi.org/10.1016/j.actamat.2016.09.030.

[87] L.A. Bendersky, W.J. Boettinger, Phase transformations in the (Ti, Nb)3 Al section of the TiAlNb system-II. Experimental tem study of microstructures, Acta Metall. Mater. 42 (1994) 2337–2352. https://doi.org/10.1016/0956-7151(94)90312-3.

[88] L.A. Bendersky, W.J. Boettinger, B.P. Burton, F.S. Biancaniello, C.B. Shoemaker, The formation of ordered ω-related phases in alloys of composition Ti 4 Al 3 Nb, Acta Metall. Mater. 38 (1990) 931–943. https://doi.org/10.1016/0956-7151(90)90165-D.

[89] A. Stark, Textur- und Gefügeentwicklung bei der thermomechanischen Umformung Nb-reicher γ-TiAl-Basislegierungen, (2009) 101.

[90] T.H. Yu, C.H. Koo, Microstructural evolution of a hot-rolled Ti – 40Al – 10Nb alloy, Mater. Sci. Eng. A. 240 (1997) 694–701.

[91] M. Schloffer, B. Rashkova, T. Schöberl, E. Schwaighofer, Z. Zhang, H. Clemens, S. Mayer, Evolution of the ωo phase in a β-stabilized multi-phase TiAl alloy and its effect on hardness, Acta Mater. 64 (2014) 241–252. https://doi.org/10.1016/j.actamat.2013.10.036.

[92] X. Wang et al., Atomic-scale observations of B2→ ω-related phases transition in high-Nb containing TiAl alloy, Mater. Charact. 130 (2017) 135–138.

[93] A. Stark, M. Oehring, F. Pyczak, T. Lippmann, L. Lottermoser, A. Schreyer, The transformation mechanism of β phase to ω-related phases in Nb-rich γ-TiAl alloys studied by in situ high-energy X-ray diffraction, Mater. Sci. Forum. 772 (2014). https://doi.org/10.4028/www.scientific.net/MSF.772.85.

[94] H.W. Yang, C. Lin, Phase transformation and microstructural evolution in Ti-44Al-4Nb-4Zr alloy during heat treatment, Metall. Mater. Trans. A Phys. Metall. Mater. Sci. 37 (2006) 3191–3196. https://doi.org/10.1007/BF02586153.

[95] A. Stark, M. Oehring, F. Pyczak, A. Schreyer, In situ observation of various phase transformation paths in Nb-rich TiAl alloys during quenching with different rates, Adv. Eng. Mater. 13 (2011) 700–704. https://doi.org/10.1002/adem.201000289.

[96] L. Song, C. Peng, X. Xu, L. You, Y. Wang, J. Lin, ωo phase precipitation in annealed high Nb containing TiAl alloys, Prog. Nat. Sci. Mater. Int. 25 (2015) 147–152. https://doi.org/10.1016/j.pnsc.2015.03.007.

[97] H. Dosch, A. v. Schwerin, J. Peisl, Point-defect-induced nucleation of the ω phase, Phys. Rev. B. 34 (1986) 1654–1661. https://doi.org/10.1103/PhysRevB.34.1654.

[98] M. Göken, M. Kempf, W.D. Nix, Hardness and modulus of the lamellar microstructure in PST-TiAl studied by nanoindentations and AFM, Acta Mater. 49 (2001) 903–911.

https://doi.org/10.1016/S1359-6454(00)00375-X.

[99] Z.W. Huang, Ordered ω phases in a 4Zr-4Nb-containing TiAl-based alloy, Acta Mater. 56 (2008) 1689–1700. https://doi.org/10.1016/j.actamat.2007.12.013.

[100] J.C. Schuster, M. Palm, Reassessment of the binary aluminum-titanium phase diagram, J. Phase Equilibria Diffus. 27 (2006) 255–277. https://doi.org/10.1361/154770306X109809.

[101] C. McCullough, J.J. Valencia, C.G. Levi, R. Mehrabian, Phase equilibria and solidification in Ti-Al alloys, Acta Metall. 37 (1989) 1321–1336. https://doi.org/10.1016/0001-6160(89)90162-4.

[102] H.F. Chladil, H. Clemens, A. Otto, V. Güther, S. Kremmer, R. Gerling, A. Bartels, Charakterisierung einer β-erstarrenden γ-TiAl-Basislegierung, BHM Berg- Und Hüttenmännische Monatshefte. 9 (2006) 356–361.

[103] H. Clemens, W. Wallgram, S. Kremmer, V. Güther, A. Otto, A. Bartels, Design of novel β-solidifying TiAl alloys with adjustable β/B2-phase fraction and excellent hot-workability, Adv. Eng. Mater. 10 (2008) 707–713. https://doi.org/10.1002/adem.200800164.

[104] B.J. Inkson, H. Clemens, J. Marien, γ + α2 + B2 lamellar domains in rolled TiAl, Scr. Mater. 38 (1998) 1377–1382. https://doi.org/10.1016/S1359-6462(98)00058-X.

[105] H. Clemens, S. Mayer, Intermetallic Titanium Aluminides as Innovative High Temperature Lightweight Structural Materials – How Materialographic Methods Have Contributed to Their Development, Pract. Metallogr. 52 (2015) 691–721. https://doi.org/10.3139/147.110366.

[106] T. Leitner, M. Schloffer, S. Mayer, J. Eßlinger, H. Clemens, R. Pippan, Fracture and R-curve behavior of an intermetallic β-stabilized TiAl alloy with different nearly lamellar microstructures Dedicated to Dr. Wilfried Smarsly on the occasion of his 60th birthday, Intermetallics. 53 (2014) 1–9. https://doi.org/10.1016/j.intermet.2014.04.005.

[107] F. Appel, J.D.H. Paul, M. Oehring, U. Fröbel, U. Lorenz, Creep behavior of TiAl alloys with enhanced high-temperature capability, Metall. Mater. Trans. A Phys. Metall. Mater. Sci. 34 A (2003) 2149–2164. https://doi.org/10.1007/s11661-003-0279-6.

[108] P. Erdely, R. Werner, E. Schwaighofer, H. Clemens, S. Mayer, In-situ study of the time - Temperature-transformation behaviour of a multi-phase intermetallic ??-stabilised TiAl alloy, Intermetallics. 57 (2015) 17–24. https://doi.org/10.1016/j.intermet.2014.09.011.

[109] S. Bolz, M. Oehring, J. Lindemann, F. Pyczak, J. Paul, A. Stark, T. Lippmann, S. Schrüfer, D. Roth-Fagaraseanu, A. Schreyer, S. Weiß, Microstructure and mechanical properties of a forged β-solidifying γ TiAl alloy in different heat treatment conditions, Intermetallics. 58 (2015) 71–83. https://doi.org/10.1016/j.intermet.2014.11.008.

[110] Allegheny Technologies Incorporated, Technical Datasheet ATI Ti-6Al-4V, Grade 5 ATI Ti-6Al-4V, Grade 5 Titanium Alloy, 1 (2012) 4–7.

[111] Smiths High Performance, Datasheet 6242 Titanium, 2016.

[112] AMG titanium alloys & coating, GfE Metalle und Materialien GmbH, Datasheet Titanium Aluminides TNM, 2010. https://doi.org/10.1201/9781420006063.ch8.

[113] R. Aune, L. Battezzati, R. Brooks, I. Egry, H.-J. Fecht, J.-P. Garandet, K.C. Mills, A. Passerone, P.N. Quested, E. Ricci, S. Schneider, S. Seetharaman, R.K. Wunderlich, B. Vinet, Surface tension and viscosity of industrial alloys from parabolic flight experiments — Results of theThermoLab project, Microgravity - Sci. Technol. 16 (2005) 11–14. https://doi.org/10.1007/BF02945937.

[114] R.K. Wunderlich, Surface Tension and Viscosity of Industrial Ti-Alloys Measured by the Oscillating Drop Method on Board Parabolic Flights, High Temp. Mater. Process. 27 (2008)

401–412.

[115] Thyssenkrupp Materials Schweiz, Werkstoffdatenblatt γ-Titanaluminid, 41 (n.d.) 64–65. http://www.thyssenkrupp.ch/documents/gamma_titanium_0213.pdf.

[116] M. Müller, Basischarakterisierung der β-erstarrenden TNM ™ -Legierung für die Anwendung als Turbinenrad im Turbolader, (2012).

[117] T. DebRoy, S.A. David, Physical processes in fusion welding, Revies Mod. Phys. 67 (1995).

[118] S.A. Uspenskiy, V.N. Petrovskiy, D.P. Bykovskiy, V.D. Mironov, N.M. Prokopova, E. V Tret'yakov, Spectral diagnostics of a vapor-plasma plume produced during welding titanium with a high-power ytterbium fiber laser, J. Phys. Conf. Ser. 594 (2015) 012033. https://doi.org/10.1088/1742-6596/594/1/012033.

[119] P.Y. Shcheglov, S.A. Uspenskiy, A. V Gumenyuk, V.N. Petrovskiy, M. Rethmeier, V.M. Yermachenko, Plume attenuation of laser radiation during high power fiber laser welding, Laser Phys. Lett. 8 (2011) 475–480. https://doi.org/DOI 10.1002/lapl.201110010.

[120] X.L. Gao, L.J. Zhang, J. Liu, J.X. Zhang, Porosity and microstructure in pulsed Nd:YAG laser welded Ti6Al4V sheet, J. Mater. Process. Technol. 214 (2014) 1316–1325. https://doi.org/10.1016/j.jmatprotec.2014.01.015.

[121] M.Y. Krasnoperov, R.R.G.M. Pieters, I.M. Richardson, Weld pool geometry during keyhole laser welding of thin steel sheets, Sci. Technol. Weld. Join. 9 (2004) 501–506. https://doi.org/10.1179/136217104225021733.

[122] O. Jin, S. Mall, Effects of microstructure on short crack growth behavior of Ti-6Al-2Sn-4Zr-2Mo-0.1Si alloy, Mater. Sci. Eng. A. 359 (2003) 356–367. https://doi.org/10.1016/S0921-5093(03)00377-0.

[123] H.L. Wei, J.W. Elmer, T. DebRoy, Crystal growth during keyhole mode laser welding, Acta Mater. 133 (2017) 10–20. https://doi.org/10.1016/j.actamat.2017.04.074.

[124] S.R.K. Rao, G.M. Reddy, M. Kamaraj, K.P. Rao, Grain refinement through arc manipulation techniques in Al-Cu alloy GTA welds, Mater. Sci. Eng. A. 404 (2005) 227–234. https://doi.org/10.1016/j.msea.2005.05.080.

[125] S. Kou, Welding Metallurgy, second ed., Hoboken, NJ, 2003.

[126] S. Pang, X. Chen, X. Shao, S. Gong, J. Xiao, Dynamics of vapor plume in transient keyhole during laser welding of stainless steel: Local evaporation, plume swing and gas entrapment into porosity, Opt. Lasers Eng. 82 (2016) 28–40. https://doi.org/10.1016/j.optlaseng.2016.01.019.

[127] C. Panwisawas, B. Perumal, R.M. Ward, N. Turner, R.P. Turner, J.W. Brooks, H.C. Basoalto, Keyhole formation and thermal fluid flow-induced porosity during laser fusion welding in titanium alloys: Experimental and modelling, Acta Mater. 126 (2017) 251–263. https://doi.org/10.1016/j.actamat.2016.12.062.

[128] F. Fomin, N. Kashaev, Influence of Porosity on the High Cycle Fatigue Behaviour of Laser Beam Welded Ti-6Al-4V Butt Joints, Procedia Struct. Integr. 7 (2017) 415–422. https://doi.org/10.1016/j.prostr.2017.11.107.

[129] B. Cárcel, A. Serrano, J. Zambrano, V. Amigó, A.C. Cárcel, Laser cladding of TiAl intermetallic alloy on Ti6Al4V. Process optimization and properties, Phys. Procedia. 56 (2014) 284–293. https://doi.org/10.1016/j.phpro.2014.08.173.

[130] I. Gibson, D. Rosen, B. Stucker, Standard Terminology for Additive Manufacturing Technologies, Rapid Manuf. Assoc. (2013) 10–12. https://doi.org/10.1520/F2792-12A.2.

[131] S. Nowotny, S. Scharek, E. Beyer, K.H. Richter, Laser beam build-up welding: Precision in repair, surface cladding, and direct 3D metal deposition, J. Therm. Spray Technol. 16 (2007) 344–348. https://doi.org/10.1007/s11666-007-9028-5.

[132] S.K. Rittinghaus, Schlussbericht 130273 LUFO REPTIL Entwicklung einer automatisierten Reparatur- und Fertigungstechnologie mittels Laserauftragschweißen für Triebwerksschaufeln aus Titanaluminiden, Aachen, 2017.

[133] B. Liu, R. Wildman, C. Tuck, I. Ashcroft, R. Hague, Investigation the Effect of Particle Size Distribution on Processing Parameters Optimisation in Selective Laser Melting Process, in: Int. Solid Free. Fabr. Symp. an Addit. Manuf. Conf. Univ. Texas Austin, 2011: pp. 227–238. https://doi.org/10.1017/CBO9781107415324.004.

[134] H. Qi, M. Azer, A. Ritter, Studies of standard heat treatment effects on microstructure and mechanical properties of laser net shape manufactured INCONEL 718, Metall. Mater. Trans. A Phys. Metall. Mater. Sci. 40 (2009) 2410–2422. https://doi.org/10.1007/s11661-009-9949-3.

[135] E. Brandl, C. Leyens, F. Palm, Mechanical properties of additive manufactured Ti-6Al-4V using wire and powder based processes, IOP Conf. Ser. Mater. Sci. Eng. 26 (2011). https://doi.org/10.1088/1757-899X/26/1/012004.

[136] J.C. Lippold, Welding Metallurgy and Weldability, WILEY-VCH Verlag GmbH & Co. KGaA, Weinheim, 2015.

[137] E. Brandl, A. Schoberth, C. Leyens, Morphology, microstructure, and hardness of titanium (Ti-6Al-4V) blocks deposited by wire-feed additive layer manufacturing (ALM), Mater. Sci. Eng. A. 532 (2012) 295–307. https://doi.org/10.1016/j.msea.2011.10.095.

[138] T. Wang, Y.Y. Zhu, S.Q. Zhang, H.B. Tang, H.M. Wang, Grain morphology evolution behavior of titanium alloy components during laser melting deposition additive manufacturing, J. Alloys Compd. 632 (2015) 505–513. https://doi.org/10.1016/j.jallcom.2015.01.256.

[139] L. Kempen, L. Thijs, B. Vrancken, S. Buls, J. Van Humbeeck, J.-P. Kruth, Producing crack-free, high density M2 HSS parts by Selective Laser Melting: Pre-heating the baseplate, Proc. 24th Int. Solid Free. Fabr. Symp. (2013) 131–139.

[140] L. N. Carter, M. M. Attallah, R. C. Reed, Laser powder bed fabrication of nickel-base superalloys: influence of parameters; characterisation, quantification and mitigation of cracking, Superalloys 2012. (2012) 577--586.

[141] T. Mukherjee, W. Zhang, T. DebRoy, An improved prediction of residual stresses and distortion in additive manufacturing, Comput. Mater. Sci. 126 (2017) 360–372. https://doi.org/10.1016/j.commatsci.2016.10.003.

[142] F. Caiazzo, Additive manufacturing by means of laser-aided directed metal deposition of titanium wire, Int. J. Adv. Manuf. Technol. (2018). https://doi.org/10.1007/s00170-018-1760-0.

[143] Q. Liu, Y. Wang, H. Zheng, K. Tang, H. Li, S. Gong, Wire feeding based laser additive manufacturing TC17 titanium alloy, Mater. Technol. 31 (2016) 108–114. https://doi.org/10.1179/1753555715Y.0000000075.

[144] P.A. Kobryn, E.H. Moore, S.L. Semiatin, THE EFFECT OF LASER POWER AND TRAVERSE SPEED ON MICROSTRUCTURE , POROSITY , AND BUILD HEIGHT IN LASER-DEPOSITED Ti-6Al-4V, Scr. Mater. 43 (2000) 299–305.

[145] B.E. Carroll, T.A. Palmer, A.M. Beese, Anisotropic tensile behavior of Ti-6Al-4V components fabricated with directed energy deposition additive manufacturing, Acta Mater. 87 (2015) 309–320. https://doi.org/10.1016/j.actamat.2014.12.054.

[146] D.C. et al Austin, Microstructural Investigation and Impact Testing of Additive Manufactured Ti-6Al-4V.pdf, Charact. Miner. Met. Mater. 2017. (2017).

[147] W.E. King, H.D. Barth, V.M. Castillo, G.F. Gallegos, J.W. Gibbs, D.E. Hahn, C. Kamath, A.M. Rubenchik, Observation of keyhole-mode laser melting in laser powder-bed fusion additive manufacturing, J. Mater. Process. Technol. 214 (2014) 2915–2925. https://doi.org/10.1016/j.jmatprotec.2014.06.005.

[148] R. Rai, J.W. Elmer, T.A. Palmer, T. Debroy, Heat transfer and fluid flow during keyhole mode laser welding of tantalum, Ti-6Al-4V, 304L stainless steel and vanadium, J. Phys. D. Appl. Phys. 40 (2007) 5753–5766. https://doi.org/10.1088/0022-3727/40/18/037.

[149] W.J. Sames, F. Medina, W.H. Peter, S.S. Babu, R.R. Dehoff, Effect of process control and powder quality on inconel 718 produced using electron beam melting, 8th Int. Symp. Superalloy 718 Deriv. 2014. (2014) 409–423. https://doi.org/10.1002/9781119016854.ch32.

[150] G. Kasperovich, J. Haubrich, J. Gussone, G. Requena, Correlation between porosity and processing parameters in TiAl6V4 produced by selective laser melting, Mater. Des. 105 (2016) 160–170. https://doi.org/10.1016/j.matdes.2016.05.070.

[151] K. Kumar, T. Sparks, F. Liou, Parameter determination and experimental validaion of a wire feed additive manufacturing model, in: Proc. Annu. Int. Solid Free. Fabr. Symp. Austin, Texas, USA, 2015: pp. 1129–1153.

[152] A.R.C. Sharman, J.I. Hughes, K. Ridgway, Characterisation of titanium aluminide components manufactured by laser metal deposition, Intermetallics. 93 (2018) 89–92. https://doi.org/10.1016/j.intermet.2017.11.013.

[153] S. Nowotny, S. Scharek, A. Schmidt, Advanced laser technology applied to cladding and buildup, Weld. J. (Miami, Fla). 86 (2007) 48–51.

[154] W.J. Sames, F.A. List, S. Pannala, R.R. Dehoff, S.S. Babu, The metallurgy and processing science of metal additive manufacturing, Int. Mater. Rev. 61 (2016) 315–360. https://doi.org/10.1080/09506608.2015.1116649.

[155] S.A. David, J.M. Vitek, Correlation between solidification parameters and weld microstructures, Int. Mater. Rev. 34 (1989) 213–245. https://doi.org/10.1179/imr.1989.34.1.213.

[156] H.L. Wei, J.W. Elmer, T. Debroy, Origin of grain orientation during solidification of an aluminum alloy, Acta Mater. 115 (2016) 123–131. https://doi.org/10.1016/j.actamat.2016.05.057.

[157] H. Yin, S.D. Felicelli, Dendrite growth simulation during solidification in the LENS process, Acta Mater. 58 (2010) 1455–1465. https://doi.org/10.1016/j.actamat.2009.10.053.

[158] D. Rosenthal, Mathematical Theory of Heat Distribution during Welding and Cutting, Weld. J. 20 (1941) 220–234.

[159] S.A. David, S.C. Deevi, Welding of unique and advanced ductile intermetallic alloys for high-temperature applications, Sci. Technol. Weld. Join. 22 (2017) 681–705. https://doi.org/10.1080/13621718.2017.1304859.

[160] M.. Chaturvedi, N.. Richards, Q. Xu, Electron beam welding of a Ti–45Al–2Nb–2Mn+0.8 vol.% TiB2 XD alloy, Mater. Sci. Eng. A. 239–240 (1997) 605–612. https://doi.org/10.1016/s0921-5093(97)00637-0.

[161] L. Löber, F.P. Schimansky, U. Kühn, F. Pyczak, J. Eckert, Selective laser melting of a beta-solidifying TNM-B1 titanium aluminide alloy, J. Mater. Process. Technol. 214 (2014) 1852–1860. https://doi.org/10.1016/j.jmatprotec.2014.04.002.

[162] P.E. Denny, E. Metzbower, Laser Beam Welding of Titanium Microstructure of Ti 6-4, Weld. Res. Suppl. (1989) 342–348.

[163] F. Fomin, M. Horstmann, N. Huber, N. Kashaev, Probabilistic fatigue-life assessment model for laser-welded Ti-6Al-4V butt joints in the high-cycle fatigue regime, Int. J. Fatigue. 116 (2018) 22–35. https://doi.org/10.1016/j.ijfatigue.2018.06.012.

[164] A. Squillace, U. Prisco, S. Ciliberto, A. Astarita, Effect of welding parameters on morphology and mechanical properties of Ti-6Al-4V laser beam welded butt joints, J. Mater. Process. Technol. 212 (2012) 427–436. https://doi.org/10.1016/j.jmatprotec.2011.10.005.

[165] J. Ahn, L. Chen, C.M. Davies, J.P. Dear, Parametric optimisation and microstructural analysis on high power Yb-fibre laser welding of Ti-6Al-4V, Opt. Lasers Eng. 86 (2016) 156–171. https://doi.org/10.1016/j.optlaseng.2016.06.002.

[166] J. Iammi, J. Folkes, Welding of Ti-6Al-4V Using a Fibre Laser , Part I : Investigation of the Process Characteristics, Lasers Eng. 21 (2010) 77–94.

[167] A. Costa, R. Miranda, L. Quintino, D. Yapp, Analysis of Beam Material Interaction in Welding of Titanium with Fiber Lasers, Mater. Manuf. Process. 22 (2007) 798–803. https://doi.org/10.1080/10426910701446671.

[168] G. Casalino, F. Curcio, F. Memola Capece Minutolo, Investigation on Ti6Al4V laser welding using statistical and Taguchi approaches, J. Mater. Process. Technol. 167 (2005) 422–428. https://doi.org/10.1016/j.jmatprotec.2005.05.031.

[169] F. Caiazzo, V. Alfieri, G. Corrado, F. Cardaropoli, V. Sergi, Investigation and Optimization of Laser Welding of Ti-6Al-4V Titanium Alloy Plates., J. Manuf. Sci. Eng. 135 (2013) 1–8. https://doi.org/10.1115/MSEC2013-1134.

[170] F. Caiazzo, F. Curcio, G. Daurelio, F.M.C. Minutolo, Ti6Al4V sheets lap and butt joints carried out by CO2 laser: Mechanical and morphological characterization, J. Mater. Process. Technol. 149 (2004) 546–552. https://doi.org/10.1016/j.jmatprotec.2003.12.026.

[171] T.S. Balasubramanian, M. Balakrishnan, V. Balasubramanian, M.A.M. Manickam, Influence of welding processes on microstructure, tensile and impact properties of Ti-6Al-4V alloy joints, Trans. Nonferrous Met. Soc. China (English Ed. 21 (2011) 1253–1262. https://doi.org/10.1016/S1003-6326(11)60850-9.

[172] C. Lavogiez, S. Dancette, S. Cazottes, C. Le Bourlot, E. Maire, In situ analysis of plasticity and damage nucleation in a Ti-6Al-4V alloy and laser weld, Mater. Charact. 146 (2018) 81–90. https://doi.org/10.1016/j.matchar.2018.09.039.

[173] M.J. Donachie, Titanium: A Technical Guide, ASM Int. (2000) 381. https://doi.org/10.1016/j.scriptamat.2006.08.010.

[174] J. Liu, P. Staron, S. Riekehr, A. Stark, N. Schell, N. Huber, A. Schreyer, M. Müller, N. Kashaev, In situ study of phase transformations during laser-beam welding of a TiAl alloy for grain refinement and mechanical property optimization, Intermetallics. 62 (2015) 27–35. https://doi.org/10.1016/j.intermet.2015.03.003.

[175] Y. Chen, K. Zhang, X. Hu, Z. Lei, L. Ni, Study on laser welding of a Ti-22Al-25Nb alloy: Microstructural evolution and high temperature brittle behavior, J. Alloys Compd. 681 (2016) 175–185. https://doi.org/10.1016/j.jallcom.2016.04.212.

[176] X. Cai, D. Sun, H. Li, H. Guo, X. Gu, Z. Zhao, Microstructure characteristics and mechanical properties of laser-welded joint of γ-TiAl alloy with pure Ti filler metal, Opt. Laser Technol. 97 (2017) 242–247. https://doi.org/10.1016/j.optlastec.2017.07.011.

[177] Y.-W. Kim, Gamma titanium aluminides: Their status and future, Jom. 47 (1995) 39–42.

https://doi.org/10.1007/BF03221229.

[178] L. Xiong, G. Mi, C. Wang, Microsturcture and mechanical properties of laser-welded joints of Ti-22Al-25Nb-Ti-6Al-4V dissimilar titanium alloys, J. Laser Appl. 30 (2018).

[179] J. Liu, V. Ventzke, P. Staron, N. Schell, N. Kashaev, N. Huber, Investigation of in situ and conventional post-weld heat treatments on dual-laser-beam-welded y-TiAl-based alloy, Adv. Eng. Mater. 14 (2012) 923–927. https://doi.org/10.1002/adem.201200113.

[180] S.H. Mok et al., Deposition of Ti – 6Al – 4V using a high power diode laser and wire ,Part I & Part II : Investigation on the process characteristics and Investigation on the mechanical properties, Surf. Coatings Technol. 202 (2008). https://doi.org/10.1016/j.surfcoat.2008.02.008.

[181] M. Neikter, P. Åkerfeldt, R. Pederson, M.-L. Antti, Microstructural characterization and comparison of Ti-6Al-4V manufactured with different additive manufacturing processes, Mater. Charact. 143 (2018) 68–75. https://doi.org/10.1016/j.matchar.2018.02.003.

[182] S.M. Kelly, S.L. Kampe, Microstructural-evolution-in-laser-deposited-multilayer-Ti-6AI-4V-builds-Part-II-Thermal-modeling, Metall. Mater. Trans. A. 35A (2004) 1869–1879.

[183] N. Chekir, Y. Tian, R. Gauvin, N. Brodusch, J.J. Sixsmith, M. Brochu, Laser Wire Deposition of Thick Ti-6Al-4V Buildups: Heat Transfer Model, Microstructure, and Mechanical Properties Evaluations, Metall. Mater. Trans. A. (2018). https://doi.org/10.1007/s11661-018-4927-2.

[184] P. Åkerfeldt, M.L. Antti, R. Pederson, Influence of microstructure on mechanical properties of laser metal wire-deposited Ti-6Al-4V, Mater. Sci. Eng. A. 674 (2016) 428–437. https://doi.org/10.1016/j.msea.2016.07.038.

[185] E. Brandl, F. Palm, V. Michailov, B. Viehweger, C. Leyens, Mechanical properties of additive manufactured titanium (Ti – 6Al – 4V) blocks deposited by a solid-state laser and wire, Mater. Des. 32 (2011) 4665–4675. https://doi.org/10.1016/j.matdes.2011.06.062.

[186] F. et al. Spranger, Build-up strategies for additive manufacturing of three dimensional Ti-6Al-4V-parts produced by laser metal deposition, J. Laser Appl. 30 (2018).

[187] P.L. Blackwell, A. Wisbey, Laser-aided manufacturing technologies; their application to the near-net shape forming of a high-strength titanium alloy, J. Mater. Process. Technol. 170 (2005) 268–276. https://doi.org/10.1016/j.jmatprotec.2005.05.014.

[188] P. Surrey, M. Möller, C. Emmelmann, M. Heilemann, J. Weber, From Powder to Solid: The Material Evolution of Ti-6Al-4V during Laser Metal Deposition, Key Eng. Mater. 770 (2018) 135–147. https://doi.org/10.4028/www.scientific.net/KEM.770.135.

[189] A. Saboori, S. Biamino, S. Tusacciu, E. Reggio, M. Busatto, M. Lai, P. Fino, M. Lombardi, Characterization of single track formation from Ti-6AL-4V alloy at different process parameters by Direct Energy Deposition, Euro PM2017 Congr. Exhebition. (2017) 1–5.

[190] J. Yu, M. Rombouts, G. Maes, F. Motmans, Material properties of Ti6Al4V parts produced by laser metal deposition, in: Phys. Procedia, 2012: pp. 416–424. https://doi.org/10.1016/j.phpro.2012.10.056.

[191] B. Vrancken, L. Thijs, J.P. Kruth, J. Van Humbeeck, Microstructure and mechanical properties of a novel β titanium metallic composite by selective laser melting, Acta Mater. 68 (2014) 150–158. https://doi.org/10.1016/j.actamat.2014.01.018.

[192] M. Heilemann, M. Möller, C. Emmelmann, I. Burkhardt, S. Riekehr, V. Ventzke, N. Kashaev, J. Enz, Laser metal deposition of Ti-6Al-4V structures: Analysis of the build height dependent microstructure and mechanical properties, in: Contrib. Pap. from Mater. Sci. Technol. 2017, 2017: pp. 289–291. https://doi.org/10.7449/2017/MST.

[193] J.S. Keist, T.A. Palmer, Role of geometry on properties of additively manufactured Ti-6Al-4V structures fabricated using laser based directed energy deposition, Mater. Des. 106 (2016) 482–494. https://doi.org/10.1016/j.matdes.2016.05.045.

[194] J. Lu, L. Chang, J. Wang, L. Sang, S. Wu, Y. Zhang, In-situ investigation of the anisotropic mechanical properties of laser direct metal deposition Ti6Al4V alloy, Mater. Sci. Eng. A. 712 (2018) 199–205. https://doi.org/10.1016/j.msea.2017.11.106.

[195] Y. Ma, D. Cuiuri, N. Hoye, H. Li, Z. Pan, Effects of wire feed conditions on in situ alloying and additive layer manufacturing of titanium aluminides using gas tungsten arc welding, J. Mater. Res. 29 (2014) 2066–2071. https://doi.org/10.1557/jmr.2014.203.

[196] J. Wang, Z. Pan, Y. Ma, Y. Lu, C. Shen, D. Cuiuri, H. Li, Characterization of wire arc additively manufactured titanium aluminide functionally graded material: Microstructure, mechanical properties and oxidation behaviour, Mater. Sci. Eng. A. 734 (2018) 110–119. https://doi.org/10.1016/j.msea.2018.07.097.

[197] C. Shen, K.-D. Liss, M. Reid, Z. Pan, Y. Ma, X. Li, H. Li, In-situ neutron diffraction characterization on the phase evolution of γ-TiAl alloy during the wire-arc additive manufacturing process, J. Alloys Compd. (2018). https://doi.org/10.1016/j.jallcom.2018.11.150.

[198] S. Rittinghaus, W.G. Vargas, L.M. Deposition, A. Manufacturing, I.G. Atomization, Laser Metal Deposition of Titanium Aluminides – A Future Repair Technology for Jet Engine Blades ?, in: Proc. 13th World Conf. Titan., 2016: pp. 1205–1210. https://doi.org/10.1002/9781119296126.ch205.

[199] F. Brueckner, A. Seidel, A. Straubel, R. Willner, C. Leyens, E. Beyer, Laser-based manufacturing of components using materials with high cracking susceptibility, J. Laser Appl. 28 (2016) 022305. https://doi.org/10.2351/1.4943902.

[200] E. Brogle, M. Staubli et al., Friction welding of y titanium aluminide to steel body with nickel alloy connecting piece there between, United States Pat. 5 431 752. (1995).

[201] W.B. Lee, M.G. Kim, J.M. Koo, K.K. Kim, D.J. Quesnel, Y.J. Kim, S.B. Jung, Friction welding of TiAl and AISI4140, J. Mater. Sci. 39 (2004) 1125–1128. https://doi.org/10.1023/B:JMSC.0000012960.59095.5a.

[202] X. Zheng, B. Dogan, K. Bohm, Microstructural and Mechanical Characterization of TiAl / Ti6242 Diffusion Bonds, (2007) 1393–1400. https://doi.org/10.4028/www.scientific.net/MSF.546-549.1393.

[203] T. Noda, T. Shimizu, M. Okabe, T. Iikubo, Joining of TiAl and steels by induction brazing, Mater. Sci. Eng. A. 239–240 (1997) 613–618. https://doi.org/10.1016/S0921-5093(97)00638-2.

[204] X. Song, B. Ben, S. Hu, J. Feng, D. Tang, Vacuum brazing high Nb-containing TiAl alloy to Ti60 alloy using Ti-28Ni eutectic brazing alloy, J. Alloys Compd. 692 (2017) 485–491. https://doi.org/10.1016/j.jallcom.2016.09.074.

[205] L. Yan, X. Chen, Y. Zhang, J.W. Newkirk, F. Liou, Fabrication of Functionally Graded Ti and γ-TiAl by Laser Metal Deposition, JOM. (2017) 1–6. https://doi.org/10.1007/s11837-017-2582-5.

[206] J. Li, J. Shen, S. Hu, H. Zhang, X. Bu, Microstructure and mechanical properties of Ti-22Al-25Nb/TA15 dissimilar joint fabricated by dual-beam laser welding, Opt. Laser Technol. 109 (2019) 123–130. https://doi.org/10.1016/j.optlastec.2018.07.077.

[207] W. Ge, F. Lin, C. Guo, Functional Gradient Material of Ti-6Al-4V And γ-TiAl Fabricated by Electron Beam Selective Melting, Solid Free. Fabr. Symp. (2015) 12.

https://doi.org/10.1007/s13398-014-0173-7.2.

[208] D. Li, S. Hu, J. Shen, H. Zhang, X. Bu, Microstructure and Mechanical Properties of Laser-Welded Joints of Ti-22Al-25Nb/TA15 Dissimilar Titanium Alloys, J. Mater. Eng. Perform. 25 (2016). https://doi.org/10.1007/s11665-016-2025-4.

[209] T. Vilaro, V. Kottman-Rexerodt, M. Thomas, C. Colin, P. Bertrand, L. Thivillon, S. Abed, V. Ji, P. Aubry, P. Peyre, T. Malot, Direct Fabrication of a Ti-47Al-2Cr-2Nb Alloy by Selective Laser Melting and Direct Metal Deposition Processes, Adv. Mater. Res. 89–91 (2010) 586–591. https://doi.org/10.4028/www.scientific.net/AMR.89-91.586.

[210] H.P. Qu, P. Li, S.Q. Zhang, A. Li, H.M. Wang, Microstructure and mechanical property of laser melting deposition (LMD) Ti/TiAl structural gradient material, Mater. Des. 31 (2010) 574–582. https://doi.org/10.1016/j.matdes.2009.07.004.

[211] M. Thomas, Progress in the understanding of the microstructure evolution of direct laser fabricated TiAl To cite this version : microstructure evolution of direct, in: THERMEC 2016, 2016.

[212] Y. Bin Zhang, B.Y. Huang, H.X. Li, Influence of the Parameters on the Laser Deposited TiAl Layer, Adv. Mater. Res. 306–307 (2011) 496–499. https://doi.org/10.4028/www.scientific.net/AMR.306-307.496.

[213] M. Doubenskaia, A. Domashenkov, I. Smurov, P. Petrovskiy, Comprehensive analysis of selective laser melting of TiAl powder, in: WLT LiM 2017, 2017.

[214] J. Bauch, R. Rosenkranz, Physikalische Werkstoffdiagnostik, Springer-Verlag, 2017. https://doi.org/10.1007/978-3-662-53952-1.

[215] J. Herrnring, P. Staron, N. Kashaev, B. Klusemann, Multiscale process simulation of residual stress fields of laser beam welded precipitation hardened AA6082, Materialia. 3 (2018) 243–255. https://doi.org/10.1016/j.mtla.2018.08.010.

[216] A.C. Popescu, C. Delval, M. Leparoux, Control of porosity and spatter in laser welding of thick AlMg5 parts using high-speed imaging and optical microscopy, Metals (Basel). 7 (2017). https://doi.org/10.3390/met7110452.

[217] DIN EN ISO 13919-1:1996, Elekronen- und Laserstrahl-Schweißverbindungen Leitfaden für Bewertungsgruppen für Unregelmäßigkeiten Teil 1: Stahl, (1996).

[218] DIN EN ISO 5817:2014, Schweißen - Schmelzschweißverbindungen an Stahl, Nickel, Titan und deren Legierungen (ohne Strahlschweißen) - Bwertungsgruppen von Unregelmäßigkeiten, (2014).

[219] C. Löffl, H. Saage, M. Göken, In situ X-ray tomography investigation of the crack formation in an intermetallic beta-stabilized TiAl-alloy during a stepwise tensile loading, Int. J. Fatigue. 124 (2019) 138–148. https://doi.org/10.1016/j.ijfatigue.2019.02.035.

[220] D. Hu, H. Jiang, Martensite in a TiAl alloy quenched from beta phase field, Intermetallics. 56 (2015) 87–95. https://doi.org/10.1016/j.intermet.2014.09.007.

[221] S.L. Semiatin, T.M. Lehner, J.D. Miller, R.D. Doherty, D.U. Furrer, Alpha/beta heat treatment of a titanium alloy with a nonuniform microstructure, Metall. Mater. Trans. A Phys. Metall. Mater. Sci. 38 (2007) 910–921. https://doi.org/10.1007/s11661-007-9088-7.

[222] I. Burkhardt, V. Ventzke, S. Riekehr, N. Kashaev, J. Enz, Laser welding and microstructural characterization of dissimilar γ-TiAl-Ti6242 joints, Intermetallics. 104 (2019) 74–83. https://doi.org/10.1016/J.INTERMET.2018.09.012.

[223] A. Hellwig, Experimentelle Untersuchungen zur Konstitution des Systems Aluminium-Titan-Niob, (1990).